

**A Surface Science and Thin Film  
Approach to the Development of  
Functional Materials**

**James Naughton**

Submitted for the degree of Doctor of Philosophy

**The University of York**

**Departments of Chemistry and Physics**

**September 2011**

## Abstract

Nanoscale properties are becoming increasingly important for the successful utilisation of modern materials and devices, where surfaces or interfaces often largely define functionality. It is critical to understand surface behaviour and its impact on properties for the development of new and existing materials. Current surface science and thin-film techniques have been utilised and developed to investigate promising functional materials.

The surface chemistry of Au/Pd surface alloys was examined for the selective oxidation (selox) of crotyl alcohol to crotonaldehyde. X-ray Photoelectron Spectroscopy (XPS) and Thermal Desorption Spectroscopy (TDS) have been used to elucidate the reaction pathway for the alcohol and the main products. Au moderates the surface reaction by ‘turning off’ the main decomposition pathway of the aldehyde. The amount of surface Au has a critical role in determining the selectivity. To mimic ‘true’ selox, the influence of co-adsorbed O over the Au/Pd alloys was also investigated. O plays an important role in aiding desorption of the aldehyde. The exact nature and role of Au and O in moderating the reaction over Pd(111) requires further investigation.

A key area of technological interest is field of spintronics, whereby the spin and charge of electrons are exploited for electronics. Thin-films of  $\text{Fe}_3\text{O}_4$ , a promising spin injector, were grown on a variety of substrates to characterise the magnetic/magnetoresistive (MR) properties. The Magnetorefractive Effect (MRE), an optical technique, was used for non-contact measurements of the MR. Despite no difference in the MR, the MRE shows a thickness dependence, which is partly due to the large skin-depth associated with  $\text{Fe}_3\text{O}_4$ . Modelling the complex dielectric function for  $\text{Fe}_3\text{O}_4/\text{MgO}$  allowed simulations to be carried out of the IR and MRE spectra. With further work, the model may be used to determine film thickness, examine the conductivity mechanisms and their influence on the MR/MRE.

## Contents

<b>Chapter 1 – Introduction</b>	<b>1</b>
1.1 – Motivation	1
1.1.1 – Advanced Functional Materials	1
1.1.2 – Surfaces and Thin-Films	1
1.1.3 – Surface Science Techniques	2
1.1.4 – Thin-Film Growth	2
1.2 – Heterogeneous catalysis	3
1.3 – Selective oxidation of alcohols by heterogeneous catalysts	6
1.3.1 – Allylic alcohols over single crystal surfaces	8
1.3.2 – Aldehyde over single crystal surfaces	9
1.3.3 – Au/Pd systems for selox	10
1.3.4 – Formation of Au/Pd(111) surface alloys	11
1.4 – Magnetic Thin-Films for Spintronics	12
1.4.1 – Giant Magnetoresistance	13
1.4.2 – Spintronics	17
1.4.3 – Half metals	20
1.4.4 – Oxide Materials for Spintronics	21
1.4.5 – Magnetite (Fe <sub>3</sub> O <sub>4</sub> )	21
1.5 – Combinatorial Methods	28
1.6 – Thesis Aims	28
1.7 – References	30
<b>Chapter 2 – Experimental</b>	<b>39</b>
2.1 – Ultra High Vacuum (UHV) Equipment	39
2.1.1 – UHV Single Crystal Chamber	39
2.1.1.1 – Manifold and adsorbates	42
2.1.1.2 – Pd crystal mounting	43
2.1.2 – Molecular Beam Epitaxy (MBE)	44
2.1.3 – Metastable De-excitation Spectroscopy (MDS)	49
2.1.4 – Combinatorial sputtering rig	50
2.2 – Composition Analysis	51
2.2.1 – X-ray Photoelectron Spectroscopy (XPS)	51
2.2.2 – Auger Electron Spectroscopy (AES)	54
2.2.3 – Ultraviolet Photoelectron Spectroscopy (UPS)	55
2.3 – Thermal Desorption Spectroscopy (TDS)	56
2.4 – Temperature Programmed XP studies	57

2.5 – Structural Analysis	58
2.5.1 – Low Energy Electron Diffraction (LEED)	58
2.5.2 – Reflection Energy Electron Diffraction (RHEED)	59
2.5.3 – Transmission Electron Microscopy (TEM)	60
2.6 – Magnetic Analysis	60
2.6.1 – Vibrating Sample Magnetometry (VSM)	60
2.6.2 – Magnetoresistive (MR) measurements	61
2.6.3 – Magneto refractive Effect (MRE) measurements	62
2.7 – References	65
<b>Chapter 3 – Reactivity of crotyl alcohol over Au/Pd(111) surface alloys</b>	<b>68</b>
3.1 – Introduction	68
3.1.1 – Pd selox deactivation	68
3.1.2 – Au/Pd systems	70
3.2 – Results and Discussion	71
3.2.1 – Growth of Au on Pd(111)	71
3.2.1.1 – Au/Pd surface preparation	71
3.2.2 – Surface Ensembles in Au/Pd(111) surface alloys	75
3.2.2.1 – CO adsorption over Pd(111)	75
3.2.2.2 – CO adsorption over Au/Pd(111) alloys	77
3.2.3 – Crotyl alcohol reactivity over Au/Pd(111) surface alloys	81
3.2.3.1 – Temperature Programmed XPS (TP XPS) studies	81
3.2.3.2 – Temperature Programmed Desorption (TP XPS) studies	85
3.2.3.3 – Optimum Au/Pd alloy composition for crotyl alcohol selox	88
3.2.4 – Errors	90
3.3 – Conclusions	90
3.4 – References	93
<b>Chapter 4 – Reactivity of crotonaldehyde and propene over Au/Pd(111) surface alloys</b>	<b>96</b>
4.1 – Introduction	96
4.2 – Results and Discussion	97
4.2.1 – Formation of Au/Pd(111) surface alloys	97
4.2.2 – Crotonaldehyde adsorption studies	98
4.2.2.1 – Adsorption of crotonaldehyde Pd(111)	98
4.2.2.2 – Adsorption of crotonaldehyde over an unannealed 4 ML Au film on Pd(111)	99
4.2.2.3 – Adsorption of crotonaldehyde on Au/Pd(111) surface alloys	101
4.2.2.4 – Decomposition of crotonaldehyde to propene on Au/Pd(111) surfaces	103

4.2.3 – Propene adsorption	104
4.2.3.1 – Adsorption of propene on Pd(111)	104
4.2.3.2 – Adsorption of propene on 4 ML Au on Pd(111)	107
4.2.3.3 – Adsorption of propene on Au/Pd(111) surface alloys	109
4.2.4 – The effect of co-adsorbed O	112
4.2.4.1 – Adsorption of crotonaldehyde on O pre-covered Au/Pd(111) surfaces	112
4.2.4.2 – Adsorption of propene on O pre-covered Au/Pd(111) surface alloys	116
4.2.5 – The effect of Au and O <sub>2</sub> on crotyl alcohol selox	120
4.2.6 – Errors	123
4.3 – Conclusions	123
4.4 – References	124
<b>Chapter 5 – Meta-stable De-excitation Spectroscopy of crotyl alcohol over Pd(111)</b>	<b>126</b>
5.1 – Introduction	126
5.2 – Results and Discussion	127
5.2.1 – MDS of crotyl alcohol on Pd(111)	127
5.2.2 – Density Functional Theory	131
5.2.3 – Temperature programmed MDS	137
5.2.3.1 – I. < 200 K: Low-temperature crotyl alcohol adsorption	138
5.2.3.2 – II. 200-250 K: Selox of crotyl alcohol to crotonaldehyde	142
5.2.3.3 – III. > 250 K: Decarbonylation	144
5.3 – Conclusions	145
5.4 – References	146
<b>Chapter 6 – Magnetorefractive Effect in Fe<sub>3</sub>O<sub>4</sub> thin-films</b>	<b>148</b>
6.1 – Introduction	148
6.2 – Results and Discussion	149
6.2.1 – Preparation of Fe <sub>3</sub> O <sub>4</sub> thin-films	149
6.2.2 – Reflectance High Energy Electron Diffraction (RHEED)	151
6.2.3 – X-ray Photoelectron Spectroscopy (XPS)	154
6.2.4 – Transmission Electron Microscopy (TEM)	156
6.2.5 – Vibrating Sample Magnetometry (VSM)	160
6.2.6 – Magnetoresistance (MR) measurements	165
6.2.7 – Skin depth measurements	166
6.2.8 – Infrared Spectroscopy	168
6.2.9 – Magnetorefractive Effect (MRE) measurements	170
6.2.10 – MRE modelling	172
6.2.10.1 – The complex dielectric function	172
6.2.10.2 – The Drude model	173

6.2.10.3 – Plasma frequency	173
6.2.10.4 – Phonon resonances	174
6.2.10.5 – Fresnel equations	174
6.2.10.6 – Modelling parameters	176
6.2.10.7 – Multiple reflections	178
6.2.10.8 – Linear approximation for thin-films	181
6.2.10.9 – Magnetic field dependence	183
6.2.10.10 – Modelling the MRE	184
6.3 – Conclusions	185
6.4 – References	186
<b>Chapter 7 – Conclusions</b>	<b>191</b>
7.1 – Conclusions	191
7.2 – References	193
<b>Appendices:</b>	
<b>Appendix 1</b>	
A1.1 – List of Publications	194
A1.2 – Conferences/workshops attended	195
A1.3 – Awards received	195
<b>Appendix 2 – Development of a combinatorial sputtering rig</b>	<b>196</b>
A2.1 – Introduction	196
A2.2 – Results and Discussion	199
A2.2.1 – Calibration matrix	199
A2.2.1.1 – Sputter Gun Power	201
A2.2.1.2 – Sputtering time	201
A2.2.1.3 – Ar pressure	202
A2.2.1.4 – Gun angle variation	203
A2.2.1.5 – Relative deposition rates	207
A2.2.1.6 – XRF results	208
A2.2.2 – CoAg combinatorial sample	210
A2.2.3 – AuPd combinatorial sample	214
A2.3 – Future Work	215
A2.4 – Conclusions	220
A2.5 – Flux Calculations/ Scale drawings of gun angles	221
A2.6 – AuPd XRF results	223
A2.7 – References	225
<b>Appendix 3</b>	<b>227</b>
Chapters 3 and 4 - Mass Spectrometer Fragments	227
Chapter 6	227
6.1 – Cross-section TEM sample preparation	227
6.2 – Crystal lattice spacing calculation based on diffraction pattern	229
6.3 – Derivation of linear approximation (Equations 6.21 to 6.22)	233
<b>List of Acronyms</b>	<b>237</b>

## List of Figures

	Page
<b>Figure 1.1</b> – A schematic diagram of the three growth models usually observed for metal overlayers.	2
<b>Figure 1.2</b> – Diagram of a typical supported nanoparticulate catalyst	4
<b>Figure 1.3</b> – <b>(a)</b> A cartoon of a simple nanoparticle (truncated octahedron), showing the different crystal faces exposed. <b>(b)</b> The chemistry of single crystal surfaces can be used as experimental ‘models’ for the various surface facets within nanoparticles.	5
<b>Figure 1.4</b> - The oxidative dehydrogenation of crotyl alcohol to crotonaldehyde.	6
<b>Figure 1.5</b> – The reaction scheme for selox of a general allylic alcohol <b>(1)</b> , to an allylic aldehyde <b>(2)</b> , with by-products due to double bond hydrogenation <b>(3)</b> , hydrogenolysis <b>(4)</b> , decarbonylation <b>(5)</b> and over-oxidation to carboxylic acid <b>(6)</b> . Modified from references <sup>23, 24</sup> .	8
<b>Figure 1.6</b> - ADF-STEM image of a bimetallic Au/Pd nanoparticle supported on TiO <sub>2</sub> . This composition map image was created using a multivariate statistical analysis of processed STEM-XEDS maps of the Au-M <sub>2</sub> , Pd-L <sub>α</sub> , O-K <sub>α</sub> , and Ti-K <sub>α</sub> signals (Ti, red; Au, blue; and Pd, green). <sup>21</sup>	11
<b>Figure 1.7</b> - The results of Fert’s experiments that lead to the discovery of GMR - taken from <sup>82, 87</sup>	14
<b>Figure 1.8</b> – The spin split band structure present within ferromagnetic materials	15
<b>Figure 1.9</b> - A diagram illustrating the basic theory behind giant magnetoresistance for a simple magnetic trilayer system – adapted from <sup>93</sup> .	16
<b>Figure 1.10</b> – An example of a spin valve, used as a read head in hard disks.	17
<b>Figure 1.11</b> - A simple diagram representing a proposed racetrack memory	19

concept. The racetrack consists of ferromagnetic nanowire with data encoded as a pattern of magnetic domains along a portion of the wire – obtained from 107.

**Figure 1.12** - A simple diagram showing the density of states of a half-metallic system. 20

**Figure 1.13 (a)** – The inverse spinel crystal structure of  $\text{Fe}_3\text{O}_4$ , showing the tetrahedrally coordinated  $\text{Fe}^{3+}$  A site and mixed-valent ( $\text{Fe}^{2+}, 3\text{d}^6 / \text{Fe}^{3+}, 3\text{d}^5$ ) octahedrally coordinated B site (adapted from <sup>113, 125</sup>). **(b)** – A simple diagram showing the A and B sublattice configuration<sup>125</sup>. **(c)** – A crystal field splitting diagram of the  $\text{Fe}^{2+}$  and  $\text{Fe}^{3+}$  3d states, along with the itinerant (“hopping”) electron<sup>125</sup>. 23

**Figure 1.14** – The phase diagram for the iron oxygen system (modified from Darken<sup>126</sup> and Voogt<sup>127</sup>).  $\alpha$ ,  $\gamma$ ,  $\delta$  indicate the various phases of metallic iron (b.c.c., f.c.c and high temperature b.c.c. respectively). W, M and H stand for wüstite ( $\text{FeO}$ ), magnetite ( $\text{Fe}_3\text{O}_4$ ) and haematite ( $\text{Fe}_2\text{O}_3$ ) respectively. L stands for liquid. Dashed lines show oxygen equilibrium pressures. 24

**Figure 1.15** – **(a)** The APB shifts formed according to the different translational and rotational symmetry of the initial  $\text{Fe}_3\text{O}_4$  monolayer and the  $\text{MgO}(100)$  surface (modified from Eerenstein<sup>113</sup>).  $\text{Fe}_3\text{O}_4$  monolayers are shifted relative to reference **(i)**, forming in-plane shifts of **(ii)**  $\frac{1}{2}[100]$  **(iii)**  $\frac{1}{4}[110]$ . A rotated monolayer, **(iv)**, forms an out-of plane shift. **(b)** Side profile of an  $\text{Fe}_3\text{O}_4$  APB in the 110 direction on  $\text{MgO}(100)$  modified from Arras et al.<sup>118</sup> 26

**Figure 1.16** – Dark field transmission electron micrographs of APBs from within **(a)** 6 nm, **(b)** 12 nm, **(c)** 25 nm and **(d)** 50 nm thick films of  $\text{Fe}_3\text{O}_4/\text{MgO}(100)$  – taken from<sup>122</sup> 27

**Figure 2.1** – Diagram of the Ultra High Vacuum Chamber 40

**Figure 2.2** – A photograph of the UHV chamber used for mechanistic 41

studies of crotyl alcohol selox over model Au/Pd(111) surfaces

- Figure 2.3** – Single crystal sample mounting for TDS experiments 43
- Figure 2.4** - A photograph of the Northeastern MBE system used for the preparation of thin films of Fe<sub>3</sub>O<sub>4</sub> on MgO 45
- Figure 2.5** – A diagram of the York MBE system 47
- Figure 2.6** - A photograph of the York MBE system used for the preparation of thin films of Fe<sub>3</sub>O<sub>4</sub> on MgO 48
- Figure 2.7** – A simple diagram of the combinatorial sputtering rig 50
- Figure 2.8** – Schematic representation of photoionisation 52
- Figure 2.9** – A simple diagram of a typical XPS experiment of a Pd(111) surface 53
- Figure 2.10** – Auger emission due to ionisation by an incident electron or photon 55
- Figure 2.11** – A schematic of a simple VSM set-up 61
- Figure 2.12** – A diagram of the apparatus used to measure the magnetoresistance of samples 62
- Figure 2.13** – Colour photographs of the MRE acquisition setup: **(a)** A view from above the entire setup, **(b)** A close-up shot of the set-up showing the IR beam (red line) 64
- Figure 2.14** - Diagram of a simple MRE setup, showing the reflection (R) and transmission (T) of the IR beam off and through the sample 65
- Figure 3.1** - Temperature Programmed X-ray Photoelectron spectra, acquired at the ELETTRA synchrotron of the C 1s binding energy region for a saturated crotyl alcohol adlayer (adsorbed at 100 K) over Pd(111) – modified from source<sup>2</sup> 69
- Figure 3.2** – The variation in intensity of Au 4f<sub>7/2</sub> and Pd 3d<sub>5/2</sub> XPS signals 72

with increasing Au deposition time

**Figure 3.3** – Variation in Au/Pd surface composition as a function of annealing temperature for a 3.9 ML Au film deposited on Pd(111) at room temperature. 73

**Figure 3.4** – A flow chart diagram illustrating the experimental procedure devised for monitoring both the formation of surface Au/Pd alloys by XPS and also the temperature dependent reactivity of each alloy by temperature programmed XPS. 74

**Figure 3.5** – A diagram showing atop, bridge and hollow adsorption sites on Pd(111). 75

**Figure 3.6** – In situ C 1s XP spectra during adsorption of a CO adlayer over Pd(111) at 100 K. Inset shows fitted intensities of CO components as a function of coverage. 76

**Figure 3.7** – C 1s XP spectra of saturated CO adlayers over Au/Pd surfaces alloys at 100 K as a function of annealing temperature. These surfaces were prepared by the successive annealing a 3.9 ML Au/Pd(111). The bold lines show the acquired data; whereas the thin/dashed lines show the fitted states determined using CasaXPS software. Inset shows saturation CO coverage as a function of annealing temperature. Pd states are highlighted by blue lines, whereas Au states are highlighted in red. 78

**Figure 3.8 - (a)** Integrated C 1s XP intensities of fitted CO components for experiments involving saturated CO adlayers adsorbed at 100 K over Au/Pd alloys prepared by annealing a 3.9 ML Au/Pd(111) surfaces. **(b)** The Monte Carlo simulation data of Pd ensembles available for CO adsorption as a function of Au/Pd surface composition. Surface Au rapidly suppresses CO adsorption over larger Pd ensembles. 80

**Figure 3.9** - Temperature-programmed C 1s XP spectra of a saturated crotyl alcohol adlayer prepared over an unannealed 3.9 ML Au/Pd(111) film at 82

100 K. Inset shows fitted crotyl alcohol coverage as a function of temperature.

**Figure 3.10** - Temperature-programmed C 1s XP spectra of a saturated crotyl alcohol adlayer over an ultrathin 3.9 ML Au/Pd(111) film annealed to 973 K ( $X_{Au} = 0.15$ ) 83

**Figure 3.11** - C 1s snapshot spectra during the temperature programmed reaction of a saturated crotyl alcohol adlayer over a 3.9 ML Au/Pd(111) film annealed to 973 K ( $X_{Au} = 0.15$ ) 84

**Figure 3.12** - Integrated C 1s XP intensities of fitted crotyl alcohol, crotonaldehyde and carbonaceous components for a saturated crotyl alcohol adlayer adsorbed at 100 K over a 973 K ( $X_{Au} = 0.15$ ) pre-annealed 3.9 ML Au/Pd(111) surface 85

**Figure 3.13** - Thermal desorption mass spectra of a saturated crotyl alcohol adlayer adsorbed at 100 K over 3.9 ML Au/Pd(111) films. A comparative spectrum is shown for Pd(111). 86

**Figure 3.14** - Thermal desorption mass spectra of reactively-formed crotonaldehyde from a saturated crotyl alcohol adlayer adsorbed at 100 K over 3.9 ML Au/Pd(111) films. A comparative spectrum is shown for Pd(111). 87

**Figure 3.15** – In situ XPS derived crotyl alcohol conversion to surface-bound crotonaldehyde, and net decomposition to residual surface carbon as a function of Au alloy composition. The normalised desorption yields (determined by TDS) of reactively-formed crotonaldehyde are also shown. 89

**Figure 4.1** - Thermal desorption mass spectra for the adsorption of crotonaldehyde at 120 K over a clean Pd(111) surface. Inset shows the fitted intensities of crotonaldehyde monolayer, multilayer and reactively formed propene as a function of exposure. 99

**Figure 4.2** - Thermal desorption mass spectra for the adsorption of crotonaldehyde at 120 K over a thick (~ 4 ML) Au adlayer on Pd(111). Inset 100

shows the fitted intensities of the crotonaldehyde monolayer and multilayer states as a function of exposure.

**Figure 4.3** - Thermal desorption mass spectra of 3 L crotonaldehyde adsorbed on Pd(111) and an Au/Pd(111) surface alloy (4 ML Au film annealed to 773 K, AES Au mole fraction of 0.56) at 120 K. 102

**Figure 4.4** - Thermal desorption mass spectra for the formation of propene from the adsorption of crotonaldehyde (3 L) at 120 K over Au/Pd(111) surface alloys. Inset shows the fitted intensities of propene as a function of surface Au mole fraction (X<sub>Au</sub>). 104

**Figure 4.5** - Thermal desorption spectra for propene over a clean Pd(111) surface. Inset shows the fitted intensities for the propene monolayer, multilayer and reactively formed hydrogen as a function of exposure. Saturation coverage,  $\theta$ , (0.25 ML) is assumed to be identical to that of ethylene over both Pt(111)<sup>13</sup> and Pd(110)<sup>14</sup>. 106

**Figure 4.6** - Thermal desorption mass spectra for the adsorption propene at over a 4 ML Au adlayer on Pd(111). Inset shows the fitted intensities for the propene monolayer and multilayer as a function of exposure. Saturation coverage (0.25 ML) is assumed to be identical to that of ethylene over both Pt(111)<sup>13</sup> and Pd(110)<sup>14</sup>. 108

**Figure 4.7** - Thermal desorption mass spectra of a 3 L exposure of propene adsorbed on Pd(111) and an Au/Pd(111) surface alloy (AES Au mole fraction of 0.56) at 120 K. 110

**Figure 4.8** - TPD series of evolved hydrogen from the adsorption of propene over Au/Pd(111) surface alloys. Inset shows the integrated hydrogen area resulting from methyl fragments (485 K peak). Also plotted is the propene peak area for comparison. 111

**Figure 4.9** - Thermal desorption mass spectrum of 3 L crotonaldehyde adsorbed on an O pre-covered (60 L O<sub>2</sub>) Pd(111) and Au/Pd(111) surface alloy (AES Au mole fraction of 0.56) at 120 K. 114

**Figure 4.10** – Series of thermal desorption mass spectra for the formation of propene from the adsorption of crotonaldehyde (3 L) at 120 K over oxygen pre-covered (60 L O<sub>2</sub>) Au/Pd(111) surface alloys. Inset shows the fitted intensities of propene as a function of surface Au mole fraction. 115

**Figure 4.11** – Thermal desorption mass spectrum of 3 L propene adsorbed on an oxygen pre-covered (60 L O<sub>2</sub>) Pd(111) surface, and an oxygen pre-covered Au/Pd(111) surface alloy (AES Au mole fraction of 0.56) at 120 K. 117

**Figure 4.12** – TPD series of evolved hydrogen from the adsorption of propene over O pre-covered (60 L O<sub>2</sub>) Au/Pd(111) surface alloys. Inset shows the integrated hydrogen area resulting from methyl fragments (485 K peak). Also plotted is the propene peak area for comparison. 119

**Figure 4.13** – The variation in the amount of reacted adsorbate for crotonaldehyde and propene adsorption with and without co-adsorbed oxygen as a function of the surface Au mole fraction. 122

**Figure 5.1 (a)** – MDS spectra from a clean Pd(111) surface where the dominant de-excitation mechanism is resonance ionization followed by Auger neutralization, and from a saturation coverage of crotyl alcohol where significant Auger de-excitation takes place. **(b)** - DFT calculation for clean Pd(111) showing metallic *d*-band states close to *EF*. **(c)** - UPS spectra for clean Pd(111) and for a surface exposed to a saturation coverage of crotyl alcohol at 150 K and 245 K. 130

**Figure 5.2** – DFT calculated spectra for isolated crotyl alcohol and crotonaldehyde molecules and, for comparison, the experimentally obtained MDS spectrum of a crotyl alcohol saturated Pd surface at 150 K. 133

**Figure 5.3** – The five different molecular orientations of crotyl alcohol adsorbed on the Pd(111) surface used in DFT calculations. 134

**Figure 5.4** – Density of states spectra of crotyl alcohol calculated by DFT for the molecular adsorption states shown in **Figure 5.3**. The top spectrum is that of the MDS of the alcohol on Pd shown for comparison. 136

**Figure 5.5** – Temperature evolution of MDS spectra for crotyl alcohol adsorption on clean Pd(111) at 150 K. Temperature regimes where noticeable changes in the spectra occur are highlighted with different colours and grouped together into three distinct adsorption regimes. Note the non-linear temperature scale above room temperature. 137

**Figure 5.6** – MDS spectra obtained at critical temperatures from a Pd(111) substrate exposed to 3 L of crotyl alcohol at 150 K, warmed to room temperature and then heated. Key features in the spectra are also labelled A, B and C, the assignment of which is detailed in section 5.2.3.1. 138

**Figure 5.7** – Molecular orbitals and peak analysis of the MDS data shown in **Figure 5.6** at three distinct temperature regimes. The dotted red lines show the fitted individual components. 139

**Figure 5.8 (a)** – Peak positions of the first three molecular orbitals (assigned in **Figure 6**) as a function of temperature. **(b)** – The resulting schematic of the energy level correlation of the O *n* and C=C  $\pi$  MOs 142

**Figure 6.1** – RHEED patterns recorded for MgO(111) substrates **(a)** as received ( $1 \times 1$ ) **(b)** after annealing at 973 K in a furnace for 4 hours **(c)** after exposure to a 100 W O plasma for 1 hour. Samples were run by Dr. Zhuhua Cai. 152

**Figure 6.2** – RHEED patterns recorded for MgO(111) substrates **(a)** as received ( $1 \times 1$ ) **(b)** after annealing at 1073 K in a furnace for 6 hours **(c)**  $\sqrt{3} \times \sqrt{3}$  surface reconstruction after exposure to a 100 W O plasma for 1 hour. Samples were run by Dr. Zhuhua Cai. 153

**Figure 6.3** – RHEED patterns recorded for thin-films of Fe<sub>3</sub>O<sub>4</sub> on reconstructed MgO(111)  $\sqrt{3} \times \sqrt{3}$  substrates **(a)**  $\sim 10$  nm Fe<sub>3</sub>O<sub>4</sub> **(b)**  $\sim 30$  nm Fe<sub>3</sub>O<sub>4</sub> **(c)**  $\sim 60$  nm Fe<sub>3</sub>O<sub>4</sub> 154

**Figure 6.4** – **(a)** A representative Fe 2p XP spectrum from a Fe<sub>3</sub>O<sub>4</sub> thin-film sample grown in the York MBE **(b)** A Fe 2p XP spectrum recorded from a Fe<sub>2</sub>O<sub>3</sub> thin-film sample grown in the York MBE, showing the characteristic Fe<sup>3+</sup> satellite **(c)** Background subtracted and fitted intensities from the York 155

Fe<sub>3</sub>O<sub>4</sub> sample **(d)** Background subtracted and fitted intensities from the York Fe<sub>2</sub>O<sub>3</sub> sample, again showing the characteristic Fe<sup>3+</sup> satellite.

**Figure 6.5** – Cross sectional TEM of Fe<sub>3</sub>O<sub>4</sub>/MgO(111) 1 × 1 nominal thickness of 15 nm. Inset shows the electron diffraction obtained from the sample. 157

**Figure 6.6** – High resolution cross sectional TEM of an Fe<sub>3</sub>O<sub>4</sub> thin-film on MgO(100), with corresponding FFT images from both the Fe<sub>3</sub>O<sub>4</sub> and MgO layers. This sample was prepared and imaged by Mr. James Sizeland. 158

**Figure 6.7** – A representative dark field TEM plan view image of an Fe<sub>3</sub>O<sub>4</sub> thin film. The film was lifted off the MgO(100) substrate using a concentrated solution of (NH<sub>4</sub>)<sub>2</sub>SO<sub>4</sub>. The jagged lines in the figure correspond to the interfaces between the APBs in the thin-film. This sample was prepared and imaged by Mr. James Sizeland. 159

**Figure 6.8** – Representative VSM hysteresis loops for Fe<sub>3</sub>O<sub>4</sub> thin-film samples. The series shown is for various thicknesses of Fe<sub>3</sub>O<sub>4</sub> on MgAl<sub>2</sub>O<sub>4</sub>(111). The inset shows the same hysteresis loops over a larger field range. 161

**Figure 6.9** – The coercivity values obtained from VSM data obtained for all thin-film Fe<sub>3</sub>O<sub>4</sub> samples prepared in the Northeastern and York MBEs. 162

**Figure 6.10** – Remanence values obtained from VSM data obtained for all thin-film Fe<sub>3</sub>O<sub>4</sub> samples prepared in the Northeastern and York MBEs. 164

**Figure 6.11** – A representative MR curve from a thin-film of Fe<sub>3</sub>O<sub>4</sub> on MgO. The MR shown in the figure is from a 100 nm Fe<sub>3</sub>O<sub>4</sub> thin-film on MgO(111) substrate. 165

**Figure 6.12** – The skin depth calculated for thin-film Fe<sub>3</sub>O<sub>4</sub> samples on MgO(111). 168

**Figure 6.13** – Infrared spectra recorded for the thin-film Fe<sub>3</sub>O<sub>4</sub>/MgO(111) samples 170

- Figure 6.14** – Stacked MRE spectra recorded for the Fe<sub>3</sub>O<sub>4</sub>/MgO(111) samples. 172
- Figure 6.15** – A diagram showing the electric field polarisation of light at the Fe<sub>3</sub>O<sub>4</sub> surface. The two polarisations result from the electric field being perpendicular (s) and parallel (p) to the plane of incidence. 175
- Figure 6.16** – A modelled infrared reflectivity spectrum for the bare MgO substrate using the parameters from **Table 7.6**. For comparison, an experimentally determined spectrum is also shown in the figure. 177
- Figure 6.17** – The modelled reflectivity spectrum for a bulk Fe<sub>3</sub>O<sub>4</sub> sample, along with experimentally determined spectra from Gasparov70. 178
- Figure 6.18** – A diagram representing a multiple reflection model for infrared reflectivity of thin-films of Fe<sub>3</sub>O<sub>4</sub> on MgO. 179
- Figure 6.19** – Modelled infrared reflectivity spectra of various film thicknesses of Fe<sub>3</sub>O<sub>4</sub> for MgO (analogous to **Figure 7.14**). 183
- Figure 6.20** – Stacked modelled MRE spectra of various film thicknesses of Fe<sub>3</sub>O<sub>4</sub> for MgO (analogous to **Figure 7.15**). 184

## List of Tables

	Page
<b>Table 2.1</b> – Gases and adsorbates used in the system	42
<b>Table 4.1</b> – The surface Au mole fraction ( $X_{Au}$ ) resulting from annealing a 4 ML thin-film of Au on Pd(111) to various different temperatures.	97
<b>Table 5.1</b> - The energies of the surface molecular orientations shown in <b>Figure 5.3</b> .	134
<b>Table 6.1</b> – Empirical optimum growth conditions determined for thin-film growth of Fe <sub>3</sub> O <sub>4</sub> on various substrates for each MBE chamber.	150
<b>Table 6.2</b> – A table showing the substrates and desired Fe <sub>3</sub> O <sub>4</sub> film thicknesses used to prepare samples.	151
<b>Table 6.3</b> – Coercivity values for various iron oxide thin-films from literature.	163
<b>Table 6.4</b> – A table to show the nominal thickness and electrical MR of all samples prepared in the York and Northeastern MBE systems.	166
<b>Table 6.5</b> – Literature values for the various resonant phonon modes for both substrates and thin-films.	169
<b>Table 6.6</b> – The various modelling parameters necessary in order to calculate infrared reflectivity spectra for Fe <sub>3</sub> O <sub>4</sub> films and MgO substrates	176

## **Acknowledgments**

First and foremost, thanks should go to my supervisors, Prof. Adam F. Lee, Dr. Karen Wilson and Dr. Sarah Thompson for giving me the opportunity to carry out my research and aiding me with every aspect of my work. Their patience, dedication and guidance were utterly invaluable.

I would also like to thank Dr. Vlado Lazarov for his enthusiasm, good nature and help over the past few years. Thanks also should go to Prof. Jim Matthew, whose mathematical discussions were most stimulating and useful.

I would like to thank Dr. Kate Ziemer of Northeastern University, for the use of the Department of Chemical Engineering MBE growth chamber, and Dr. Zhuhua Cai (now at MIT) for help in Fe<sub>3</sub>O<sub>4</sub> sample growth.

Thank you to all of the various members of the Cardiff Surfaces and Materials, and York Nanophysics groups, both past and present for their friendship and help with my work.

I would also like to thank and recognise the efforts of all of my supervisee students, some of who helped with some of the measurements taken for this thesis.

I'd like to thank especially Mr. Andrew Vick and Dr. Simon Hackett, who helped me out enormously during the start of my PhD.

Many thanks also to all of the workshop technicians in chemistry and physics at York, and the station-masters at the various synchrotrons where I have carried out experiments.

My parents have helped and supported me enormously over the past eight years at the University of York. Love you Mum and Dad!

I'd also like to thank Coleen and Dave for their crucial help and support.

Finally, I would like to thank my darling wife Lydia, whose patience and understanding know no bounds.

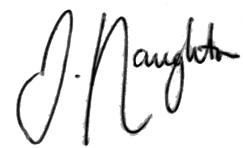
**For George**

### **Author's Declaration**

I hereby declare that the work presented in this thesis is based on my own research, unless otherwise stated. It has neither been submitted nor accepted for any degree at this or any other university before.

Some of the results in this thesis were obtained either by colleagues or by students under the supervision of the author and are fully acknowledged in the text.

The results within this text have also been published in journal articles and presented at conferences; citation details can be found in the appendix.

A handwritten signature in black ink, appearing to read 'J. Naughton', written in a cursive style.

James Naughton

September 2011

# Chapter 1

## Introduction

### 1.1 Motivation

#### 1.1.1 Advanced Functional Materials

The development and improvement of materials brings about huge social change and benefits to human society. The 20th century saw rapid technological advances, particularly due to the preparation of novel materials with specific functional properties. Today, advanced functional materials have numerous applications in a wide variety of fields, including the catalytic cracking of crude oil, automotive emission treatment, fine chemical synthesis and information storage; to give but a few examples. In order to meet the demands and challenges of the future there is an ever-expanding need for advanced materials.

#### 1.1.2 Surfaces and Thin-Films

The surface layer plays a very important role in defining the properties of a material. In terms of chemistry, catalysis occurs at the interface between of the solid surface of the catalyst and the liquid or gaseous reactants. This surface reactivity arises because of the lower surface coordination number relative to the bulk. As we shall see, due to the complexity of dispersed solid catalysts, single crystals and thin-films are useful ‘model’ systems for the study of heterogeneous catalysts.

Thin-films also display novel behaviour, in that they often have properties that greatly differ from those of their bulk counterparts, as a result of their reduced size and dimensionality<sup>1</sup>. This divergence from bulk properties in magnetic materials means that thin-film magnetic materials are of great technological importance<sup>1-3</sup>, and as a result many modern electronic devices exploit thin-film architecture. Research into thin-film magnetism is therefore critical to meet consumer demands in terms of faster devices with increased data storage capacity.

### 1.1.3 Surfaces Science Techniques

Surface science techniques that operate in ultra-high vacuum (UHV) and/or high vacuum (HV) regimes allow us to understand the fundamental properties of surfaces and thin-films. This often involves the preparation and characterisation of many samples *in-situ* and can afford unique advantages over classical wet chemical methods. As advanced functional materials are complex, the rate-limiting factor in their development is often the empirical trial-and-error method of synthesis and *ex-situ* characterisation<sup>4</sup>.

The preparation and *in-situ* characterisation of experimental models of different compositions within a single set of experiments would therefore help to accelerate the development of functional materials. This involves the deposition of material by evaporation, or co-sputter deposition of different metals in UHV or HV to form thin films on substrates. Surface analytic techniques then allow molecular level insight into important surface processes.

### 1.1.4 Thin-Film Growth

When preparing and characterising thin-films, we must consider the growth mode of the film onto a substrate, which influences the overall properties of the film. For metal films, experimental evidence suggests that three distinct growth models exist (see **Figure 1.1**) for coverage beyond a monolayer<sup>5</sup>.

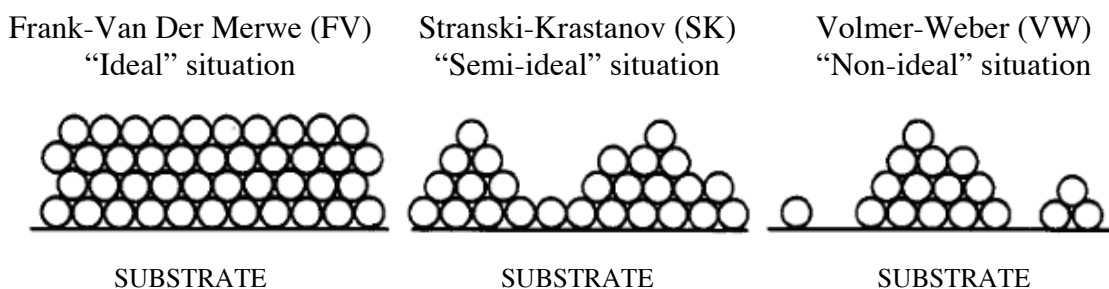


**Figure 1.1** - A schematic diagram of the three growth models usually observed for metal overlayers<sup>5</sup>.

The ideal situation (layer by layer) FV model, is expected when...

$$\Delta\tau = \tau_A + \tau_{A-S} - \tau_S < 0 \quad \text{Equation 1.1}$$

Where  $\Delta\tau$  is the relative change in surface energy,  $\tau_A$  is the surface energy of the pure metal adlayer,  $\tau_S$  is the surface energy of the pure substrate and  $\tau_{A-S}$  is the energy of the interface between the adlayer and the substrate.

$$\Gamma_{AS} = 2 \left| \frac{\tau_A - \tau_S}{\tau_A + \tau_S} \right| \quad \text{Equation 1.2}$$

$\Gamma_{AS}$ , is known as the surface energy mismatch parameter, and generally less than approximately 0.5 for FV systems.

For the non-ideal VW mode, cluster crystallites form due to low coverage (a uniform monolayer cannot form):

$$\Delta\tau = \tau_A + \tau_{A-S} - \tau_S > 0 \quad \text{Equation 1.3}$$

It is therefore critical to consider these scenarios when preparing thin-films either for the study of the magnetic properties or the reaction mechanisms in heterogeneous catalysis.

## 1.2 Heterogeneous catalysis

Catalytic processes that are heterogeneous in nature are highly desirable from an industrial perspective, due to ease of product separation, continuous processing and ease of handling. Homogeneous systems by contrast cannot be readily recycled and can also lead to large volumes of hazardous waste. However, homogeneous catalysts are easily probed by spectroscopy, have distinct oxidation states and exist as pure compounds. Heterogeneous catalysts are less well defined, meaning that homogeneous systems are typically favoured industrially.

'Real' heterogeneous catalysts employed industrially usually consist of nanoparticles composed of a precious metal or metal oxide imbedded on an inexpensive support material (e.g. carbon, alumina or silica), as shown in **Figure**

**1.2.** This conserves expensive material, whilst also increasing the surface area of the active catalyst, which in turn greatly increases the overall efficiency and turnover number.

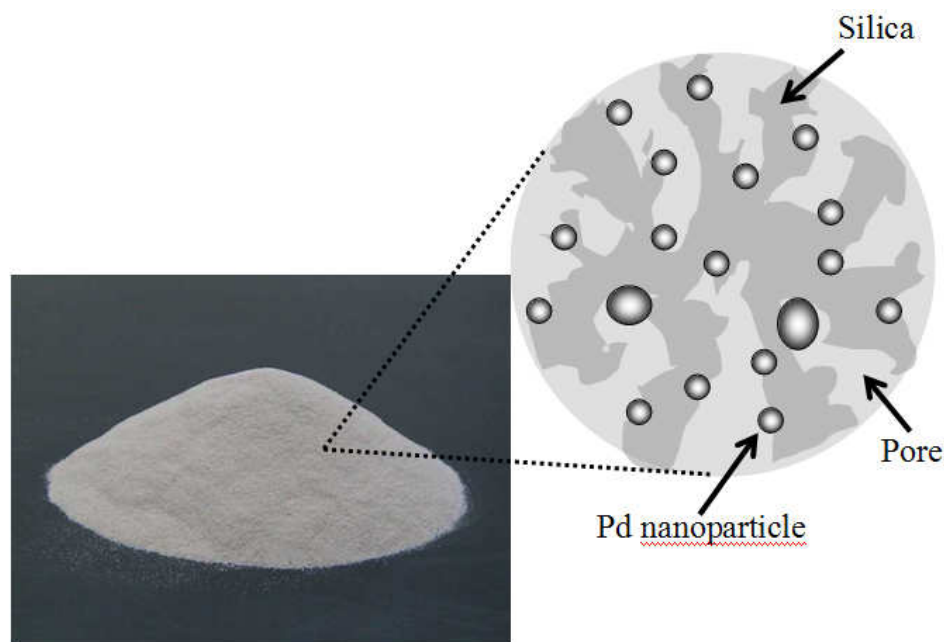
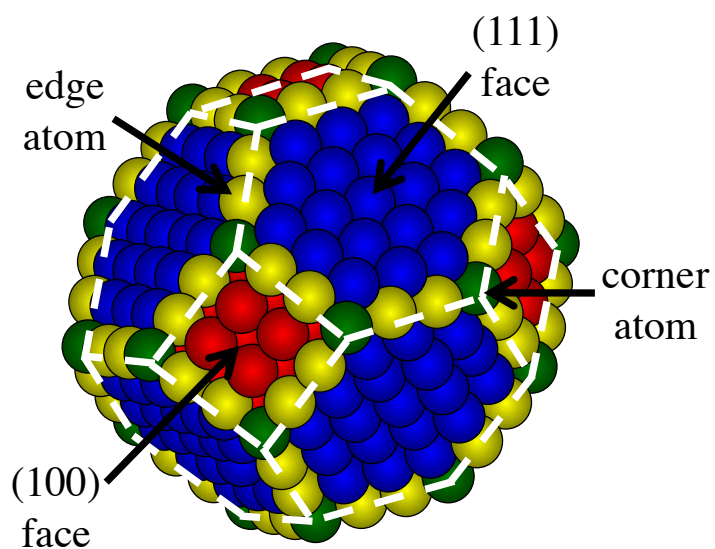


**Figure 1.2** - Diagram of a typical supported nanoparticulate catalyst

Nanoparticles are complex structures containing multiple facets with the chemistry of each differing enormously. **Figure 1.3 (a)**, a truncated octahedron, can be taken as a simple example of a nanoparticle. As lower coordination sites have high potential energy facilitating bond dissociation, corner and edge sites will have a higher activity relative to other sites present within a nanoparticle. Since the advent of UHV techniques in the 1950 and 1960s, single crystal surfaces have been widely employed experimentally as simple models for different nanoparticle facets (**Figure 1.3 (b)**) in order to examine the surface chemistry of a wide variety of adsorbates.

(a)



(b)

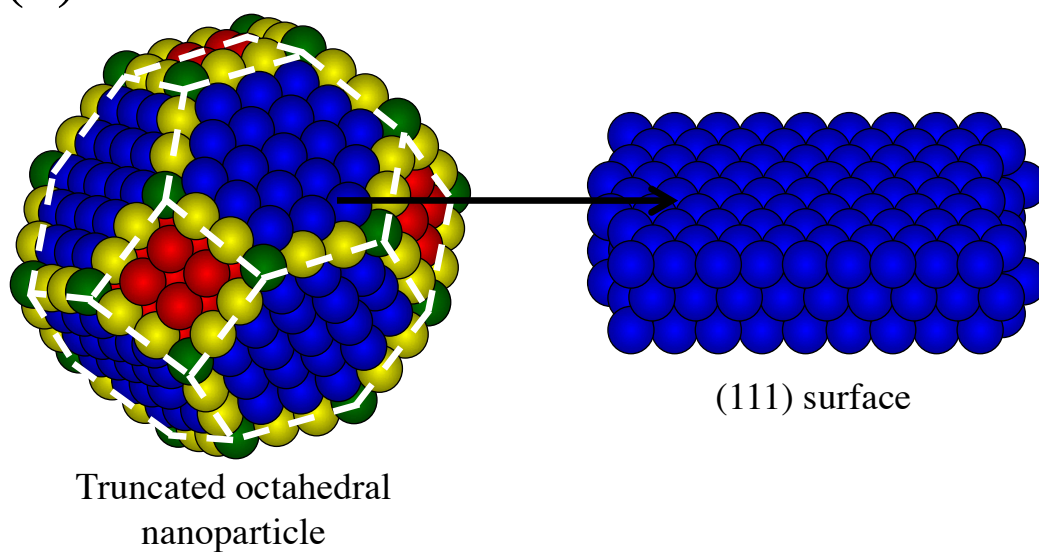


**Figure 1.3** – (a) A cartoon of a simple nanoparticle (truncated octahedron), showing the different crystal faces exposed. (b) The chemistry of single crystal surfaces can be used as experimental ‘models’ for the various surface facets within nanoparticles.

### 1.3 Selective oxidation of alcohols by heterogeneous catalysts

The aerobic selective oxidation (selox) of alcohols by heterogeneous catalysts is a novel way to synthesise a wide range of important fine chemical and pharmaceutical intermediates<sup>6, 7</sup>. These powerful catalytic technologies have the potential to replace stoichiometric inorganic oxidants such as Cr<sup>VI</sup> salts or expensive homogeneous complexes (e.g. Mn salens), and their associated process disadvantages and safety issues<sup>8</sup>.

For example, crotyl alcohol (CrOH, CH<sub>3</sub>CH=CHCH-OH, 2-buten-1-ol) is an allylic alcohol, which is an important agrochemical and precursor to the food preservative sorbic acid. The selox of crotyl alcohol (as shown in **Figure 1.4**) produces crotonaldehyde (CrCHO, CH<sub>3</sub>CH=CHCHO, but-2-enal), a versatile intermediate important for organic synthesis. Through the use of an appropriate catalyst, it should be possible to perform this chemical transformation using oxygen in the air as the oxidant. Ideally, this would produce water as the sole by-product, thereby having clear environmental benefits.

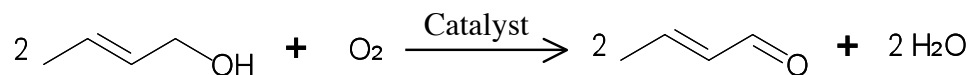


**Figure 1.4** - The oxidative dehydrogenation of crotyl alcohol to crotonaldehyde.

Indeed, Pt Group Metal (PGM) particles are particularly promising partial oxidation catalysts<sup>6, 9, 10</sup>, able to activate a range of alcohols and carbohydrates under mild conditions employing either neat substrate or green solvents including ionic liquids<sup>11,12</sup>, supercritical fluids<sup>13-17</sup> and even water<sup>18</sup>.

An industrially important reaction involving PdAu is the oxidation of ethylene and acetic acid to form vinyl acetate monomer (VAM), which is catalysed by both supported Pd<sup>19</sup> and PdAu alloys<sup>20</sup>. Alloying the Pd with Au leads to a substantial increase in selectivity from ~ 85% for pure Pd to ~ 92% for the alloy<sup>21</sup>. This enhanced selectivity has been extensively studied by both DFT and experimental studies (TPDs/IRAS), mainly by Goodman and co-workers<sup>19, 20, 22, 23</sup>. This work has aided the understanding of the nature of the active site by showing that the activity of such systems mainly stems from the presence of second neighbor Pd ensemble

pairs on Au(001)<sup>24</sup>. This example illustrates the importance of surface alloy composition for activity and selectivity.

It has also been recently shown that isolated Pd centres anchored within both alumina<sup>25</sup> and silica<sup>10</sup> frameworks are efficient selox catalysts for alcohols. The recent discoveries of Ru<sup>26</sup> and promoted Au catalysts<sup>27</sup> for such reactions is especially noteworthy, as these systems offer high turnover frequencies even during scale-up, although some require radical initiators and high air/O<sub>2</sub> partial pressures<sup>28</sup>. These reactions are highly regioselective (often > 95 %) towards the aldehyde product, even in the presence of diverse functionalities including aryl, allylic groups.

In spite of the high selectivity conferred through the use of PGM catalysts, it is important to consider the formation of any by-products. **Figure 1.5** shows the main reaction products formed in allylic alcohol selox. This work was originally reported for the selox of cinnamyl alcohol to cinnamaldehyde over Pd/alumina<sup>29</sup>. There are a large number of by-products for this deceptively simple reaction. This is not only undesirable for the selectivity of catalysts, but the chemistry of these by-products may also affect the activity and therefore the efficacy of the catalyst over time.

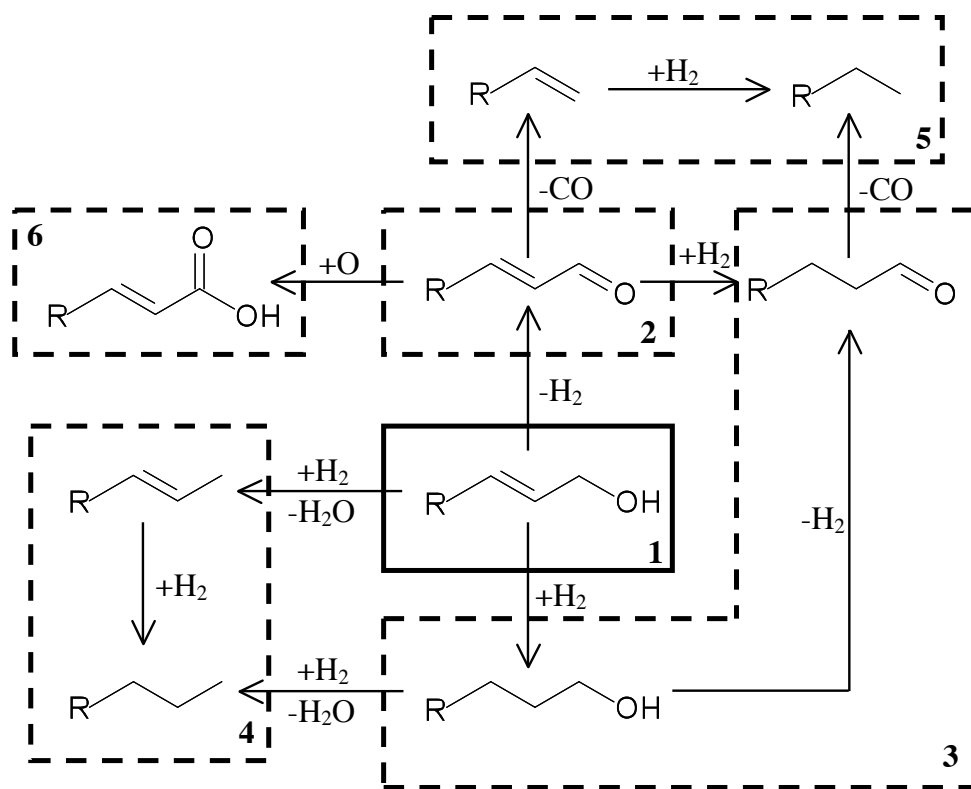


**Figure 1.5** – The reaction scheme for selox of a general allylic alcohol (1), to an allylic aldehyde (2), with by-products due to double bond hydrogenation (3), hydrogenolysis (4), decarbonylation (5) and over-oxidation to carboxylic acid (6).

Modified from references<sup>29, 30</sup>.

In order to study the reaction mechanisms involved in alcohol selox, UHV studies over single crystal surfaces are utilised as ‘model’ catalysts in order to identify reaction and decomposition products.

### 1.3.1 Allylic alcohols over single crystal surfaces

There are very few single crystal studies of allylic alcohols available in the literature. The surface chemistry is poorly understood due to complex surface interactions which dominate the adsorption mode, as it is possible for coordination to occur through either the C=C or C-OH bonds. Allyl alcohol has been previously studied over Ag(110), where reversible adsorption occurs via the C=C bond, which was found to be co-planar with the surface<sup>31, 32</sup>. Despite this interaction, no chemistry occurs over the Ag(110) surface. Over Cu(110), allyl alcohol undergoes oxidation to acrolein whilst also hydrogenating to n-propyl alcohol and propanal<sup>33</sup>.

For Rh(111), vibrational and desorption work showed that at low temperature an allyl alkoxide intermediate was formed<sup>34</sup>. It is thought that this intermediate binds strongly through both the oxygen and alkene functionalities. It is this interaction which leads to strong C=C binding, responsible for decarbonylation.

DFT calculations show that allyl alcohol adsorbs with a di- $\sigma$  coordination over both Pt(111) and Pd(111), an interaction which is also augmented by a much weaker interaction through the C-OH functionality<sup>35</sup>. Binding to the surface through multiple functionalities may explain the different reaction mechanisms observed experimentally.

Previous work by the York Surface Chemistry and Catalysis group at the ELETTRA synchrotron on the selox of crotyl alcohol to crotonaldehyde over Pd(111), identified secondary decarbonylation reactions as the major factor in the deactivation of practical monometallic Pd selox catalysts<sup>36</sup>. This work will be discussed in more detail in chapter 3. This thesis will augment this research area through the further investigation of the mechanism of alcohol selox over Pd using surface science techniques.

### **1.3.2 Aldehydes over single crystal surfaces**

As with alcohols, there is a general dearth of knowledge regarding the surface chemistry of aldehydes over metallic single crystal surfaces. The thermal chemistry of formaldehyde has been previously studied over Cu(100)<sup>9</sup>, Cu(110)<sup>37, 38</sup>, Fe(100)<sup>39</sup>, Pt(110)<sup>40</sup>, Pt(111)<sup>41</sup>, Rh(111)<sup>42</sup> and V(100)<sup>43</sup>. It was discovered that formaldehyde spontaneously polymerises to disordered poly(oxymethylene) species over Cu and Rh, which either desorb or decompose upon heating. Acetaldehyde also polymerises over Pt(111)<sup>41, 44</sup>, Pd (110) and (111)<sup>45, 46</sup>, in competition with decarbonylation to methane and CO. Propionaldehyde has also been studied over Pd(110)/(111)<sup>45</sup> and Ni/Pt(111)<sup>47</sup> surfaces, which favour decarbonylation to ethene.

Even less is known regarding unsaturated aldehydes, although acrolein has been investigated on Au(111)<sup>48</sup>, Pt(111)<sup>49-52</sup>, and Ni/Pt(111)<sup>53</sup> with decarbonylation or reduction to propene, ketene or alcohols prevalent over group 10 surfaces.

Crotonaldehyde has been studied over Cu(111)<sup>54</sup>, Pt(111)<sup>49, 50</sup> and Sn/Pt(111)<sup>55, 56</sup> single crystal surfaces, with decarbonylation to CO and propene the dominant reaction pathway<sup>55, 57-59</sup>.

### 1.3.3 Au/Pd systems for selox

Bimetallic systems frequently display properties which are significantly different from their component metals<sup>5, 60</sup>. As a result, many of these bimetallic alloys show an enhanced catalytic activity, selectivity or stability when compared to their monometallic counterparts. In particular, Pd/Au systems have displayed improved or even ‘tunable’ properties when compared to pure Pd or Au catalysts<sup>61-63</sup>.

Numerous investigations have focussed on the catalysis of many different reactions by Pd-Au systems including the oxidation of glycerol<sup>64, 65</sup>, hydrogen peroxide synthesis<sup>63, 66, 67</sup>, the cyclisation of acetylene to benzene<sup>68-70</sup>, and the hydrodechlorination of dichlorofluoromethane<sup>71</sup> to name but a few. Recently, various computational studies have also been conducted in order to understand the composition and reactivity of such systems<sup>72, 73</sup>.

In particular, there has been significant interest in Au-Pd systems as catalysts for selective oxidation reactions<sup>74-76</sup>. A major breakthrough occurred when Hutchings et al<sup>61</sup>, discovered that by combining Pd and Au over a titania support 25-fold rate enhancements for alcohol oxidation under mild solvent-free conditions were possible. The introduction of Au also improves selectivities to aldehydes and ketones compared to pure Pd.

High-resolution STEM chemical mapping of these nanoparticles<sup>27</sup> indicates that the active nanoparticles possess a Pd-rich shell encapsulating a Au-rich core<sup>62, 63, 77, 78</sup> (as shown in **Figure 1.6**), and it is likely that surface Au atoms are crucial in regulating the electronic structure and thereby promoting selox chemistry over surface Pd. The details of the active surface ensemble and role of Au in promoting selox were unknown however, making such systems ideal for investigation by utilising ‘model’ single crystal studies by *in situ* XPS using synchrotron radiation.

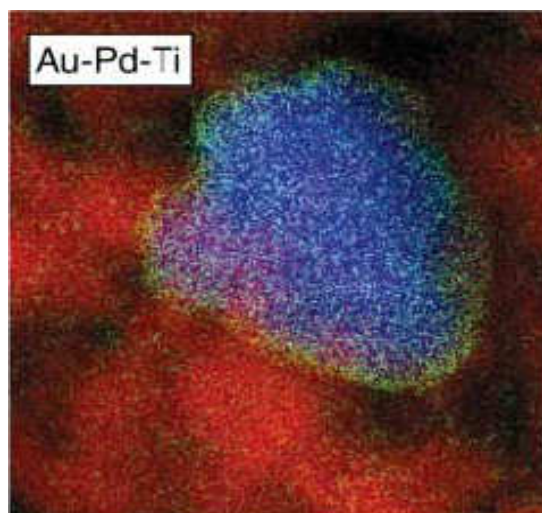


**Figure 1.6** - ADF-STEM image of a bimetallic Au/Pd nanoparticle supported on TiO<sub>2</sub>. This composition map image was created using a multivariate statistical analysis of processed STEM-XEDS maps of the Au-M<sub>2</sub>, Pd-L<sub>α</sub>, O-K<sub>α</sub>, and Ti-K<sub>α</sub> signals (Ti, red; Au, blue; and Pd, green).<sup>27</sup>

It is likely that surface Au atoms promote selox chemistry over surface Pd by regulating the electronic structure. However, the exact details of the active surface ensemble and role of Au in promoting selox in such systems are unclear. This thesis will contribute to this exciting area by implementing a thin-film/surface science approach for elucidating the reaction mechanism of such systems.

### 1.3.4 Formation of Au/Pd(111) surface alloys

The growth and surface alloy formation of Au on Pd(111) has been studied by a variety of techniques including AES<sup>21, 79-81</sup>, XPS<sup>81, 82</sup>, LEED<sup>79, 83</sup>, LEIS<sup>83, 84</sup> and STM<sup>80</sup>. It was found that at room temperature Au grows epitaxial (Frank-Van Der Merwe (FV)) overlayers on Pd(111). This is due to the relatively low lattice mismatch (~ 4.9 %) between Au and Pd<sup>81</sup>. When annealed above 600 K, Au and Pd intermixing occurs (due to the bulk miscibilities of the metal components<sup>81</sup>) where random substitutional surface alloys form. Due to its lower surface free energy, Au would be expected to segregate on the surface of PdAu alloys, prepared under thermodynamic equilibrium<sup>85-87</sup>, although the driving force for segregation is relatively small<sup>73, 88, 89</sup>. As a result, it is possible for entropic driven diffusion of Au into the bulk to occur in contrast to the predicted surface segregation of Au.

Recent theoretical analyses for Au/Pd(111) alloy surfaces suggests weak repulsion between Au and Pd atoms may drive local ordering<sup>90</sup>. The higher the annealing temperature, the more Pd rich the surface alloys become. In this way, in a single set of experiments an Au overlayer can be deposited and then annealed to various different temperatures in order to produce a range of Au/Pd(111) surface alloys in order to study the chemistry of such surfaces. The formation and reactivity of Au/Pd(111) surface alloys will be discussed in more detail in chapters 3 and 4.

#### **1.4 Magnetic Thin-Films for Spintronics**

Depending upon how a given material responds to an external magnetic field, it can be classified as diamagnetic, paramagnetic, antiferromagnetic or ferromagnetic/ferrimagnetic. Most elements in the periodic table are diamagnetic, meaning they have a weak, negative susceptibility to magnetic fields. This means that such materials are slightly repelled by the external field and magnetic properties are not retained when the external field is removed<sup>1</sup>. Diamagnetic properties arise from the realignment of the electron pairs.

Paramagnetic materials have a very small, positive susceptibility to magnetic fields. These materials are slightly attracted by a magnetic field and the material does not retain the magnetic properties when the external field is removed. Paramagnetic properties are due to the presence of some unpaired electrons, and from the realignment of the electron paths caused by the external magnetic field<sup>1</sup>. Paramagnetic materials include magnesium, molybdenum, lithium, and tantalum.

Ferromagnetic materials have a large, positive susceptibility to an external magnetic field. They exhibit a strong attraction to magnetic fields and are able to retain their magnetic properties after the external field has been removed. Ferromagnetic materials have some unpaired electrons so their atoms have a net magnetic moment. They get their strong magnetic properties due to the presence of magnetic domains. In these domains, large numbers of atom's moments are aligned parallel so that the magnetic force within the domain is strong<sup>91</sup>. When a ferromagnetic material is in the un-magnetised state, the domains are nearly randomly organised and the net magnetic field for the part as a whole is zero.

When a magnetizing force is applied, the domains become aligned to produce a strong magnetic field within the part. Iron, nickel, and cobalt are examples of ferromagnetic materials. Components with these materials are commonly inspected using the magnetic particle method.

Antiferromagnetic materials are those in which the neighbouring spins are aligned antiparallel to one another, so that their magnetic moments cancel. Therefore an antiferromagnet produces no spontaneous magnetisation and shows only feeble magnetism. The magnetic susceptibility of such materials is of the same order as that of paramagnetic materials<sup>91</sup>. Antiferromagnets can be therefore thought of as being paramagnetic substances with a characteristic temperature at which the magnetic susceptibility shows a pronounced maximum<sup>92</sup>.

Ferrimagnets behave similarly to ferromagnets, in that they exhibit a spontaneous magnetisation below some critical temperature  $T_c$ , even in the absence of an applied field. In fact, ferrimagnets are also related to antiferromagnets, in that the exchange coupling between adjacent magnetic ions leads to antiparallel alignment of the localised moments. The overall magnetisation occurs because the magnetisation of one sublattice is greater than that of the oppositely orientated sublattice<sup>1</sup>. The fact that ferrimagnets are ionic solids means that they are electrically insulating, whereas most ferromagnets are metals.

Magnetic materials can be found almost everywhere in our every-day modern lives and thin-films are of particular technological interest. Research into this field began in the 1970's with the advent of UHV technologies (particularly that of molecular beam epitaxy<sup>93</sup>), which allowed precise crystallographic control over the growth of thin-films. The study of thin-film magnetism itself has aided the understanding of the fundamental physics of magnetism<sup>1-3, 94-98</sup>, which, in turn, has had important ramifications for magnetic data storage, exemplified by the discovery of Giant Magnetoresistance.

#### **1.4.1 Giant Magnetoresistance**

In the late 1980's it was discovered that when materials composed of multilayers of Fe and a non-magnetic spacing layer (e.g. Cr) were placed in a magnetic field, the overall electrical resistance for the material would decrease by as much as 80% (see **Figure 1.7**). Due to the nature of this effect, it was given the name 'giant

magnetoresistance' (GMR). This phenomenon was recognised by two independent research groups – one in France, headed by Albert Fert<sup>99</sup>; the other being in Germany, lead by Peter Grünberg<sup>100</sup>. In recognition of this discovery, both researchers were awarded the Nobel Prize for physics in 2007<sup>101</sup>. The GMR effect was almost immediately exploited for use in the read heads of modern hard drives, which has facilitated an increase in data storage capacity by approximately 3 orders of magnitude<sup>102-104</sup>.

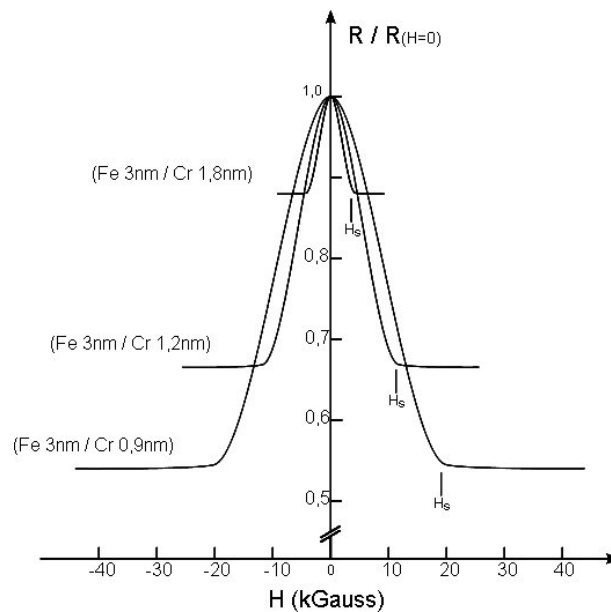


**Figure 1.7** - The results of Fert's experiments that lead to the discovery of GMR - taken from<sup>94, 99</sup>

Further experiments by many other research groups lead to the formation of the theory behind the mechanism of GMR in these multilayer structures. For special cases, in the absence of an applied magnetic field, the direction of magnetization of adjacent ferromagnetic layers is anti-parallel. A lower level of resistance is experienced in an applied external field when the magnetisations of the adjacent layers align<sup>100</sup>. It was discovered that spin dependent scattering is the cause of this phenomenon<sup>105-109</sup>.

Within a ferromagnetic material, a quantum mechanical exchange interaction between the electrons results in a spin-split band structure (as shown below in **Figure 1.8**). As we shall see, there are a number of essential factors that lead to spin-dependent scattering in metallic ferromagnets, which are derived from this

spin-split band structure. Ferromagnets are usually transition metals, which have a relatively high resistivity compared with noble metals. This is unusual, as both sets of metals have a similar number and density of conduction electrons. The difference in resistivity is due to the availability of unoccupied states in partially filled d-bands, which are also available for scattering. This reduces the overall mean free path of the electrons in ferromagnets relative to noble metals<sup>1</sup>.

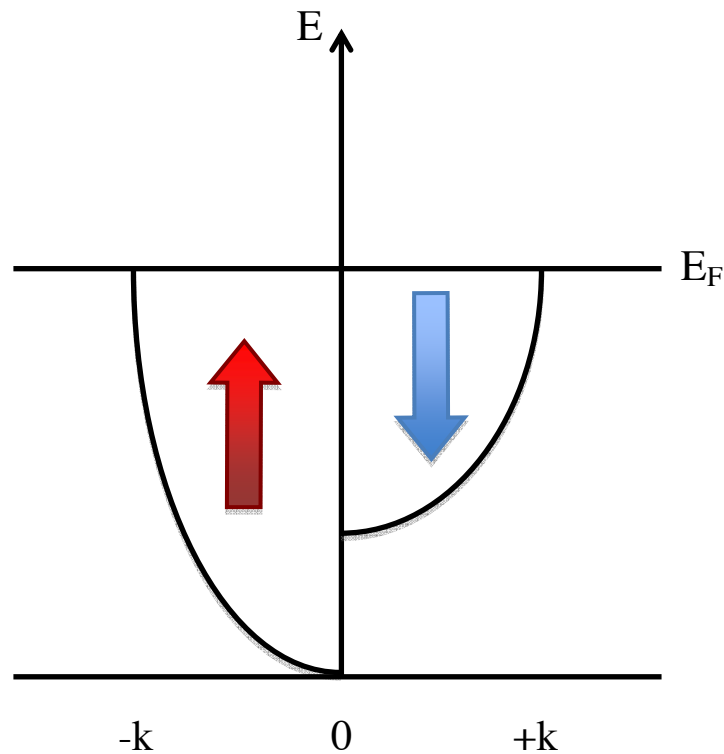


**Figure 1.8** – The spin split band structure present within ferromagnetic materials

From **Figure 1.8**, it can be observed that the spin-split d bands also cause a different density of states at the Fermi surface for spin-up and spin-down electrons. This leads to a different scattering probability for the spin-up and spin-down electrons<sup>110</sup>. The minority electrons usually have the greatest scattering probability. There also has to be little or no spin-flip scattering, which allows the spin-up and spin-down conduction electrons to be considered as two independent channels for current<sup>110, 111</sup>. Therefore, spin-dependent scattering effects result in the spin filtering of the electron current when it passes through a ferromagnetic material, with the minority electrons experiencing more scattering. In other words, the material can be thought of as being a ‘valve’ that selectively permits the flow of one spin over the other. As a result of such behaviour, these types of magnetic

multilayer are known as ‘spin valves’. GMR materials in the read-heads of hard-drives are spin valves that have been specifically designed to exploit spin-dependent scattering<sup>105</sup>.

For a trilayer structure (Fe/Cr/Fe, as shown in **Figure 1.9**), we can consider this mechanism using a simple resistor network in which the independent spin-up and spin-down electron current channels are represented by two parallel circuits. The resistance of the different layers is represented by resistors, with the size of each resistor representing the magnitude of the resistance<sup>105</sup>. For the case when the layers are non-aligned, both spin-up and spin-down channels experience significant scattering, and therefore we have a high electrical resistance. The resistance is lower when the layers are aligned, as the spin-up channel experiences less spin scattering through either of the layers and we have a situation analogous to a short circuit.

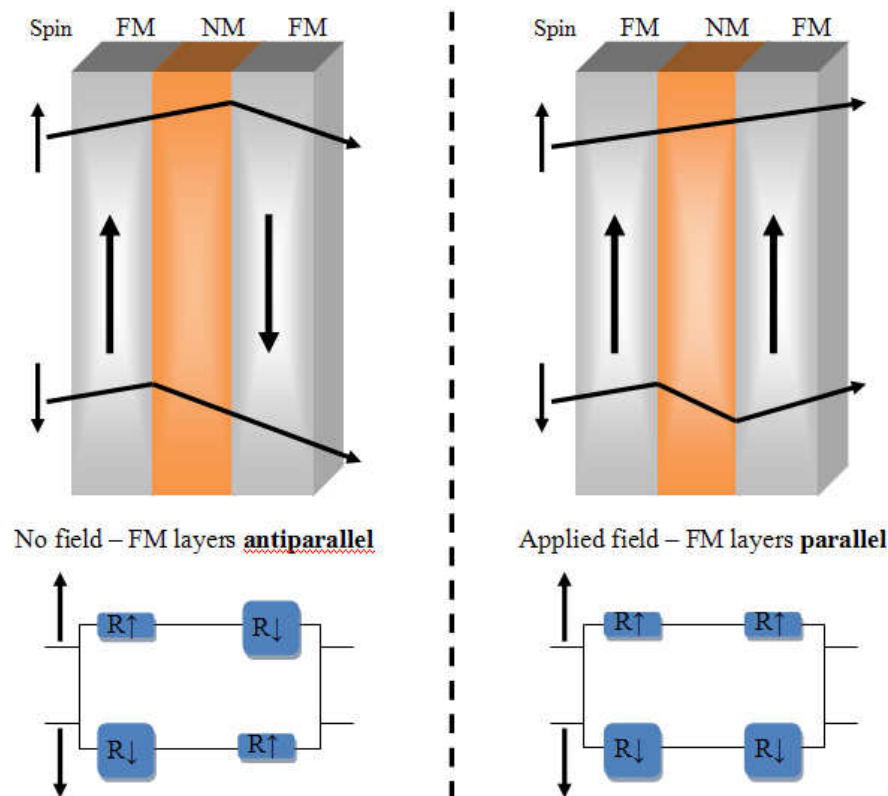


**Figure 1.9** - A diagram illustrating the basic theory behind giant magnetoresistance for a simple magnetic trilayer system – adapted from<sup>105</sup>.

When adopting this simple model, the overall change in resistance can be represented mathematically in **Equation 1.4**.

$$\frac{\Delta R}{R} = \frac{R_{AP} - R_P}{R_P} = \frac{(R_{\downarrow} - R_{\uparrow})^2}{4R_{\downarrow}R_{\uparrow}} \quad \text{Equation 1.4}$$

where  $R_{AP}$  is the overall resistance for the anti-parallel case and  $R_P$  is the overall resistance for the parallel case.  $R_{\uparrow}$  and  $R_{\downarrow}$  represent the resistances of the individual resistors shown in **Figure 1.9**.

The discovery of the GMR effect and its associated mechanism represented a new area of physics; a field now known as ‘spintronics’, which will be described in the following section.

### 1.4.2 Spintronics

Spin transport electronics (spintronics), is an emerging research field in solid-state electronics<sup>112, 113</sup>. As the name suggests, it concerns not only the fundamental electronic charge, but also the intrinsic spin of the electron in order to create new devices. It emerged from spin dependent electron transfer experiments, including the discovery of GMR and the observation of spin-polarized electron injection from a ferromagnetic metal to a normal metal<sup>114</sup>.

The storage capacity of modern hard disks has been increased by the introduction of GMR based spintronic devices, known as spin valves (see **Figure 1.10**). The need for the preparation and characterisation of spintronic materials is essential in order to ensure that this increase in storage trend continues<sup>102, 115</sup>.

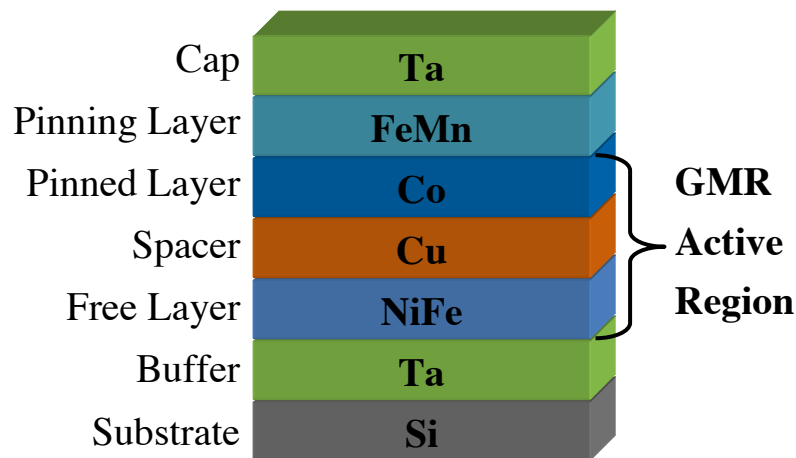


**Figure 1.10** – An example of a spin valve, used as a read head in hard disks.

Magnetic Random Access Memory (MRAM) is a technology, which is also reliant on developments in materials for spintronics. In MRAM grids of magnetic tunnelling junctions (MTJ's) are used as magnetic storage elements, permitting the storage of information even when no electrical power is supplied<sup>115-117</sup>. Due to greater capacity Dynamic RAM (DRAM) is the current standard used in personal computers, however MRAM offers greater speed and lower operating voltage<sup>118</sup>. As a result, research into novel spintronic materials is necessary in order to increase the storage capacity of MRAM.

'Racetrack' memory is another emerging technology based on spintronics, which has been developed by Stuart Parkin and co-workers at IBM<sup>115, 119, 120</sup>. The 'racetrack' consists of a ferromagnetic nanowire, with data encoded as a pattern of magnetic domains along a portion of the wire (see **Figure 1.11**). A spin-polarized current moves the entire pattern of domain wall (DWs) coherently in either direction along the length of the wire past read and write elements. Reading of stored data is achieved by measuring the tunnel magnetoresistance of a magnetic tunnel junction element connected to the racetrack (as shown in **Figure 1.11 C**). Writing data can be accomplished through utilising the fringing fields of a DW moved in a second ferromagnetic nanowire, which is oriented at right angles to the storage nanowire. High storage density can be achieved by creating a series of U shaped arrays relative to the substrate (**Figure 1.11 A and E**). Spin injection in order to apply a spin- polarised current is essential for the operation of such devices.

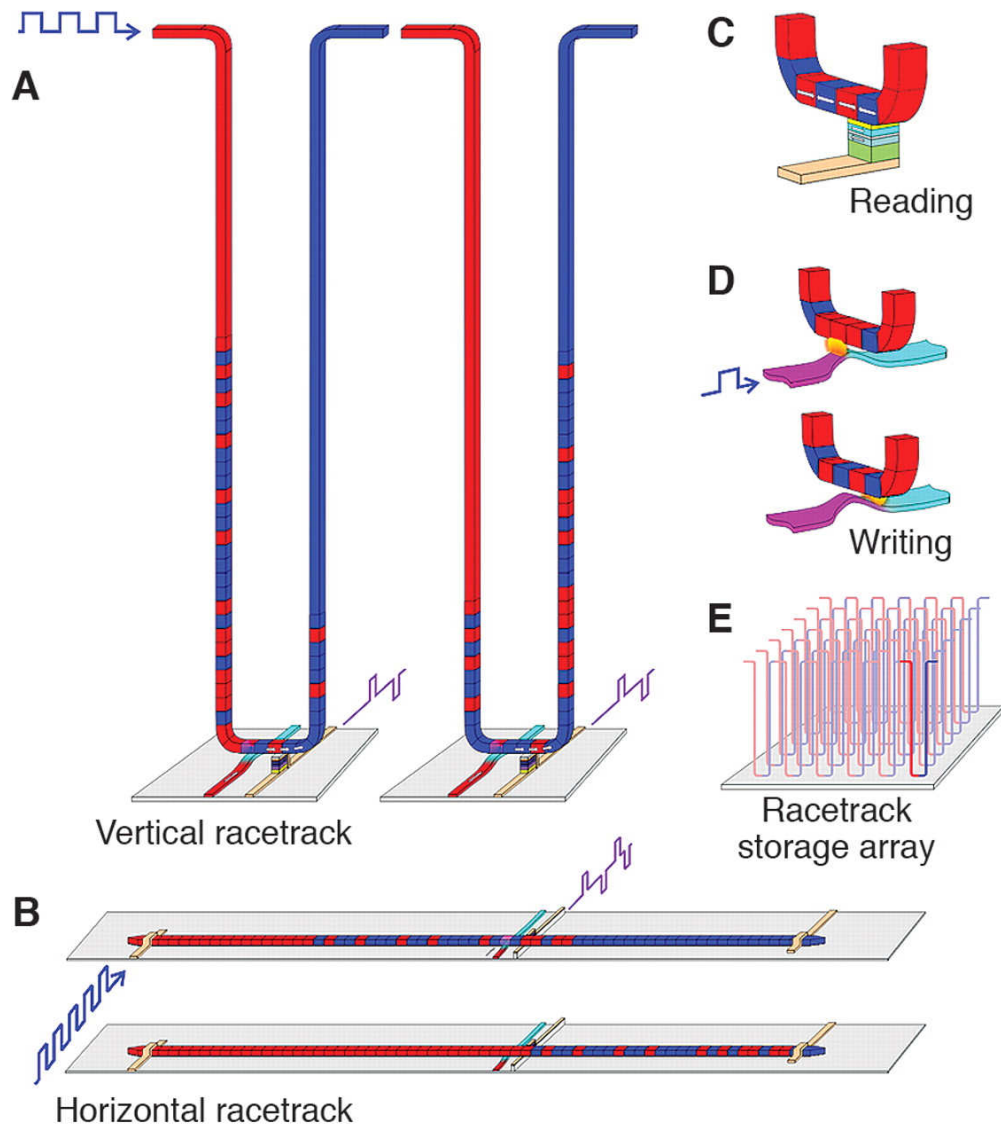


**Figure 1.11** - A simple diagram representing a proposed racetrack memory concept. The racetrack consists of ferromagnetic nanowire with data encoded as a pattern of magnetic domains along a portion of the wire – obtained from<sup>119</sup>.

These examples highlight the fact that there is a huge drive to investigate a wide variety of materials, which have spin-dependent properties, which could be used for applications in spintronic devices. In order to create novel and successful spintronic devices, spin accumulation is a key factor. It represents a huge challenge, as it is the process by which non-equilibrium electron spins are generated and build up within a material. Spin-injection is the most useful technique in order to bring about this spin accumulation in materials. It involves transporting an electron of a particular spin from a source (usually ferromagnet) to a semiconducting material. In doing so, the spin orientation (i.e. up or down) of the

electron must be conserved<sup>121</sup>. Therefore, materials that exhibit a high level of spin polarisation are essential for this process.

### 1.4.3 Half metals

Half metals (also known as Half Metallic Ferromagnets) are ferromagnets whose density of states has exclusively one occupied sub-band at the Fermi energy ( $E_F$ ) as shown below in **Figure 1.12**. As a result, they theoretically give rise to 100% spin polarisation, as only electrons with the same spin orientation as the partially filled band can be transported through the material. It is hoped that these interesting properties can be exploited in future magnetoresistive devices<sup>112, 113, 115, 122, 123</sup>.

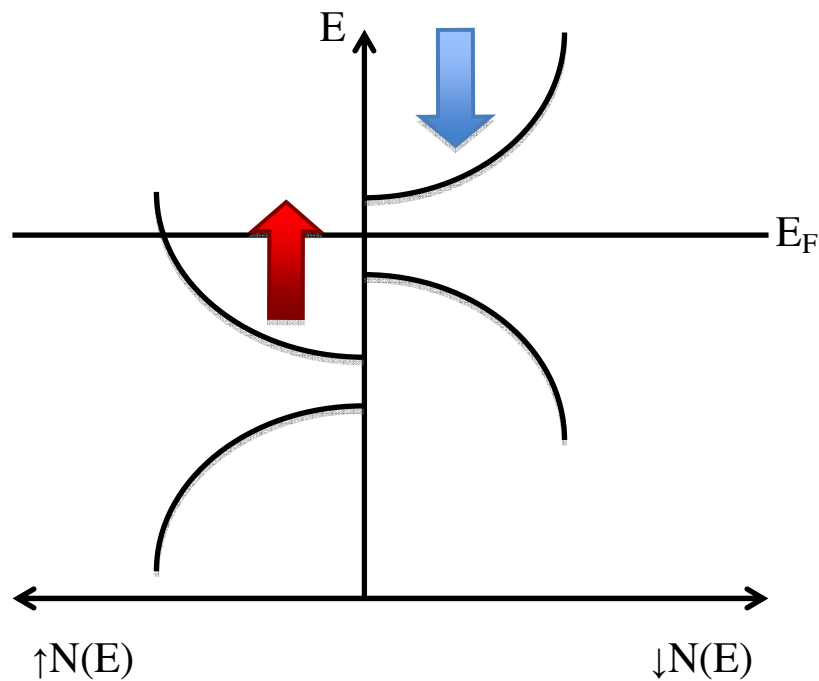


**Figure 1.12** - A simple diagram showing the density of states of a half-metallic system.

Half metals are typically oxide materials, which include  $\text{CrO}_2$ , mixed valence manganites ( $\text{La}_{(1-x)}\text{A}_x\text{MnO}_3$ ,  $\text{A} = \text{Ca, Ba, Sr}$ ), double perovskites<sup>124</sup> ( $\text{A}_2\text{BB}'\text{O}_6$ ,  $\text{A} = \text{Ca, Sr, Ba}$ ,  $\text{B} = 3\text{d transition metal (Fe, Co)}$ ,  $\text{B}' = 4\text{d transition metal (Mo, Re)}$ ) and  $\text{Fe}_3\text{O}_4$ .

#### 1.4.4 Oxide Materials for Spintronics

Transition metal oxides are receiving a great deal of attention, as they display a wide range of fascinating physical properties such as high temperature superconductivity, ferro- and antiferromagnetism, ferroelectricity and even multiferroicity<sup>122</sup>. The enormous progress in oxide thin-film technology allows us to integrate these materials with semiconducting, normal conducting, dielectric, or non-linear optical oxides in complex oxide heterostructures, providing the basis for novel multi-functional materials and potentially making them suitable for various spintronic applications.

#### 1.4.5 Magnetite (Fe<sub>3</sub>O<sub>4</sub>)

Magnetite (Fe<sub>3</sub>O<sub>4</sub>), was discovered in Greece around 2000 BC making it the oldest magnetic material known to man<sup>125</sup>. Magnetite is a half-metallic conducting ferrimagnetic oxide material, which is magnetic at room temperature, having a very high Curie temperature of approximately 858 K<sup>126</sup>. Band calculations predict that conduction electrons are fully spin polarised<sup>127-130</sup>, which makes it a very suitable candidate for use as a spin injector for magnetic recording/spintronic applications.

Whilst naturally occurring magnetite has been used for thousands of years, its properties, particularly those of thin-films are not fully understood<sup>125, 127</sup>. Thin films of magnetite have properties which deviate from the bulk<sup>131</sup>, including the fact that the magnetisation does not saturate in high fields<sup>132</sup>, and ultra-thin films (< 5 nm) are superparamagnetic<sup>133</sup>, the resistivity is increased relative to the bulk<sup>134</sup> and epitaxial films show magnetoresistance<sup>135</sup>.

Fe<sub>3</sub>O<sub>4</sub> is an example of a spinel ferrite, all of which have the general formula of MFe<sub>2</sub>O<sub>4</sub>. M represents a divalent ion, which in the case of Fe<sub>3</sub>O<sub>4</sub> M is a Fe<sup>2+</sup> ion. Spinel ferrites have two distinct crystallographic variants, one known as ‘normal’ spinel and other being ‘inverse’ spinel<sup>136</sup>. Fe<sub>3</sub>O<sub>4</sub> is an inverse spinel, having a crystal structure with two different Fe sublattices, as shown in **Figure 1.13 (a)**. Tetrahedral (A) sites are exclusively occupied by eight Fe<sup>3+</sup> ions in the unit cell, where as the octahedral sites (B) are occupied by eight Fe<sup>2+</sup> and eight Fe<sup>3+</sup> ions, as represented in **Figure 1.13 (b)**.

Due to the close proximity and orbital overlap of surrounding  $O^{2-}$  ions, a crystal field is established which splits the 3d states of the  $Fe^{2+}$  and  $Fe^{3+}$  ions in the B site into two states with  $e_g$  and  $t_{2g}$  symmetry (see **Figure 1.13 (c)**). The  $t_{2g}$  spin-down electron can “hop” between the  $Fe^{2+}$  and  $Fe^{3+}$  ions<sup>137</sup> (also shown in **Figure 1.13 (c)**), which gives rise to the electrical conductivity within  $Fe_3O_4$ . It should be noted that, in accordance with Hund’s rule, this 2g B spin is coupled antiparallel to the local moment formed by the spin-up electrons.

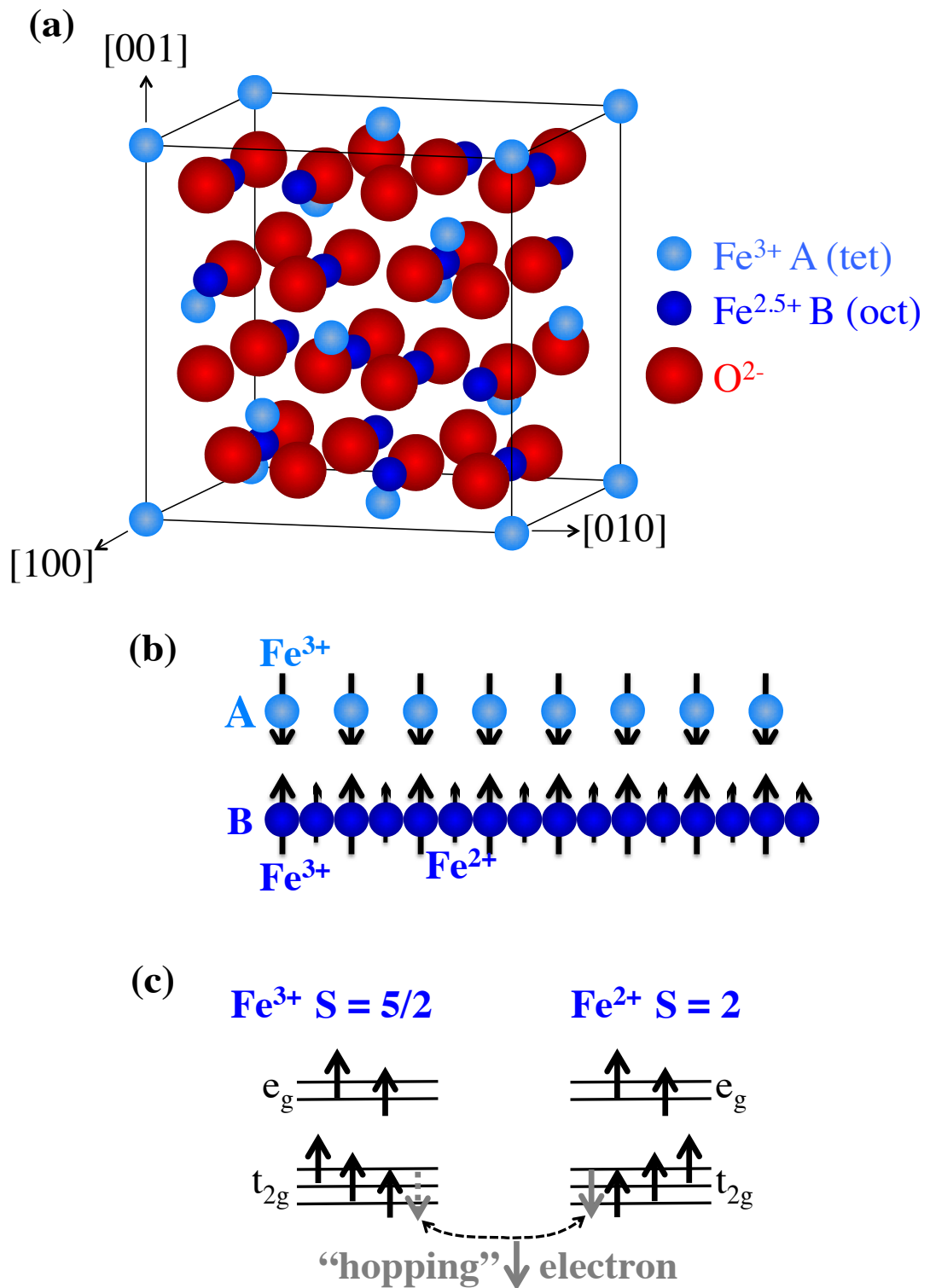


**Figure 1.13** (a) – The inverse spinel crystal structure of  $\text{Fe}_3\text{O}_4$ , showing the tetrahedrally coordinated  $\text{Fe}^{3+}$  A site and mixed-valent ( $\text{Fe}^{2+}$ ,  $3d^6$  /  $\text{Fe}^{3+}$ ,  $3d^5$ ) octahedrally coordinated B site (adapted from<sup>137,138</sup>). (b) – A simple diagram showing the A and B sublattice configuration<sup>137</sup>. (c) – A crystal field splitting diagram of the  $\text{Fe}^{2+}$  and  $\text{Fe}^{3+}$  3d states, along with the itinerant (“hopping”) electron<sup>137</sup>.

The growth of  $\text{Fe}_3\text{O}_4$  is extremely challenging, as there are many different phases of iron oxide. The phase diagram of the iron oxygen system is shown below in **Figure 1.14**.  $\text{Fe}_3\text{O}_4$  is represented in the phase diagram by the letter M, which represents a very small, narrow region on the phase diagram. It is therefore crucial to carefully control the various different growth parameters (such as substrate temperature, O partial pressure, Fe flux etc.) in order to select growth of the desired iron oxide from the phase diagram. In order to calibrate the growth and select  $\text{Fe}_3\text{O}_4$  it is also necessary to prepare a wide variety of samples whilst varying all growth parameters. In doing so, it should be possible to consistently prepare the desired phase of iron oxide. It is also critical to use a wide variety of surface science techniques to correctly determine the phase of each sample grown.

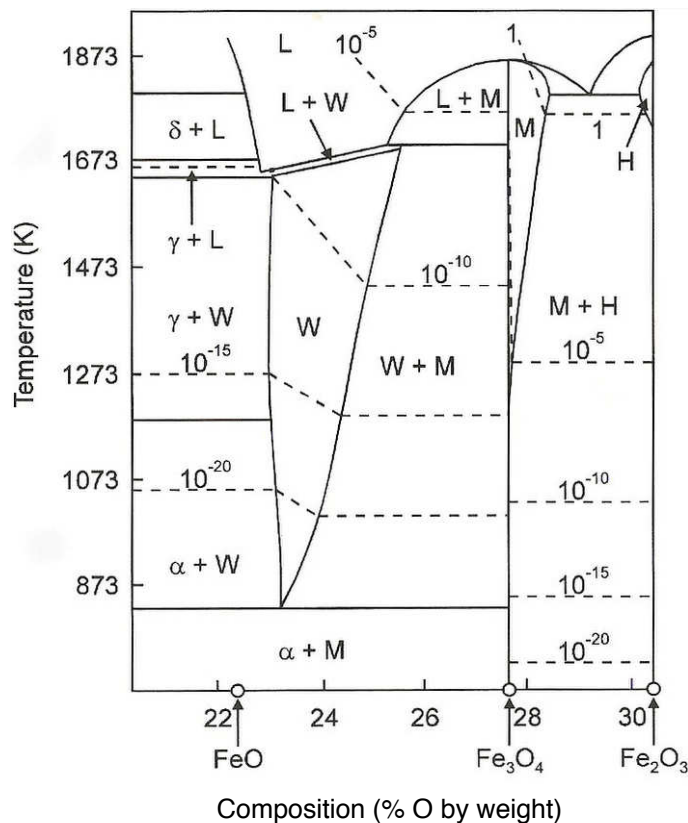
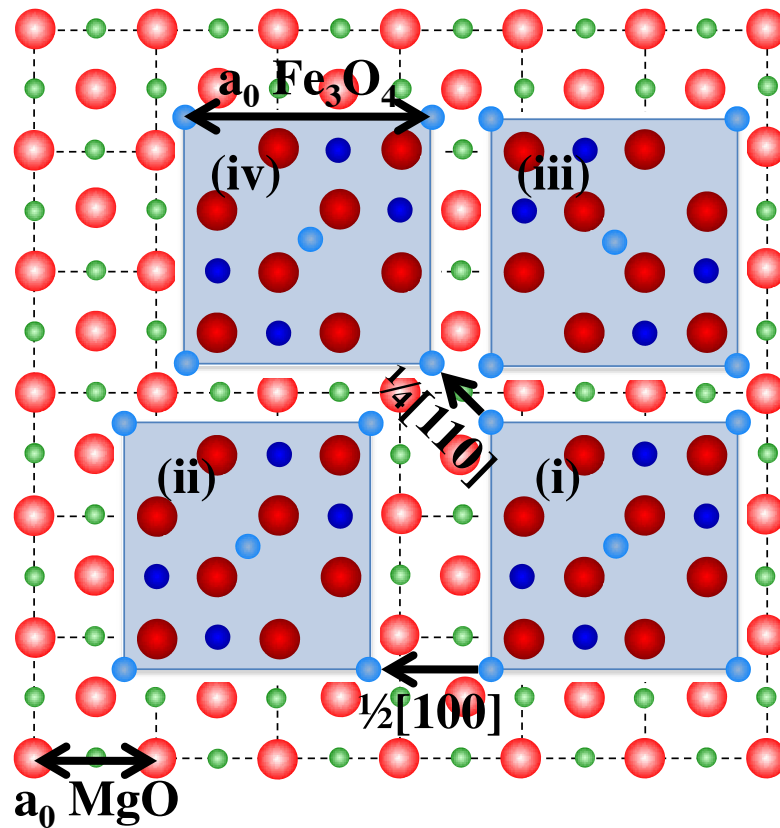


**Figure 1.14** – The phase diagram for the iron oxygen system (modified from Darken<sup>139</sup> and Voogt<sup>140</sup>).

$\alpha$ ,  $\gamma$ ,  $\delta$  indicate the various phases of metallic iron (b.c.c., f.c.c and high temperature b.c.c. respectively). W, M and H stand for wüstite ( $\text{FeO}$ ), magnetite ( $\text{Fe}_3\text{O}_4$ ) and haematite ( $\text{Fe}_2\text{O}_3$ ) respectively. L stands for liquid. Dashed lines show oxygen equilibrium pressures.

MgO is often used as a substrate for the growth of thin-films of Fe<sub>3</sub>O<sub>4</sub>. This is because, in the crystal structure of Fe<sub>3</sub>O<sub>4</sub> and MgO, the O atoms form an approximate face-centred cubic lattice. As a result, there is only a slight mismatch (~ 0.3 %) in *d* for the O lattices in MgO and Fe<sub>3</sub>O<sub>4</sub>, meaning that epitaxial growth is favoured. However, the unit cell of Fe<sub>3</sub>O<sub>4</sub> (*a*<sub>0</sub> = 8.397 Å) is twice the size of the MgO unit cell (*a*<sub>0</sub> = 4.212 Å)<sup>136</sup>, resulting in initial island formation. When different islands meet during growth, they can be shifted or rotated with respect to each other, forming what is known as an antiphase boundary (APB)<sup>132-134, 141</sup>. A simplified diagram of APB formation including the various shift vectors for Fe<sub>3</sub>O<sub>4</sub> on MgO(100) is shown below in **Figure 1.15**.

(a) Plan view:



(b) Profile view:

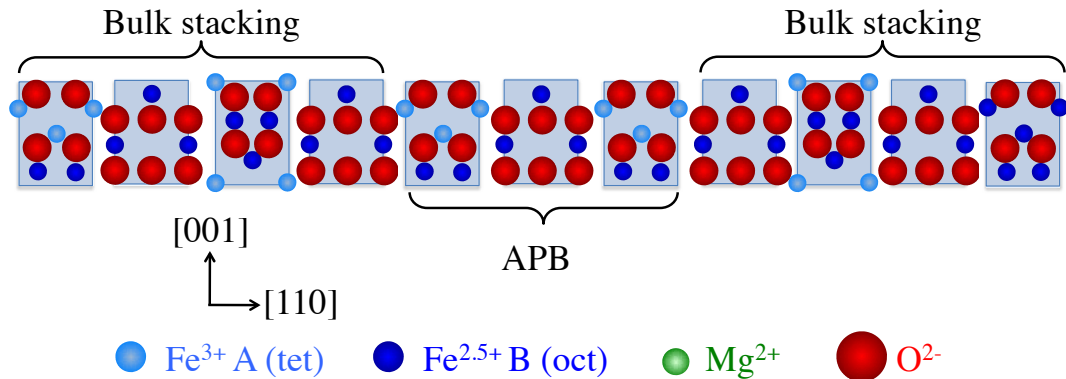


**Figure 1.15** – (a) The APB shifts formed according to the different translational and rotational symmetry of the initial Fe<sub>3</sub>O<sub>4</sub> monolayer and the MgO(100) surface (modified from Eerenstein<sup>138</sup>). Fe<sub>3</sub>O<sub>4</sub> monolayers are shifted relative to reference (i), forming in-plane shifts of (ii)  $\frac{1}{2}[100]$  (iii)  $\frac{1}{4}[110]$ . A rotated monolayer, (iv), forms an out-of plane shift. (b) Side profile of an Fe<sub>3</sub>O<sub>4</sub> APB in the 110 direction on MgO(100) modified from Arras et al.<sup>130</sup>

The magnetic coupling over a large fraction of these boundaries is anti-ferromagnetic (AF). These AF interfaces hinder spin-polarised electron transport

between neighbouring APBs, which is the cause of the increased resistance relative to the bulk. However, when a magnetic field is applied, the AF spins align and the electron transport across the boundaries increases, resulting in a decrease in resistance<sup>142</sup>. As crystallographic defects, APBs can be imaged by dark field and high-resolution transmission electron microscopy. It has been demonstrated that the density of APBs is dependent upon the film thickness, as shown the dark field electron micrographs in **Figure 1.16 (a)-(d)**<sup>134</sup>. The dark lines in these figures show the APBs, the density of which is largest for thin-films.

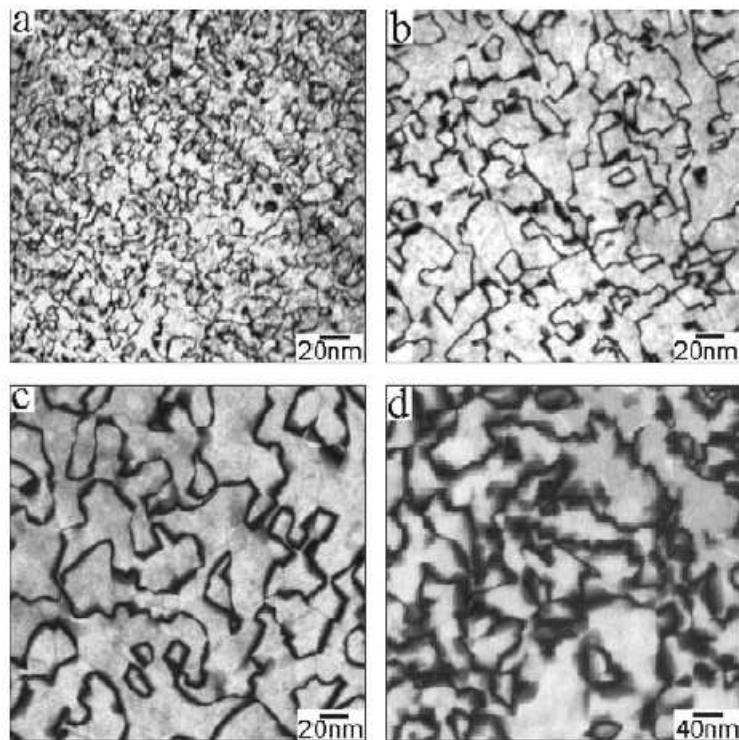


**Figure 1.16** – Dark field transmission electron micrographs of APBs from within (a) 6 nm, (b) 12 nm, (c) 25 nm and (d) 50 nm thick films of  $\text{Fe}_3\text{O}_4/\text{MgO}(100)$  – taken from<sup>134</sup>

Experiments have also been carried out to modify the density of the APBs by annealing samples<sup>143, 144</sup>. The density of the APBs decreased dramatically with increasing temperature, having a great impact upon the magnetoresistance. The density of the APBs determines the magnitude of the magnetoresistance, and therefore the greater the number (and density) of APBs, the higher the magnetoresistance<sup>145, 146</sup>.

These results all show that the magnetoresistance of magnetite strongly correlates to the thickness and structure of the material<sup>128, 147</sup>, with APB density heavily dominating properties<sup>131, 132, 145, 148</sup>. Despite this relationship, most studies have focussed on the MgO(100) surface, with very little work being conducted on the MgO(110) and MgO(111) surfaces. This thesis will therefore examine these materials using thin-film and surface science methods in order to determine the effect of the substrate upon the magnetoresistance. Crucially, magneto-optical non-contact methods will be employed and developed in order to examine these effects. Simulations will also be performed to aid in the interpretation of results.

## **1.5 Combinatorial methods**

The development of materials typically proceeds *via* trial and error methodologies, where many similar compounds are both prepared and also characterised individually. An alternative procedure for the simultaneous preparation and characterisation of large numbers of inorganic compounds was first proposed by Hanak in 1970<sup>4</sup>.

An analogous approach has long been adopted for drug discovery in pharmaceutical research. This method is known as ‘Combinatorial Chemistry’<sup>149, 150</sup> and is frequently being adapted for the rapid synthesis and *in-situ* characterisation of materials<sup>150, 151</sup>. This approach is often also referred to as parallel synthesis or high-throughput synthesis<sup>152, 153</sup>. Materials which have been investigated using this combinatorial approach<sup>154</sup>, include, but are not limited to, catalysts<sup>153, 155-157</sup>, optical<sup>158, 159</sup>, magnetic<sup>152, 160</sup>, and dielectric<sup>160, 161</sup> materials, hydrogen storage materials<sup>162, 163</sup> and structural polymers<sup>154</sup>. This thesis will add to this research area through the development of a combinatorial sputtering rig for the rapid preparation of vast arrays of materials for heterogeneous catalysis and magnetic materials for spintronics.

## **1.6 Thesis Aims**

As this introduction has highlighted, the preparation and optimisation of advanced functional materials presents a huge challenge for chemists, physicists and

materials scientists. Such systems are often very complex and therefore require empirical trial-and-error methods involving the synthesis and characterisation of a large number of materials with varying compositions. It has also been shown that surface science techniques involving model single crystals and/or thin-films allow the mechanisms of a wide variety of chemical and physical phenomena to be probed with a great deal of precision and accuracy, giving molecular or even atomic level insight.

The aim of this thesis is to utilise such surface science techniques in order to prepare and characterise model thin-film materials for the mechanistic study of heterogeneous catalysis and spintronics. To this end, the reaction pathway for the selective oxidation of crotyl alcohol, an important fine chemical, over Au/Pd thin-films will be determined. This will involve the preparation and catalytic characterisation of a large number of Au/Pd alloy compositions. Powerful surface science techniques will be employed to elucidate the reaction pathway and examine the adsorption and chemistry of all by-products. Once the chemistry of such films is known, it would then be possible, through the development of a combinatorial sputtering rig, to prepare vast libraries of catalysts through co-sputtering Au and Pd onto Si (100) substrates. The catalytic activities of such catalysts could then be rapidly screened by means of infrared thermography, enabling the alloy composition with optimum activity to be determined. Similarly, magnetic materials could also be investigated in the same manner, using well characterised exemplar materials to highlight the potential and wide range of applications for combinatorial methods.

Thin-films of magnetite ( $\text{Fe}_3\text{O}_4$ ) will be prepared on various substrates and their magnetoresistive properties characterised. Magneto-optical methods will be developed, which will allow the non-contact study of both the composition and the magnetoresistive properties. By modelling the complex index of refraction, it will also be possible to probe the thickness dependent magnetoresistance and eventually probe different conductivity mechanisms exhibiting characteristic spectral dependences. As a result, this model could also be used to determine sample thickness. Further work could be carried out in the future in order to adapt such simple systems for use for other oxide materials, such as those for spin injection in thin-film spintronic devices.

## 1.7 References

1. N. A. Spaldin, *Magnetic Materials: Fundamentals and Applications*, 2 edn., Cambridge University Press, 2011.
2. J. Shen and J. Kirschner, *Surface Science*, 2002, **500**, 300-322.
3. C. A. F. Vaz, J. Bland and G. Lauhoff, *Reports on Progress in Physics*, 2008, **71**, 1-78.
4. J. Hanak, *Journal of materials science*, 1970, **5**, 964-971.
5. J. A. Rodriguez and D. W. Goodman, *J. Phys. Chem.*, 1991, **95**, 4196-4206.
6. T. Mallat and A. Baiker, *Chem. Rev.*, 2004, **104**, 3037-3058.
7. A. Corma, H. Garcia and A. Leyva, *Journal of Molecular Catalysis A*, 2005, **230**, 97-105.
8. R. Sheldon, *Pure and applied chemistry*, 2000, **72**, 1233-1246.
9. T. Mallat and A. Baiker, *Catalysis Today*, 1994, **19**, 247-283.
10. A. Lee, C. Ellis, J. Naughton, M. A. Newton, C. M. A. Parlett and K. Wilson, *Journal of the American Chemical Society*, 2011, **133**, 5724-5727.
11. P. Dash, N. Dehm and R. Scott, *Journal of Molecular Catalysis A: Chemical*, 2008, **286**, 114-119.
12. C. Hardacre, E. A. Mullan, D. W. Rooney and J. M. Thompson, *Journal of Catalysis*, 2005, **232**, 355-365.
13. M. Caravati and A. Baiker, *Catalysis Today*, 2004, **92-92**, 1-5.
14. J.-D. Grunwaldt, M. Caravati and A. Baiker, *The Journal of Physical Chemistry B*, 2006, **110**, 9916-9922.
15. J.-D. Grunwaldt, M. Caravati, M. Ramin and A. Baiker, *Catalysis Letters*, 2003, **90**, 221-229.
16. B. Kimmerle, J.-D. Grunwaldt and A. Baiker, *Topics in Catalysis*, 2007, **44**, 285-291.
17. X. Wang, N. Venkataramanan, H. Kawanami and Y. Ikushima, *Green Chem.*, 2007, **9**, 1352-1355.
18. T. Mallat, Z. Bodnar, P. Hug and A. Baiker, *Journal of Catalysis*, 1995, **153**, 131-143.
19. D. Kumar, M. Chen and D. Goodman, *Catalysis Today*, 2007, **123**, 77-85.

20. M. Chen, D. Kumar, C.-W. Yi and D. Goodman, *Science*, 2005, **310**, 291-293.
21. F. Calaza, F. Gao, Z. Li and W. Tysoe, *Surf. Sci.*, 2007, **601**, 714-722.
22. C. Mingshu and D. Goodman, *Chinese Journal of Catalysis*, 2008, **29**, 1178-1186.
23. M. Chen, K. Luo, T. Wei, Z. Yan, D. Kumar, C.-W. Yi and D. Goodman, *Catalysis Today*, 2006, **117**, 37-45.
24. M. Chen, D. Kumar, C.-W. Yi and D. W. Goodman, *Science*, 2005, **310**, 291-293.
25. S. Hackett, Rik M. Brydson, M. Gass, I. Harvey, A. Newman, K. Wilson and A. Lee, *Angewandte Chemie International Edition*, 2007, **46**, 8593 – 8596.
26. K. Yamaguchi and N. Mizuno, *Angewandte Chemie*, 2002, **114**, 4720-4724.
27. D. I. Enache, J. K. Edwards, P. Landon, B. Solsona-Espriu, A. F. Carley, A. A. Herzing, M. Watanabe, C. J. Kiely, D. W. Knight and G. J. Hutchings, *Science*, 2006, **311**, 362.
28. M. Hughes, Y. Xu, P. Jenkins, P. McMorn, P. Landon, D. Enache, A. Carley, G. Attard, G. Hutchings and F. King, *Nature*, 2005, **437**, 1132-1135.
29. C. Keresszegi, T. Bürgi, T. Mallat and A. Baiker, *Journal of Catalysis*, 2002, **211**, 244-251.
30. S. Hackett, University of York, 2008.
31. J. L. Solomon and R. J. Madix, *Journal of Physical Chemistry*, 1987, **91**, 6241-6244.
32. J. L. Solomon, R. J. Madix and J. Stöhr, *The Journal of Chemical Physics*, 1988, **89**, 5316.
33. R. L. Brainard, C. G. Peterson and R. J. Madix, *J. Am. Chem. Soc.*, 1989, **111**, 4553-4561.
34. N. F. Brown and M. A. Barteau, *J. Am. Chem. SOC*, 1992, **114**, 4258-4265.
35. F. Delbecq and P. Sautet, *Journal of Catalysis*, 1995, **152**, 217-236.
36. A. Lee, Z. Chang, P. Ellis, S. Hackett and K. Wilson, *J. Phys. Chem. C*, 2007, **111**, 18844-18847.
37. T. R. Bryden and S. J. Garrett, *The Journal of Physical Chemistry B*, 1999, **103**, 10481-10488.

38. B. A. Sexton, A. E. Hughes and N. R. Avery, *Surface Science*, 1985, **155**, 366-386.
39. W.-H. Hung and S. L. Bernasek, *Surface Science*, 1996, **346**, 165-188.
40. G. A. Attard, H. D. Ebert and R. Parsons, *Surface Science*, 1990, **240**, 125-135.
41. H. B. Zhao, J. Kim and B. E. Koel, *Surface Science*, 2003, **538**, 147-159.
42. C. Houtman and M. A. Barteau, *Surface Science*, 1991, **248**, 57-76.
43. M. Shen and F. Zaera, *Journal of the American Chemical Society*, 2009, **131**, 8708-8713.
44. R. W. McCabe, C. L. DiMaggio and R. J. Madix, *The Journal of Physical Chemistry*, 2002, **89**, 854-861.
45. R. Shekhar, M. A. Barteau, R. V. Plank and J. M. Vohs, *The Journal of Physical Chemistry B*, 1997, **101**, 7939-7951.
46. M. Bowker, R. Holroyd, N. Perkins, J. Bhantoo, J. Counsell, A. Carley and C. Morgan, *Surface Science*, 2007, **601**, 3651-3660.
47. L. E. Murillo and J. G. Chen, *Surface Science*, 2008, **602**, 2412-2420.
48. M. Akita, N. Osaka and K. Itoh, *Surface Science*, 1998, **405**, 172-181.
49. C. J. Kliewer, M. Bieri and G. A. Somorjai, *Journal of the American Chemical Society*, 2009, **131**, 9958-9966.
50. J. C. de Jesús and F. Zaera, *Surface Science*, 1999, **430**, 99-115.
51. J. C. de Jesús and F. Zaera, *Journal of Molecular Catalysis A: Chemical*, 1999, **138**, 237-240.
52. J. C. d. Jesús and F. Zaera, *Surface Science*, 1999, **430**, 99-115.
53. L. E. Murillo and J. G. Chen, *Surface Science*, 2008, **602**, 919-931.
54. M. E. Chiu, D. J. Watson, G. Kyriakou, M. S. Tikhov and R. M. Lambert, *Angew. Chem.-Int. Edit.*, 2006, **45**, 7530-7534.
55. D. I. Jerdev, A. Olivas and B. E. Koel, *Journal of Catalysis*, 2002, **205**, 278-288.
56. E. Janin, H. von Schenck, S. Ringler, J. Weissenrieder, T. Åkermark and M. Göthelid, *Journal of Catalysis*, 2003, **215**, 245-253.
57. J. Haubrich, D. Loffreda, F. Delbecq, Y. Jugnet, P. Sautet, A. Krupski, C. Becker and K. Wandelt, *Chemical Physics Letters*, 2006, **433**, 188-192.

58. J. Haubrich, D. Loffreda, F. Delbecq, P. Sautet, A. Krupski, C. Becker and K. Wandelt, *The Journal of Physical Chemistry C*, 2009, **113**, 13947-13967.
59. E. Janin, H. von Schenck, S. Ringler, J. Weissenrieder, T. Åkermark and M. Göthelid, *Journal of Catalysis*, 2003, **215**, 245-253.
60. M. Ruff, N. Takehiro, P. Liu, J. K. Nørskov and R. J. Behm, *ChemPhysChem*, 2007, **8**, 2068 – 2071.
61. M. D. Hughes, Y. J. Xu, P. Jenkins, P. McMorn, P. Landon, D. I. Enache, A. F. Carley, G. A. Attard, G. J. Hutchings, F. King, E. H. Stitt, P. Johnston, K. Griffin and C. J. Kiely, *Nature*, 2005, **437**, 1132-1135.
62. G. J. Hutchings, *Catalysis Today*, 2007, **122**, 196–200.
63. G. J. Hutchings, *Chem. Commun.*, 2007, **2008**, 1148–1164.
64. N. Dimitratos, F. Porta and L. Prati, *Applied Catalysis A: General*, 2005, **291**, 210-214.
65. W. C. Ketchie, M. Murayama and R. J. Davis, *Journal of Catalysis*, 2007, **250**, 264-273.
66. F. Menegazzo, P. Burti, M. Signoretto, M. Manzoli, S. Vankova, F. Boccuzzi, F. Pinna and G. Strukul, *Journal of Catalysis*, 2008, **257**, 369-381.
67. J. K. Edwards, A. Thomas, A. F. Carley, A. A. Herzing, C. J. Kiely and G. J. Hutchings, *Green Chem.*, 2008, **10**, 388–394.
68. A. F. Lee, C. J. Baddeley, C. Hardacre, R. M. Ormerod, R. M. Lambert, G. Schmid and H. West, *J. Phys. Chem.*, 1995, **99**, 6096-6102.
69. C. J. Baddeley, J. R. M. Ormerod, A. W. Stephenson and R. M. Lambert, *J. Phys. Chem.*, 1995, **99**, 5146-5151.
70. C. J. Baddeley, M. Tikhov, C. Hardacre, J. R. Lomas and R. M. Lambert, *J. Phys. Chem.*, 1996, **100**, 2189-2194.
71. M. Bonarowska, J. Pielaszek, V. A. Semikolenov and Z. Karpinski, *Journal of Catalysis*, 2002, **209**, 528–538.
72. A. B. Jorge, P. Craig, N. Matthew and T. T. Wilfred, *Physical Review B (Condensed Matter and Materials Physics)*, 2008, **77**, 045422.
73. D. Yuan, X. Gong and R. Wu, *Phys. Rev. B*, 2007, **75**, 085428.
74. A. Abad, P. Concepción, A. Corma and H. García, *Angew. Chem. Int. Ed.*, 2005, **44**, 4066 –4069.

75. N. Dimitratos, A. Villa, D. Wangb, F. Porta, D. Su and L. Prati, *J. Cat.*, 2006, **244**, 113-121.
76. X. Wang, N. S. Venkataramanan, H. Kawanami and Y. Ikushima, *Green Chem.*, 2007, **9**, 1352-1355.
77. D. I. Enache, J. K. Edwards, P. Landon, B. Solsona-Espriu, A. F. Carley, A. A. Herzing, M. Watanabe, C. J. Kiely, D. W. Knight and G. J. Hutchings, *Science*, 2006, **311**, 362-365.
78. G. J. Hutchings, *Catalysis Today*, 2008, **138**, 9-14.
79. C. Baddeley, M. Tikhov, C. Hardacre, J. Lomas and R. Lambert, *J. Phys. Chem.*, 1996, **100**, 2189-2194.
80. B. Gleich, M. Ruff and R. Behm, *Surf. Sci.*, 1997, **386**, 48-55.
81. Z. Li, F. Gao, Y. Wang, F. Calaza, L. Burkholder and W. Tysoe, *Surf. Sci.*, 2007, **601**, 1898-1908.
82. R. Ormerod, C. Baddeley and R. M. Lambert, *Surface Science*, 1991, **259**, L709-L713.
83. Z. Li, O. Furlong, F. Calaza, L. Burkholder, H. Poon, D. Saldin and W. Tysoe, *Surf. Sci.*, 2008, **602**, 1084-1091.
84. C.-W. Yi, K. Luo, T. Wei and D. W. Goodman, *J. Phys. Chem. B*, 2005, **109**, 18535-18540.
85. T. Wei, J. Wang and D. Goodman, 2007.
86. A. V. Ruban, H. L. Skriver and J. K. Norskov, *Physical Review B*, 2012, **59**, 15990-16000.
87. A. Ruban, B. Hammer, P. Stoltze, H. L. Skriver and J. K. Norskov, *Journal of Molecular Catalysis A*, 1997, **115**, 421-429.
88. L. Kibler, *Electrochimica Acta*, 2008, **53**, 6824-6828.
89. S. Guerin, B. E. Hayden, D. Pletcher, M. E. Rendall and J.-P. Suchsland, *J. Comb. Chem.*, 2006, **8**, 679-686.
90. J. A. Boscoboinik, C. Plaisance, M. Neurock and W. T. Tysoe, *Phys. Rev. B*, 2008, **77**, 045422.
91. S. Chikazumi, *Physics of Ferromagnetism*, Oxford University Press, 1997.
92. L. Pauling, *The Nature of the Chemical Bond*, 3 edn., Cornell University Press., 1960.
93. J. Arthur, *Surface Science*, 2002, **500**, 189-217.
94. S. Bader, *Proceedings of the IEEE*, 1990, **78**, 909-922.

95. P. Grundy, *Journal of Physics D: Applied Physics*, 1998, **31**, 2975-2990.
96. J. Bland and B. Heinrich, *Ultrathin Magnetic Structures I*, Springer, 2005.
97. B. Heinrich and J. A. C. Bland, *Ultrathin Magnetic Structures II*, Springer, 2005.
98. J. Bland and B. Heinrich, *Ultrathin Magnetic Structures III*, Springer, 2005.
99. M. N. Baibich, J. M. Broto, A. Fert, F. N. V. Dau, F. Petroff, P. Eitenne, G. Creuzet, A. Friederich and J. Chazelas, *Physical Review Letters*, 1988, **61**, 2472-2475.
100. G. Binasch, P. Grünberg, F. Saurenbach and W. Zinn, *Phys. Rev. B.*, 1989, **39**.
101. [http://www.kva.se/Documents/Priser/Nobel/2007/pop\\_fy\\_en\\_07.pdf](http://www.kva.se/Documents/Priser/Nobel/2007/pop_fy_en_07.pdf),  
*Information for the Public, The Royal Swedish Academy of Sciences*, 2007, 1-7.
102. E. Grochowski and D. A. Thompson, *IEEE Transactions on Magnetics*, 1994, **30**, 3797-3800.
103. A. Moser, K. Takano, D. Margulies, M. Albrecht, Y. Sonobe, Y. Ikeda, S. Sun and E. E. Fullerton, *Journal of Physics D*, 2002, **35**, R157-R167.
104. R. Wood, *Journal of Magnetism and Magnetic Materials*, 2009, **321**, 555-561.
105. S. Thompson, *Journal of Physics D: Applied Physics*, 2008, **41**, 093001.
106. S. S. P. Parkin, 1993, **71**, 1641-1644.
107. A. Fert, P. A. Grünberg, A. Barthélémy, F. Petroff and W. Zinn, *Journal of Magnetism and Magnetic Materials*, 1995, **140-144**, 1-8.
108. P. A. Grünberg, *Journal of Magnetism and Magnetic Materials*, 2001, **226-230**, 1688-1693.
109. P. A. Grünberg, *Acta mater.*, 2000, **48**, 239-251.
110. A. Fert and I. Campbell, *Physical Review Letters*, 1968, **21**, 1190-1192.
111. A. Fert, *Journal of Physics C: Solid State Physics*, 1969, **2**, 1784.
112. V. A. Ivanov, T. G. Aminov, V. M. Novotortsev and V. T. Kalinnikov, *Russ. Chem. Bull.*, 2004, **53**, 2357-2405.
113. I. Zutic, J. Fabian and S. D. Sarma, *Review of Modern Physics*, 2004, **76**, 323-410.
114. M. Johnson and R. H. Silsbee, *Physical Review Letters*, 1985, **55**, 1790.
115. S. Parkin, *International Electron Devices Meeting*, 2004, **4**, 903-906.

116. T. M. Maffitt, J. K. DeBrosse, J. A. Gabric, E. T. Gow, M. C. Lamorey, J. S. Parenteau, D. R. Willmott, M. A. Wood and W. J. Gallagher, *IBM J. Res. Dev.*, 2006, **50**, 25-39.
117. S. Tehrani, B. Engel, J. M. Slaughter, E. Chen, M. DeHerrera, M. Durlam, P. Naji, R. Whig, J. Janesky and J. Calder, *IEEE Transactions on Magnetics*, 2000, **36**.
118. S. Tehrani, J. M. Slaughter, E. Chen, M. Durlam, J. Shi and M. DeHerrera, *IEEE Transactions on Magnetics*, 1999, **35**.
119. S. Parkin, M. Hayashi and L. Thomas, *Science*, 2008, **320**, 190-194.
120. D. Clark and R. Earles, in *Ninth Annual Freshman Conference*, University of Pittsburgh, Editon edn., 2009, pp. 1-6.
121. J. Fabian and I. Zutic, *Arxiv preprint arXiv:0903.2500*, 2009.
122. M. Bibes and A. Barthelemy, *IEEE Transactions on Electron Devices*, 2007, **54**, 1003-1023.
123. M. Calderón and S. D. Sarma, *Annals of Physics*, 2007, **322**, 2618-2634.
124. R. Borges, R. Thomas, C. Cullinan, J. M. D. Coey, R. Suryanarayanan, L. Ben-Dor, L. Pinsard-Gaudart and A. Revcolevschi, *Journal of Physics: Condensed Matter*, 1999, **11**, L445 - L450.
125. W. Eerenstein, PhD Thesis, Groningen, 2003.
126. N. T. H. Kim-Ngan, A. G. Balogh, J. D. Meyer, J. Brotz, S. Hummelt, M. Zajac, T. Slezak and J. Korecki, *Surface Science*, 2008, **602**, 2358-2362.
127. L. A. Kaley and L. Niesen, *Physical Review B*, 2003, **67**, 224403.
128. S. K. Arora, H. C. Wu, H. Z. Yao, W. Y. Ching, R. J. Choudhary, I. V. Shvets and O. N. Mryasov, International Magnetics Conference (Intermag), Madrid, SPAIN, 2008.
129. S. Jain, A. O. Adeyeye and C. B. Boothroyd, *Journal of Applied Physics*, 2005, **97**, 093713.
130. R. Arras, L. Calmels and B. Warot-Fonrose, *Physical Review B*, 2010, **81**, 104422.
131. J. B. Moussy, S. Gota, A. Bataille, M. J. Guittet, M. Gautier-Soyer, F. Delille, B. Dieny, F. Ott, T. D. Doan, P. Warin, P. Bayle-Guillemaud, C. Gatel and E. Snoeck, *Physical Review B*, 2004, **70**, 9.
132. D. T. Margulies, F. T. Parker, M. L. Rudee, F. E. Spada, J. N. Chapman, P. R. Aitchinson and A. E. Berkowitz, *Physical Review Letters*, 1997, **79**, 4.

133. F. C. Voogt, T. T. M. Palstra, L. Niesen, O. C. Rogojanu, M. A. James and T. Hibma, *Physical Review B*, 1998, **57**, R8107-R8110.
134. W. Eerenstein, T. T. M. Palstra, T. Hibma and S. Celotto, *Physical Review B*, 2002, **66**, 4.
135. M. Ziese and H. J. Blythe, *J. Phys.: Condens. Matter*, 2000, **12**, 13-28.
136. R. Waldron, *Physical Review*, 1955, **99**, 1727-1735.
137. D. Venkateshvaran, M. Althammer, A. Nielsen, S. Geprags, M. S. R. Rao, S. T. B. Goennenwein, M. Opel and R. Gross, *Physical Review B*, 2009, **79**, 134405.
138. W. Eerenstein, University of Groningen, 2003.
139. L. S. Darken and R. W. Gurry, *J. Am. Chem. Soc.*, 1946, **67**, 1398.
140. F. C. Voogt, PhD Thesis, Rijksuniversiteit Groningen, 1998.
141. F. Voogt, T. Palstra, L. Niesen, O. Rogojanu, M. James and T. Hibma, *Physical Review B*, 1998, **57**, R8107-R8110.
142. W. Eerenstein, T. Palstra and T. Hibma, *Thin solid films*, 2001, **400**, 90-94.
143. W. Eerenstein, T. Palstra, T. Hibma and S. Celotto, *Physical Review B*, 2003, **68**, 014428.
144. Y. Zhou, C. McEvoy and I. Shvets, *Journal of magnetism and magnetic materials*, 2005, **290-291**, 1033-1036.
145. A. V. Ramos, J. B. Moussy, M. J. Guittet, A. M. Bataille, M. Gautier-Soyer, M. Viret, C. Gatel, P. Bayle-Guillemaud and E. Snoeck, *Journal of Applied Physics*, 2006, **100**, 8.
146. J. Moussy, S. Gota, A. Bataille, M. Guittet, M. Gautier-Soyer, F. Delille, B. Dieny, F. Ott, T. Doan, P. Warin, P. Bayle-Guillemaud, C. Gatel and E. Snoeck, *Physical Review B*, 2004, **70**, 174448(174449).
147. A. V. Ramos, S. Matzen, J. B. Moussy, F. Ott and M. Viret, *Physical Review B*, 2009, **79**, 8.
148. W. Eerenstein, T. T. M. Palstra, S. S. Saxena and T. Hibma, *Phys Rev Lett*, 2002, **88**, 247204.
149. M. B. Brennan, *Chemical and Engineering News*, 2000, **78**, 63-73.
150. H. Koinuma, *Applied surface science*, 2002, **189**, 179-187.
151. J. Cooper, G. Zhang and P. J. McGinn, *Review of Scientific Instruments*, 2005, **76**, 062221.

152. W. Maier, K. Stöwe and S. Sieg, *Angewandte Chemie International Edition*, 2007, **46**, 6016-6067.
153. D. Farrusseng, *Surface Science Reports*, 2008, **63**, 487-513.
154. E. McFarland and W. H. Weinberg, *Trends in biotechnology*, 1999, **17**, 107-115.
155. J. Engstrom and W. Henry Weinberg, *AIChE journal*, 2000, **46**, 2-5.
156. R. Hendershot, C. Snively and J. Lauterbach, *Chemistry – A European Journal*, 2005, **11**, 806-814.
157. F. Moates, M. Somani, J. Annamalai, J. T. Richardson, D. Luss and R. C. Willson, *Ind. Eng. Chem. Res.*, 1996, **35**, 4801-4803.
158. S. Henderson, J. Armstrong, A. Hector and M. T. Weller, *J. Mater. Chem.*, 2005, **15**, 1528-1536.
159. J. Perkins, C. Teplin, M. v. Hest, J. Alleman, X. Li, M. Dabney, B. Keyes, L. Gedvilas, D. Ginley, Y. Lin and Y. Lu, *Applied surface science*, 2004, **223**, 124-132.
160. X. Xiang, *Materials Science and Engineering B*, 1998, **56**, 246-250.
161. R. Van Dover, L. Schneemeyer and R. M. Fleming, *Nature*, 1998, **392**, 162-164.
162. C. Olk, *Measurement Science and Technology*, 2005, **16**, 14-20.
163. C. Olk, G. Tibbetts, D. Simon and J. J. Moleski, *Journal of applied physics*, 2003, **94**, 720-725.

# Chapter 2

## Experimental

A short introduction to the *in-situ* and *ex-situ* techniques used to obtain data for this thesis is provided in this chapter.

### 2.1 Ultra High Vacuum (UHV) Equipment

Ultra High Vacuum (UHV) equipment is crucial not only to preparing thin film materials, but also for studying their surface properties. An outline of the UHV equipment and techniques used will be detailed in the following section.

#### 2.1.1 UHV Single Crystal Chamber

A UHV chamber was employed for mechanistic studies of crotyl alcohol selox over ultra-thin Au on Pd(111) model surfaces. The design of the chamber was based upon a 300 mm (12") spherical stainless steel chamber available commercially from Vacuum Generators (VG). A simplified diagram of this chamber is shown in **Figure 2.1**, and a colour photograph in **Figure 2.2**. The chamber typically operated at a base pressure of  $< 1 \times 10^{-10}$  Torr. This pressure was achieved through the use of a Pfeiffer Turbomolecular pump, backed by an Edwards 8 rotary pump. In addition, a three filament titanium sublimation pump (2 mm titanium filaments at  $\sim 50$  A) was used for short periods overnight to remove hydrogen from the chamber and was placed on a side arm to negate the possibility of Ti sublimation onto the crystal itself.

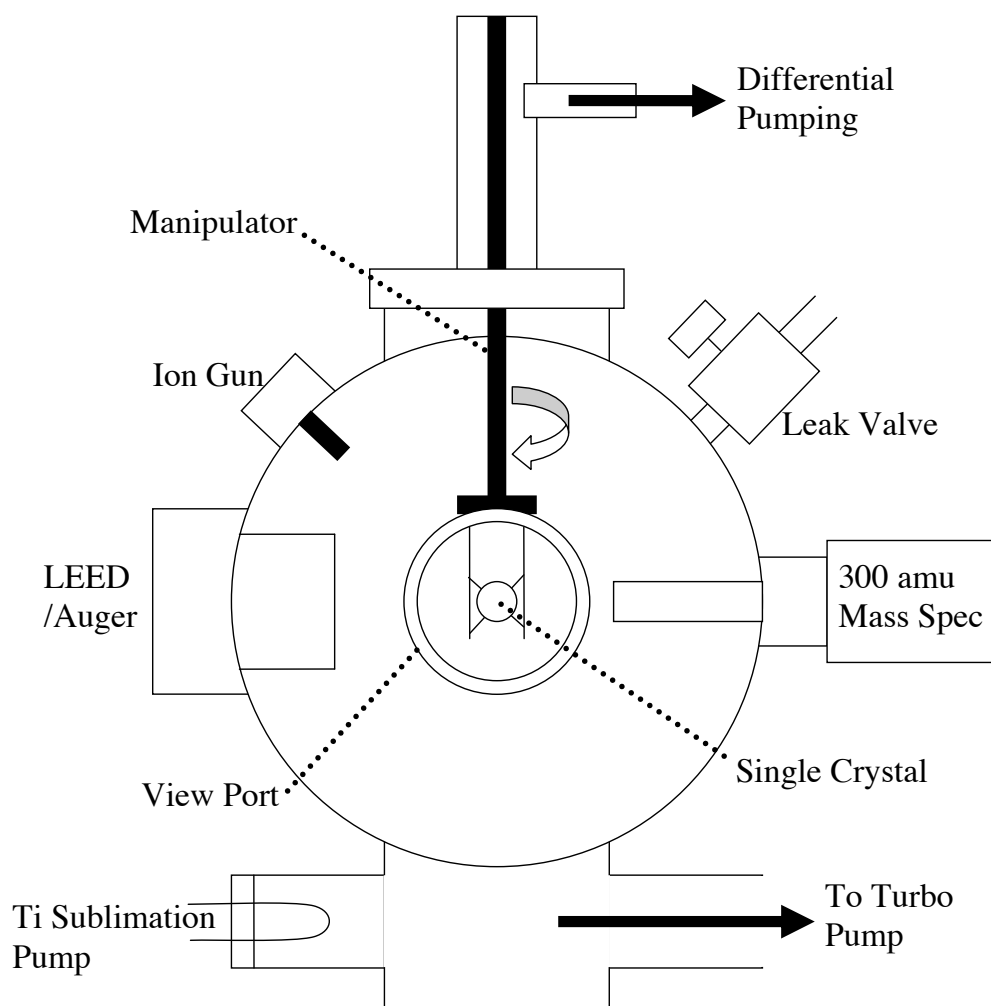


**Figure 2.1** – Diagram of the Ultra High Vacuum Chamber

A freely ( $x$ ,  $y$  and  $z$ ) rotatable manipulator was employed to hold a Pd(111) crystal in the centre of the chamber. The mounting of this crystal is described in more detail later in section 2.1.1.2. The manipulator head was differentially pumped by a Leybold Turbovac 151 turbomolecular pump to ensure a closed system.

A VG 300 amu quadrupole mass spectrometer (MS) was employed for observing species desorbing from the surface of the crystal during Temperature Desorption Spectroscopy (TDS) studies, further details of which will be described later in section 2.3. The spectrometer was mounted on a linear drive arm (500 mm travel) allowing it to be held approximately 2 mm away from (and perpendicular to) the crystal during operation. The quadrupole was housed in a custom stainless steel cone, to avoid detection of species from the chamber background. The secondary electron multiplier (SEM) was set at 2.8 kV for all TDS experiments.

The main chamber was equipped with an Omicron SpectraView 4-grid rear view Retarding Field Analyser (RFA) combining Low Energy Electron Diffraction (LEED, see section 2.5.1) and Auger Electron Spectroscopy (AES, see section 2.2.2). An incident beam energy of 1.8 keV was used for each AES spectra. It featured an internal retraction mechanism, to allow greater space for sample movement.

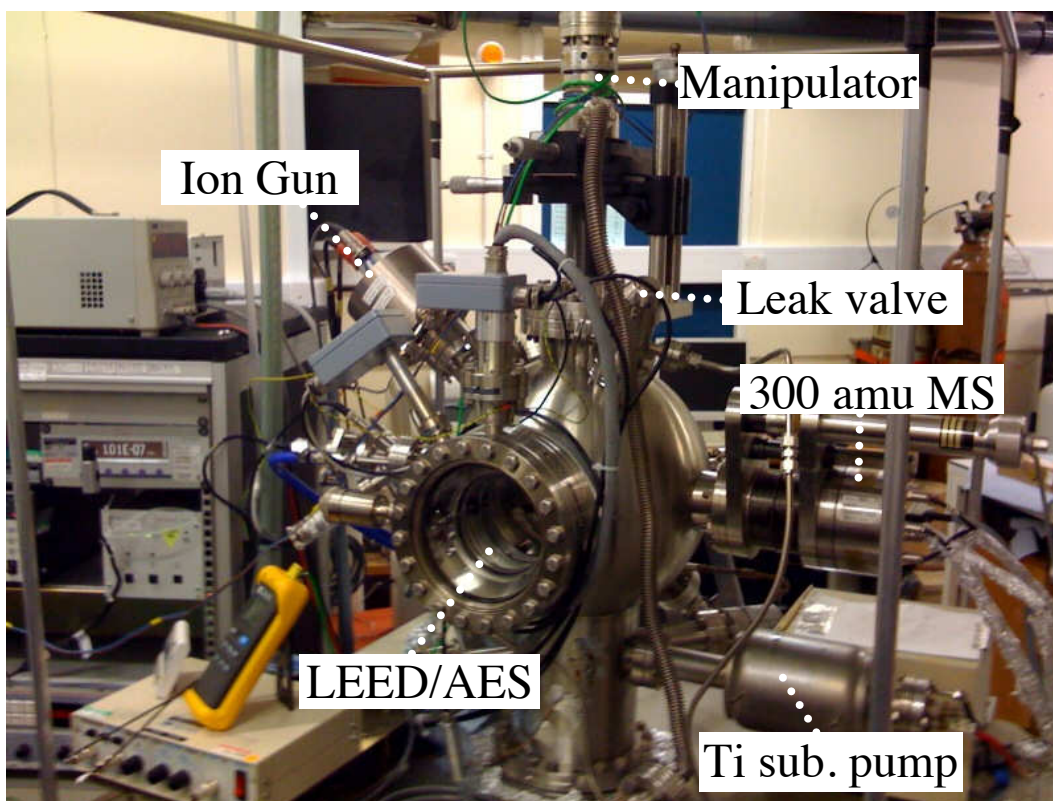


**Figure 2.2** – A photograph of the UHV chamber used for mechanistic studies of crotyl alcohol selox over model Au/Pd(111) surfaces

Sample cleaning was achieved by using a VG AGS2 ion gun attached to the chamber at 45 degrees to the mass spectrometer and LEED/AES. A  $1 - 3 \times 10^{-6}$  Torr pressure of background Ar (Air Liquide 99.999%) was accelerated using a high voltage (1.6 kV). Crystal currents of approximately  $3 - 5 \mu\text{A}$  were generated and monitored via a digital multi-meter.

Surface bound carbon was removed by performing an ‘oxygen roast’, in which the crystal was heated to 800 K in  $1 \times 10^{-7}$  Torr of oxygen for approximately 10 mins. Carbon and hydrocarbon deposits present on the surface react with  $\text{O}_2$  forming

CO/CO<sub>2</sub>, which readily desorb. After the 10 minute period, the crystal was then cooled to room temperature in the same pressure of O<sub>2</sub>. A Temperature Programmed Desorption (TPD) was then carried out in order to check for CO/CO<sub>2</sub> desorption. As a C-free surface exhibits no CO or CO<sub>2</sub> desorption when exposed to O<sub>2</sub> near room temperature<sup>1,2</sup>, the roast and desorption cycle was repeated, until no CO or CO<sub>2</sub> was observed in the TPD.

Ultra-thin films of Au were deposited onto the Pd(111) crystal surface at room temperature through the use of an EFM3 Omicron/Focus electron bombardment evaporation source with integral flux monitor. The growth mode and characterization of such films has been described in detail elsewhere<sup>3-5</sup>. Typical Au growth rates were 10 min ML<sup>-1</sup>, (1 ML is defined as  $1.5 \times 10^{15}$  atoms cm<sup>-2</sup>).

#### 2.1.1.1 Manifold and adsorbates

All adsorbates were background dosed into the UHV chamber through high pressure leak valves, connected to a dosing manifold by ¼ inch Swagelok. All gaseous samples were dosed as received after evacuation of the manifold, either by an Edwards 5 rotary pump down to  $\sim 8 \times 10^{-3}$  Torr, or alternatively by a Leybold Turbovac 151, capable of attaining pressures of  $\sim 5 \times 10^{-4}$  Torr. All liquid samples were purified by a minimum of three freeze-pump-thaw cycles until mass spectrometry showed the resulting vapours to be contaminant free. Quoted exposures are given in Langmuirs ( $1 \text{ L} = 1 \times 10^{-6} \text{ Torr s}^{-1}$ ) and are uncorrected for ion gauge sensitivity. The purity and origin of adsorbates used in both the preparation of clean crystal surfaces as well as the adsorbates investigated in this work are summarised in **Table 2.1**.

Adsorbate	Purity / %	Supplier
Argon	99.999	Air Liquide
Oxygen	99.998	Air Liquide
Carbon Monoxide	99+	Sigma Aldrich
Propene	99.99	Air Liquide
Crotyl Alcohol	99	Sigma Aldrich
Crotonaldehyde	99	Sigma Aldrich

**Table 2.1** – Gases and adsorbates used in the system

### 2.1.1.2 Pd crystal mounting

A high purity (99.9999%) Pd single crystal (2 mm × 10 mm) with a polished (111) front face was employed for temperature programmed desorption/reaction (TPD/R) studies. This was mounted via four 0.25 mm Ta heating wires, threaded through holes in the crystal edge, spot-welded onto two 1.5 mm Ta support rods and thus onto the previously described X-Y-Z sample manipulator.

A crystal temperature could be measured between 80 and 1000 K using a 0.15 mm K-Type Chromel-Alumel (T1/T2) thermocouple, spot-welded to the crystal edge. The sample could be resistively heated by applying an electric current of up to 12 A across the Ta heating wires from external insulating ceramic feed-throughs. Sample cooling (to ~ 90 K) was possible by filling the hollow Cu central reservoir of the rotatable manipulator with liquid nitrogen. A simplified schematic of the crystal mounting is shown in **Figure 2.3**.

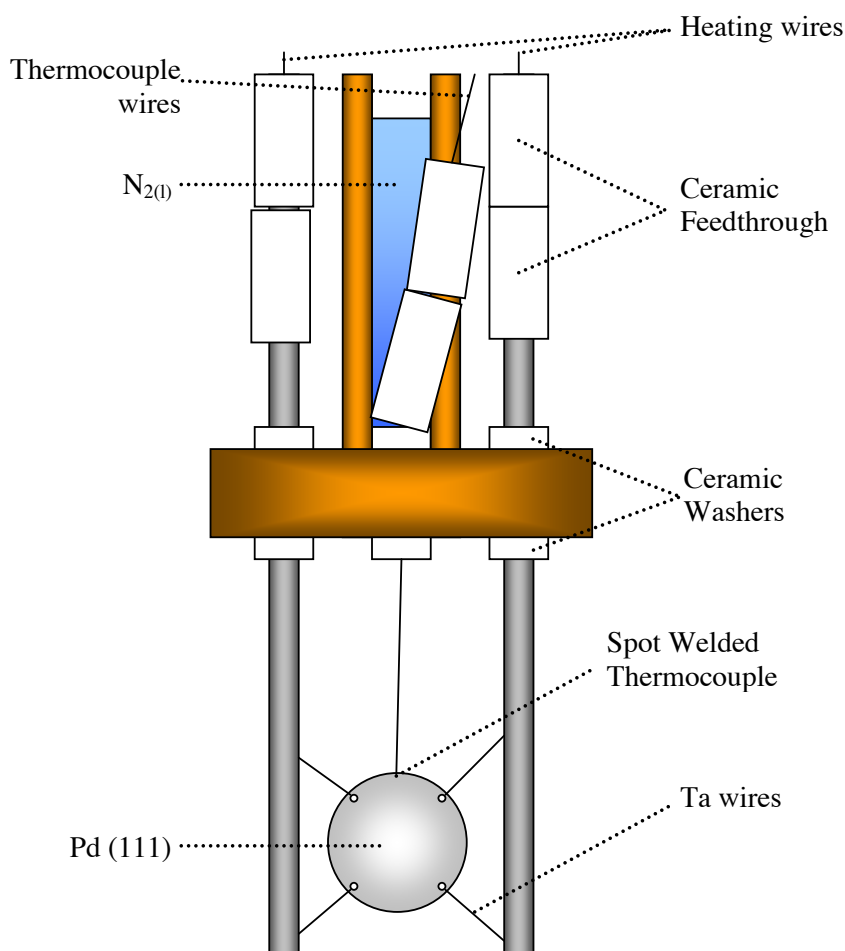


**Figure 2.3** – Single crystal sample mounting for TDS experiments

For temperature programmed XP experiments (carried out at the ELETTRA synchrotron, SuperESCA beam-line, see section 2.4 for more details) the Pd(111) single crystal was clamped to the UHV chamber manipulator. For such XP experiments, the crystal was cleaned using the exact sample procedure as described in section 2.1.1, except that the cleanliness of the crystal was monitored using XPS taken of the C 1s (282 – 288 eV) region, thereby observing any residual surface carbon. As with TPD studies, sample cooling could be achieved by filling the hollow stainless steel central reservoir of the rotatable manipulator with liquid nitrogen. Heating was achieved by electron bombardment of the back of the sample holder.

### **2.1.2 Molecular Beam Epitaxy (MBE)**

Molecular Beam Epitaxy (MBE) was utilised to prepare thin films of magnetite ( $\text{Fe}_3\text{O}_4$ ) on different orientations of MgO substrates. Two chambers were utilised for the preparation of such films. A chamber at Northeastern University in Boston, USA was used in order to prepare thin films of  $\text{Fe}_3\text{O}_4$  / MgO (111). Subsequent to this, a chamber at York was modified in order to prepare magnetite on different substrates.

The Northeastern MBE system consisted of two interconnected, custom-built UHV chambers: one for analysis and the other for growth (both of which are shown in a colour photograph - **Figure 2.4**). All samples were loaded through a small load lock chamber attached directly to the analysis chamber but separated by a UHV-compatible manual gate valve. The load lock chamber was independently pumped by a Leybold Turbovac 50 turbomolecular pump, able to achieve a base pressure of  $\sim 5 \times 10^{-7}$  Torr. Samples were transferred into the analysis chamber onto a manipulation stage (with x, y, z, and  $\theta$  movement) by using a magnetic linear transfer arm.

The analysis chamber was pumped by a Varian 500181B ion pump, which maintained a background pressure of  $\sim 2 \times 10^{-9}$  Torr, in use to minimise vibrational noise during XPS and AES characterization. The analysis chamber was equipped with AES, XPS, and an Ar ion gun. The analysis chamber was connected to another UHV growth chamber, separated by a UHV manual gate valve. Another

magnetic linear transfer arm was used for sample transfer between the growth and analysis chambers.

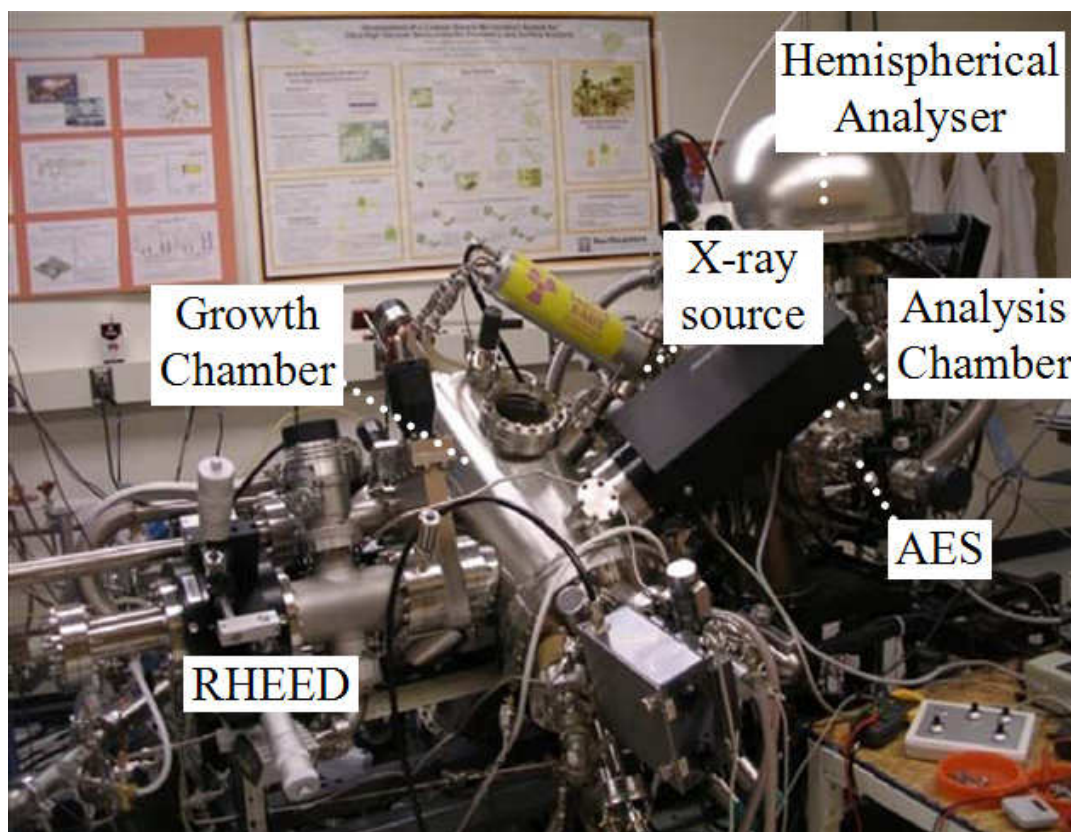


**Figure 2.4** - A photograph of the Northeastern MBE system used for the preparation of thin films of  $\text{Fe}_3\text{O}_4$  on MgO

The growth chamber maintained a base pressure of  $\sim 2 \times 10^{-9}$  Torr by means of a Leybold Turbovac 600C turbomolecular pump and a Leybold Trivac D25B rotary vane roughing pump. This chamber was equipped with a Veeco high temperature effusion cell which was used for the evaporation of Fe (99.999%, Sigma-Aldrich), an Oxford Applied Research HD25 remote oxygen RF-plasma source, and a Staib RH15 RHEED system. A custom built Mo 'puck' substrate heater could be moved in and out (z movement) as well as rotate ( $\theta$  rotation). The heater was capable of heating the substrate from room temperature up to 1173 K, as measured by a type C thermocouple in direct contact to the Mo 'puck'. A more accurate temperature measurement was performed using a two-color optical pyrometer, which typically read 50 – 75 K below the thermocouple reading.

Thin films of magnetite were prepared on MgO (111), by the following procedure. Atomic oxygen was first introduced into the chamber through the use of the RF plasma source. A pressure of oxygen was introduced into the chamber ( $\sim 1 \times 10^{-6}$  Torr) and ionised using an RF power of  $\sim 100$  W. An Fe growth rate of  $0.07 - 0.08$   $\text{\AA min}^{-1}$  was achieved by heating Fe in the effusion cell to 1553 K.

The York MBE system was designed by Balzers. A schematic representation of the York MBE chamber is displayed in **Figure 2.5**, and a colour photograph of the system is also shown in **Figure 2.6**. The chamber base pressure of  $\sim 8 \times 10^{-10}$  Torr was achieved through the use of a Varian turbomolecular pump, backed by an Edwards 8 rotary pump. A cryogenic pump in the form of a nitrogen cold trap was also used during experiments to aid in obtaining the optimum base pressure. Gases and/or vapours condense on the surface of the cold trap thereby decreasing the overall chamber pressure. This trap was constructed out of copper tubing and liquid nitrogen forced through the trap by a compressed air line. In addition, a three filament titanium sublimation pump (2 mm titanium filaments at  $\sim 50$  A) was used for short periods overnight to remove hydrogen and other contaminants from the chamber. To avoid deposition on the unwanted surfaces, the Ti filaments were placed at the bottom of the chamber.

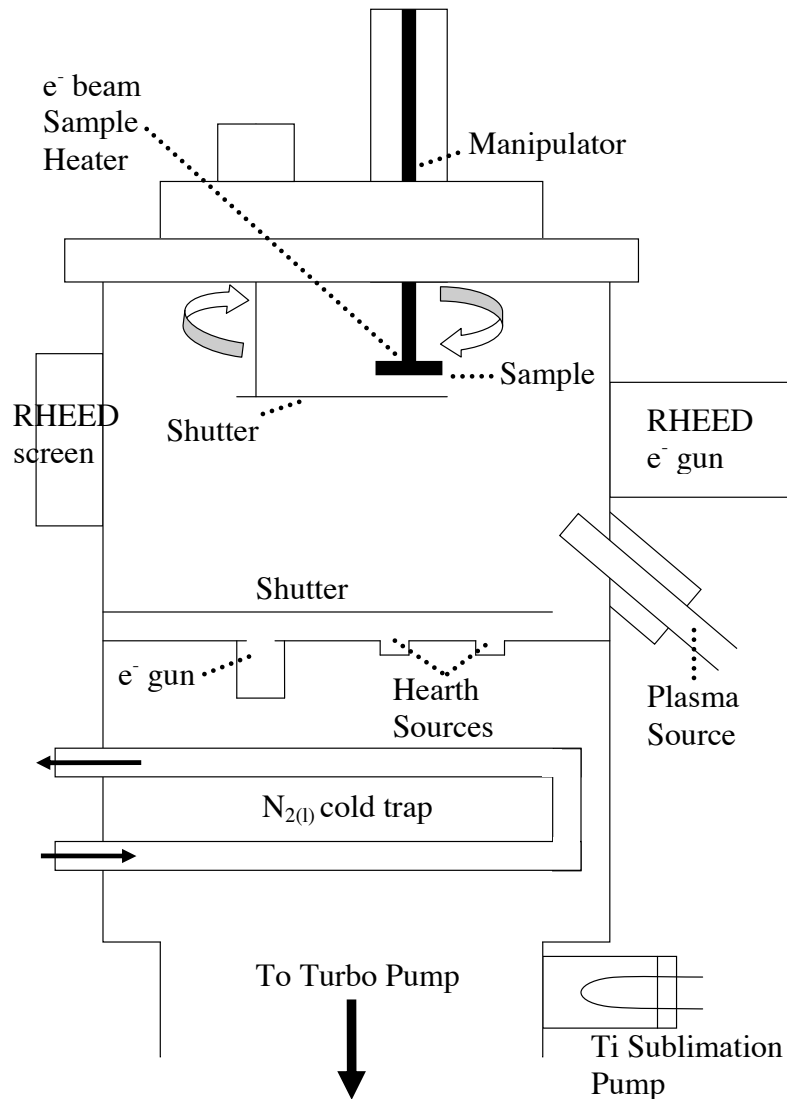


**Figure 2.5** – A diagram of the York MBE system

A modified VSW freely (x, y and z) rotatable manipulator was employed to hold a single crystal substrate contained in a modified Omicron sample plate in the centre of the chamber. The manipulator head was differentially pumped by an Edwards 8 rotary pump to ensure a closed system. The loading of sample plates into the main chamber was achieved by a sample exchange arm, housed in a separate chamber and isolated from the main chamber by a gate valve. The pumping of this exchange arm section was carried out by a small Pfeiffer turbomolecular pump and Edwards 5 rotary pump, achieving a base pressure of  $\sim 1 \times 10^{-7}$  Torr.

The York MBE chamber also housed two 0.25 cm (1") water cooled hearth evaporation sources at the base of the chamber with an independent shutter. Evaporation of source material(s) placed in the hearths was possible by means of

electron bombardment heating. In addition to this in-built hearth source, several small UHV custom made evaporation sources could be mounted on 2 ¾" flanges on the side of the chamber.

The deposition rate and overall thickness was estimated by means of a Sycon STM-100 MF quartz crystal microbalance (QCM) rate meter. This device measures the mass per unit area by measuring the change in frequency of a quartz crystal resonator. The resonance is shifted by the addition or removal of a small mass due to oxide growth/decay or film deposition at the surface of the resonator.

The chamber was also equipped with an Omicron Reflectance High Energy Electron Diffraction (RHEED) electron gun and phosphorescent screen (see section 2.5.2 for more details). It featured an internal screening mechanism, to avoid thin film deposition on the phosphor screen.

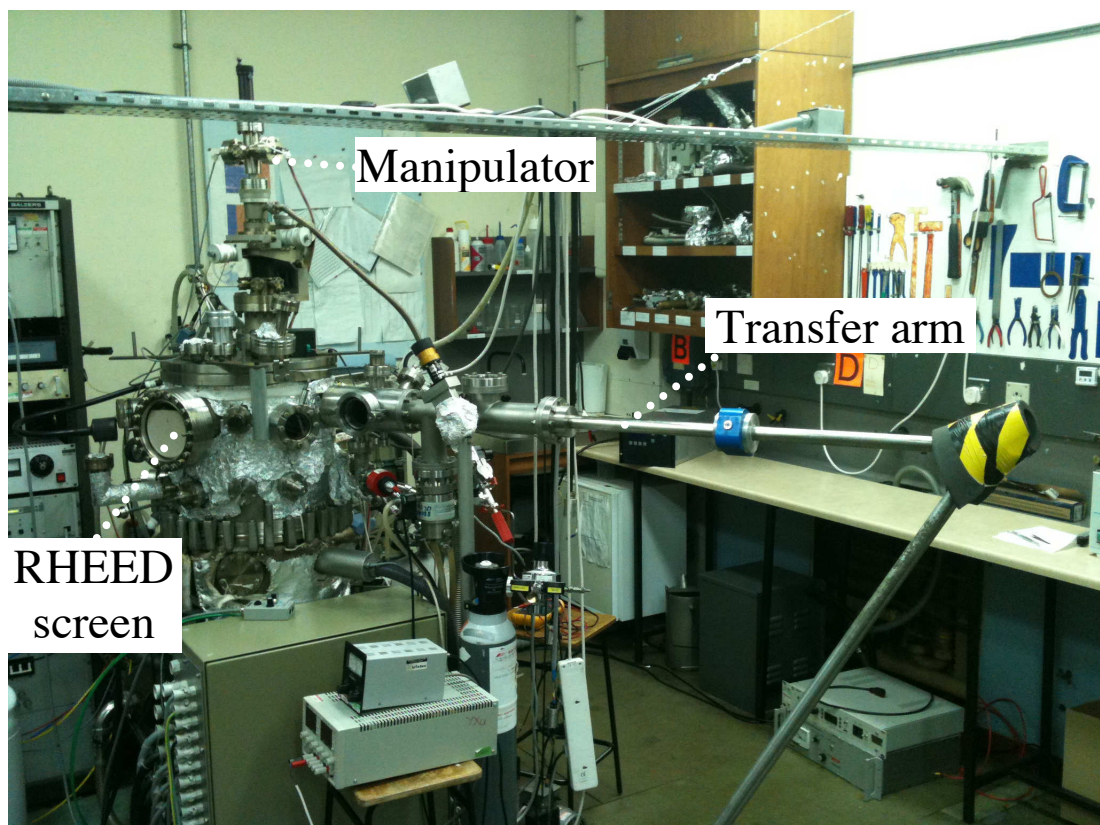


**Figure 2.6** - A photograph of the York MBE system used for the preparation of thin films of  $\text{Fe}_3\text{O}_4$  on  $\text{MgO}$

The chamber also contained a MANTIS RF atom source for the formation of radical oxygen. The RF forward/reflected power could be tuned by means of dual

capacitors in order to maintain a stable plasma. As with the source on the Northeastern MBE, the plasma was generated within an  $\text{Al}_2\text{O}_3$  discharge tube and exited the source through an  $\text{Al}_2\text{O}_3$  aperture plate. This aperture initially contained  $5 \times 0.2$  mm diameter holes in order to restrict the flow of oxygen into the chamber. The size, quantity, and dispersion of the holes therefore determine the pressure at which a stable plasma can be obtained. Initially the source had a plate which had 37 holes, which resulted in a pressure range too high for magnetite growth. As a result, a new aperture plate was made in order to obtain a plasma at a lower oxygen pressure. The source was also equipped with ion filter bias plates that were located at the top of the discharge tube. These parallel plates were aligned parallel to the flow of oxygen. By supplying a high voltage bias between the two plates, any charged oxygen species could be deflected, meaning that only neutral species with lower kinetic energy were involved in film growth.

A great deal of work was carried out in order to calibrate the source and obtain the correct phase of iron oxide during growth. To this end, a calibration matrix was prepared by growing numerous samples at various different growth rates, plasma powers and oxygen partial pressures. Samples were analysed using vibrating sample magnetometry (see section 2.6.1) four-point probe magnetoresistance (see section 2.6.2), infra-red techniques (see section 2.6.3), and transmission electron microscopy (see section 2.5.3). In this way, the stoichiometry, structure and thickness of the films could be obtained, by which the conditions required to grow magnetite could be determined.

The plasma source was typically operated at a pressure of  $2 \times 10^{-5}$  mbar and with a plasma power of 200 W. Substrates were first prepared and cleaned by in-situ annealing to  $\sim 1073$  K in the presence of atomic oxygen and then held at a temperature of  $\sim 523$  K during deposition in order to promote epitaxial growth of  $\text{Fe}_3\text{O}_4$ . Whilst maintaining the same flux of atomic oxygen, Fe was then evaporated at a rate of  $\sim 0.1 \text{ \AA s}^{-1}$  allowing thin films of magnetite to be prepared.

### **2.1.3 Metastable De-excitation Spectroscopy (MDS)**

Metastable De-excitation Spectroscopy (MDS) is a technique that probes the surface electronic structure of a material using metastable atoms<sup>6</sup> (in the case of

this work He  $2^3S$ ). When the orbitals of metastable atoms overlap with those of a target atom or molecule; de-excitation of the metastable atom occurs, a process dependent on the work function of the target. As the metastable atoms only interact with the surface of a material, the technique allows an electron energy spectrum to be obtained that is characteristic of the surface electronic structure. For more information on this technique, see chapter 5.

#### 2.1.4 Combinatorial sputtering rig

A custom built high vacuum chamber was designed in order to co-sputter materials to prepare thin films with a composition gradient across the substrate. In this manner, an infinite library of thin film catalysts could be prepared in a single experiment. A simple schematic of this chamber is shown in **Figure 2.7**. A base pressure of  $\sim 1 \times 10^{-6}$  Torr was achieved through pumping the chamber by a Varian turbomolecular pump and an Edwards 12 rotary pump.

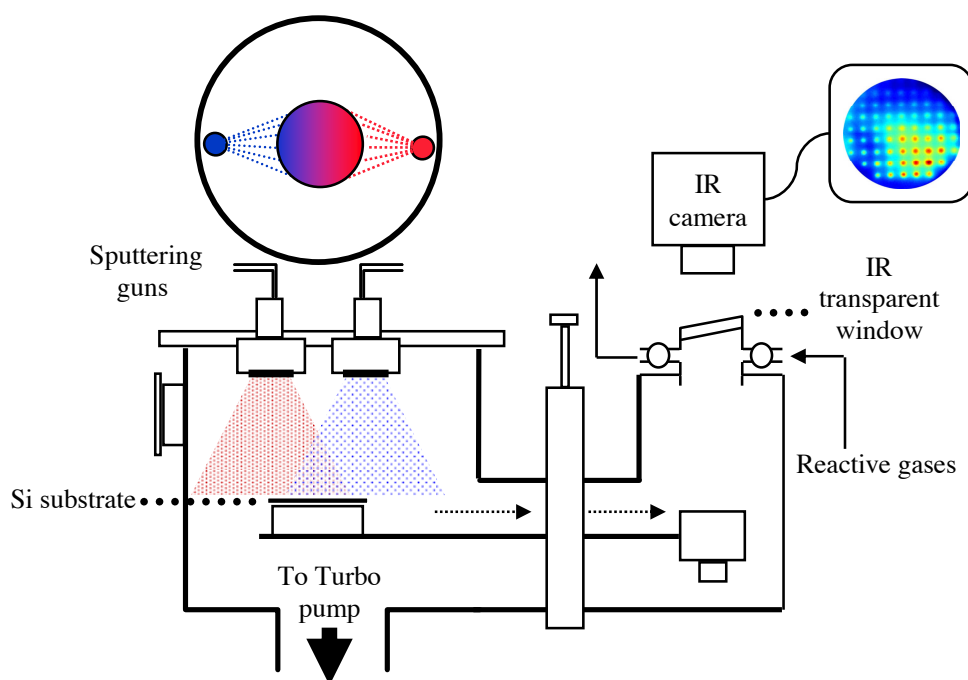


**Figure 2.7** – A simple diagram of the combinatorial sputtering rig

The chamber consists of two sections, the main chamber and reaction chamber, separated by a gate valve. The main chamber houses four Kurt J. Lesker 25.4 mm (1") Torus sputter guns, housing different sputtering targets (e.g. Cu, Au, Ag, Co etc), which could all be used simultaneously. By introducing a pressure of He (of

the order of tens of mTorr), and applying a high voltage across each gun, a magnetically confined plasma could be created in order to sputter the target material. The gun angle, gun power and chamber pressure were all altered independently, and for each case, several thick (~ 100 nm) films of Cu grown onto Si (100). The thickness across the substrate for each of the corresponding films could be measured using a Rank Taylor Hobson Talystep 1, and the varying chemical composition determined by Horiba Jobin Yvon XGT-7000 micro X-ray Fluorescence measurements. In this way, a calibration matrix could be prepared, which provided that the relative sputtering rate for each target was known, a sample with a desired thickness and composition could be grown.

Bi-metallic thin-film model catalyst libraries could then be prepared with a desired composition and thickness by co-sputtering. These libraries could then be introduced into the attached reaction chamber *via* a transfer mechanism. In this chamber, reactive gases could be introduced and the catalytic activity of the library rapidly screened by means of infrared thermography. An infrared camera could be placed directly above the substrate, and the temperature accurately measured across the sample during the course of a reaction *via* an infrared transparent window at the top of the chamber. For exothermic reactions, the most active catalyst composition could be determined by means of the ‘hottest spot’ on the surface. Conversely for endothermic reactions, this would correspond to a ‘cold spot’ on the film surface.

## **2.2 Composition Analysis**

The chemical composition and reactivity of thin-film surfaces were determined using a variety of techniques, which are briefly outlined in the following section.

### **2.2.1 X-ray Photoelectron Spectroscopy (XPS)**

X-ray Photoelectron Spectroscopy (XPS) also referred to as Electron Spectroscopy for Chemical Analysis (ESCA), is a technique which allows surface elemental analysis and characterisation of differing chemical environments. This technique affords the measurement of chemical composition and characterisation of active and decomposed species on the surface of a sample. Monochromatic X-rays are fired at the sample; these photons excite and emit core level electrons from atoms

in the surface, and the binding energy of these electrons is characteristic of the element from which they are emitted<sup>7,8</sup>. The binding energy can be calculated by measuring the kinetic energy of escape, according to the following relationship:

$$E_B = h\nu - E_{kin} - \Phi \quad \text{Equation 2.1}$$

Where  $E_B$  is the electron binding energy,  $h\nu$  is the photon energy,  $E_{kin}$  is the measured kinetic energy of the photoelectron, and  $\Phi$  is the workfunction. A schematic representation of photoionisation is shown in **Figure 2.8**.

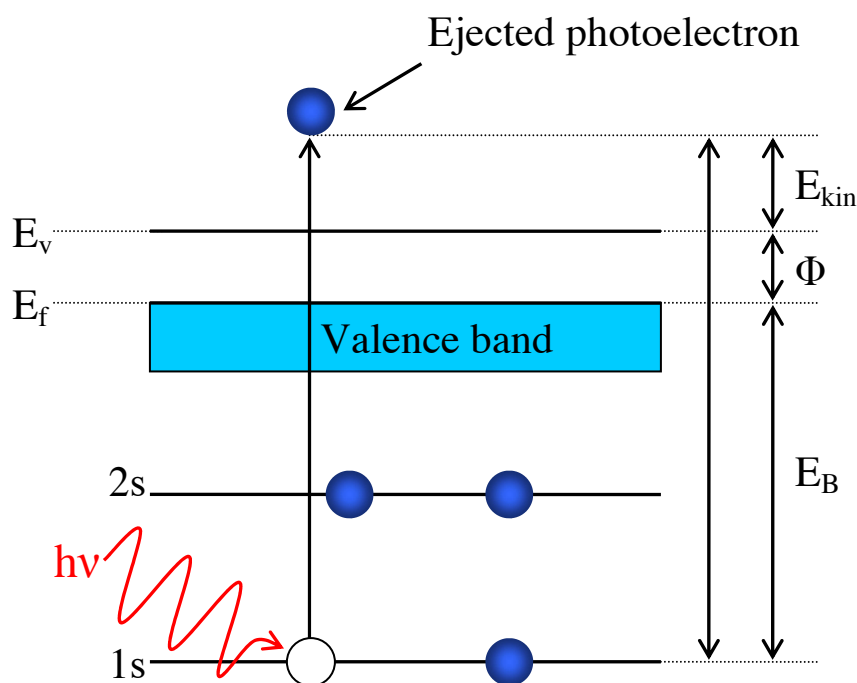


**Figure 2.8** – Schematic representation of photoionisation

The  $E_{kin}$  of the emitted photoelectrons from the surface is measured by a hemispherical analyser (HSA). Electrostatic fields within the HSA are established to only allow electrons of a certain energy to arrive at the detection slits. A simple schematic of an XPS setup, showing the energy analyser is shown in **Figure 2.9**.

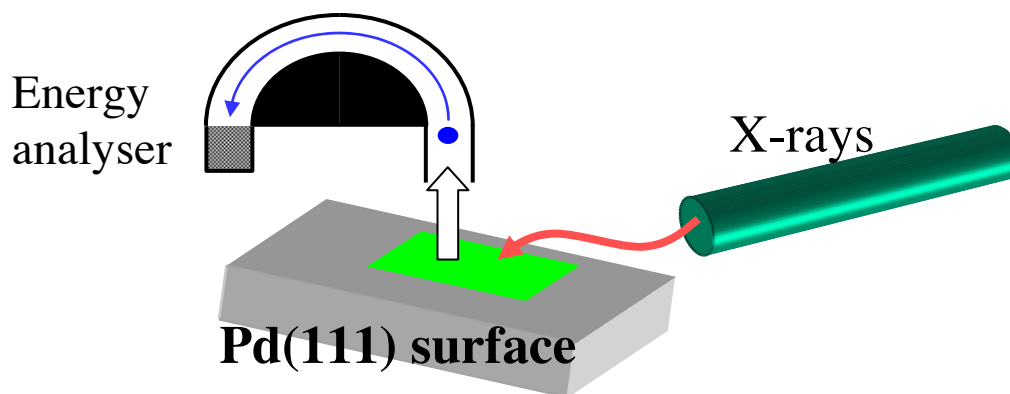


**Figure 2.9** – A simple diagram of a typical XPS experiment of a Pd(111) surface

Depending on the orbital being probed, the peak may be split by spin orbit coupling into a doublet with a separation characteristic of the element. For quantum number  $l > 0$  (p, d and f orbitals), the total angular momentum  $j$  for each state is the sum of the spin angular momentum  $s$ , and the orbital momentum  $l$ . As the spin of the electron can be up or down,  $s$  can have a value of  $\pm \frac{1}{2}$ , leading to two  $j$  values. The ratio of the occupancy of these two states is fixed by the multiplicity of the states equal to  $2j + 1$ . Therefore, for elements containing 3d orbitals, such as Pd, orbitals where  $l = 2$ , the two  $j$  values are therefore  $5/2$  and  $3/2$ , leading to two peaks with a 3:2 ratio in area. For elements containing 2p orbitals, such as iron,  $l = 1$ , the two  $j$  values are  $3/2$  and  $1/2$  leading to two peaks with a 2:1 ratio in area. The Full Width Half Maximum (FWHM) and lineshape are the same for both of the peaks. Probing the d-electrons such as in Pd leads to a characteristic asymmetric line broadening towards higher binding energy. This is due to ‘shake-up’ of the valence band electrons. This is a multielectron process, whereby an atom is left in an excited state following photoionisation, with the outgoing electron therefore having a  $E_K$  less than that of the parent photoelectron.

Small variations in binding energy arising from different chemical environments can be detected and quantified by peak fitting. These shifts can be up to 3 – 4 eV and can be due to either initial or final state effects. Binding energies as well as doublet splittings are readily available on the NIST photoelectron spectroscopy database<sup>9</sup>.

Initial state effects are due to the charge on the atom being probed. For example, electron deficient PdO has a Pd  $3d_{5/2}$  binding energy about 2 eV higher than its metallic counterpart. This effect also scales with orbital energy, meaning that the higher the energy of the orbital from which an electron is photoionised, the larger the effect upon the binding energy. Therefore it is advantageous to probe the outer shells for greatest resolution of different oxidation states.

Final state effects occur after photoemission, and are far more subtle than initial state effects. They include any combination of core-hole screening, orbital relaxation and polarisation; features already observed in palladium systems<sup>10, 11</sup>. In a bulk solid like Pd metal, a core-hole generated by photoemission is shielded by neighbouring atoms. With decreasing cluster size, the probed atom becomes increasingly co-ordinately unsaturated. With fewer neighbouring atoms to screen the generated core-hole, the energy needed to eject the electron is increased, typically by about 1 eV.

Spectral fitting was performed using CasaXPS version 2.3.5, with a common lineshape based on a Gaussian/Lorentzian (50:50) mix, as well as asymmetry based on a Doniach-Sunjić<sup>12</sup> mix of 0.005 with a FWHM of 2.56 eV adopted for all Pd components.

### **2.2.2 Auger Electron Spectroscopy (AES)**

Auger Electron Spectroscopy (AES) is analogous to XPS, in that it is a surface sensitive technique for the characterization of surface elemental composition. Auger emission occurs in an atom after a core electron is removed, either by an incident photon or electron of sufficient energy, resulting in an electron hole in the core shell<sup>13</sup>. An electron from an outer orbital may then drop down in order to fill this core shell hole. The energy released by this process is passed onto another less tightly bound electron, which may, if the energy is sufficient, be liberated into the vacuum<sup>14</sup>. This process is shown below in **Figure 2.10**.

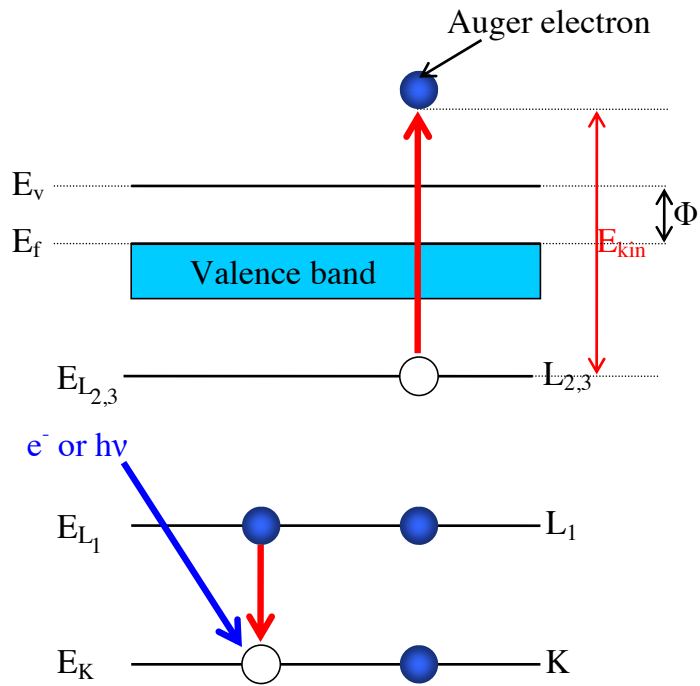


**Figure 2.10** – Auger emission due to ionisation by an incident electron or photon

These electrons may originate from depths of typically a few angstroms, giving great surface sensitivity<sup>15</sup>. The energy of the ejected Auger electron may therefore be obtained by the following expression:

$$E_{\text{kin}} \sim E_K - E_{L_1} - E_{L_{2,3}} \quad \text{Equation 2.2}$$

This phenomenon can be exploited to obtain the elemental composition of a sample, as the energies of the ejected Auger electrons are characteristic<sup>13, 16</sup>.

### 2.2.3 Ultraviolet Photoemission Spectroscopy (UPS)

Ultraviolet Photoemission Spectroscopy (UPS) is a method of probing the occupied density of states (DOS) of the near surface of a material<sup>7</sup>. UV photons are created in a continuous discharge source through the application of a high voltage through a portion of helium gas. These UV photons are then targeted onto the sample under investigation.

As with XPS (see section 2.2.1), the UV photons liberate electrons into the vacuum, due to the photoelectric effect (as depicted in **Figure 2.8**). The kinetic energy of the emitted electrons is detected using a hemispherical analyser (HSA). Such photons may penetrate several nanometers into the surface, and as such some

bulk states as well as the surface electronic states will be probed. As a result, the escape depth of the electron involved is of importance.

For the York UPS system, photons are generated by the He I  $\alpha$  transition which have an energy of 21.22 eV ( $\lambda = 58.43$  nm). This is at an energy close to that of the  $2^3S$  metastable He state used in MDS (see section 2.1.3), and as a result it is a very useful complementary technique to MDS.

### **2.3 Thermal Desorption Spectroscopy (TDS)**

Thermal Desorption Spectroscopy (TDS) is used to monitor reversibly bound reactants as well as reactively formed products desorbing from a crystal surface. By monitoring these desorbing species, important information on the strength of lateral adatom interactions, the activation enthalpy for desorption and the relative surface coverage of an adsorbate can be obtained<sup>17</sup>. A quadrupole mass spectrometer is positioned to within 2 mm of the sample surface under UHV conditions. The sample is then rapidly heated from a low temperature ( $\sim 120$  K) and a quadrupole mass spectrometer combined with electron multiplier filter detects species which desorb from the surface. A heated filament causes ionisation of the desorbed molecules, which are then accelerated into the quadrupole detector with a potential difference. Through a combined series of variable A.C. and D.C. voltages applied to the quadrupole detector, only ions with a specific mass reach the electron multiplier, where they are subsequently identified.

A thermocouple attached to the single crystal records accurate temperatures. A plot of the temperature versus the various mass fragments is known as a TPD/R spectrum. This provides information about the type of species formed at a surface, the nature of the surface intermediates produced from chemical reactions and, importantly, fundamental kinetic data regarding their formation and desorption. A typical quadrupole mass spectrometer is capable of simultaneously sampling up to 16 different mass fragments in the range of 0 – 300 atomic mass units at sufficiently fast scan rates ( $< 0.2$  s scan<sup>-1</sup>). TPD/TPR spectra were acquired using the system described in section 2.1.1, using a VG 300 amu quadrupole mass spectrometer, with a heating rate of  $\sim 10$  K s<sup>-1</sup>.

## 2.4 Temperature Programmed XP studies

Temperature programmed XPS involves the same principles as standard XPS, as discussed in section 2.2.1. Ordinarily, synchrotron radiation is not required in order to perform XPS<sup>14</sup>, but it is essential for temperature programmed studies<sup>18-21</sup>, which require fast spectral acquisition (seconds as opposed to minutes). Third-generation synchrotrons afford a very high photon flux, along with the use of advanced double-pass hemispherical analysers, both of which allow XPS spectra to be acquired rapidly. A smaller x-ray line width also affords superior signal to noise as well as high spectral resolution.

Adsorbates are typically dosed onto the crystal surface at low temperature ( $\sim 100$  K) and then monitored by XPS. This gives information regarding the nature of the adsorbate binding, and also allows measurement of the adsorbate surface coverage. The thermal chemistry of the adsorbates is then monitored by increasing the temperature of the metal surface whilst also acquiring ‘fast’ XP spectra. This technique therefore allows qualitative identification of the surface intermediates in real time, which therefore greatly aids elucidation of the reaction pathway of the adsorbate over catalytically relevant metal surfaces<sup>22</sup>.

XPS measurements were carried out at the SuperESCA beamline of the ELETTRA synchrotron in Trieste, Italy. The Pd(111) crystal was mounted, prepared and cleaned by standard procedure (as described in sections 2.1.1 and 2.1.1.2) and maintained in UHV ( $\sim 1 \times 10^{-10}$  Torr). Quoted exposures are given in Langmuirs and are uncorrected for ion gauge sensitivity. The crystal was held at  $\sim 90$  K whilst dosing.

C 1s XP spectra were acquired at a photon energy of 400 eV and energy referenced to the Fermi level. The limiting spectral resolution was  $\sim 150$  meV. Individual spectra were acquired approximately every 30 seconds during Fast XP measurements and Shirley background subtracted over the entire elemental region. Temperature programmed XP spectra were acquired by application of a linear heating rate ( $\sim 0.4$  K  $s^{-1}$ ) to the exposed sample. Spectra were fitted using CasaXPS version 2.3.5 using the minimum number of peaks required in order to minimise the R factor. A common lineshape derived from graphitic carbon was employed for all C 1s components, based on a Gauss/Lorentzian (70:30) mix, with a common

FWHM of 0.58 eV. Coverages are defined in terms of monolayers (adsorbates/surface Pd atom) with 1 ML =  $1.5 \times 10^{15}$  atoms. Absolute carbon coverages were determined by calibration with CO which has a saturation value of 0.75 ML on Pd(111) at 100 K<sup>23,24</sup>. Temperature programmed reaction spectra were also acquired in a separate system (described in section 2.1.1), to examine desorbing species, using a VG 300 amu quadrupole mass spectrometer, with a heating rate of  $\sim 10 \text{ K s}^{-1}$ , to complement the XP studies and complete the elucidation of the reaction pathway.

## 2.5 Structural Analysis

The structure of thin-films was characterised using the following techniques, either *in-situ* (in UHV) for Low Energy Electron Diffraction and Reflectance High Energy Electron Diffraction, or *ex-situ* using Transmission Electron Microscopy.

### 2.5.1 Low Energy Electron Diffraction (LEED)

LEED is a technique which is used to obtain detailed information of the crystal structure of a surface. It was first employed by researchers in 1927, who were demonstrating the wave-like nature of electrons<sup>25</sup>. Low energy electrons do not penetrate far into the surface of a material, meaning that they are an ideal surface structural probe<sup>16</sup>. Indeed, it is possible to examine the atomic arrangement of atoms making up the first 5 to 20 Å of a metal surface<sup>26</sup>. Due to the high surface sensitivity of the technique, a well-ordered, clean surface is necessary.

UHV pressures are needed due to the extreme surface sensitivity of LEED to changes in the surface structure or long-range order. The low energy electrons (20 – 500 eV) employed have a short elastic mean free path of approximately 2 mm at atmospheric pressure. These electrons are fired at the crystal surface, where they will be diffracted by the crystal structure and a small proportion will be backscattered. Such electrons then pass through a series of retarding grids at varying potentials which are employed to selectively allow only elastically backscattered electrons through and are detected on a phosphor detection screen.

In terms of the interference pattern obtained, the arrangement of maxima corresponds to the reciprocal lattice of the surface. Regularly ordered surfaces or

adsorbates produce regular diffraction spots which can be used to deduce the 2D structure of the surface, although the interpretation can be very difficult. Due to the high surface sensitivity of the technique, slight surface disorder causes diffuse patterns, but due to the large analysis area (mm scale) information on the partial ordering of surface atoms can still be obtained.

### **2.5.2 Reflection High Energy Electron Diffraction (RHEED)**

As detailed above, LEED utilises the inherent surface sensitivity associated with low energy electrons in order to sample the surface structure of a material. As the primary electron energy is increased the surface sensitivity decreases, and the forward scattering also becomes much more important. Therefore, in order to extract surface structural information from the diffraction of high energy electrons, a reflection geometry can be utilised, in which the electron beam is incident at a grazing angle; a technique referred to as Reflection High Energy Electron Diffraction (RHEED).

This technique is commonly used to measure the surface crystallography in an MBE experiment, as glancing angle geometry has several practical advantages over LEED, namely being the ease of access around a sample<sup>16</sup>. As RHEED does not rely on back-scattered electrons it also has the added advantage that it can be conducted through a wide variety of angles, allowing the beam to be aligned along specific crystallographic directions on the surface. However, the angle at which the electrons intersect the crystal lattice (the azimuthal angle) affects both the geometry and intensity of patterns obtained<sup>13</sup>.

In terms of the operation of the technique, a high energy electron beam (3 - 100 keV) is directed at the sample surface at a grazing angle. The electrons are diffracted by the crystal structure of the sample and then impinge on a phosphor screen mounted opposite to the electron gun. The resulting diffraction pattern formed is a series of streaks. The distance between the streaks is an indication of the unit cell size of the surface lattice. If a surface is atomically flat, sharp RHEED streaks are observed, whereas a rough surface produces diffuse streaks. Using this technique, it is possible to monitor the atomic layer-by-atomic layer growth of

epitaxial films by monitoring the distances between streaks and the oscillations in the intensity of the RHEED pattern.

### **2.5.3 Transmission Electron Microscopy (TEM)**

Transmission Electron Microscopy (TEM) is a versatile tool in the characterisation of materials, as it allows the crystal structure, chemical identity and microstructure of a sample to be determined. Due to the small de Broglie wavelength of electrons, TEM is capable of imaging at a significantly higher resolution than light microscopes. A beam of electrons is passed through an ultra-thin specimen (< 50 nm), allowing an image to be formed from the interaction of the transmitted electrons with the material. The electrons are magnetically focused to a small spot on the sample, before being directed onto an imaging device (diffraction screen, CCD camera etc).

In combination with ion milling techniques, TEM allows cross sectional images of thin films to be obtained. This not only gives information about the interface between the substrate and the film, but also allows determination of the microstructure and film thickness.

Depending upon the microscope and the material under study, atomic resolution is possible, provided one can correct for the spherical aberration inherent with magnetic lenses. At smaller magnifications TEM image contrast is due to absorption of electrons in the material, due to the thickness and composition of the material. At higher magnifications complex wave interactions modulate the intensity of the image, requiring expert analysis of observed images.

## **2.6 Magnetic Analysis**

The magnetic properties of thin films were characterised by the following *ex-situ* techniques.

### **2.6.1 Vibrating Sample Magnetometry (VSM)**

Vibrating Sample Magnetometry (VSM) can be used to probe the magnetic properties of thin films. In VSM, samples are placed between two magnetic pole

pieces and are physically vibrated sinusoidally, through the use of a piezo-electric material, as the uniform external magnetic field is varied. The magnetisation of the sample under analysis can be determined at a given field, as the sinusoidal motion induces a current in pick-up coils located directly on the magnetic pole pieces. A schematic of a simple VSM is shown in **Figure 2.11**. A lock in amplifier is used to measure the induced voltage in the pick up coils, using the piezoelectric as a reference signal. In this way, the magnetic properties of samples can be probed and a hysteresis curve plotted.

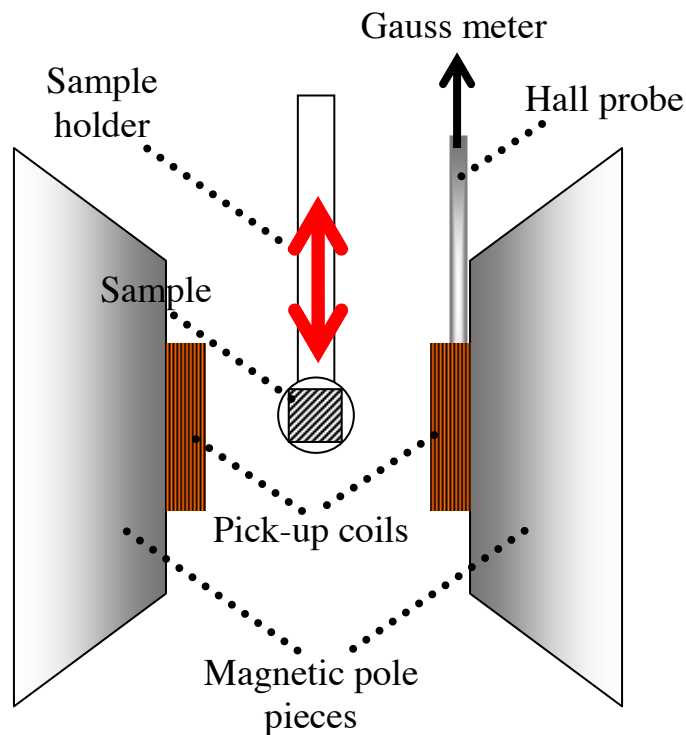


**Figure 2.11** – A schematic of a simple VSM set-up

In addition to VSM measurements performed in York described above, supplementary measurements were also performed at the University of Leeds.

### **2.6.2 Magneto-resistive (MR) measurements**

The magnetoresistance (MR) of samples at York was measured using a four-point probe technique. Four spring loaded Au coated sharp contacts were brought into contact with a sample. A Keithley 236 source measure unit was used to supply a direct current and measure the resulting voltage. A General Purpose Interface Bus (GPIB) integrated within the Keighley allowed external control and acquisition of data by a PC. The two outer pins were used to source a current ( $I$ ), whereas two

central pins measured the voltage through the sample. A simple schematic diagram of the apparatus is shown in **Figure 2.12**. The resistance (R) of the sample was then calculated according to Ohm's law (**Equation 2.3**).

$$R = \frac{V}{I} \quad \text{Equation 2.3}$$

The voltage (V) was monitored as the magnetic field was swept to maximum, minimum and then zero field. The resistance of the sample could then be plotted against the magnetic field strength (as measured by the hall probe). In this way, the field dependent MR of the samples could be demonstrated.

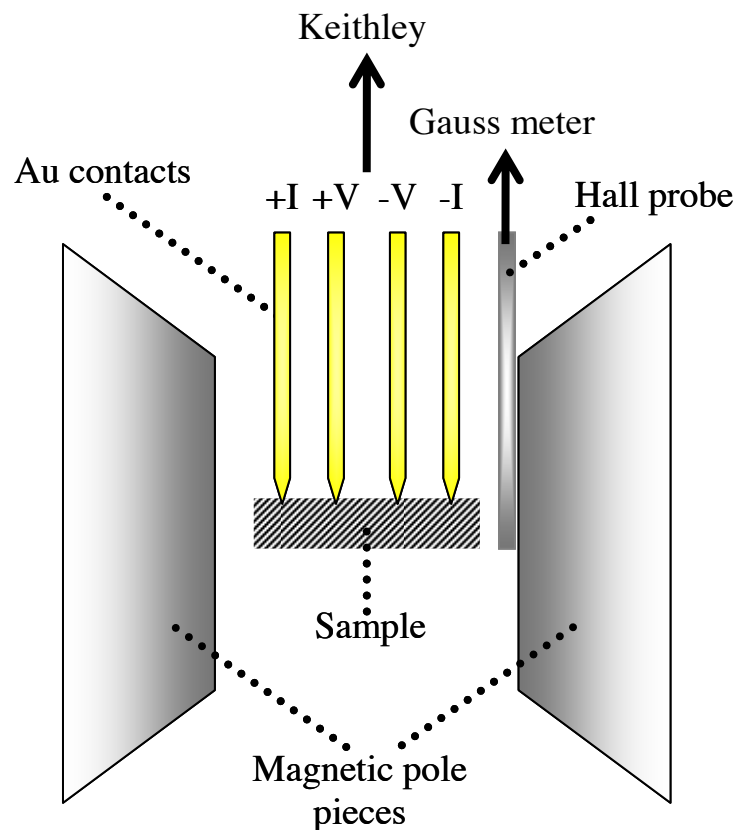


**Figure 2.12** – A diagram of the apparatus used to measure the magnetoresistance of samples

### 2.6.3 Magnetorefractive Effect (MRE) measurements

The Magnetorefractive Effect (MRE) is a magneto-optical technique which offers the ability to probe magnetotransport properties of materials<sup>27-29</sup>, whilst also

allowing the composition of a sample to be determined. The technique is based upon Fourier-transform infrared spectroscopy (FTIR). Spectra can be obtained by either reflecting light from or transmitting light through a given thin film sample. IR reflectivity spectra of a thin film sample are acquired in the absence and presence of a magnetic field. The MRE can be defined mathematically as:

$$\text{MRE}(\%) = \frac{R_0 - R_H}{R_H} \times 100 \quad \text{Equation 2.4}$$

Where  $R_0$  is the IR reflectivity in zero field, and  $R_H$  is the IR reflectivity in an applied magnetic field.

The infrared spectra were produced using a Nicolet Fourier Transform Infrared (FTIR) Spectrometer, in which an infrared light source emitted un-polarised light of approximately  $2.5 - 25 \mu\text{m}$  ( $400 - 4000 \text{ cm}^{-1}$ ). The IR beam entered a perspex box, where it was reflected off an aluminium coated mirror, onto the sample attached to a goniometer (movable sample holder), between magnetic pole pieces. The perspex box contained hygroscopic crystals and was also coupled to a  $\text{CO}_2$  scrubber in order to minimise the contribution of water and carbon dioxide to the IR spectra. Two photographs of the set-up are shown in **Figure 2.13**.

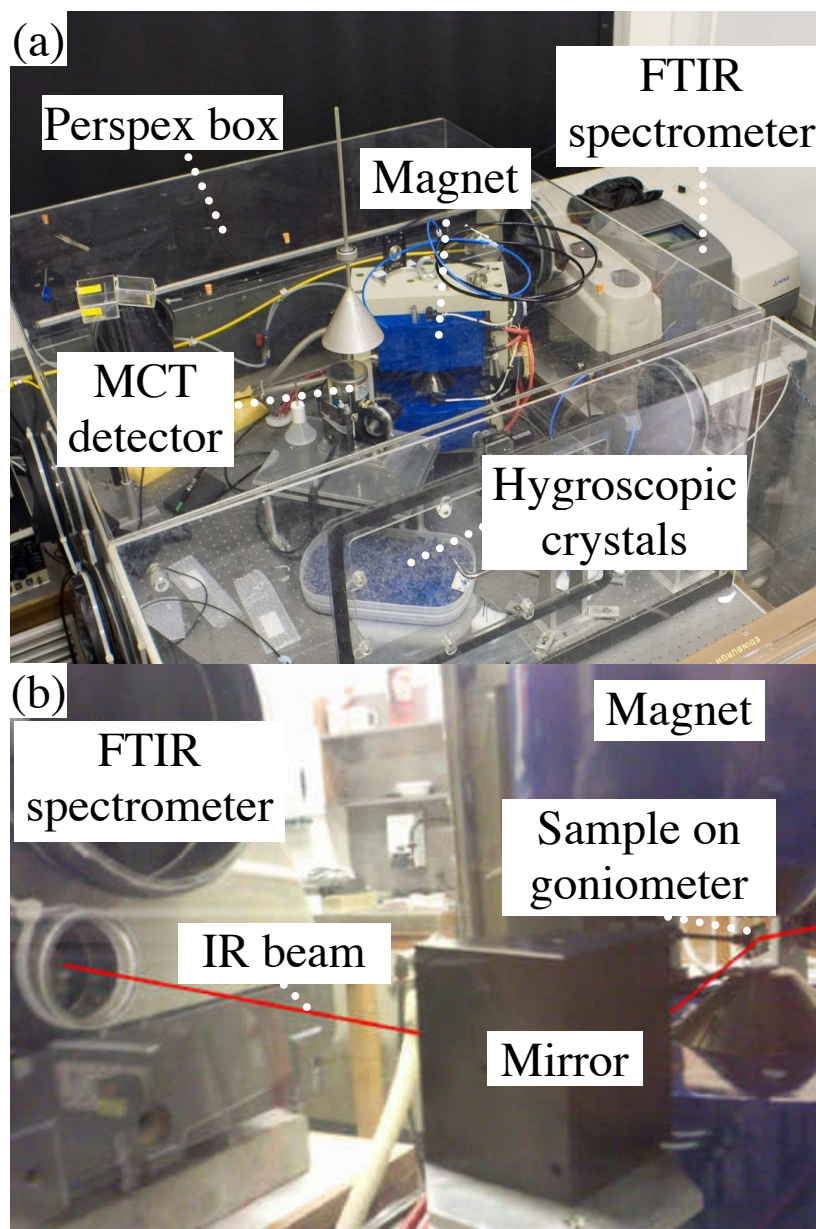


**Figure 2.13** – Colour photographs of the MRE acquisition setup: (a) A view from above the entire setup, (b) A close-up shot of the set-up showing the IR beam (red line).

The reflection of IR light from the sample was incident on another convex aluminium coated mirror and into a liquid nitrogen cooled mercury cadmium telluride (MCT) detector, which was coupled to the FTIR so a reflection spectrum could be produced. The FTIR was controlled *via* the OMNIC computer programme, which was also used to produce the spectra. The goniometer, and therefore the sample, was positioned between the pole pieces of a magnet, which

produces fields up to 1.25 T. A simple diagram of the set-up is shown in **Figure 2.14**.

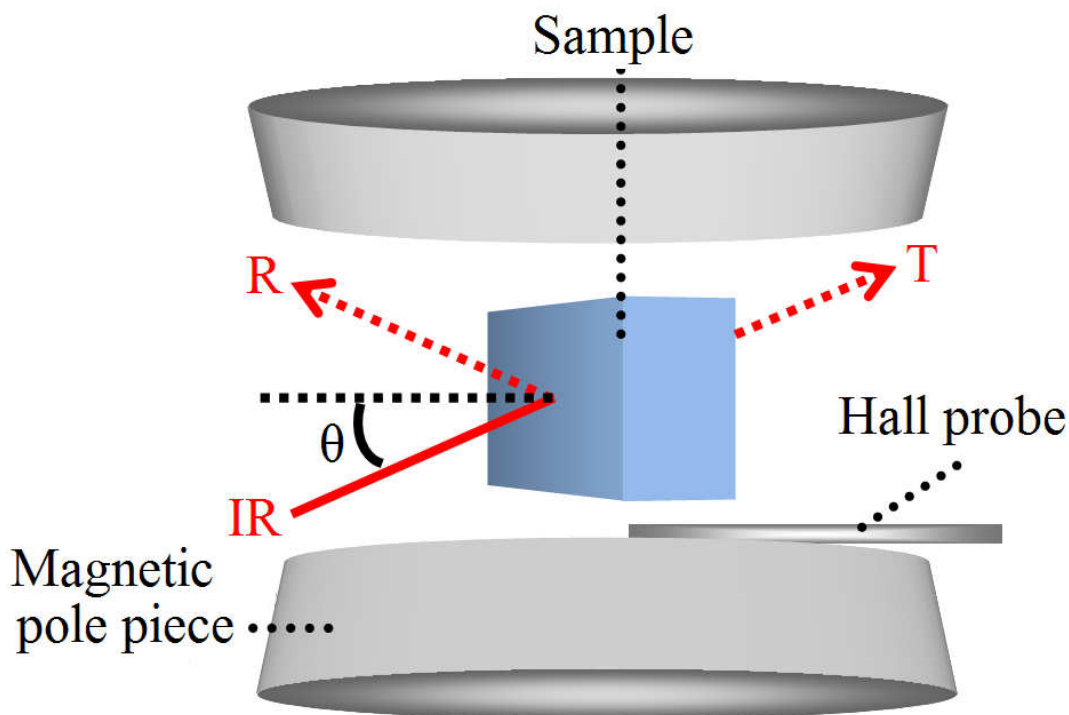


**Figure 2.14** - Diagram of a simple MRE setup, showing the reflection (R) and transmission (T) of the IR beam off and through the sample

MRE has the advantage of being a non-contact (and therefore non-destructive) method, which, not only allows magnetotransport and compositional information to be obtained, but also in theory can be applied to *in-situ* analysis of samples (e.g. within a vacuum chamber). Further information on the theory of this technique will be supplied in chapter 7.

## 2.7 References

1. R. D. Ramsier, K. W. Lee and J. J. T. Yates, *Journal of Vacuum Science & Technology A: Vacuum, Surfaces, and Films*, 1995, **13**, 188-194.
2. G. Zheng and E. I. Altman, *Surf. Sci.*, 2000, **462**, 151-168.
3. Z. Li, F. Gao, Y. Wang, F. Calaza, L. Burkholder and W. T. Tysoe, *Surf. Sci.*, 2007, **601**, 1898–1908.
4. Z. Li, O. Furlong, F. Calaza, L. Burkholder, H. C. Poon, D. Saldin and W. T. Tysoe, *Surface Science*, 2008, **602**, 1084-1091.
5. A. F. Lee, S. F. J. Hackett, G. J. Hutchings, S. Lizzit, J. Naughton and K. Wilson, *Catalysis Today*, 2008.

6. Y. Harada, S. Masuda and H. Ozaki, *Chem. Rev.*, 1997, **97**, 1897-1952.
7. J. Naughton, A. Lee, S. Thompson, C. P. Vinod and K. Wilson, *Phys. Chem. Chem. Phys.*, 2010, **12**, 2670-2678.
8. J. Szanyi, W. K. Kuhn and D. W. Goodman, *J. Phys. Chem.*, 1994, **98**, 2978-2981.
9. NIST, *X-ray Photoelectron Database*, <http://srdata.nist.gov/xps/>.
10. T. Cheung, *Surface Science*, 1984, **140**, 151-164.
11. G. K. Wertheim and S. DiCenzo, *Physical Review B*, 1988, **32**, 844-847.
12. S. Doniach and M. Sunijic, *Journal of Physics C: Solid State Physics*, 1970, **3**, 285.
13. Z. Mitura and P. A. Maksym, *Physical Review Letters*, 1993, **70**, 2904.
14. D. Briggs and M. P. Seah, *Practical Surface Analysis*, Second Edition edn., Wiley, 1990.
15. M. Prutton, *Introduction to Surface Physics*, Oxford University Press, 1994.
16. J. A. Venables, *Introduction to Surface and Thin Film Processes*, Cambridge University Press, 2000.
17. S. L. M. Schroeder and M. Gottfried, *Temperature Programmed Desorption (TPD) Thermal Desorption Spectroscopy (TDS)*, <http://pcprakt.userpage.fu-berlin.de/tds.pdf>.
18. A. Lee, K. Wilson, R. Middleton, A. Baraldi, A. Goldoni, G. Paolucci and R. M. Lambert, *J. Am. Chem. Soc.*, 1999, **121**, 7969-7970.
19. A. Baraldi, G. Comelli, S. Lizzit, M. Kiskinova and G. Paolucci, *Surface Science Reports*, 2003, **49**, 169-224.
20. A. Baraldi, G. Comelli, S. Lizzit, D. Cocco, G. Paolucci and R. Rosei, *Surface Science*, 1996, **367**, L67-L72.
21. A. Baraldi, M. Barnaba, B. Brena, D. Cocco, G. Comelli, S. Lizzit, G. Paolucci and R. Rosei, *Journal of Electron Spectroscopy and Related Phenomena*, 1995, **76**, L45-L49.
22. C. P. Norris, *Trends in Surface Science Research*, Nova Science, New York, 2006.
23. M. Tüshaus, W. Berndt, H. C. I, A. M. Bradshaw and B. Persson, *Applied Physics A*, 1990, **51**, 91-98.
24. V. V. Kaichev, I. P. Prosvirin, V. I. Bukhtiyarov, H. Unterhalt, G. Rupprechter and H.-J. Freund, *J. Phys. Chem. B*, 2003, **107**, 3522-3527.

25. C. Davisson and L. H. Germer, *Physical Review*, 1927, **30**, 705.
26. C. N. Banwell, *Fundamentals of Molecular Spectroscopy*, Third Edition edn., McGraw Hill, 1983.
27. J. C. Jaquet and T. Valet, *Magnetic Ultrathin Films, Multilayers and Surfaces, MRS Symposia Proceedings*, 1995, **348**, 477.
28. D. Bozec, V. G. Kravets, J. A. D. Matthew, S. M. Thompson and A. F. Kravets, *J. App. Phys.*, 2002, **91**.
29. M. Vopsaroiu, D. Bozec, J. A. D. Matthew, S. M. Thompson, C. H. Marrows and M. Perez, *Physical Review B*, 2004, **70**, 214423.

## Chapter 3

# Reactivity of crotyl alcohol over Au/Pd(111) surface alloys

### 3.1 Introduction

In this chapter, new light will be shed into the selective oxidation of crotyl alcohol over Au/Pd catalysts; a particularly promising heterogeneous alternative.

#### 3.1.1 Pd selox deactivation

Previous work by the York Surface Chemistry and Catalysis group at the ELETTRA synchrotron on the oxidative dehydrogenation of crotyl alcohol (CrOH,  $\text{CH}_3\text{CH}=\text{CHCH-OH}$ , 2-buten-1-ol) to crotonaldehyde (CrCHO,  $\text{CH}_3\text{CH}=\text{CHCHO}$ , but-2-enal) over Pd(111), identified secondary decarbonylation reactions as the major factor in the deactivation of practical monometallic Pd selox catalysts<sup>1</sup>. These results are exemplified by **Figure 3.1**, a C 1s temperature programmed XP spectra of a saturated crotyl alcohol adlayer over Pd(111). A contour plot of peak intensity is also displayed as an inset to the figure.

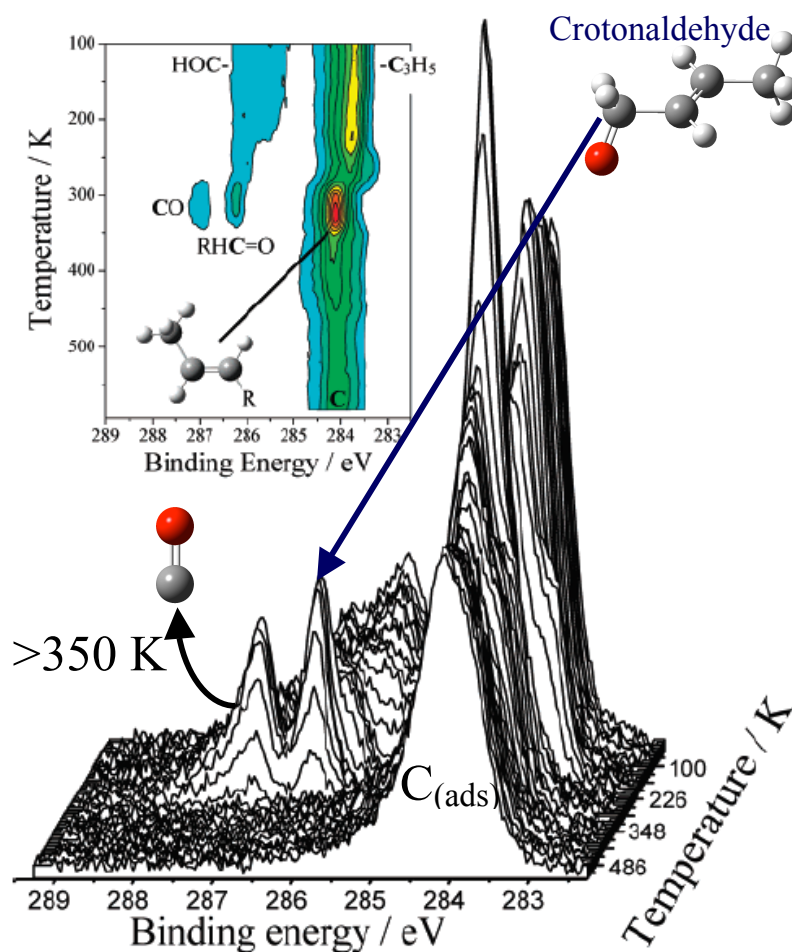


**Figure 3.1** - Temperature Programmed X-ray Photoelectron spectra, acquired at the ELETTRA synchrotron of the C 1s binding energy region for a saturated crotyl alcohol adlayer (adsorbed at 100 K) over Pd(111) – modified from source<sup>2</sup>

From **Figure 3.1**, it can be seen that adsorption of the molecule at 100 K results in two distinct XPS peaks in a three to one ratio. The peak centred at  $\sim 284$  eV can therefore be attributed to the C=C-C carbon backbone of the molecule, with the peak at higher binding energy ( $\sim 285.6$  eV) corresponding to the C-OH moiety. This peak is shifted in binding energy due to the electro-negativity of the oxygen.

Heating the crotyl alcohol adlayer results in various peak shifts, attributed to the formation of different reactively formed species on the Pd(111) surface. Upon heating to room temperature, a large shift of approximately +0.6 eV in binding energy of the 285.6 eV (C-OH moiety) state is observed, which can be attributed to the formation of the aldehyde product on the surface. This shift in binding energy is due to increase in bond order to the electro-negative oxygen. This assignment has been confirmed by

independently dosing crotonaldehyde at low temperature onto Pd(111) and recording XP spectra; which results in two peaks centred around 284 eV and 286.2 eV in a three to one ratio.

From the figure, a third peak is also observed when the crotyl alcohol adlayer is heated to room temperature. This state exists at higher binding energy ( $\sim 287$  eV), which can be attributed to CO. The formation of this by-product is due to the rapid breakdown of the crotonaldehyde by decarbonylation into propene and carbon monoxide. This is further evidenced from the increased intensity of the 284 eV state, which is due to the formation of propylidyne fragments on the surface. Ultimately it is this secondary decarbonylation reaction that poisons the surface and causes rapid deactivation. Further heating results in a single C 1s peak being observed due to the formation of a large amount of irreversibly bound graphitic carbon. This coking of the surface also prevents any subsequent surface reactions.

### 3.1.2 Au/Pd systems

Poor selectivity and/or activity of heterogeneous systems when compared to homogeneous counterparts are not uncommon, and often necessitate *ad hoc* promotion by non-noble metals to obtain even modest yields<sup>3</sup>. This reflects the uncertainty in the active site responsible for the oxidative dehydrogenation step, which is broadly regarded as the rate-limiting step.

However, bimetallic systems frequently display properties which are significantly different from their component metals<sup>4, 5</sup>. As a result, many of these bimetallic alloys show an enhanced catalytic activity, selectivity or stability when compared to their monometallic counterparts. In particular, Au/Pd nanoparticulate catalysts have displayed improved or even ‘tunable’ properties when compared to pure Au or Pd catalysts<sup>6-8</sup>.

As outlined in chapter 1, numerous investigations have focussed on the catalysis of many different reactions by Au/Pd systems. These include the oxidation of glycerol<sup>9, 10</sup>, hydrogen peroxide synthesis<sup>8, 11, 12</sup>, the cyclisation of acetylene to benzene<sup>13-15</sup>, the hydrodechlorination of dichlorofluoromethane<sup>16</sup>, and the enantioselective oxidative

dehydrogenation of aliphatic alcohols to ketones<sup>17</sup>, to name but a few. In the case of the work on acetylene cyclisation, the genesis of Pd<sub>6</sub>Au ensembles reduced hydrocarbon decomposition and promoted benzene desorption, in agreement with analogous studies on ‘real’ dispersed AuPd colloids<sup>18</sup>. Recently, various computational studies have also been conducted in order to understand the composition and reactivity of such systems<sup>19,20</sup>.

In particular, there has been significant interest in Pd/Au nanoparticle systems as catalysts for selective oxidation reactions<sup>21-23</sup>. A major breakthrough occurred when Hutchings et al<sup>24</sup>, discovered that by combining Pd and Au over a titania support 25-fold rate enhancements for alcohol oxidation under mild, solvent-free conditions were possible. The introduction of Au also improves selectivities to aldehydes and ketones compared to pure Pd.

## **3.2 Results and Discussion**

### **3.2.1 Growth of Au on Pd(111)**

Au/Pd(111) surface alloys have been previously characterised *in vacuo* by AES<sup>25-28</sup>, XPS<sup>28,29</sup>, LEED<sup>25,30</sup>, LEIS<sup>30,31</sup> and STM<sup>26</sup>. Epitaxially deposited Au overlayers form apparently random substitutional surface alloys upon annealing above 600 K, reflecting the small lattice mismatch (~ 4.9 %) and bulk miscibilities of the metal components<sup>28</sup>. It should be noted that recent theoretical analyses for Au/Pd(111) alloy surfaces suggest weak repulsion between Au and Pd atoms may drive local ordering<sup>19</sup>.

#### **3.2.1.1 Au/Pd surface preparation**

As described in chapter 2, Au films were grown on Pd(111) at room temperature using a water cooled OMICRON/Focus UHV evaporator, with integral flux monitor. Whilst the growth mode of Au on Pd(111) and thermal alloying is well described in literature<sup>17, 25, 27, 28, 30</sup>, it was necessary to briefly replicate the results of Tysoe’s group<sup>28</sup> in order to ensure correct operation of the evaporator and uniform coverage of the Pd substrate. The growth of Au on Pd(111) was examined by monitoring the Au 4f<sub>7/2</sub> and Pd 3d<sub>5/2</sub> XPS signals. The change in the intensity of these signals during Au growth is shown below in **Figure 3.2**.

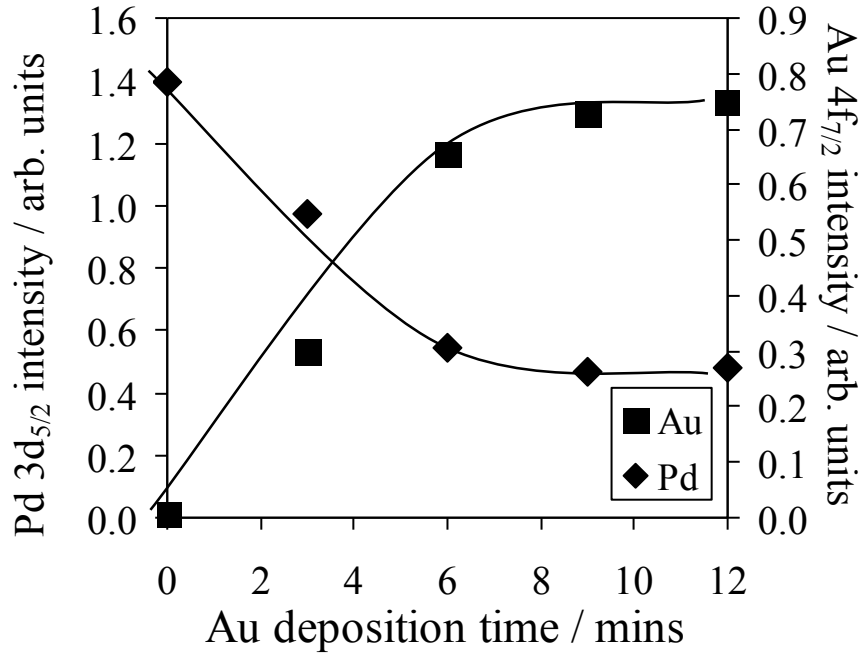


**Figure 3.2** – The variation in intensity of Au 4f<sub>7/2</sub> and Pd 3d<sub>5/2</sub> XPS signals with increasing Au deposition time

Assuming uniform epitaxial growth of a Au overlayer deposited on Pd(111), the thickness of such thin-films can be determined by examining the attenuation of the intensity of the Pd 3d peak. The relationship between the Pd 3d attenuation and the Au film thickness can be expressed as:

$$\left( \frac{I}{I_0} \right) = \exp\left( \frac{-\lambda_{Pd} t}{t_{Au} \cos \varphi} \right) \quad \text{Equation 3.1}$$

where  $I$  is Pd AES or XPS peak intensity,  $I_0$  is initial Pd AES or XPS intensity,  $\lambda_{Pd}$  is the inelastic mean free path of an electron from Au within a Pd matrix<sup>32, 33</sup> (in Angstroms),  $t$  is the thickness of the resulting Au film (in monolayers),  $t_{Au}$  is the thickness of one monolayer of Au (in Angstroms) and  $\varphi$  is the angle of the incident electrons/X-rays into the detector.

The impact of annealing a 3.9 ML Au film on Pd(111) was measured by examining the ratio of the Au 4f<sub>7/2</sub> and Pd 3d<sub>5/2</sub> peak intensity ratios. A plot of this data is shown in **Figure 3.3**. It should be noted that these are the raw data for the outermost several

layers – data presented later on in the chapter is corrected (using published LEIS data<sup>30</sup>) to give a composition purely for the surface layer. In any case, **Figure 3.3** clearly shows that as the sample temperature increases, the surface composition changes; namely that the amount of Au in the outermost layers decreases, with intermixing of the Au thin-film with the Pd(111) substrate. It should be noted that mass spectrometry has confirmed that Au does not thermally desorb from Pd(111) and therefore that alloying is genuine<sup>28</sup>.

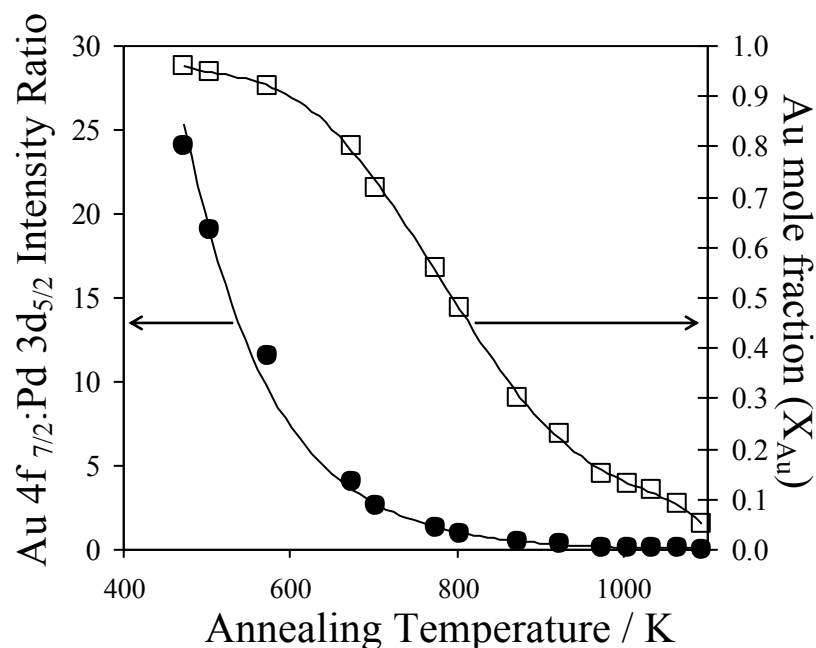


**Figure 3.3** – Variation in Au/Pd surface composition as a function of annealing temperature for a 3.9 ML Au film deposited on Pd(111) at room temperature.

Therefore, through the successive annealing of an epitaxial Au film on Pd(111), a variety of Au/Pd surface ensembles can be prepared. The temperature dependent reactivity of each of these ensembles can then be gauged in a single set of temperature programmed experiments. This experimental procedure is shown visually as a flow diagram in Figure 3.4 below.

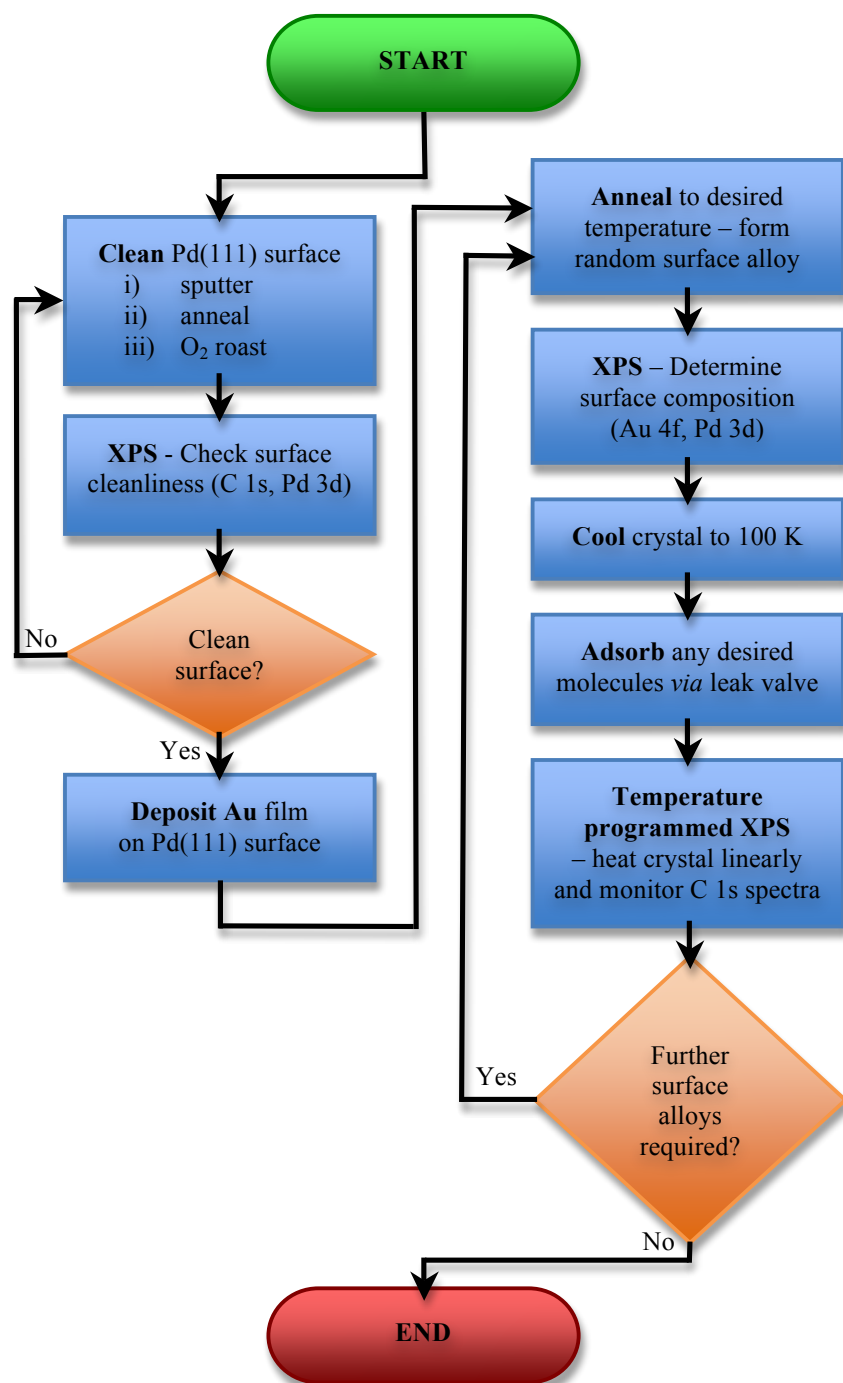


**Figure 3.4** – A flow chart diagram illustrating the experimental procedure devised for monitoring both the formation of surface Au/Pd alloys by XPS and also the temperature dependent reactivity of each alloy by temperature programmed XPS.

### 3.2.2 Surface Ensembles in Au/Pd(111) surface alloys

The effect of Au/Pd alloying on the resulting surface ensembles available for selox was studied via CO adsorption as an active chemical titrant. The CO/Pd(111) system is of huge importance for automotive emission treatment, and as a result has been the subject of numerous surface science investigations<sup>34-47</sup>. Studies have revealed many molecular bonding modes, both attractive and repulsive lateral interactions, and associated ordered structures, all of which are highly dependent upon CO coverage.

Various adsorption sites have been proposed for well-defined CO arrays at one third  $\{(\sqrt{3}\times\sqrt{3})R30^\circ\}$  and half monolayer  $\{c(4\times 2)\}$  coverages. A diagram showing the basic adsorption sites (atop, bridge and hollow) for Pd(111) is shown in **Figure 3.5**. At half monolayer, preferential occupancy of either bridge or fcc/hcp hollow sites has been proposed as a result of respective vibrational<sup>45</sup> and photoelectron diffraction work<sup>46</sup>. STM investigations by Salmeron's group suggests that both models are partially correct, with co-existing domains of bridge-bonded and hollow-bound CO at half a monolayer<sup>47</sup>.

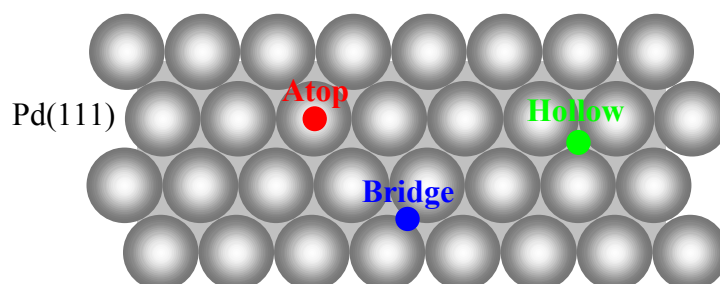


**Figure 3.5** – A diagram showing atop, bridge and hollow adsorption sites on Pd(111).

#### 3.2.2.1 CO adsorption over Pd(111)

Coverage dependent adsorption of CO at 100 K was tracked by running time resolved C 1s XP spectra over clean Pd(111) in order to fingerprint the chemical shifts associated with different CO bonding modes. A common lineshape derived from graphitic carbon was adopted for all C 1s components, based on a Duniach Sunjic profile convoluted with a Gaussian/Lorentzian (4:1) mix, with a FWHM between 0.35 and 0.5 eV and asymmetry index = 0.0618. Fitting was performed using CasaXPS Version 2.3.15. **Figure 3.6** shows the resulting data, from which it is evident that two distinct CO environments can be distinguished at 286.9 and 287.2 eV. Examples of

the Pd fit can be observed in **Figure 3.7**. Only the low binding energy (BE) state is populated below 0.5 ML CO, and can therefore be confidently assigned to CO bound in fcc or hcp hollow sites. At the half monolayer point the hollow site occupancy falls at the expense of the higher BE state, with 50:50 population of both states (**Figure 3.6 inset**). This is in excellent agreement with STM observations<sup>47</sup>, which assign this new state to bridge bound CO. This site-switching becomes much more pronounced close to saturation coverage, with the hollow sites heavily depleted.

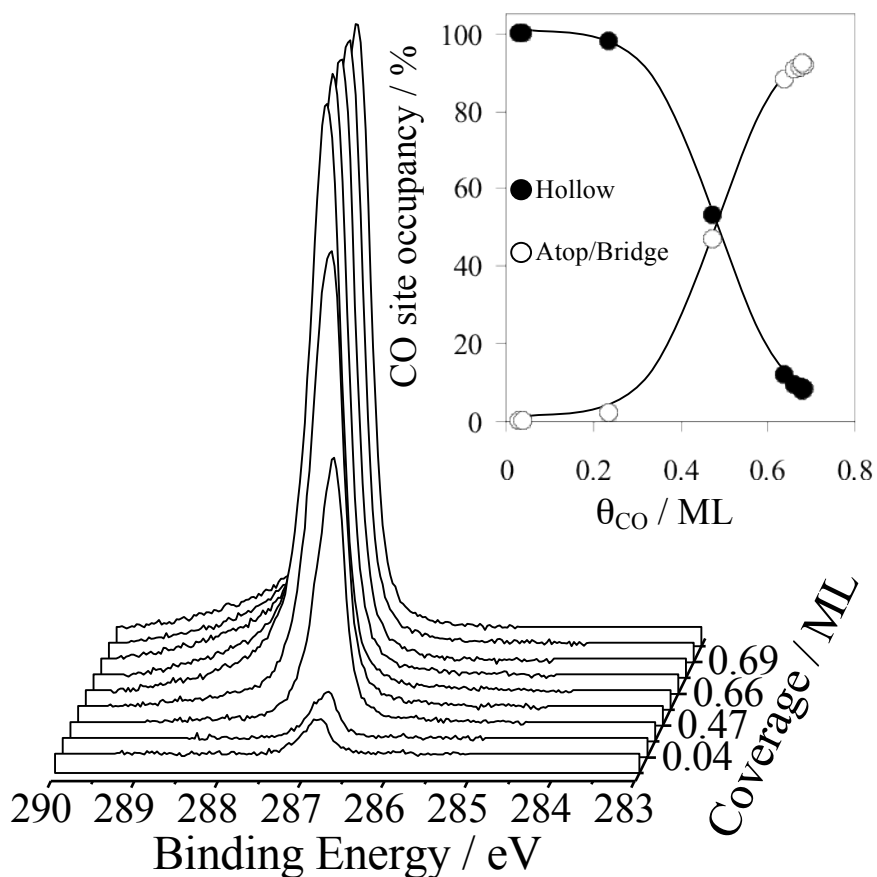


**Figure 3.6** – In situ C 1s XP spectra during adsorption of a CO adlayer over Pd(111) at 100 K. Inset shows fitted intensities of CO components as a function of coverage.

Such extreme depopulation of hollow sites is not seen for high coverage ordered CO structures on Pd(111), wherein hollow and atop bound CO are proposed. Due to surface crowding, slight coverage differences can drive the formation of disordered structures (in this case the introduction of relatively few additional molecules), with preferential occupancy of less sterically-demanding bridge and atop sites. At high coverages a third C 1s component attributable uniquely to atop sites could not be distinguished, hence it is reasonable to assume that the 287.2 eV contains

contributions from both bridge and atop CO. The energies of these two species is consistent with initial state expectations from the Blyholder model of charge donation from the CO  $2\sigma$  orbital into the surface, and back donation from the metal d-orbitals into the CO  $\pi^*$  orbital; the latter contribution increasing with surface coordination number with hollow > bridge > atop.

### 3.2.2.2 CO adsorption over Au/Pd(111) alloys

Available surface ensembles for CO adsorption over a range of Au/Pd surface alloys (see Figure 3.3) were subsequently investigated. This was achieved by progressively annealing a 3.9 ML thin-film Au adlayer, to produce the desired Au/Pd composition. This was then subsequently exposed to a saturation CO dose at 100 K, as shown in **Figure 3.7**. In contrast to previous work, there was no CO adsorption over the Au thin-film at 100 K<sup>28</sup>. Anneals above 600 K cause Au dissolution into the Pd(111) substrate, which facilitated weak CO chemisorption into two high binding energy states at 287.7 and 288.5 eV. Higher temperature anneals drive further Au/Pd intermixing, increasing the saturation CO coverage as displayed in the inset of **Figure 3.7**. The re-emergence of the two CO adsorption states at 286.9 and 287.2 eV, characteristic of clean Pd(111) are also evident for these higher temperature anneals.

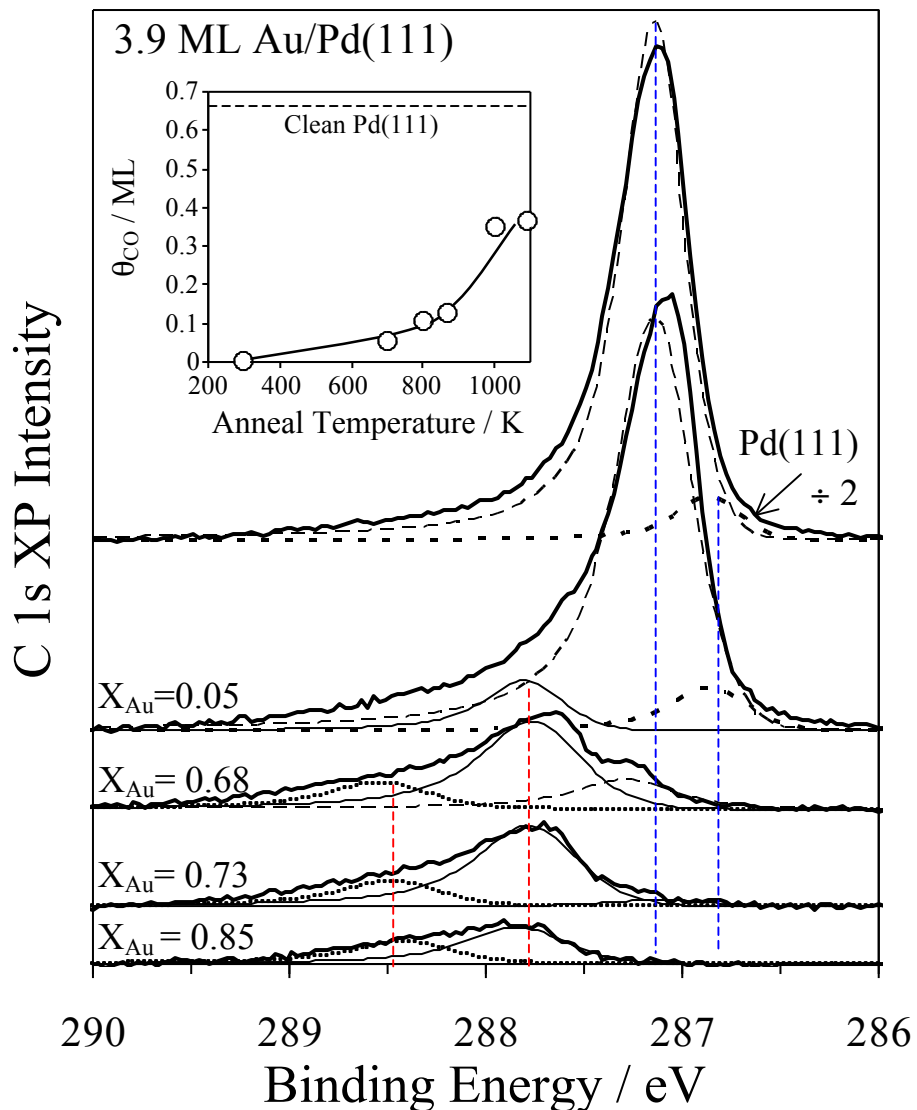


**Figure 3.7** – C 1s XPS spectra of saturated CO adlayers over Au/Pd surfaces alloys at 100 K as a function of annealing temperature. These surfaces were prepared by the successive annealing a 3.9 ML Au/Pd(111). The bold lines show the acquired data; whereas the thin/dashed lines show the fitted states determined using CasaXPS software. Inset shows saturation CO coverage as a function of annealing temperature. Pd states are highlighted by blue lines, whereas Pd/Au states are highlighted in red.

It should be noted that the surface compositions that follow are derived from AES measurements of the overall Au mole fraction in the outermost several layers, corrected using published LEIS data<sup>30</sup> to determine the actual Au coverage in the terminal surface layer. This correction is significant for alloys containing less than 90% Au in the selvedge since strong Au surface segregation occurs in dilute Au/Pd

alloys<sup>30</sup>. It is interesting to note that significant (~ 16 %) surface Au was retained even following the highest annealing temperature in this work.

The coverage-dependent integrated intensities (determined using CasaXPS) of the four experimentally observed CO surface species from **Figure 3.7** are shown in **Figure 3.8 (a)**. It should be noted that within this figure the observed trends are emphasised using guidelines. Simple Monte–Carlo simulations (performed by Prof. A. F. Lee) of Au/Pd alloys were also conducted on a 144 atom 2D lattice assuming random substitution of non-interacting atoms at 300 K. These simulations were carried out to model the distribution of surface ensembles available as a function of Au/Pd composition, and thereby help assign the new high binding energy CO states observed on Au-rich surface alloys. In each simulation a random Au/Pd lattice was generated, where the different types of environment were identified according to the number and type of neighbours surrounding each Pd or Au atom. How the modelled site distribution changed as a function of Au content was plotted in order to mimic the variation in CO sites. The same procedure was also carried out for pure Pd hollow and bridge/atop sites. Both sets of simulations can be found in **Figure 3.8 (b)**. These theoretical results are in good agreement with the experimental trends, confirming that even small amounts of Au (~ 10 %) inhibits CO binding at three-fold hollow sites.

As expected, the occupancy of *Pd*<sub>2</sub>(Pd) bridge and *Pd*(Pd<sub>2</sub>) atop sites decay more slowly, with significant populations present up to ~ 50 % Au. The corresponding growth of *Pd*<sub>2</sub>(Au) bridge and *Pd*(Au<sub>2</sub>) sites quantitatively tracks that of the respective 288.5 and 287.7 eV CO states, enabling assignment to Au perturbed bridge and isolated Pd ensembles. Cartoons of these ensembles, along with the CO XP spectra are displayed above the figure. The chemical shift of both CO alloy adsorption states is consistent with charge donation from Pd to Au, as previously reported within the Au/Pd(111) system<sup>28, 48</sup>, and associated reduced metal back donation into the CO  $\pi^*$  orbital.

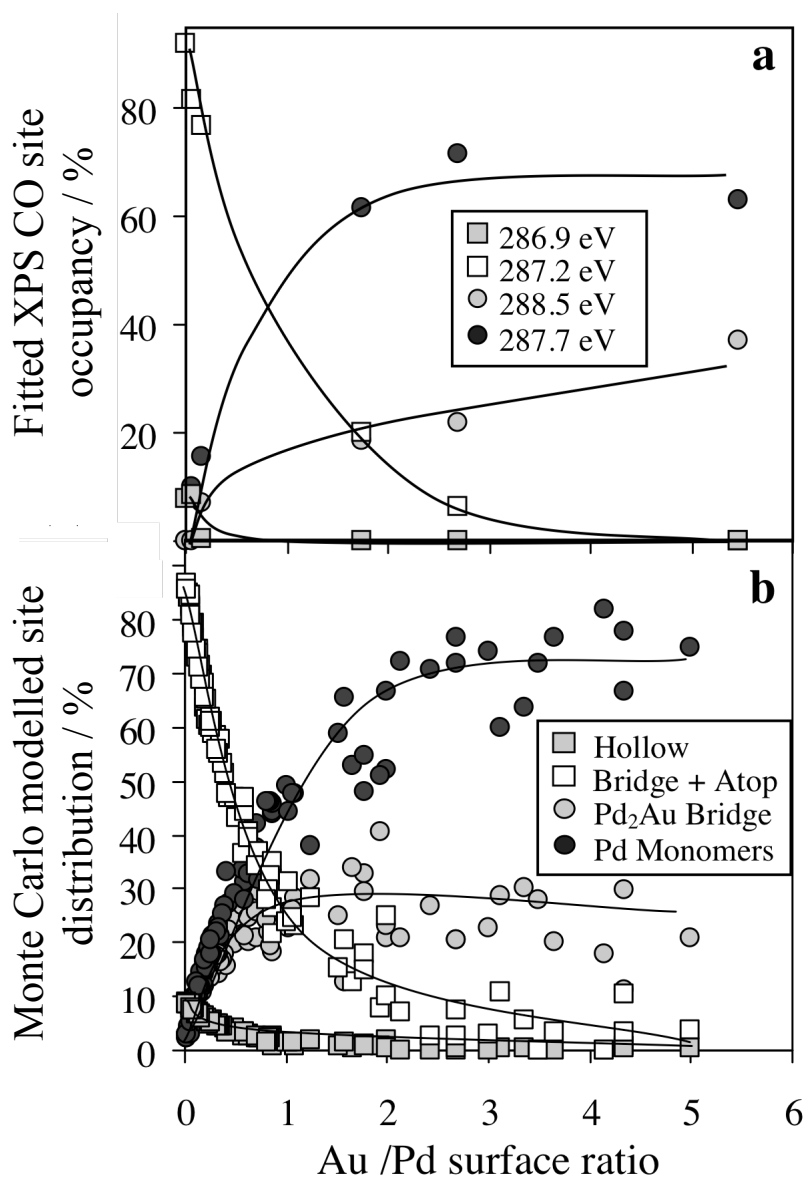
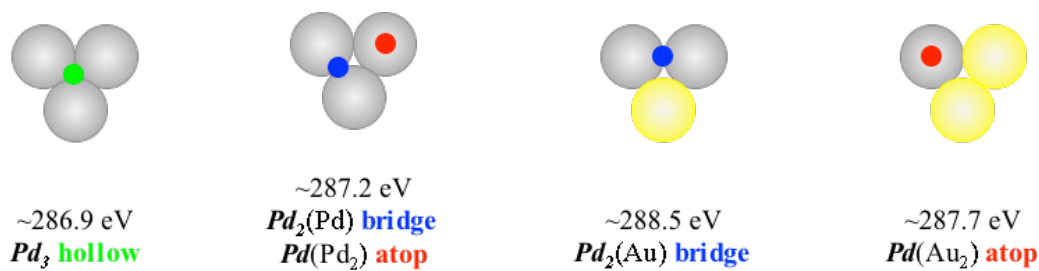


**Figure 3.8 - (a)** Integrated C 1s XP intensities of fitted CO components for experiments involving saturated CO adlayers adsorbed at 100 K over Au/Pd alloys prepared by annealing a 3.9 ML Au/Pd(111) surfaces. **(b)** The Monte Carlo simulation data of Pd ensembles available for CO adsorption as a function of Au/Pd surface composition. Surface Au rapidly suppresses CO adsorption over larger Pd ensembles.

### 3.2.3 Crotyl alcohol reactivity over Au/Pd(111) surface alloys

With the identification of the surface ensembles available for selox complete, the thermal chemistry of crotyl alcohol over various Au/Pd(111) surface alloys could now be explored by temperature programmed XPS studies. As detailed earlier, and highlighted in Figure 3.4, the desired surface composition was first prepared either by deposition of Au onto the Pd(111) substrate or by annealing the Au pre-covered Pd(111). The sample was then cooled to 100 K, before dosing a saturation exposure of the alcohol. The thermal chemistry of the alcohol and evolution of reaction products could then be tracked by C 1s XP spectra as the sample was slowly heated (see chapter 2, section 2.4 for further details).

#### 3.2.3.1 Temperature Programmed XPS (TP XPS) studies

The adsorption of a crotyl alcohol adlayer over an unannealed 3.9 ML Au thin-film was studied. The raw XPS data (as shown in **Figure 3.3**) shows that there is some intermixing of the outermost layers, although when this is corrected to take into account only the surface layer (using published LEIS data<sup>30</sup>), there is no substantial alloying of the surface layer below 600 K. This means that the thermal chemistry of this adlayer could be explored by temperature-programmed fast XPS without complications from changes in the surface metal composition, as Au/Pd alloying of the surface layer does not begin below 600 K. In this way the reactivity of bulk Au surfaces towards allylic alcohols could be benchmarked. The results of this experiment are shown in **Figure 3.9**.

As with low temperature adsorption over pure Pd(111), from **Figure 3.9**, it can be seen that two distinct C 1s environments are evident (in this case at 285.2 and 286.8 eV) in a 3:1 ratio, attributed to -H<sub>2</sub>-C-OH and propylidene moieties respectively. The saturation coverage over the Au thin-film is around two-thirds that over Pd(111) at 0.1 ML. This lower coverage may be due to disordered packing arrangements due to the weaker molecular interaction with Au.

In stark contrast to pure Pd(111), crotyl alcohol does not undergo any chemistry over the thin-film of Au, with the molecule simply desorbing above 170 K (**Figure 3.9**), and leaving only trace carbon behind amounting to ~ 3 % of the saturated monolayer.

This suggests that the selective alcohol oxidation activity reported for supported<sup>49-51</sup> and stabilised<sup>52</sup> Au nanoparticles is not associated with extended Au (111) terraces, and therefore must be confined to higher surface energy facets/defects or electronically perturbed (111) ensembles decorating clusters only a few nanometres across.

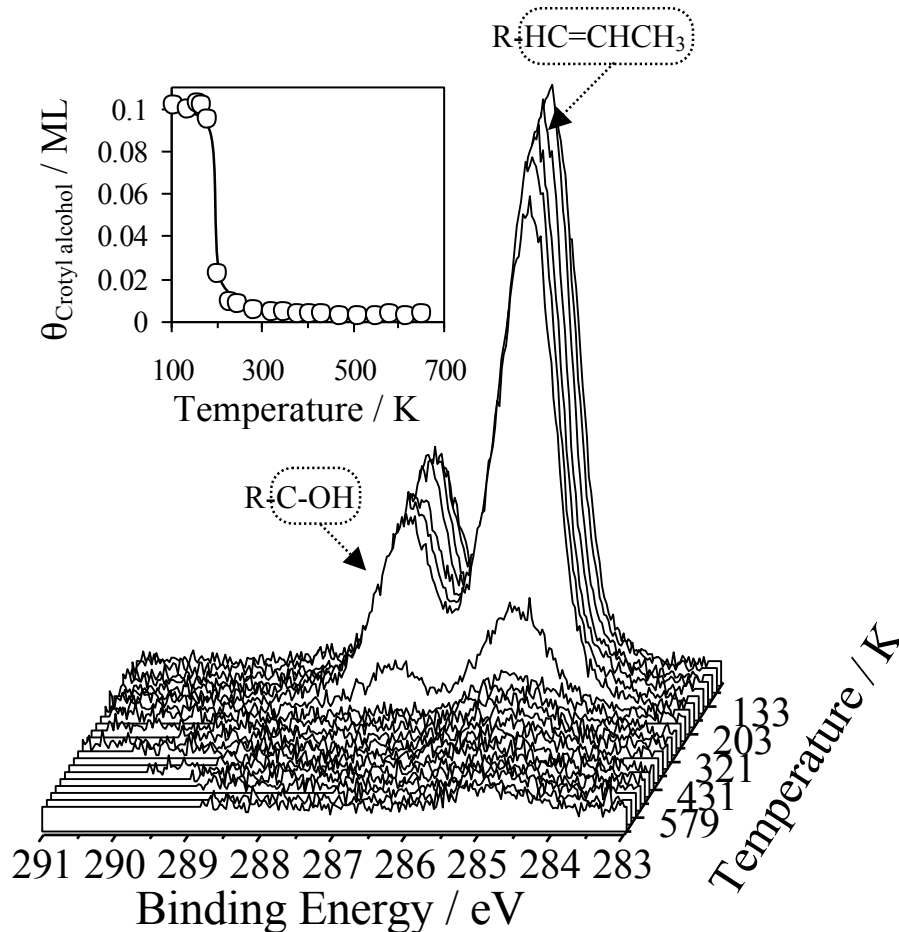


**Figure 3.9** - Temperature-programmed C 1s XP spectra of a saturated crotyl alcohol adlayer prepared over an unannealed 3.9 ML Au/Pd(111) film at 100 K. Inset shows fitted crotyl alcohol coverage as a function of temperature.

Alloying below  $\sim 950$  K has negligible impact upon either the saturation coverage of the alcohol, the degree of subsequent decomposition or carbon lay-down. Surfaces containing  $\geq 15\%$  Pd in the outermost layer (achieved for anneals above 973 K) are sufficient to switch on a new reaction pathway for the alcohol. This is evidenced from **Figure 3.10**, temperature programmed XP spectra for a saturated crotyl alcohol adlayer adsorbed on a 973 K annealed surface ( $X_{Au} = 0.15$ ).

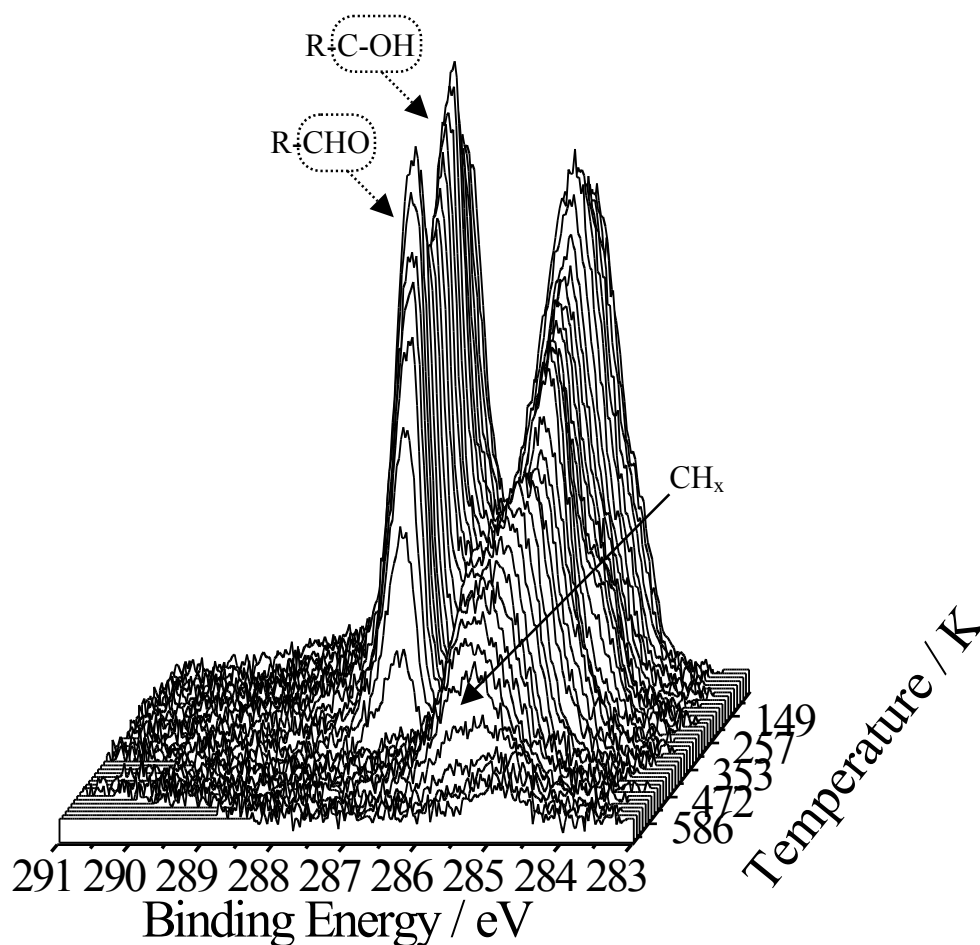


**Figure 3.10** - Temperature-programmed C 1s XP spectra of a saturated crotyl alcohol adlayer over an ultrathin 3.9 ML Au/Pd(111) film annealed to 973 K ( $X_{\text{Au}} = 0.15$ ).

From **Figure 3.10**, it can be observed that the 286.8 eV component sharpens noticeably above  $\sim 170$  K and also shifts by approximately +0.3 eV. The same is also apparent for the low binding energy component, with the associated shift being of a similar magnitude but in the opposite direction. The resulting C 1s spectral fingerprint between 170 K and 350 K matches that of crotonaldehyde on Pd(111)<sup>1</sup>, and has been confirmed by mass spectrometry. These crotonaldehyde features disappear rapidly above  $\sim 350$  K, coincident with the emergence of a broad, low energy carbon state reminiscent of alkylidyne fragments on Pt(111)<sup>53</sup>. These fragments diminish above 600 K, leaving only trace carbon fragments ( $\text{CH}_x$ ). Representative snapshot spectra are shown in **Figure 3.11**, which highlight these steps and also show the sharpening of peaks.

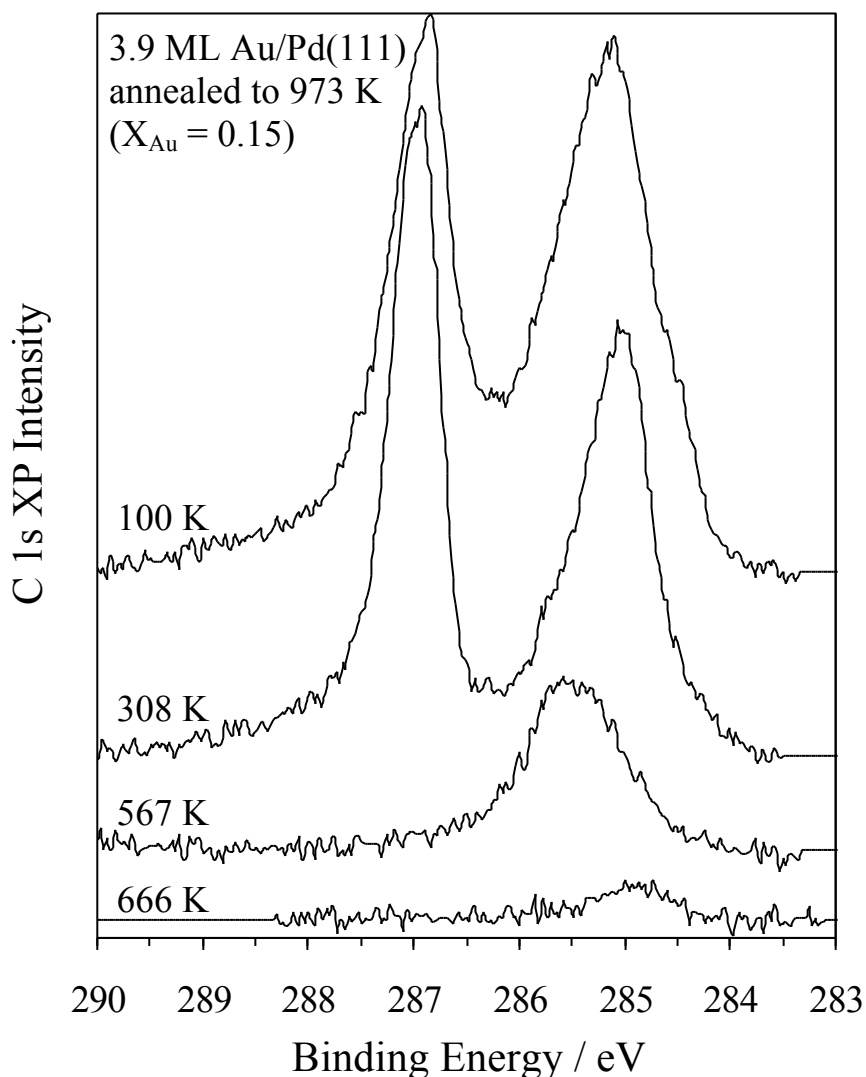


**Figure 3.11** - C 1s snapshot spectra during the temperature programmed reaction of a saturated crotyl alcohol adlayer over a 3.9 ML Au/Pd(111) film annealed to 973 K ( $X_{Au} = 0.15$ ).

Fitted surface components for this  $X_{Au} = 0.15$  surface alloy are presented in **Figure 3.12**, which clearly show that for this alloy composition the selectivity of crotyl alcohol to surface bound crotonaldehyde occurs at room temperature with 100 % efficiency. Although some of the desired crotonaldehyde product decomposes at higher temperatures, only 3 % of the initial alcohol is left behind. This is in contrast with unpromoted Pd(111) where over 70 % of a crotyl alcohol monolayer fully decomposes<sup>1</sup>.

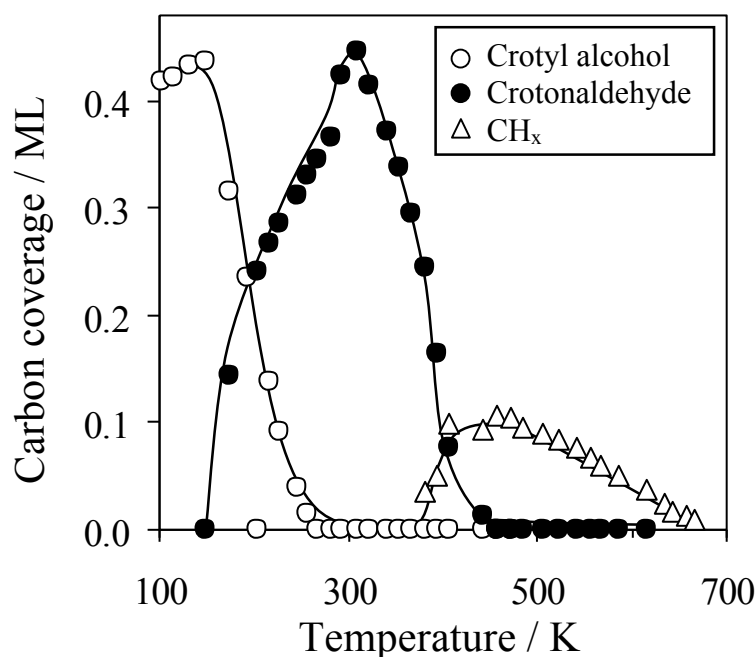


**Figure 3.12** - Integrated C 1s XP intensities of fitted crotyl alcohol, crotonaldehyde and carbonaceous components for a saturated crotyl alcohol adlayer adsorbed at 100 K over a 973 K ( $X_{Au} = 0.15$ ) pre-annealed 3.9 ML Au/Pd(111) surface.

### 3.2.3.2 Temperature Programmed Desorption (TPD) studies

XPS has been used to examine surface chemistry of the alcohol over the single crystal surface. Whilst this has determined the formation of products on the surface at different temperatures, mass spectrometry is required in order to determine which products desorb from the catalyst surface (see chapter 2, section 2.3). Experiments were conducted using the UHV single crystal chamber described in chapter 2, section 2.1.1.

Temperature programmed desorption (TPD) spectra were recorded for a range of Au/Pd alloy surfaces in order to identify the stable reaction products evolved. The parent crotyl alcohol solely desorbs from the un-annealed thin-film Au/Pd(111), which gives rise to 153 K multilayer and 183 K monolayer desorption states, as shown in **Figure 3.13**. These temperatures are slightly below those observed over Pd(111), in line with the anticipated lower enthalpy of adsorption. The amount of reactant desorption is also reduced over Au-rich alloys relative to Pd-rich alloys.

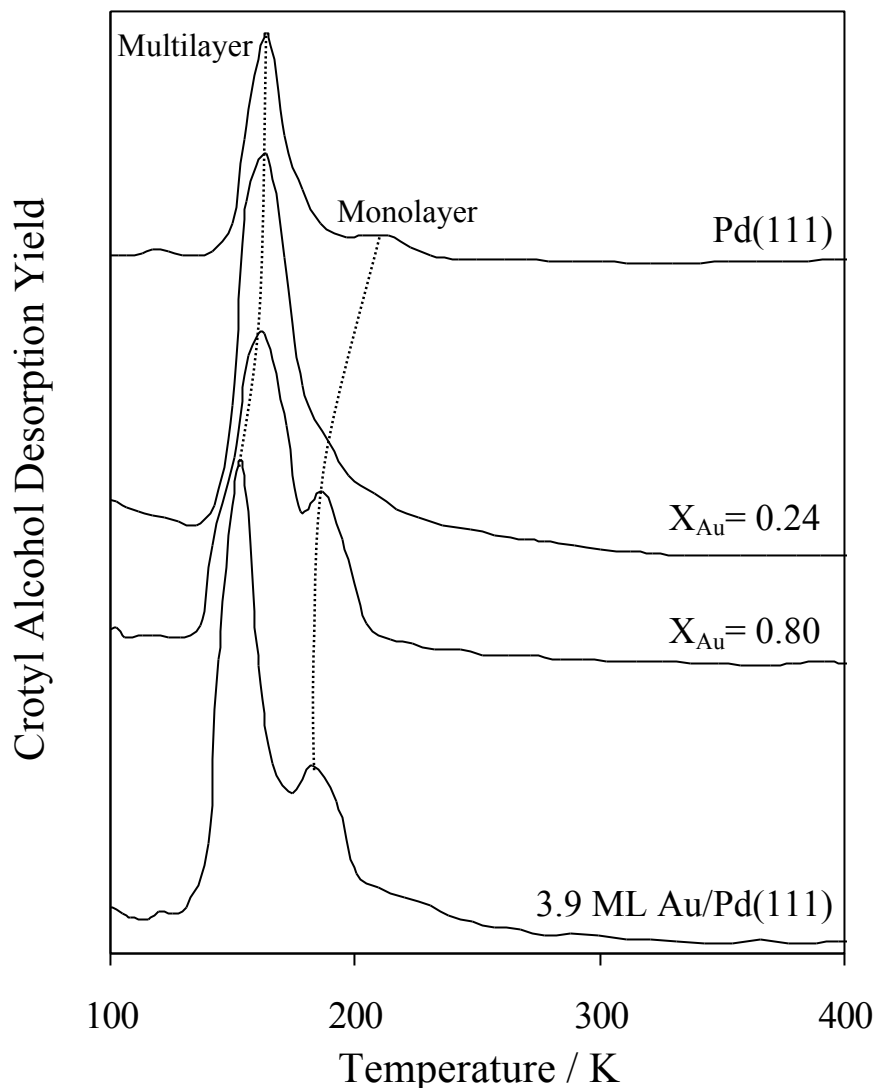


**Figure 3.13** - Thermal desorption mass spectra of a saturated crotyl alcohol adlayer adsorbed at 100 K over 3.9 ML Au/Pd(111) films. A comparative spectrum is shown for Pd(111).

The evolution of crotonaldehyde at room temperature was also observed, and is shown for a range of Au/Pd alloys are shown in **Figure 3.14**. The surface chemistry of pure Pd(111) is drastically different, with only dehydration (butene and water) and decarbonylation (CO and propene) desorption products observed. The desorption yield of crotonaldehyde initially rises with increasing surface Pd content, reaching a maximum for a AuPd<sub>5</sub> surface. This enhanced oxidation performance is accompanied by an increase in desorption peak temperature from ~ 270 K to 290 K.

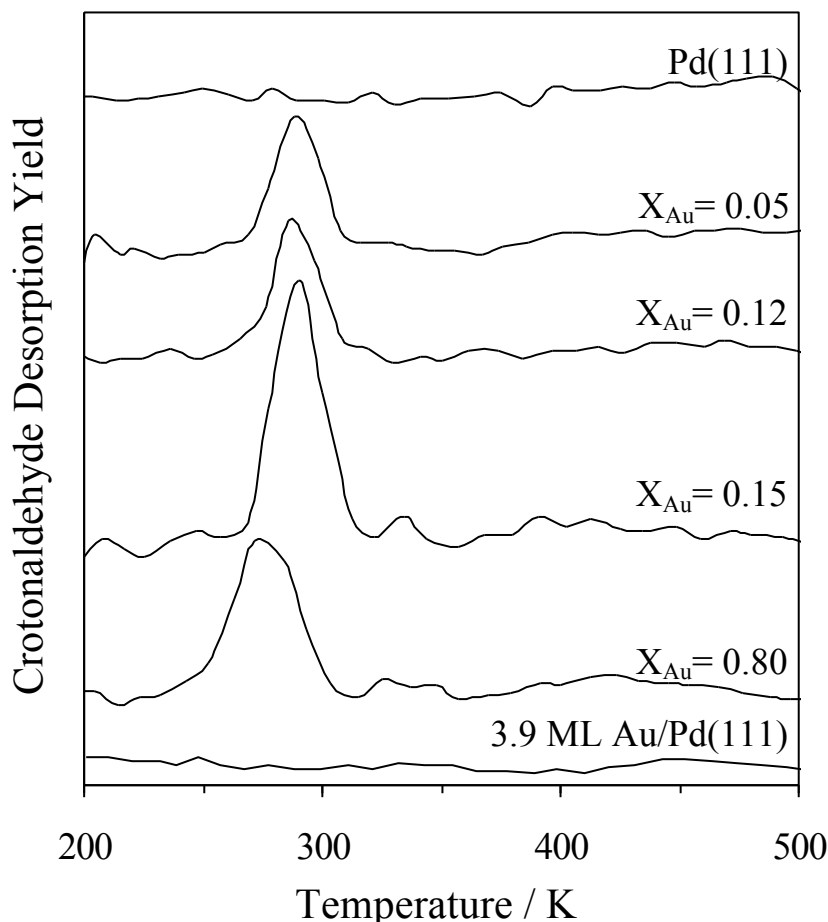


**Figure 3.14** - Thermal desorption mass spectra of reactively-formed crotonaldehyde from a saturated crotyl alcohol adlayer adsorbed at 100 K over 3.9 ML Au/Pd(111) films. A comparative spectrum is shown for Pd(111).

Crotonaldehyde is formed on the surface of Au/Pd alloys below  $\sim 200$  K (as seen in **Figure 3.10**), meaning that aldehyde evolution is desorption-rate limited. The strong binding of crotonaldehyde to Pd-rich surfaces may reflect differences in adsorption mode over different alloy compositions (e.g. flat-lying versus tilted, or  $\pi$ -bonding through both C=C and C=O moieties), or a reduced electronic perturbation as Au atoms diffuse subsurface. High temperature anneals, where alloy compositions approach 90 % Pd, result in limited aldehyde decarbonylation, revealing that small amounts of Au are enough to cause desorption of the aldehyde.

Both propene and CO desorb from Au/Pd alloy surfaces, at 300 K and 350 - 400 K respectively. The desorption profiles of these by-products are slightly perturbed compared to Pd(111), with propene evolving in a single state in the presence of

surface Au. This decarbonylation pathway operates as a minor route over Au-rich alloys, but accounts for  $\sim 50\%$  of the reactively-formed crotonaldehyde for compositions above AuPd<sub>5</sub>.

### 3.2.3.3 Optimum Au/Pd alloy composition for crotyl alcohol selox

The influence of Au/Pd surface alloy composition on both the surface chemistry of adsorbed crotyl alcohol and desorption of crotonaldehyde is summarised in **Figure 3.15**. This figure immediately highlights the limitations of each monometallic system. Pure Pd displays conversion of crotyl alcohol to crotonaldehyde at low temperature, but unfortunately is also very active towards consequent aldehyde decarbonylation, as well as the dehydrogenation of the resultant surface propylidyne fragments. Consequently no crotonaldehyde desorbs intact from extended Pd(111) ensembles in the absence of additional co-adsorbed oxygen<sup>1</sup>. This may account for the rapid deactivation of monometallic Pd nanoparticles<sup>24, 54</sup>. At the other extreme, over the pure Au thin-film crotyl alcohol chemisorbs into both monolayer and multilayer desorption states, but crucially Au cannot initiate the vital C-H/O-H activation steps. In a clear example of a strong synergetic interaction, the incorporation of a relatively small number of Au atoms, which CO chemisorption suggests is sufficient to disrupt Pd hollow sites, considerably suppresses crotonaldehyde decomposition, while actually enhancing its formation from the parent alcohol. The optimum surface alloy composition for crotyl alcohol selox, with minimal decomposition of the resultant crotonaldehyde product, is a surface Au mole fraction of approximately 0.3, which corresponds to a surface ensemble composition of Au<sub>2</sub>Pd<sub>3</sub>.

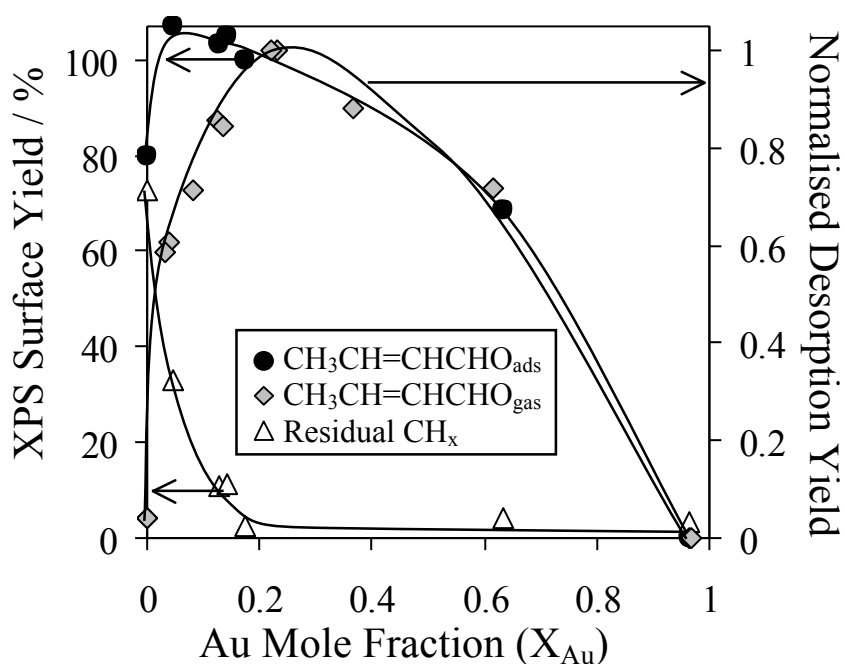


**Figure 3.15** – In situ XPS derived crotyl alcohol conversion to surface-bound crotonaldehyde, and net decomposition to residual surface carbon as a function of Au alloy composition. The normalised desorption yields (determined by TDS) of reactively-formed crotonaldehyde are also shown.

On the basis of these *in-situ* X-ray surface science studies, it can be proposed that high Pd surface concentrations should provide the optimum selox activity for dispersed Au/Pd alloy nanoparticles. This is consistent with recent studies on the aerobic oxidation of crotyl alcohol over PVP-stabilised bimetallic Au/Pd nanoparticles<sup>52</sup>. These exhibit maximum turnover frequencies and selectivities to the desired aldehydes for bulk Au:Pd ratios of 1:3 (c.f. a bulk ratio of 1:5 in this study), and also hydrogenation and isomerisation side products characteristic of pure Pd-like surface character. Similar Pd surface segregation and associated excellent selox activity has been reported for  $Al_2O_3$ ,  $TiO_2$  and  $SiO_2$  supported Au/Pd nanoparticles, wherein STEM and XPS indicate a Au-core, Pd-shell spontaneous partitioning upon calcination in air<sup>12, 24</sup>. The situation is more complex for AuPd/C particles, wherein it is postulated that the selective oxidation of glycerol to glyceric acid proceeds over Au-rich alloy surfaces decorated with Pd monomers<sup>55</sup>. However the bimetal distribution was very inhomogeneous between individual particles in this latter study, and did not utilise a surface sensitive spectroscopic method to model the terminating alloy composition.

Earlier work on allylic alcohol selox has shown that strong adsorption of a proximate C=C bond is essential for subsequent activation of primary alcohols<sup>56</sup>. This observation is supported by NEXAFS measurements on crotyl alcohol over Pd(111)<sup>1</sup> which reveal the C=C bond is bound parallel to the surface in both parent alcohol and aldehyde product. For AuPd systems, it seems likely that extended Au ensembles within Au-rich surfaces are themselves inactive towards crotyl alcohol, whilst the probability of finding two Pd monomers in close proximity, able to tether the allyl function while activating the alcohol, is too small for significant oxidation.

In addition, Au chemistry on the nano-scale generally exhibits pronounced particle size dependency; hence Au-rich alloy nanoparticles may be more active than would be predicted from this model investigation.

### **3.2.4 Errors**

It is estimated that the error associated in the surface content from the XPS data will be approximately 0.2 - 0.5 atomic%. This is an estimated error value, which will vary depending upon the element under study, as each element has an associated response factor to the XP spectrometer. Therefore, the XPS errors will be depend on the type of measurement performed (i.e. determination of alloy compositions, calculation of organic adsorbates etc). According to CasaXPS, the processing software used to analyse the data presented in this chapter, the response factors for Pd 3d<sub>5/2</sub> and Au 4f<sub>7/2</sub> are 9.54 and 9.79 respectively. This means that the associated error in the measurement of the alloy ratios / mole fractions will be approximately 3 %.

### **3.3 Conclusions**

The coverage dependent adsorption of CO was used to examine the surface ensembles available for selox by Au/Pd(111) surface alloys. The chemical shifts corresponding to different CO bonding modes were tracked by time resolved C 1s XPS. In the case of clean Pd(111), below 0.5 ML CO, a single binding energy state at 286.9 eV was observed, which can be assigned to CO binding in hollow sites. With increasing CO coverage, the hollow site occupancy decays with the population of an additional state at 287.2 eV, attributed to bridge and atop bound CO. At saturation coverage, these

bridge and atop sites are almost exclusively populated. For the 3.9 ML thin-film of Au on Pd(111), no CO adsorption was observed. However, when this film was annealed to 600 K (driving Au/Pd intermixing and surface alloy formation), weak chemisorption was observed for two high binding energy states at 287.7 and 288.5 eV. High temperature anneals drive further Au/Pd intermixing and the re-emergence of the two Pd(111) CO binding energy states. The integrated intensities of these experimentally determined states were compared to Monte Carlo simulations and were found to be in good agreement, allowing the surface ensembles to be identified. The key finding of this work is that surface Au rapidly suppresses CO adsorption over larger Pd ensembles.

Following on from this, it has been shown that thin-films of epitaxial Au prepared over a Pd(111) substrate reversibly chemisorb crotyl alcohol, but are unable to drive selective oxidation or decomposition. Au-rich surface Au/Pd alloys show moderate activity for the oxidative dehydrogenation of crotyl alcohol to crotonaldehyde, which in turn desorbs intact at room temperature with minimal side-reactions. The optimum surface alloy composition for crotyl alcohol selox, with minimal decomposition of the resultant crotonaldehyde product, is Au<sub>2</sub>Pd<sub>3</sub>, associated with a bulk alloy composition of AuPd<sub>5</sub>. Pd-rich alloy surfaces convert 100 % of a crotyl alcohol adlayer to crotonaldehyde, although as much as half of this aldehyde subsequently decarbonylates to produce gas phase CO and propene, and leave small amounts of residual carbon ( $\leq 30$  % of a monolayer). In summary, *in-situ* 'fast' XPS has been used to show that small amounts of Au can promote the selective oxidation of crotyl alcohol while suppressing crotonaldehyde decarbonylation, and that isolated Pd sites are not the active site for such catalysis in extended alloys.

In this chapter, the influence of Au upon the formation of reactively formed crotonaldehyde by the selox of crotyl alcohol over Pd(111) has been examined. However, the chemistry of the aldehyde itself and any reactively formed by-products has yet to be explored. As a result, the role of Au on the thermal chemistry of crotonaldehyde over Pd(111) surfaces will be examined by temperature programmed reaction spectroscopy in the next chapter. In addition, to imitate 'real' selox

conditions, the role of pre-adsorbed oxygen on clean and Au-promoted Pd(111) surfaces will also be determined.

### 3.4 References

1. A. Lee, Z. Chang, P. Ellis, S. Hackett and K. Wilson, *J. Phys. Chem. C*, 2007, **111**, 18844-18847.
2. S. Hackett, University of York, 2008.
3. F. Alardin, B. Delmon, P. Ruiz and M. Devillers, *Catalysis Today*, 2000, **61**, 255-262.
4. M. Ruff, N. Takehiro, P. Liu, J. Nørskov and R. Behm, *ChemPhysChem*, 2007, **8**, 2068-2071.
5. J. Rodriguez and D. Goodman, *J. Phys. Chem.*, 1991, **95**, 4196-4206.
6. M. D. Hughes, Y. J. Xu, P. Jenkins, P. McMorn, P. Landon, D. I. Enache, A. F. Carley, G. A. Attard, G. J. Hutchings, F. King, E. H. Stitt, P. Johnston, K. Griffin and C. J. Kiely, *Nature*, 2005, **437**, 1132-1135.
7. G. J. Hutchings, *Catalysis Today*, 2007, **122**, 196-200.
8. G. J. Hutchings, *Chem. Commun.*, 2007, **2008**, 1148-1164.
9. N. Dimitratos, F. Porta and L. Prati, *Applied Catalysis A: General*, 2005, **291**, 210-214.
10. W. C. Ketchie, M. Murayama and R. J. Davis, *Journal of Catalysis*, 2007, **250**, 264-273.
11. F. Menegazzo, P. Burti, M. Signoretto, M. Manzoli, S. Vankova, F. Boccuzzi, F. Pinna and G. Strukul, *Journal of Catalysis*, 2008, **257**, 369-381.
12. J. K. Edwards, A. Thomas, A. F. Carley, A. A. Herzing, C. J. Kiely and G. J. Hutchings, *Green Chem.*, 2008, **10**, 388-394.
13. A. F. Lee, C. J. Baddeley, C. Hardacre, R. M. Ormerod, R. M. Lambert, G. Schmid and H. West, *J. Phys. Chem.*, 1995, **99**, 6096-6102.
14. C. J. Baddeley, J. R. M. Ormerod, A. W. Stephenson and R. M. Lambert, *J. Phys. Chem.*, 1995, **99**, 5146-5151.
15. C. J. Baddeley, M. Tikhov, C. Hardacre, J. R. Lomas and R. M. Lambert, *J. Phys. Chem.*, 1996, **100**, 2189-2194.
16. M. Bonarowska, J. Pielaszek, V. A. Semikolenov and Z. Karpinski, *Journal of Catalysis*, 2002, **209**, 528-538.
17. F. Gao, Y. Wang, Z. Li, O. Furlong and W. Tysøe, *J. Phys. Chem. C*, 2008, **112**, 3362-3372.
18. A. Lee, C. Baddeley, C. Hardacre, R. Ormerod, R. Lambert, G. Schmid and H. West, *J. Phys. Chem.*, 1995, **99**, 6096-6102.
19. J. A. Boscoboinik, C. Plaisance, M. Neurock and W. T. Tysøe, *Phys. Rev. B*, 2008, **77**, 045422.

20. D. Yuan, X. Gong and R. Wu, *Phys. Rev. B*, 2007, **75**, 085428.
21. A. Abad, P. Concepción, A. Corma and H. García, *Angew. Chem. Int. Ed.*, 2005, **44**, 4066–4069.
22. N. Dimitratos, A. Villa, D. Wangb, F. Porta, D. Su and L. Prati, *J. Cat.*, 2006, **244**, 113-121.
23. X. Wang, N. S. Venkataramanan, H. Kawanami and Y. Ikushima, *Green Chem.*, 2007, **9**, 1352-1355.
24. D. I. Enache, J. K. Edwards, P. Landon, B. Solsona-Espriu, A. F. Carley, A. A. Herzing, M. Watanabe, C. J. Kiely, D. W. Knight and G. J. Hutchings, *Science*, 2006, **311**, 362.
25. C. Baddeley, M. Tikhov, C. Hardacre, J. Lomas and R. Lambert, *J. Phys. Chem.*, 1996, **100**, 2189-2194.
26. B. Gleich, M. Ruff and R. Behm, *Surf. Sci.*, 1997, **386**, 48-55.
27. F. Calaza, F. Gao, Z. Li and W. Tysoe, *Surf. Sci.*, 2007, **601**, 714-722.
28. Z. Li, F. Gao, Y. Wang, F. Calaza, L. Burkholder and W. Tysoe, *Surf. Sci.*, 2007, **601**, 1898-1908.
29. R. Ormerod, C. Baddeley and R. M. Lambert, *Surface Science*, 1991, **259**, L709-L713.
30. Z. Li, O. Furlong, F. Calaza, L. Burkholder, H. Poon, D. Saldin and W. Tysoe, *Surf. Sci.*, 2008, **602**, 1084-1091.
31. C.-W. Yi, K. Luo, T. Wei and D. W. Goodman, *J. Phys. Chem. B*, 2005, **109**, 18535-18540.
32. *La Surface*, <http://lasurface.com/xps/imfpgrapher.php>.
33. P. J. Cumpson and M. P. Seah, *Surface and Interface Analysis*, 1997, **25**.
34. H. Conrad, G. Ertl and J. Küppers, *Surf. Sci.*, 1978, **76**, 323-342.
35. T. Engel and G. Ertl, *J. Chem. Phys.*, 1978, **69**, 1267-1281.
36. H. Conrad, G. Ertl, J. Koch and E. E. Latta, *Surf. Sci.*, 1974, **43**.
37. P. Sautet, M. Rose, J. Dunphy, S. Behler and M. Salmeron, *Surface Science*, 2000, **453**, 25-31.
38. J. Szanyi, W. K. Kuhn and D. W. Goodman, *J. Phys. Chem.*, 1994, **98**, 2978-2981.
39. S. Surnev, M. Sock, M. Ramsey, F. Netzer, M. Wiklund, M. Borg and J. Andersen, *Surface Science*, 2000, **470**, 171-185.
40. C. Zhang and P. Hu, *J. Am. Chem. Soc.*, 2001, **123**, 1166-1172.
41. A. Santra and D. Goodman, *Electrochimica Acta*, 2002, **47**, 3595-3609.

42. T. Matsushima and H. Asada, *J. Chem. Phys.*, 1986, **85**, 1658-1668.
43. B. Bourguignon, S. Carrez, B. Dragnea and H. Dubost, *Surf. Sci.*, 1998, **418**, 171-180.
44. V. V. Kaichev, I. P. Prosvirin, V. I. Bukhtiyarov, H. Unterhalt, G. Rupprechter and H.-J. Freund, *J. Phys. Chem. B*, 2003, **107**, 3522-3527.
45. A. M. Bradshaw and F. H. Bradshaw, *Surf. Sci.*, 1978, **72**, 513-535.
46. R. L. Toomes, J. Robinson, S. M. Driver, D. P. Woodruff, P. Baumgärtel, T. Geißel, R. Lindsay, O. Schaff and A. M. Bradshaw, *J. Phys: Condens. Matter* 2000, **12**, 3981-3991.
47. M. Rose, T. Mitsui, J. Dunphy, A. Borg, D. Ogletree, M. Salmeron and P. Sautet, *Surf. Sci.*, 2002, **512**, 48-60.
48. S. Hufner, G. Wertheim and J. Wemick, *Solid State Comm.*, 1975, **17**, 1585-1590.
49. M. Hughes, Y. Xu, P. Jenkins, P. McMorn, P. Landon, D. Enache, A. Carley, G. Attard, G. Hutchings and F. King, *Nature*, 2005, **437**, 1132-1135.
50. X. Wang, N. Venkataramanan, H. Kawanami and Y. Ikushima, *Green Chem.*, 2007, **9**, 1352-1355.
51. A. Abad, P. Concepcion, A. Corma and H. Garcia, *Angew. Chem. Int. Ed.*, 2005, **44**, 4066-4069.
52. W. Hou, N. Dehm and R. Scott, *J. Catalysis*, 2008, **253**, 22-27.
53. A. Lee, K. Wilson, A. Goldoni, R. Larciprete and S. Lizzit, *Surf. Sci.*, 2002, **513**, 140-148.
54. A. F. Lee and K. Wilson, *Green Chem.*, 2004, **6**, 37-42.
55. D. Wang, A. Villa, F. Porta, L. Prati and D. Su, *J. Phys. Chem. C*, 2008, **112**, 8617-8622.
56. A. F. Lee, J. J. Gee and H. J. Theyers, *Green Chem.*, 2000, **2**, 279-282.

## Chapter 4

# Reactivity of crotonaldehyde and propene over Au/Pd(111) surface alloys

### 4.1 Introduction

Previous work using temperature programmed XPS experiments has shown that in crotyl alcohol selox, crotonaldehyde decomposition and associated self-poisoning prevails over model Pd(111) surfaces<sup>1</sup>. In the previous chapter, identical experiments performed over Au/Pd(111) surface alloys, have shown that the formation of reactively formed by-products can be inhibited, depending upon the surface alloy composition. By introducing small amounts of Au into the Pd(111) surface and performing TPD experiments, it was shown that the desorption of the reactively formed aldehyde is promoted.

Despite this, questions remain regarding the role of alloyed Au, and its possible influence upon reactively formed crotonaldehyde. For instance, does it disrupt the undesired decarbonylation and/or dehydrogenation pathways operating over pure Pd, and if so, how? In chapter 1 (section 1.5.2), it was also shown that there is also a general dearth of knowledge regarding the surface chemistry of aldehydes over metal surfaces.

In this chapter, the influence of Au upon the chemistry of crotonaldehyde over Pd(111) surfaces will be examined. The chemistry of propene, the principal by-product expected from crotonaldehyde decomposition, will also be investigated over the same Au/Pd(111) surfaces. In addition, in order to better mimic true selox conditions, the role of pre-adsorbed oxygen on clean and Au-promoted Pd surfaces will also be explored.

## 4.2 Results and Discussion

### 4.2.1 Formation of Au/Pd(111) surface alloys

As detailed in chapter 2 (section 2.1.1) and chapter 3 (section 3.2.1), Au thin-films were prepared at room temperature using a Focus/Omicron EFM3 evaporator. For the work presented in this chapter, the surface coverage was first mapped out using AES after a given deposition time and was found to be uniform across the Pd(111) crystal. By annealing a 4 ML Au thin-film on Pd(111) to various temperatures for 1 minute, a surface  $X_{Au}$  was consistently obtained as summarised in **Table 4.1** below.

Annealing temperature / K	Surface Au mole fraction ( $X_{Au}$ )
473	0.92
573	0.90
673	0.80
773	0.56
873	0.30
973	0.15

**Table 4.1** – The surface Au mole fraction ( $X_{Au}$ ) resulting from annealing a 4 ML thin-film of Au on Pd(111) to various different temperatures.

For the series of TDS experiments involving Au/Pd(111) surface alloys in this chapter, the alloying temperature for the next alloy in the series defined the maximum TPD temperature.

## 4.2.2 Crotonaldehyde adsorption studies

The thermal chemistry of crotonaldehyde ( $\text{H}_3\text{C}-\text{CH}=\text{CH}-\text{CH}_2-\text{CHO}$ , CrCHO) was studied over clean Pd(111), a pure Au overlayer, and Au/Pd(111) surface alloys as a function of aldehyde exposure.

### 4.2.2.1 Adsorption of crotonaldehyde on Pd(111)

**Figure 4.1** shows the resulting TPD spectra for the parent species over Pd(111); corresponding integrated peak areas of the reversibly adsorbed aldehyde and all major desorption products are presented in the inset. Low aldehyde exposures ( $< 1$  L) result in decarbonylation to propene and carbon monoxide (omitted for clarity), and dehydrogenation, as previously reported by Medlin and co-workers.<sup>2</sup>

Higher exposures give rise to molecular crotonaldehyde desorption at  $\sim 140$  K and 155 K. The latter state rapidly saturates around 3 L and is attributed to desorption from the monolayer, while the low temperature aldehyde feature grows continuously and can be assigned to multilayers. The enthalpy of desorption from the aldehyde monolayer, estimated from the Redhead equation<sup>3</sup> (assuming first-order kinetics and a pre-exponential factor of  $\nu=10^{13} \text{ s}^{-1}$ ), was  $37.4 \text{ kJmol}^{-1}$ , very close to the enthalpy of vapourisation<sup>4</sup> indicating a weak surface interaction while that for the multilayer was  $33.7 \text{ kJmol}^{-1}$ .

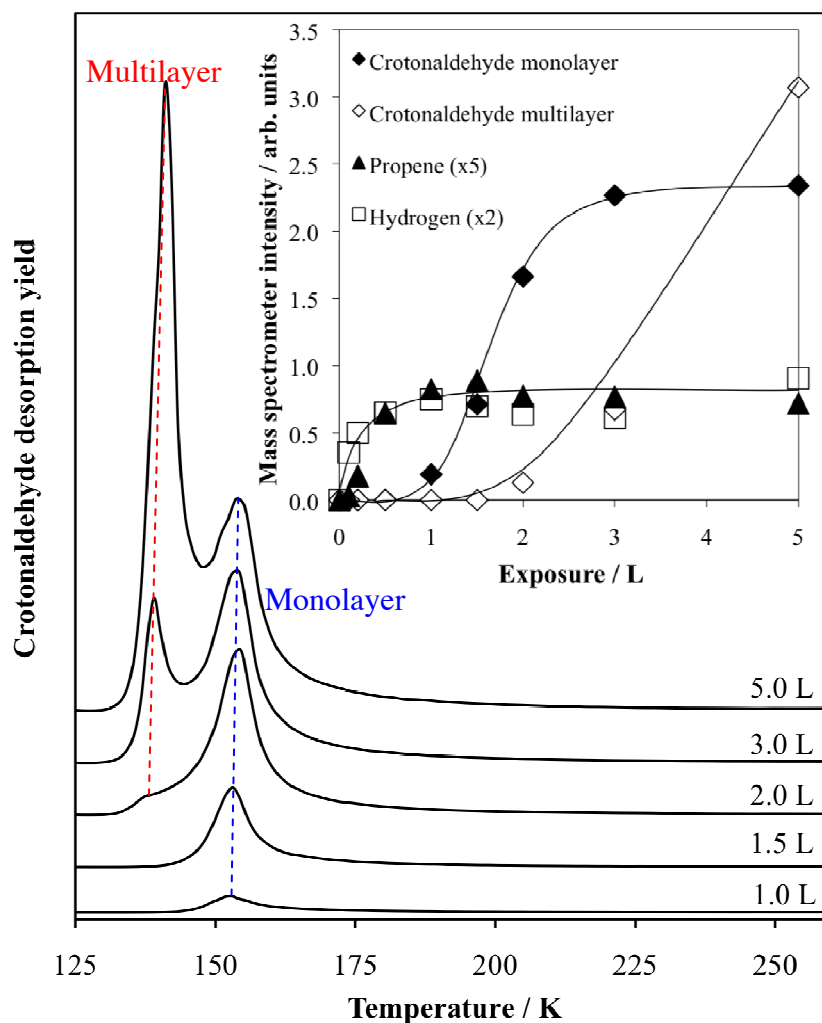


**Figure 4.1** - Thermal desorption mass spectra for the adsorption of crotonaldehyde at 120 K over a clean Pd(111) surface. Inset shows the fitted intensities of crotonaldehyde monolayer, multilayer and reactively formed propene as a function of exposure.

#### 4.2.2.2 Adsorption of crotonaldehyde over an unannealed 4 ML Au film on Pd(111)

**Figure 4.2** shows thermal desorption spectra for the continuous uptake of crotonaldehyde over a relatively thick (4 ML) Au film on Pd(111). Over this unannealed Au adlayer, crotonaldehyde simply reversibly chemisorbs, with the monolayer saturating by 1 L. The monolayer state desorbs at approximately 180 K, a higher temperature than that from clean Pd(111). This is surprising, as one would expect that from an inert surface the desorption temperature would be

lower than that of a more reactive surface. The origin of this stronger adsorption is unclear, however similar stabilisation is observed for prenal (3-methyl-2-butenal), a related unsaturated aldehyde, over analogous surfaces of ‘inert’ Sn alloyed with noble Pt(111) relative to clean Pt.<sup>5</sup>

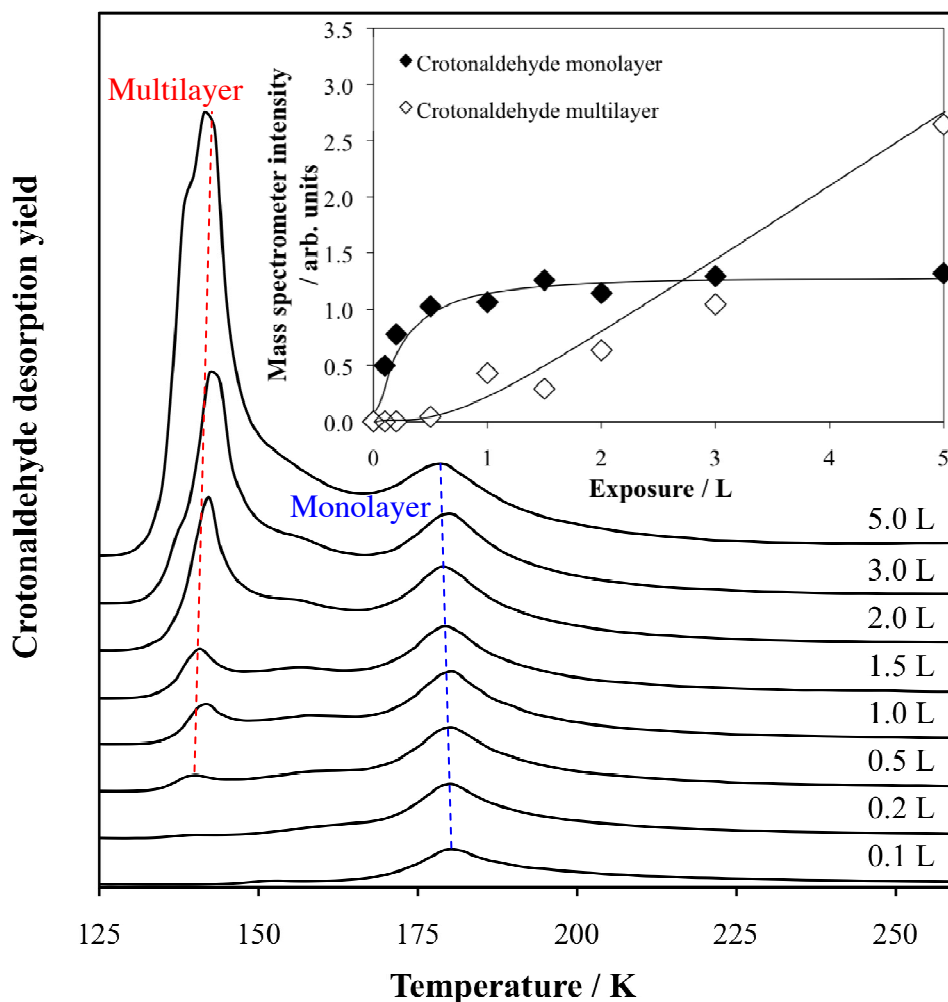


**Figure 4.2** - Thermal desorption mass spectra for the adsorption of crotonaldehyde at 120 K over a thick (~ 4 ML) Au adlayer on Pd(111). Inset shows the fitted intensities of the crotonaldehyde monolayer and multilayer states as a function of exposure.

One possible explanation for this higher temperature could be that the aldehyde forms a polymer over the Au surface resulting in a higher desorption temperature relative to Pd. Despite no prior studies of crotonaldehyde adsorption over pure Au(111), other aldehydes undergo similar polymerisation processes on surfaces, such as formaldehyde on Cu(100)<sup>6</sup> and (110)<sup>7</sup>, as well as acetaldehyde on Rh(111)<sup>8</sup> and Pt(111)<sup>9</sup>. The enthalpy of desorption was also

calculated by the Redhead equation<sup>3</sup> and was determined to be 43.7 kJmol<sup>-1</sup>. Once the monolayer saturates, physisorption occurs with multilayer desorption occurs at 142 K; essentially the same temperature as that for clean Pd(111). No reaction products are observed over the un-annealed Au surface.

#### **4.2.2.3 Adsorption of crotonaldehyde on Au/Pd(111) surface alloys**

The thermal chemistry of crotonaldehyde over several Au/Pd(111) surface alloys was investigated. **Figure 4.3** shows over-layed TPD spectra for a surface alloy with a Au mole fraction of 0.56 (determined by AES) and also for a clean Pd(111) surface. The same species desorb from both surfaces; propene and CO at similar temperatures (~320 K and 455 K respectively). For clean Pd(111), three hydrogen states are observed, the first is at 320 K, which is attributed to background hydrogen. A second and third peak desorb at ~ 400 K and 465 K. In the case of Pd(111), the same desorption temperatures have been observed in a previous study<sup>2</sup>. Over the un-annealed Au film the hydrogen desorbs at the higher temperatures of ~ 415 and 515 K.

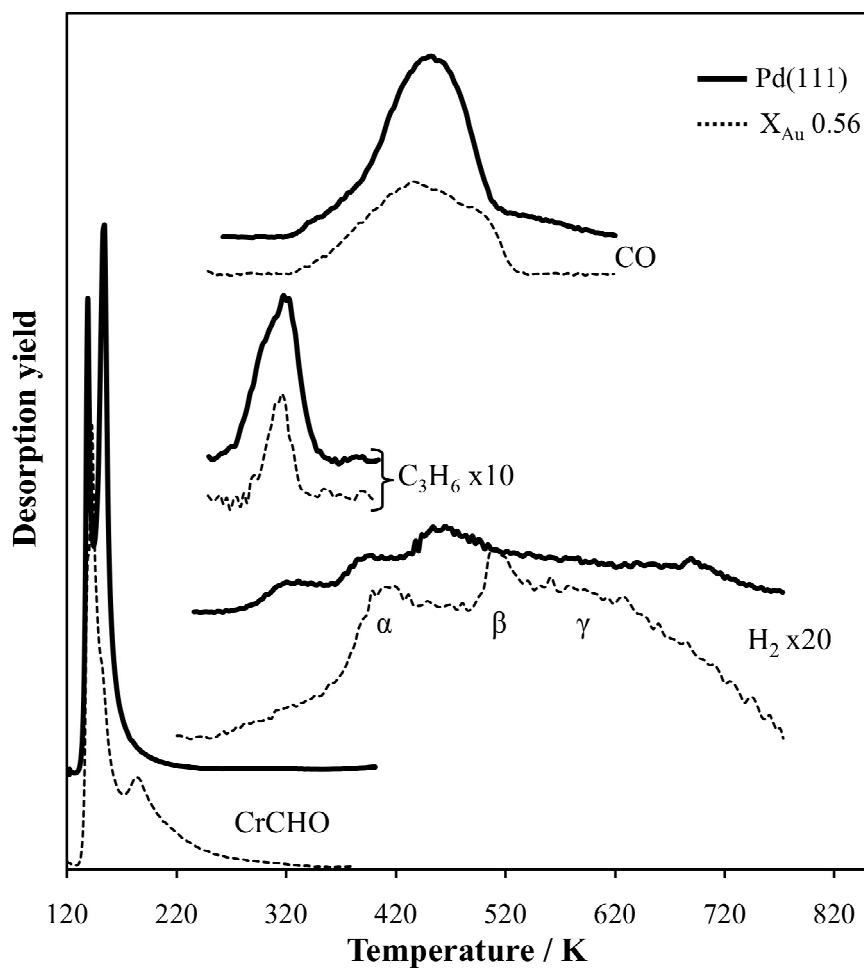


**Figure 4.3** - Thermal desorption mass spectra of 3 L crotonaldehyde adsorbed on Pd(111) and an Au/Pd(111) surface alloy (4 ML Au film annealed to 773 K, AES Au mole fraction of 0.56) at 120 K.

For both Au and Pd, the higher temperature desorption of hydrogen is of particular interest as such peaks are usually associated with the decomposition of hydrocarbons strongly bound to the metal surface.

The key observation is that the level of decomposition to propene and carbon monoxide over the  $X_{\text{Au}} 0.56$  Au/Pd(111) alloy is much lower relative to clean Pd(111). As a result of this discovery, a more detailed study of the effect of Au on the decomposition of crotonaldehyde to propene and carbon monoxide over Pd(111) was conducted.

#### 4.2.2.4 Decomposition of crotonaldehyde to propene on Au/Pd(111) surfaces

The influence of Au on desorption of reactively formed propene (due to the decomposition of crotonaldehyde) for various surface Au mole fractions ( $X_{\text{Au}}$ ) was studied. Unfortunately, reactively formed carbon monoxide could not be measured easily due to a large background contribution. **Figure 4.4** shows the  $m/z$  41 trace for several of these alloy surfaces along with the mass spectrometer intensity as a function of Au mole fraction. All surfaces were treated with the same saturation exposure of crotonaldehyde (3 L). For surfaces rich in Pd ( $X_{\text{Au}} \leq 0.56$ ) propene desorbs from the surface, indicative of aldehyde decomposition.

Conversely, propene does not desorb from surface alloys rich in Au ( $X_{\text{Au}} \geq 0.80$ ), meaning that such surfaces are essentially unable to drive decomposition chemistry. This clearly shows that Au improves the selectivity for the select of crotyl alcohol by inhibiting the decomposition of the aldehyde product. Alloy composition is crucial; determining the level of decomposition over such surfaces, and therefore the overall aldehyde reaction pathway.

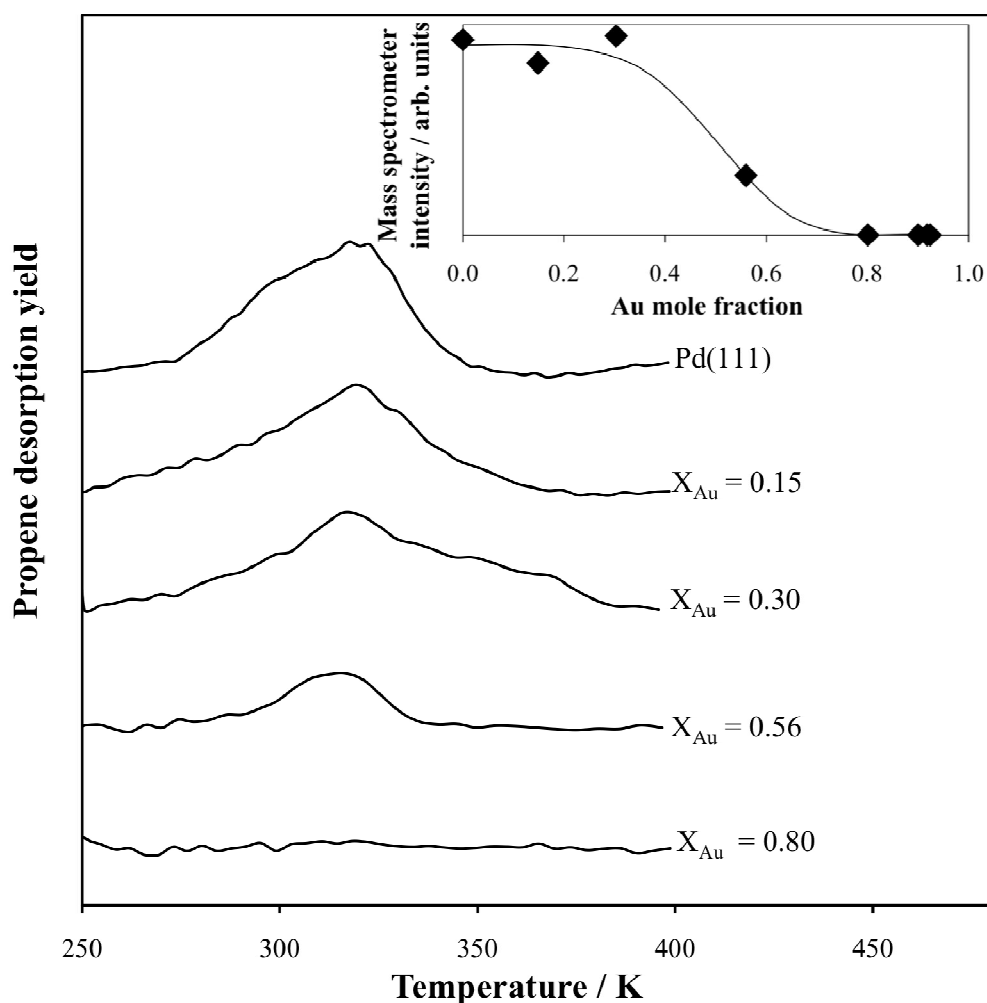


**Figure 4.4** - Thermal desorption mass spectra for the formation of propene from the adsorption of crotonaldehyde (3 L) at 120 K over Au/Pd(111) surface alloys. Inset shows the fitted intensities of propene as a function of surface Au mole fraction ( $X_{Au}$ ).

### 4.2.3 Propene adsorption

#### 4.2.3.1 Adsorption of propene on Pd(111)

The thermal chemistry of propene; a product of crotonaldehyde decomposition, was studied over Pd(111) in order to benchmark the reactivity. **Figure 4.5** shows the uptake of propene on the clean Pd(111) surface. From the inset graph we see that for low exposures propene dehydrogenates to form hydrogen and surface carbon. As stated previously (when describing **Figure 4.3**), the hydrogen of interest

is that formed at high temperature, which results from hydrocarbon decomposition. This higher temperature hydrogen state saturates around 1.5 L.

The amount of hydrogen that desorbs relative to propene is low, and has therefore been scaled by a factor of 40. This small hydrogen yield is consistent with Land's work, which showed that propene desorption is favoured over decomposition, as no more than 10% of the chemisorbed propene dehydrogenates to produce surface bound carbon<sup>10</sup>. The monolayer state desorbs at  $\sim 280$  K, which shifts to a lower temperature of  $\sim 260$  K with increasing exposure, saturating at 2 L. The multilayer state desorbs between 180 and 170 K, again depending upon exposure. Both the monolayer and multilayer desorption temperatures are consistent with literature<sup>10</sup>.

Tysoe's group carried out a TPD and RAIRS study on the low temperature adsorption of propene on Pd(111)<sup>11</sup>. At low coverages they observed a state centred at  $\sim 210$  K, which shifts to 195 K with increasing exposure. They determined that this was a result of a 'V-shaped' adsorption state that is not favoured at high coverage where the methyl group aligns perpendicular to the surface. This conclusion was made as a result of a similar trend observed for propene adsorption on Pt(111)<sup>12</sup>. As we are concerned with the chemistry at saturation coverages, we do not need to take this state into account.

For higher coverages, TPD spectra are similar to those reported in this work (propene desorbing molecularly at  $\sim 200$  and 280 K). However, they determine that propene adsorbs onto several adsorption sites, which contribute to the monolayer state. They show that at low temperature, propene binds in a di- $\sigma$  coordination on the clean Pd(111) surface. Upon heating, a small portion of this desorbs at  $\sim 200$  K and the remainder is converted to a stronger bound di- $\sigma$  state with the methyl group bound parallel to the surface, which eventually desorbs at  $\sim 280$ K.

Further heating forms an allylic species, of which a small proportion rehydrogenates at  $\sim 340$  K, but the majority dehydrogenates at  $\sim 360$  K. A second layer is found to desorb at about 190 K, which we will not discuss in this work, as we are only concerned with the chemistry of propene on Au/Pd(111) surfaces and surface alloys.

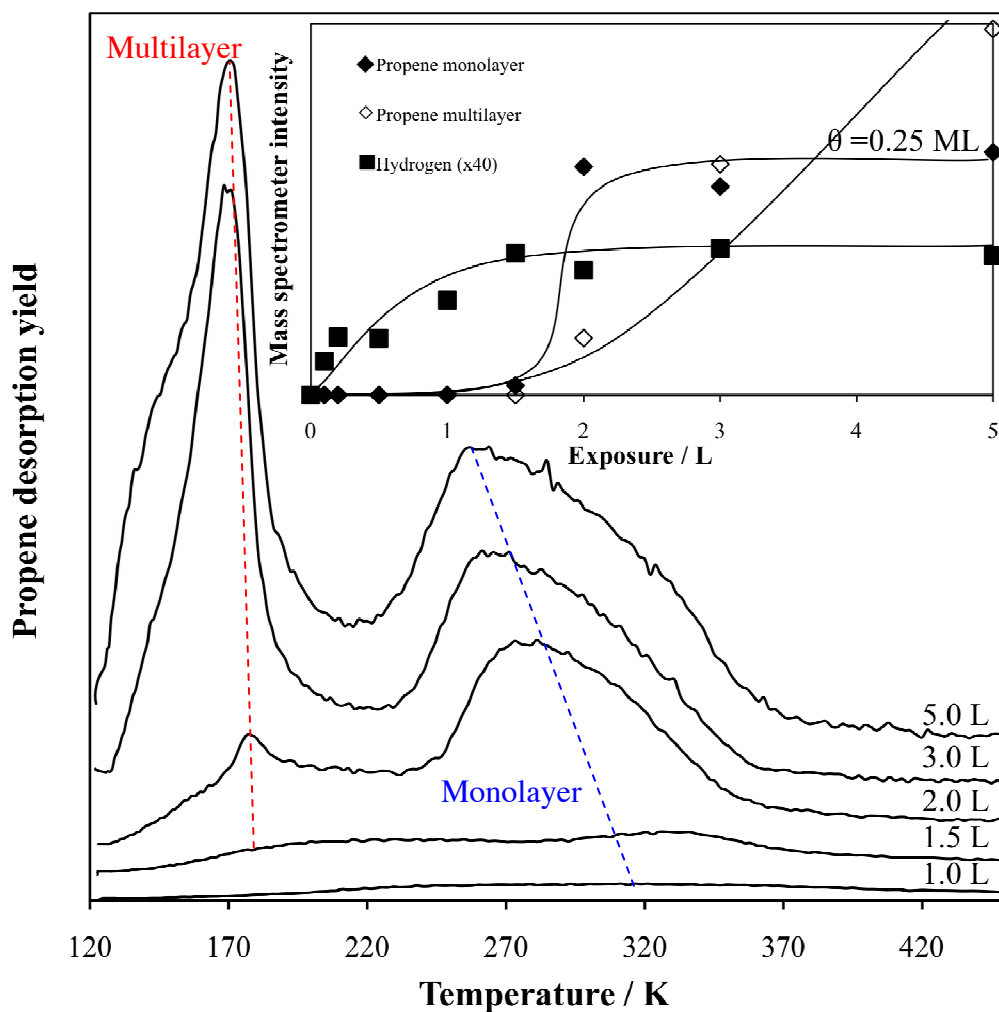


**Figure 4.5** - Thermal desorption spectra for propene over a clean Pd(111) surface.

Inset shows the fitted intensities for the propene monolayer, multilayer and reactively formed hydrogen as a function of exposure. Saturation coverage,  $\theta$ , (0.25 ML) is assumed to be identical to that of ethylene over both Pt(111)<sup>13</sup> and Pd(110)<sup>14</sup>.

In this section, we have replicated previous studies of propene adsorption on Pd(111). It has been demonstrated that the desorption temperatures and reactivity of propene are consistent with previous work. The desorption of propene is favoured over decomposition, as very little hydrogen desorbs, even for high exposures. With the chemistry of propene over Pd(111) determined, we can now focus on the adsorption over a Au film on Pd(111).

#### 4.2.3.2 Adsorption of propene on 4 ML Au on Pd(111)

The uptake of propene over a 4 ML thin-film of Au on Pd(111) is shown in **Figure 4.6**, which demonstrates that essentially no decomposition occurs, with propene simply desorbing molecularly from the surface. For low exposures, a single desorption peak is observed at  $\sim 135$  K. Previous work carried out by Goodman on propene adsorption on Au(111)<sup>15</sup>, indicates that the propene monolayer desorbs either at 145 or 150 K, dependant upon exposure. The difference in desorption temperature observed in this work is probably due to different heating rates ( $\sim 4$  Ks<sup>-1</sup> for Goodman,  $\sim 10$  Ks<sup>-1</sup> in this study) and a rougher surface. Although Au deposits epitaxially on Pd(111) at room temperature<sup>16</sup>, such surfaces will have a higher proportion of step and kinks relative to the single crystal case, hence the slight difference in desorption temperature.

At high exposure, Goodman determined that the multilayer state was found to desorb at  $\sim 120$  K. In this study, propene was dosed at  $\sim 120$  K, which was the lowest achievable temperature on the York UHV system. As a result, no multilayer state was observed from the un-annealed Au overlayer. In this study, for exposures above 2 L, two additional states can be seen, which are thought to arise from exposed Pd sites. A monolayer state desorbs at  $\sim 280$  K, saturating around 2 L. Whilst this saturation exposure is very similar to that of the clean Pd(111) surface, this shift could be a result of the difference in saturation exposure, as it is known that the monolayer peak for the Pd(111) surface shifts in temperature depending upon the exposure. A multilayer state is also observed at  $\sim 175$  K. The integrated areas for the Pd states are displayed in the inset of **Figure 4.6**. The Au monolayer state has been omitted from the inset for clarity.

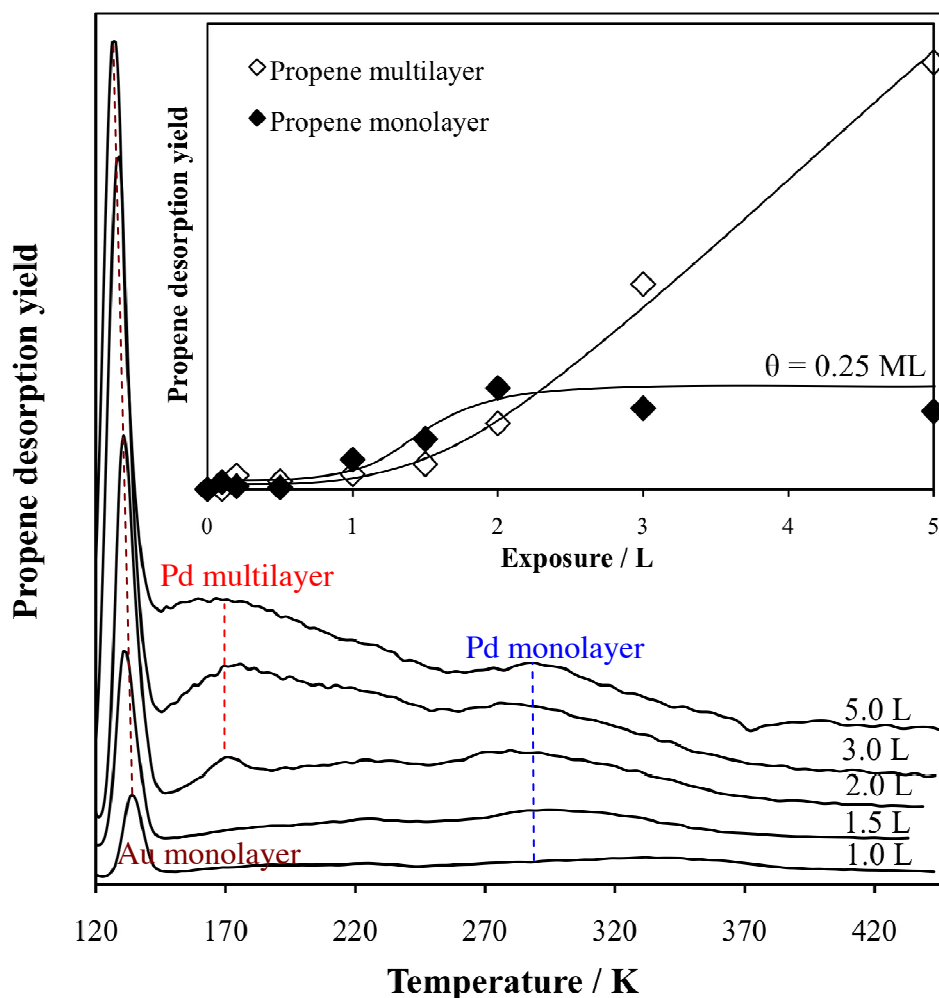


**Figure 4.6** - Thermal desorption mass spectra for the adsorption propene at over a 4 ML Au adlayer on Pd(111). Inset shows the fitted intensities for the propene monolayer and multilayer as a function of exposure. Saturation coverage (0.25 ML) is assumed to be identical to that of ethylene over both Pt(111)<sup>13</sup> and Pd(110)<sup>14</sup>.

We have shown over this Au film that propene simply desorbs molecularly with no chemistry occurring. There are a variety of different desorption temperatures to consider, which can be attributed to perturbed Au and Pd. With the uptake over the Au film complete, we can therefore move onto the chemistry of propene over Au/Pd(111) surface alloys.

#### 4.2.3.3 Adsorption of propene on Au/Pd(111) surface alloys

The adsorption of ethene has been studied on various Au/Pd(111) alloy surfaces by TPD and RAIRS recently by Tysoe<sup>17</sup>. For alloys with Au coverages greater than 0.7, they found that ethene adsorbs mostly on Au sites desorbing with an activation energy of less than 55 kJ mol<sup>-1</sup>. For coverages between 0.5 - 0.7 Au they detected  $\pi$ -bonded ethene on Pd sites, which desorbs with an activation energy between 57 and 62 kJ mol<sup>-1</sup>. Reducing the Au coverage further results in a linear increase in activation energy until it reaches 76 kJ mol<sup>-1</sup>, the value for pure Pd(111). Whilst this is a slightly different molecule, it highlights the fact that alkenes bind more weakly to Au rich surfaces.

When the 4 ML Au film (section 4.1.3.2) was annealed to 773 K, a surface alloy with a Au mole fraction of 0.56 was created (identical to the surface formed in **Figure 4.3**). 3 L propene was dosed into the chamber, and the desorption products were stacked with those observed for clean Pd(111) and are presented in **Figure 4.7**. In both cases propene and hydrogen desorb from both surfaces at similar temperatures. As previously stated, for Pd the propene monolayer desorbs at a temperature of  $\sim 270$  K and the multilayer at  $\sim 170$  K. In the case of the Au/Pd alloy there is also an additional propene state at  $\sim 135$  K, which is attributed to propene monolayer desorption from Au sites.

There is a small apparent shift of these values for the Au alloy, where the monolayer desorbs at both  $\sim 270$  and 320 K, however, it is thought these peaks are as a result of the desorption of a di- $\sigma$  bonded state and then a  $\pi$ -bonded state as revealed by Tysoe<sup>11</sup>. It is possible that this apparent shift is due to the greater population of  $\pi$ -bonded states as ethene adsorbs onto Au sites exclusively in a  $\pi$ -bonded state<sup>17</sup>. There does appear to be a small genuine shift of the monolayer state by approximately 10 K. The hydrogen which desorbs from the Pd(111) desorbs in two states at  $\sim 350$  and 485 K which as explained earlier has been recorded elsewhere<sup>10, 11</sup>. For the Au alloy, this desorption is shifted by approximately 10 K, but are thought to be essentially analogous.

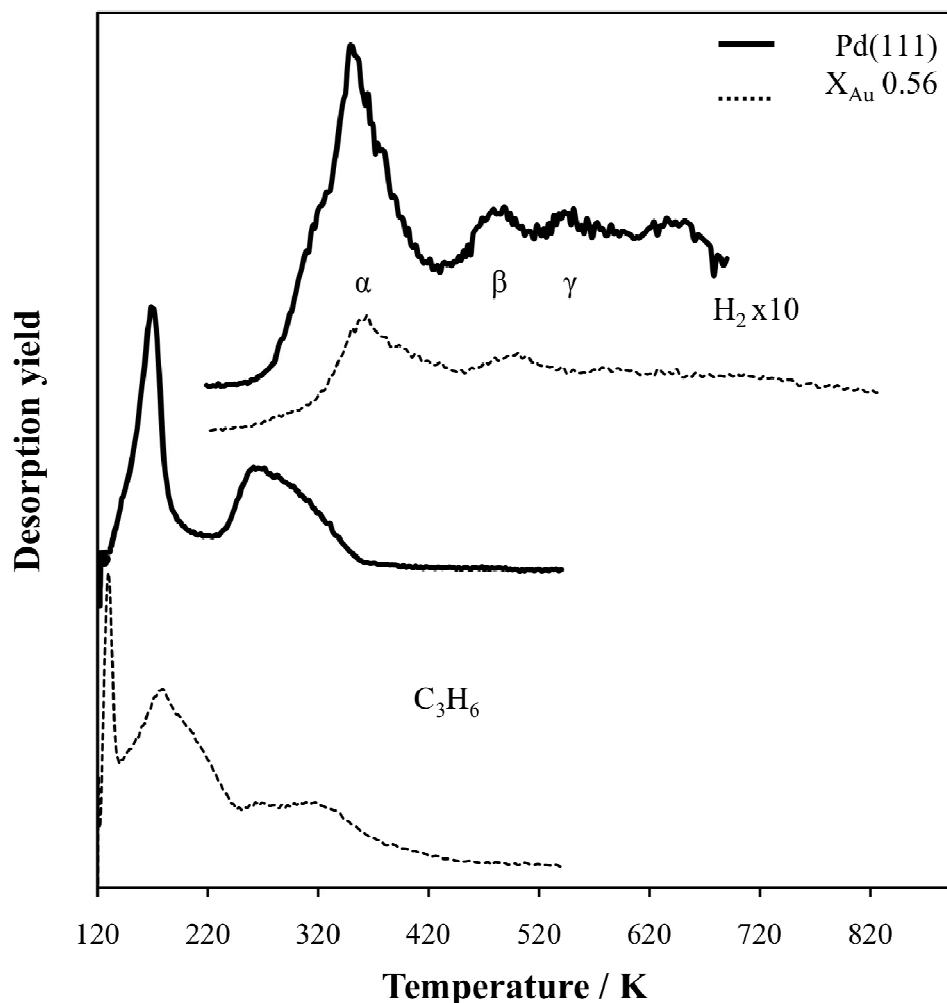


**Figure 4.7** - Thermal desorption mass spectra of a 3 L exposure of propene adsorbed on Pd(111) and an Au/Pd(111) surface alloy (AES Au mole fraction of 0.56) at 120 K.

Propene adsorption was carried out over a full range of alloys, and the thermal desorption mass spectra for these surfaces is shown in **Figure 4.8**. The inset shows that the amount of hydrogen that desorbs remains constant for Au mole fractions less than 0.8. As with crotonaldehyde chemistry (see section 4.1.2.2), this demonstrates that Au rich surfaces are unable to drive decomposition chemistry. The trend for hydrogen desorption tracks well with the amount of chemisorbed propene, which desorbs from the surface. This is consistent with the concentration of Au influencing the adsorption of propene, with less propene sticking on Au rich surface alloys.

For surfaces which have Au mole fractions greater than 0.8, the amount of hydrogen which desorbs is significantly lower than that observed for more Pd rich surface alloys. Although propene decomposition is minor over Pd alloy surfaces because most of the propene desorbs intact, Au/Pd alloys are able to turn off this reaction pathway. This is a remarkable result, as Au not only aids desorption of reactively formed crotonaldehyde from the selective oxidation of crotyl alcohol<sup>18</sup>, it also inhibits the decomposition of both crotonaldehyde and propene, thereby enhancing catalytic selectivity.

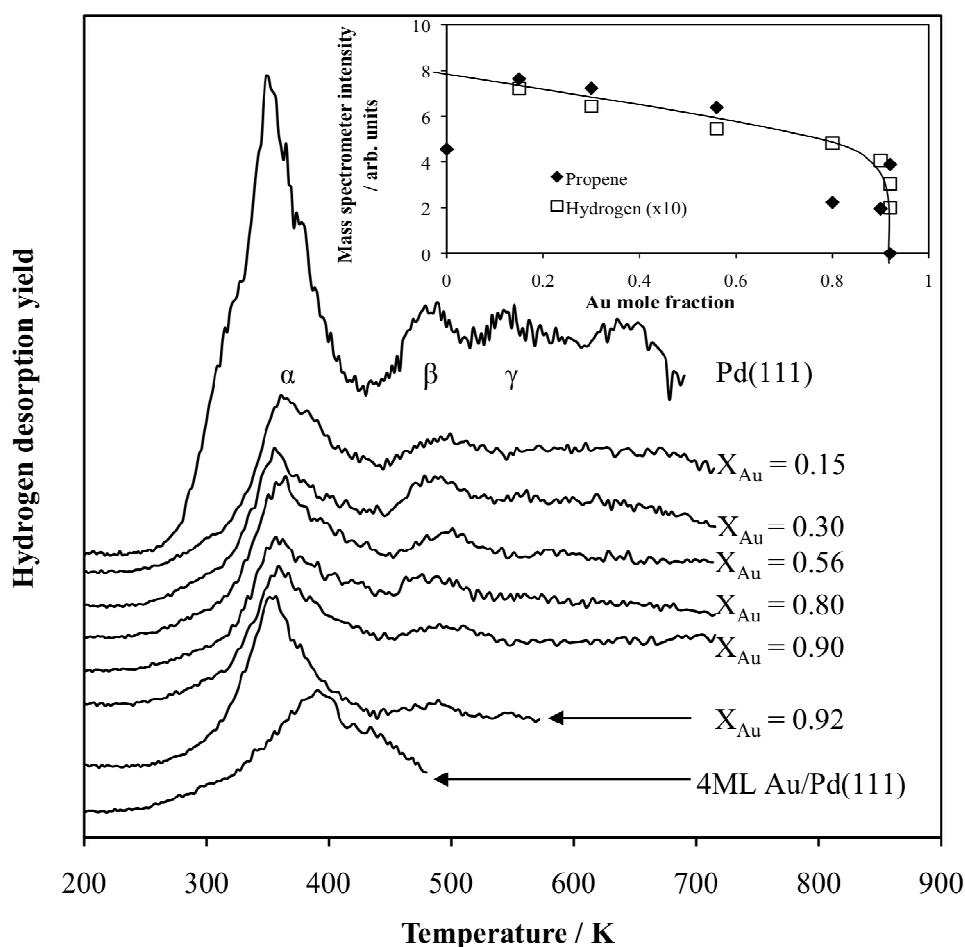


**Figure 4.8** - TPD series of evolved hydrogen from the adsorption of propene over Au/Pd(111) surface alloys. Inset shows the integrated hydrogen area resulting from methyl fragments (485 K peak). Also plotted is the propene peak area for comparison.

In this section, we have observed that the level of propene decomposition is related to the amount of Au in the surface. The Au moderates this reaction, with surface

Au mole fractions greater than 0.8 being sufficient to suppress the reaction completely.

#### **4.2.4 The effect of co-adsorbed O**

In an attempt to replicate aerobic selective oxidation over model surfaces in more 'realistic' conditions, adsorbates were dosed after such surfaces were pre-covered with O. This was achieved by exposing surfaces to ~ 60 L of O<sub>2</sub> whilst cooling to 120 K. Once this temperature was achieved, the oxygen leak valve was closed off and the desired adsorbate dosed the UHV chamber in the normal way. In surface alloys, the metal that forms the stronger bonds with a given adsorbate often will segregate to the surface. It should be noted that at high temperatures, it is known that adsorbing O onto Au/Pd surface alloys can artificially enrich the top layers with Pd<sup>19, 20</sup>. In order to avoid driving Pd into the surface and changing the surface alloy composition, O was only released into the UHV chamber when the substrate was at room temperature or lower. In order to confirm that the alloy composition remained constant, AES measurements were carried out both before and after oxygen adsorption.

##### **4.2.4.1 Adsorption of crotonaldehyde on O pre-covered Au/Pd(111) surfaces**

Thermal desorption spectra were recorded over a Pd(111) surface and a Au/Pd(111) surface alloy ( $X_{Au} = 0.56$ ), which are both shown in **Figure 4.9**. The spectrum for Pd(111) shows that both CO<sub>2</sub> and CO desorb at ~ 390 and 450 K respectively, a trend which is not observed on the clean surface and is obviously indicative of combustion. In addition, water also desorbs from the surface with a peak maxima at ~ 280 K.

Decomposition still occurs, as a small amount of propene desorbs from the surface at the characteristic temperature of ~ 320 K. Over the surface containing Au, no decomposition occurs, in direct contrast to the same oxygen free surface. From the TPR data, it is possible that a small amount of combustion occurs over the alloy

surface, but if so, it can be regarded as minor reaction pathway, as the amount that desorbs is close to the limit of detection for the mass spectrometer. Clearly, O co-adsorption over Au/Pd alloy surfaces inhibits decomposition of the aldehyde to a higher degree when compared to O free alloys.

In order to examine the relationship between the alloy composition and decomposition, the level of decomposition was investigated over several O covered alloy surfaces, the results of which are shown in **Figure 4.10**. Propene desorbs exclusively from highly Pd rich alloy surfaces (between  $X_{Au}$  of 0 and 0.15), for surfaces equal to or less than Au mole fractions of 0.3 no propene desorbs. The trend for carbon dioxide mirrors that for propene as evidenced from the inset graph. Without  $O_{(ads)}$ , propene desorbs from surfaces with a Au mole fraction greater than 0.8. In addition to this, the amount of propene that desorbs over O covered alloy surfaces is much less when compared to O free alloys.

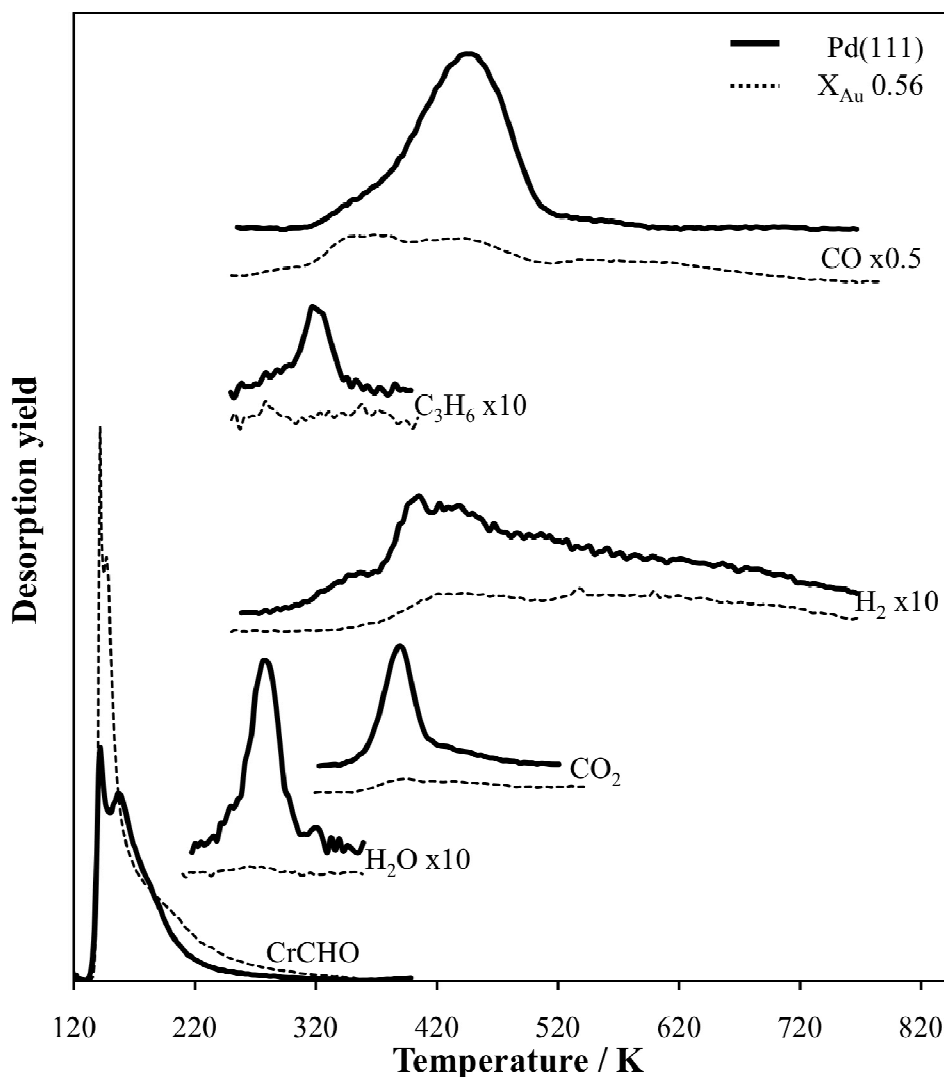


**Figure 4.9** - Thermal desorption mass spectrum of 3 L crotonaldehyde adsorbed on an O pre-covered (60 L O<sub>2</sub>) Pd(111) and Au/Pd(111) surface alloy (AES Au mole fraction of 0.56) at 120 K.

When we compare the inset graphs of **Figures 4.10 and 4.4**, the propene which desorbs from the O covered surface is only 15% of the total amount of propene which desorbs from the oxygen free Pd(111). The effect is more dramatic when we compare surfaces with a Au mole fraction of 0.15. For these alloy surfaces, ~ 10 % of the amount of propene desorbs from the O covered alloy when directly compared to the O free surface. There are two possible scenarios that explain this phenomenon. The propene formed from the adsorption of crotonaldehyde either undergoes combustion, or alternatively for Au alloy surfaces pre-saturated with an exposure of O<sub>2</sub>, desorption of crotonaldehyde is favoured, thereby meaning that it

is unable to decompose in the first place. However, it is possible that Au suppresses both the decomposition and combustion pathway to some extent, with desorption being the dominant process.

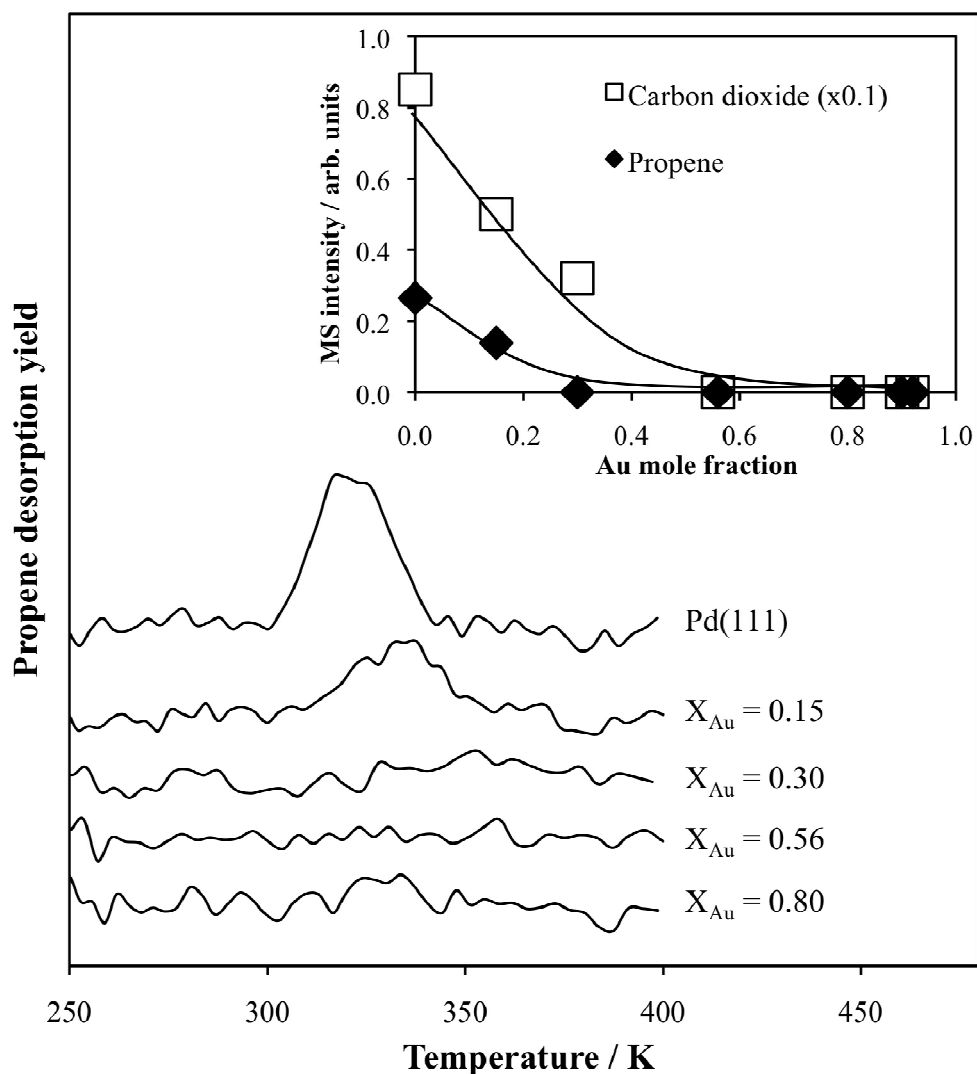


**Figure 4.10** - Series of thermal desorption mass spectra for the formation of propene from the adsorption of crotonaldehyde (3 L) at 120 K over oxygen pre-covered (60 L O<sub>2</sub>) Au/Pd(111) surface alloys. Inset shows the fitted intensities of propene as a function of surface Au mole fraction.

#### 4.2.4.2 Adsorption of propene on O pre-covered Au/Pd(111) surface alloys

The effect of O on the chemistry of propene over Au/Pd(111) alloys was examined. As for crotonaldehyde and O, surfaces were pre-covered by dosing 60 L O<sub>2</sub> whilst cooling from room temperature to 120 K prior to propene adsorption. In a series of trial experiments, alloy surfaces were examined by AES before and after O adsorption in order to ensure that composition the surface alloy remained constant. **Figure 4.11** shows TPR spectra for pure Pd(111) and an Au/Pd(111) surface alloy with a Au mole fraction of 0.56. As with the O free surfaces both hydrogen and propene desorb from Pd(111). The hydrogen desorbs at exactly the same temperatures as for the clean Pd(111) surface (~ 360 and 500 K), although less hydrogen desorbs from the 360 K state, evident from the ratio of the 360 and 500 K peaks.

In the case of Pd, two states are observed for desorption of the propene monolayer at ~ 280 and 360 K, which are essentially identical to the desorption temperatures recorded over the clean surface. These states are also observed for the Au/Pd alloy, although an additional state is also observed at ~ 135 K which is attributed to desorption of the propene monolayer from Au sites. However, the 360 K peak is more prominent over the O covered surface, which is attributed to the greater population of propene bound in the  $\pi$ -bonded adsorption state. The multilayer desorbs at ~190 K, which also is very similar over the O free surface. Both the same hydrogen and propene states are observed over the Au/Pd(111) alloy surface.

Unlike the oxygen free surface, combustion occurs over Pd(111), as both CO and CO<sub>2</sub> are evolved. In the case of Pd(111) CO desorbs in a single state at ~ 460 K, which is identical to that which desorbs as a result of crotonaldehyde adsorption over clean Pd(111) (**Figure 4.3**). CO<sub>2</sub> desorbs in two states at ~ 300 and 350 K. Water also desorbs from Pd(111) at ~ 310 K with a second peak maxima at ~ 360 K. Madix conducted a TPRS study of both alkene and arene combustion over Pd(111) in the late 1990s<sup>21</sup>, finding for propene adsorption over a 0.25 ML surface that the same products desorb as found in this study. Similar peak shapes and the evolution of the same number of states were also obtained, although desorption temperatures differed by as much as 50 K to those found in this study as well as

those for propene adsorption on clean Pd(111) mentioned earlier by Land<sup>10</sup> and Tysoe<sup>11</sup>. However, Goodman shows that the desorption temperature of propene can vary greatly depending upon the oxygen coverage<sup>15</sup>.

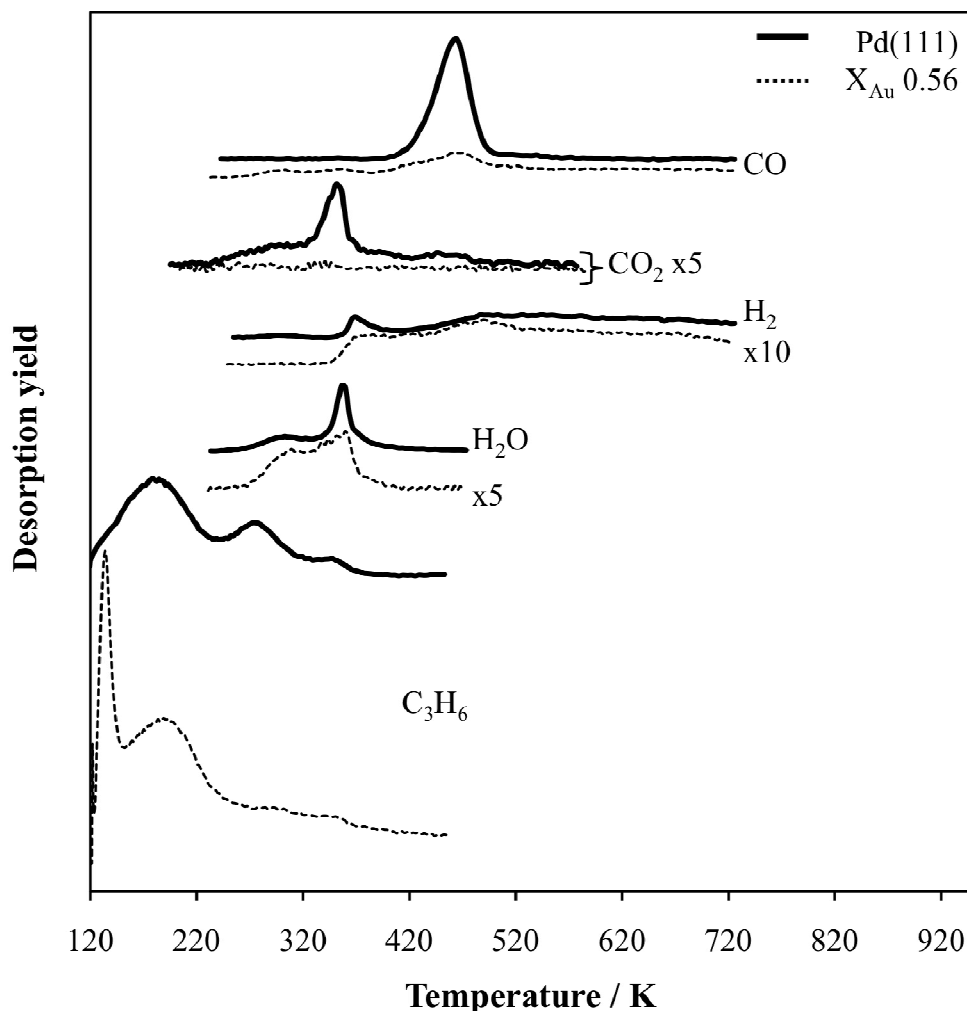


**Figure 4.11** - Thermal desorption mass spectrum of 3 L propene adsorbed on an oxygen pre-covered (60 L O<sub>2</sub>) Pd(111) surface, and an oxygen pre-covered Au/Pd(111) surface alloy (AES Au mole fraction of 0.56) at 120 K.

The same desorption states obtained for Pd(111) are mirrored for the species which desorb from the 0.56  $X_{Au}$  alloy surface. However the amount of each product which desorbs is significant lower when compared to Pd(111). This indicates that both decomposition and combustion processes are hindered by surfaces containing Au. It is thought that perhaps a small amount of combustion occurs, due to very small CO and CO<sub>2</sub> desorption peaks, but it is tenuous as to whether this is genuine,

as the amounts are close to the limit of detection for the mass spectrometer. Clearly desorption is favoured over decomposition and combustion processes over this particular alloy surface.

The adsorption of propene over a full range of oxygen pre-covered Au/Pd(111) alloys was then investigated by TPRS. The spectra for hydrogen evolved over these alloys, along with an inset displaying the mass spectrometer intensity for both hydrogen and propene, which are shown in **Figure 4.12**. A major difference is observed in terms of the ratio of hydrogen desorption states. For the clean surfaces (**Figure 4.8**), the intensity of the hydrogen desorption at  $\sim 360$  K is much larger than that observed for surfaces pre-covered with O. The state at  $\sim 485$  K remains unaffected, as from the inset figure it is clear to see that the same arbitrary intensity is observed ( $\sim 4 \times 10^{-6}$  to  $2 \times 10^{-6}$ ) in both cases. Au turns off this decomposition pathway for Au mole fractions greater than 0.8. This means that the decomposition of the propene to hydrogen is unaffected by the pre-adsorption of O, as the same general trend is observed. As with the oxygen free alloy surfaces, the hydrogen trend tracks well with that for the desorption of the propene monolayer, possibly indicating that the concentration of Au influences the adsorption of propene, with less propene sticking on Au rich surface alloys.

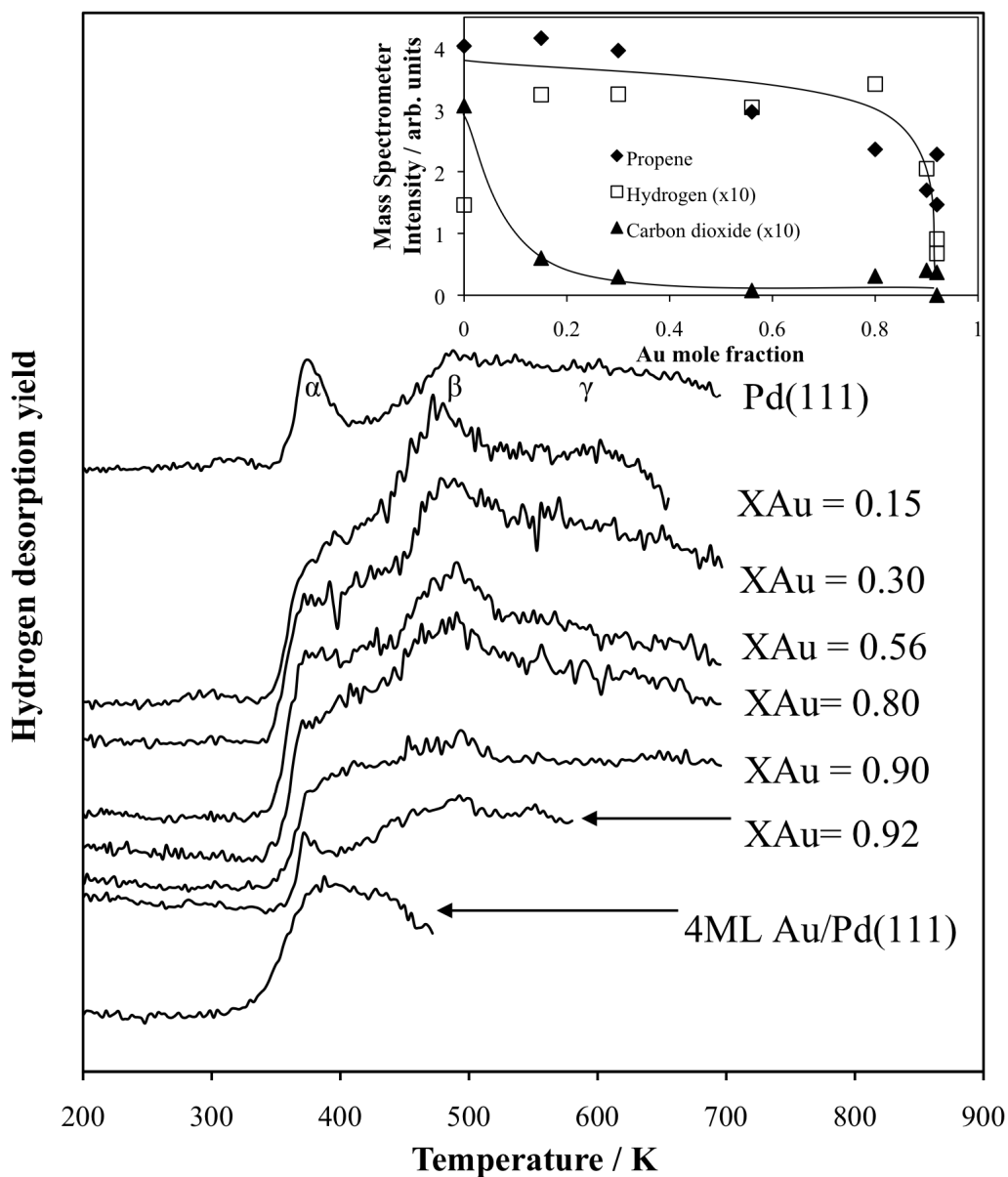


**Figure 4.12** - TPD series of evolved hydrogen from the adsorption of propene over O pre-covered (60 L O<sub>2</sub>) Au/Pd(111) surface alloys. Inset shows the integrated hydrogen area resulting from methyl fragments (485 K peak). Also plotted is the propene peak area for comparison.

It is known that propene adsorption is weak on Au(111) (literature,<sup>15</sup>  $\sim 39.3$  kJ mol<sup>-1</sup>) compared to Ag(110) (lit,<sup>22</sup> 45.1 – 52.7 kJ mol<sup>-1</sup>) and Pd(111) (literature,<sup>10</sup>  $\sim 79.4$  kJ mol<sup>-1</sup>). This difference in the adsorption enthalpy plays a major role in desorption of propene, therefore affecting decomposition. Goodman found that over oxygen covered Au(111) surfaces combustion is favoured over decomposition<sup>15</sup>, due to propene binding more tightly to O covered Au(111)

surfaces compared to the bare surface. Findings presented in this study also show the same trend, as the enthalpy of desorption oxygen covered Au/Pd(111) increases by  $\sim 9.4 \text{ kJ mol}^{-1}$  compared to the oxygen free surface. The enthalpy of propene desorption over the Pd(111) surface also increases when O is co-adsorbed, although the magnitude of this change is  $\sim 5.1 \text{ kJ mol}^{-1}$ .

#### 4.2.5 The effect of Au and O<sub>2</sub> on crotyl alcohol selox

The percentage of chemisorbed adsorbate (crotonaldehyde or propene) which underwent reaction (i.e. decomposition and/or combustion); essentially a measure equivalent to selox selectivity, was calculated by using **Equation 4.1**.

$$\% \text{ reacted adsorbate} = 100 - \left( \frac{\text{monolayer} \times 100\%}{\text{monolayer} + \text{desorption products}} \right) \quad \text{Equation 4.1}$$

Where ‘% reacted adsorbate’ is the amount of adsorbate which undergoes decomposition and/or combustion, ‘monolayer’ is the integrated MS area of the adsorbate monolayer (either crotonaldehyde or propene) and ‘desorption products’ are the integrated MS areas of all the reactively formed products.

Values were sensitivity corrected by dosing each species into the background at several pressures ( $1 \times 10^{-9}$ ,  $1 \times 10^{-8}$  and  $5 \times 10^{-8}$  Torr) and measuring the mass spectrometer intensity at each pressure. This was then divided by the same intensity for the adsorbate of interest in order to obtain a correction ratio. Each MS intensity used in **Equation 4.1** was therefore multiplied by this corresponding correction factor in order to correct for the sensitivity of the spectrometer to different masses.

The percentage of reacted adsorbate was plotted both with and without co-adsorbed oxygen for a range of Au/Pd(111) alloy surfaces (**Figure 4.13**). It is worth restating that O was only dosed into the chamber whilst cooling the substrate from room temperature to 120 K, prior to dosing the desired adsorbate. In addition to this, AES was used to monitor the surface alloy composition to ensure that it did not change as a result of introducing oxygen. For crotonaldehyde, the greatest amount of decomposition occurs over surfaces rich in Pd, where  $\sim 25 \%$  of the chemisorbed aldehyde decomposes. The amount that decomposes gradually decreases with

increasing Au content, sharply dropping off to 0 % for a pure Au surface. The same general trend is also observed for crotonaldehyde and co-adsorbed O, except the amount of reacted crotonaldehyde decreases by around a third. This indicates that Au with O further improves the selectivity for the selox of crotyl alcohol, as both aid desorption of the aldehyde.

For propene on Au/Pd(111) alloys, as the surface Au concentration increases, the level of dehydrogenation remains relatively constant, at around 15 - 12 %. A large concentration of Au is needed to affect the dehydrogenation pathway ( $X_{Au} \geq 0.8$ ). In the case of propene and oxygen adsorption, pure Pd is by far the most active surface, where  $\sim 30$  % of the adsorbed propene undergoes reaction. A small amount of Au has a dramatic effect upon the combustion pathway. For example, with the addition of 0.15 Au, the amount of reaction on the surface decreases to  $\sim 18$  %. As the amount of surface Au increases, the level of reaction remains relatively constant until high surface Au concentrations ( $X_{Au} \geq 0.92$ ). Therefore, it can be concluded that Au has a larger effect upon the combustion rather than the dehydrogenation pathway.

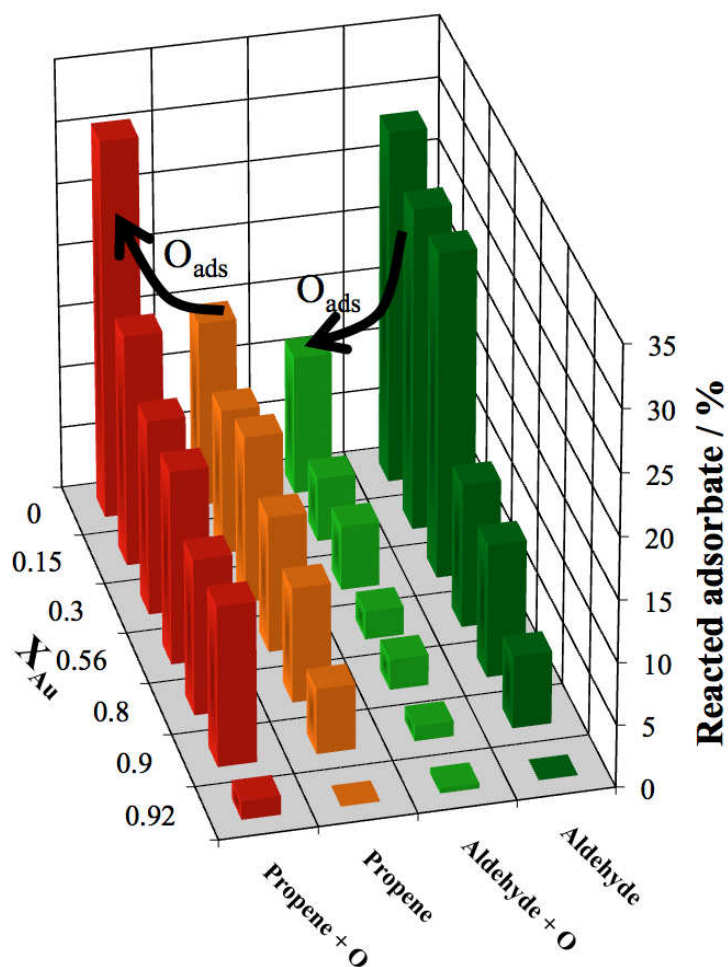


**Figure 4.13** - The variation in the amount of reacted adsorbate for crotonaldehyde and propene adsorption with and without co-adsorbed oxygen as a function of the surface Au mole fraction.

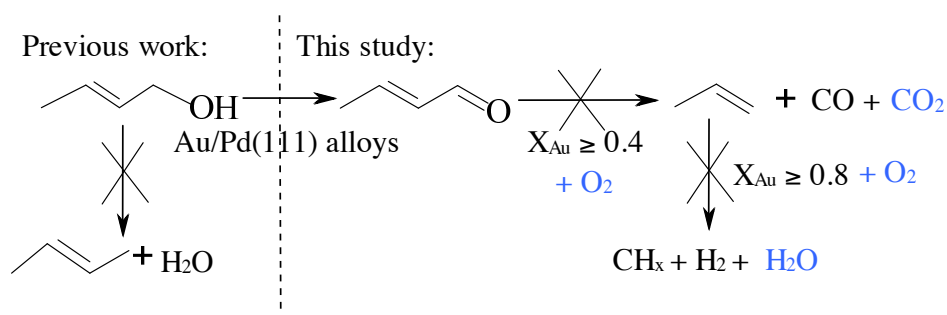
Whilst it has been demonstrated that O and Au have a large impact upon the surface chemistry of selox over Pd, the origin of this exact influence remains unclear. Many questions have arisen as a result of the work presented in this chapter. For instance, is the influence of O and Au caused by destabilisation due to steric and/or electronic effects in both cases? DFT and or RAIRS would be particularly useful in order to estimating degree of surface crowding on coadsorbate system. DFT could also be used to run molecular dynamics of the alcohol adsorption on the surface of a Au/Pd(111) random surface alloy, both with and without O. In any case, future work is warranted using a host of different techniques in order to examine this effect in greater detail.

#### 4.2.6 Errors

The systematic error in the MS is approximately 0.01 ML. The other error associated with the data presented in this chapter is the human error in subtracting any baselines in order to calculate the area of the MS peaks. This will probably be ~5 - 20 % of the peak area, with the larger errors attributed to weak peaks below 1 L exposures. Therefore, if 0.15 ML of propene desorbed, the error associated with this measurement is likely to be +/- 0.02 ML.

#### 4.3 Conclusions

TPD/TPRS studies have revealed the influence of Au on important reaction intermediates in the selective oxidation of crotyl alcohol over Pd(111). Previous work had shown that Au/Pd alloys were highly selective for the oxidation of alcohols<sup>23</sup> with Au aiding both the formation and desorption of the aldehyde<sup>18</sup>. Thick epitaxial Au over-layers prepared over a Pd(111) substrate are shown to reversibly desorb crotonaldehyde, unable to drive decomposition chemistry. Au rich surface alloys are able to turn off decomposition of both the aldehyde (for  $X_{Au} \geq 0.3$ ) and its decomposition product propene (for  $X_{Au} \geq 0.8$ ). This indicates that the decomposition reaction pathway of propene is less sensitive to surface Au when compared to crotonaldehyde. Conversely, Pd rich alloy surfaces decompose both reaction intermediates, leading to the formation of CO (solely for the aldehyde) and surface bound C; species responsible for deactivation. A reaction scheme for crotyl alcohol selox over Au/Pd(111) alloys is therefore shown in **Scheme 4.1**.



**Scheme 4.1** - Reaction pathway for crotyl alcohol over Au/Pd(111) surface alloys

In the case of the aldehyde, pre-adsorption of oxygen on Au surfaces hinders the decomposition chemistry further, with a small amount of decomposition also occurring. Propene binds more strongly to O pre-covered surfaces, which results in a small increase in the amount of propene that reacts. As a result, a larger proportion of the propene undergoes combustion when compared to the aldehyde over the same surface alloys.

#### 4.4 References

1. A. Lee, Z. Chang, P. Ellis, S. Hackett and K. Wilson, *J. Phys. Chem. C*, 2007, **111**, 18844-18847.
2. S. T. Marshall, C. M. Horiuchi, W. Zhang and J. W. Medlin, *The Journal of Physical Chemistry C*, 2008, **112**, 20406-20412.
3. P. Redhead, *Vacuum*, 1962, **12**, 203-211.
4. J. Chickos and J. William E. Acree, *J. Phys. Chem. Ref. Data*, 2003, **32**, 519-878.
5. J. Haubrich, D. Loffreda, F. Delbecq, P. Sautet, Y. Jugnet, A. Krupski, C. Becker and K. Wandelt, *Journal of Physical Chemistry C*, 2008, **112**, 3701-3718.
6. T. R. Bryden and S. J. Garrett, *The Journal of Physical Chemistry B*, 1999, **103**, 10481-10488.
7. B. A. Sexton, A. E. Hughes and N. R. Avery, *Surface Science*, 1985, **155**, 366-386.
8. C. Houtman and M. A. Barteau, *Surface Science*, 1991, **248**, 57-76.
9. H. B. Zhao, J. Kim and B. E. Koel, *Surface Science*, 2003, **538**, 147-159.
10. N. A. Thornburg, I. M. Abdelrehim and D. P. Land, *The Journal of Physical Chemistry B*, 1999, **103**, 8894-8898.
11. D. Stacchiola, L. Burkholder and W. T. Tysoe, *Surface Science*, 2003, **542**, 129-141.
12. F. Zaera and D. Chrysostomou, *Surface Science*, 2000, **457**, 71-88.
13. J. Kubota, S. Ichihara, J. N. Kondo, K. Domen and C. Hirose, *Langmuir*, 1996, **12**, 1926-1927.
14. M. Bowker, C. Morgan, N. Perkins, R. Holroyd, E. Fourre, F. Grillo and A. MacDowall, *The Journal of Physical Chemistry B*, 2004, **109**, 2377-2386.
15. K. A. Davis and D. W. Goodman, *J. Phys. Chem. B.*, 2000, **104**, 8557-8562.
16. Z. Li, F. Gao, Y. Wang, F. Calaza, L. Burkholder and W. T. Tysoe, *Surf. Sci.*, 2007, **601**, 1898-1908.

17. F. Calaza, F. Gao, Z. Li and W. T. Tysoe, *Surface Science*, 2007, **601**, 714-722.
18. A. F. Lee, S. F. J. Hackett, G. J. Hutchings, S. Lizzit, J. Naughton and K. Wilson, *Catalysis Today*, 2009, **145**, 251-257.
19. L. Hilaire, P. Légaré, Y. Holl and G. Maire, *Surf. Sci.*, 1980, **103**, 125-140.
20. G. Maire, L. Hilaire, P. Legare, F. G. Gault and A. O'Conneide, *Journal of Catalysis*, 1976, **44**, 293-299.
21. T. D. Harris and R. J. Madix, *Journal of Catalysis*, 1998, **178**, 520-532.
22. J. Pawela-Crew and R. J. Madix, *The Journal of Chemical Physics*, 1996, **104**, 1699-1708.
23. M. D. Hughes, Y. J. Xu, P. Jenkins, P. McMorn, P. Landon, D. I. Enache, A. F. Carley, G. A. Attard, G. J. Hutchings, F. King, E. H. Stitt, P. Johnston, K. Griffin and C. J. Kiely, *Nature*, 2005, **437**, 1132-1135.

## Chapter 5

# Metastable De-excitation Spectroscopy of crotyl alcohol over Pd(111)

### 5.1 Introduction

As has been demonstrated in chapters 1, 3 and 4, our understanding of the selox of crotyl alcohol over Pd(111) and the associated deactivation<sup>1</sup> has been greatly enhanced through the utilisation of temperature programmed X-ray photoelectron spectroscopy (TP XPS) combined with near edge X-ray absorption fine structure (NEXAFS)<sup>2</sup> and Temperature Programmed Reaction Spectroscopy. The XPS has shown that product decomposition and associated self-poisoning prevails over model Pd(111), while electron deficient (formally Pd<sup>II</sup>) centres confer activity in allylic alcohol selox. At low temperature, the NEXAFS indicates that the C=C bonds parallel to the Pd(111) surface, much in the same way as allyl alcohol (2-propen-1-ol) on Ag(110)<sup>3</sup>.

A further technique that is well suited to the study of molecular adsorbates is metastable de-excitation spectroscopy (MDS), which utilizes the energy associated with the metastable states of rare-gas atoms (usually the  $2^3S$  level of He) to induce electron emission from a surface or molecule<sup>14</sup>. For adsorbate systems, the de-excitation of He  $2^3S$  atoms generally involves a pseudo one-electron transition in a process that is similar to photoemission but which has the advantage that, unlike in ultraviolet photoemission spectroscopy (UPS), there is no penetration of the probe beam into the bulk.

This renders MDS extremely surface sensitive and enables the adsorbate local density of states (LDOS) at energies close to the Fermi level,  $E_F$ , to be studied in isolation. Occupied electronic states appear in this energy region as a result of chemisorption bond formation although they are largely masked in UPS due to dominant emission from metallic  $d$ -band states. As such, MDS has been widely employed in a number of previous studies investigating the electronic properties of

simple chemical adsorbates on a variety of metal surfaces<sup>4</sup>. In this chapter, MDS and supporting density functional theory (DFT) calculations are utilised to identify the states involved in bonding crotyl alcohol to the Pd surface. By using this approach, it is possible to evaluate and understand the adsorption mode and ultimately the molecular orientation of the alcohol on the Pd surface.

## **5.2 Results and Discussion**

### **5.2.1 MDS of crotyl alcohol on Pd(111)**

Experiments were performed in a stainless-steel UHV system with a base pressure of  $\sim 1 \times 10^{-10}$  Torr. The system comprises a preparation chamber; equipped with low energy electron diffraction (LEED), an analysis chamber; equipped with Auger electron spectroscopy (AES), and a beam-line for metastable He  $2^3S$  generation. Full details of the experimental setup are described elsewhere<sup>5</sup> but will be briefly outlined below. The Pd(111) single crystal sample could be heated using a pyrolytic boron nitride (PBN) heater to 1000 K and cooled to  $\sim 150$  K using a gas baffle cooled by liquid nitrogen. Preparation of a clean substrate was carried out in the preparation chamber and utilized cycles of  $\text{Ar}^+$  sputtering followed by annealing to 1000 K until LEED showed a clean well-ordered surface. Oxygen (Air Liquide, 99.998%) was then dosed as received into the chamber background to obtain a pressure of  $1 \times 10^{-7}$  Torr, while the sample was heated to 800 K to remove residual carbon. The sample was also cooled in oxygen so as to saturate the surface, before flashing to  $\sim 930$  K to desorb oxygen and any remaining contaminants. This procedure was repeated several times, until AES revealed no surface impurities. AES is insensitive to the presence of surface carbon on a Pd substrate below  $\sim 0.25$  monolayer; however, the effectiveness of this cleaning procedure has previously been confirmed using temperature-programmed desorption (TPD) studies where the lack of CO or  $\text{CO}_2$  desorption in the acquired spectra can be taken as evidence for a carbon-free surface.<sup>6</sup>

Once prepared, the sample was immediately transferred into an analysis chamber to record MDS spectra. Crotyl alcohol (Aldrich, 96%) was purified by repeated freeze-pump-thaw cycles prior to background dosing (purity checked by mass spectrometry (MS)). Quoted exposures are given in langmuirs ( $1 \text{ langmuir} = 1 \times 10^{-6} \text{ Torr s}^{-1}$ ) and are uncorrected for ion gauge sensitivity. Generally, a clean Pd(111)

surface was exposed to 3 langmuirs of crotyl alcohol with the substrate at 150 K. This dose is known to be large enough to produce a 0.15 monolayer saturation coverage of chemisorbed molecules for this system.<sup>2</sup> Additional physisorbed molecules may also be present on top of this saturation layer depending on the substrate temperature.

The metastable He  $2^3S$  beam was generated using a liquid nitrogen cooled, copper cathode, dc discharge source, the output of which was manipulated using techniques of laser cooling to provide an ultrapure and intense He  $2^3S$  atom beam at the sample.<sup>5</sup> Electrons ejected as a result of metastable atom de-excitation were collected in the normal direction using a hemi-spherical energy analyser (Omicron EA125). A He I discharge source (Focus GmbH) was used in UPS experiments with normally emitted electrons detected by the same analyzer as for MDS. For both spectroscopies, the angle of incidence of the probe beam was  $45^\circ$ .

The de-excitation of metastable He atoms at clean, transition metal surfaces is well-characterized and proceeds via the two-stage mechanism of resonance ionization (RI) followed by Auger neutralization (AN)<sup>4</sup>. When approaching a clean Pd(111) surface to within a distance of around  $5 \text{ \AA}$ , overlap of the occupied  $2s$  orbital of the He atom with an empty surface state above  $E_F$  allows a tunnelling transition to take place (RI). The resulting  $\text{He}^+$  ion continues to approach the surface until a further transition from the surface valence band to the empty ground state He  $1s$  level occurs to neutralize the atom.

The energy liberated in this process results in the emission of a second electron from the valence band in an Auger-type process (AN). As the kinetic energy of this electron is determined by the binding energies of both initial valence band states involved in the de-excitation, the resulting energy spectrum for RI + AN is essentially a self-convoluted map of the surface DOS (SDOS) modified by the de-excitation transition probability (transition matrix elements), leading to broad and generally featureless spectra, as seen in **Figure 5.1 (a)** for the clean Pd(111) surface.

Strong emission is observed in the region several eV below the kinetic energy maximum,  $E_{k,\text{max}}$ , which occurs when both electrons involved in the de-excitation process originate at  $E_F$ . Occupied Pd(111) surface states with a binding energy of

0-2 eV have been shown to have a significant local density at the surface layer and at distances of up to 3 Å away from the surface where AN transition rates are highest<sup>7</sup>, and these account for the appearance of the spectrum at high kinetic energies. At lower energies, the spectrum is dominated by true secondary electrons.

In contrast to the dominant role the SDOS plays in the AN process, penetration of UV photons into the bulk-like second atomic layer and beyond leads to features in the corresponding UPS spectrum arising from the bulk DOS (BDOS), specifically *d*-band electronic states (**Figure 5.1 (c)**). This assignment is confirmed by DFT calculations by ourselves (**Figure 5.1 (b)**) and others<sup>8</sup> which show strong *d* band peaks at energies of several eV below  $E_F$ , accounting for the peaks at ~1.4 eV and ~2.4 eV. **Figure 5.1 (c)** also shows UPS spectra for a clean surface exposed to a saturation coverage of crotyl alcohol with the substrate at 150 K and 245 K. The metallic *d* states that feature so prominently in the clean spectrum are still dominant although somewhat attenuated by the adsorbate layer.

A previous UPS study utilizing gas-phase crotyl alcohol as part of a composite molecular determination of the spectral features of opiate narcotics revealed many distinct molecular orbitals (MOs)<sup>9</sup>, as did a further UPS study of allyl alcohol<sup>10</sup>. However, for adsorption at both 150 and 245 K, direct emission from these orbitals is lacking for a saturation coverage of crotyl alcohol on Pd(111), which is known to be 0.15 ML<sup>2</sup>. The *d* states dominate the UPS spectra, due to the penetration of UV photons below the adsorbate layer. This highlights one of the benefits of using the more surface sensitive technique of MDS to study the surface electronic properties of adsorbed molecules.

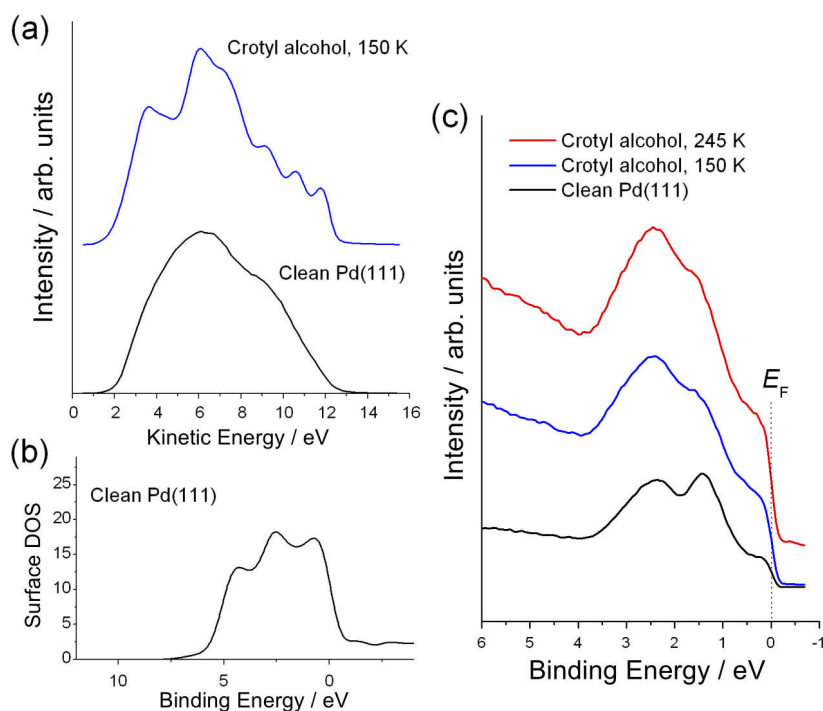


**Figure 5.1** (a) - MDS spectra from a clean Pd(111) surface where the dominant de-excitation mechanism is resonance ionization followed by Auger neutralization, and from a saturation coverage of crotyl alcohol where significant Auger de-excitation takes place. (b) - DFT calculation for clean Pd(111) showing metallic  $d$ -band states close to  $E_F$ . (c) - UPS spectra for clean Pd(111) and for a surface exposed to a saturation coverage of crotyl alcohol at 150 K and 245 K.

At adsorbate-covered surfaces, the empty electronic states of the substrate are effectively shielded by the molecule thereby suppressing the RI process so that the He  $2^3S$  atom continues to approach the surface. At a point where a (MO) of the adsorbate overlaps with the empty He  $1s$  ground state, a tunnelling transition occurs stimulating the simultaneous release of the excited He  $2s$  electron. As a quasi-one-electron process, this Auger de-excitation (AD) is reminiscent of photoemission and leads to emission spectra with features corresponding to distinct molecular electronic states. This is evident in **Figure 5.1** (a) which also shows the MDS spectrum for a saturation coverage of crotyl alcohol adsorbed onto Pd(111) at 150 K.

Emission peaks are superimposed on a background arising from de-excitation via RI + AN. The exact balance between the two de-excitation channels is determined by their relative transition rates,  $\Gamma_{AD}$  and  $\Gamma_{RI}$ , with the former depending on the

coverage, adsorption site and geometry of the molecule. The AD spectrum reflects the DOS of the adsorbed species weighted by the overlap with the He 1s wavefunction meaning that electron emission from the outermost MOs of the adsorbed molecules is strongly favoured. Therefore the features present in the spectrum represent the local DOS of the adsorbate in the energy range close to  $E_F$  which may be strongly modified by interaction with the surface. For  $\Gamma_{AD}$  to be comparable to  $\Gamma_{RI}$ , the outermost electronic states of the adsorbed crotyl alcohol must extend beyond  $\sim 3 \text{ \AA}$  from the substrate surface to efficiently suppress RI. This is approximately equal to the van der Waals radius of  $sp^2$ -hybridized carbon and so appreciable AD can be expected at a saturation coverage of crotyl alcohol even for a coplanar adsorption geometry.

### 5.2.2 Density Functional Theory

DFT calculations were also conducted (by Dr. Chris Eames), in order to aid interpretation of the MDS results. All theoretical calculations in this work used the CASTEP<sup>11</sup> ab initio DFT code. The Perdew-Burke-Ernzerhof<sup>12</sup> generalized gradient approximation was used to represent exchange and correlation effects. We have used ultrasoft pseudopotentials with a cut-off energy of 350 eV and a Monkhorst-Pack<sup>13</sup> reciprocal space sampling grid with a density of  $0.04 \text{ \AA}^{-1}$ . Convergence testing showed that the calculated energies and spectra were not affected by any further increase in the cut-off energy or the sampling grid density.

The supercell comprised three layers of bulk Pd with a vacuum gap of 20  $\text{\AA}$ . This supercell was selected in order to minimise the computational cost of the DFT calculations. However, this leads to many limitations, mainly due to the lack of interaction with a 'bulk', which need to be considered when interpreting the results. Despite these limitations, additional Pd layers were shown to have no effect on the DOS for the bare Pd surface. Molecules were adsorbed on one face of the slabs and to minimize interactions between vertical periodic images we used a large vacuum gap, which meant that adjacent surfaces were over 30  $\text{\AA}$  apart. The molecules were arranged in a  $3 \times 3$  grid, which resulted in a lateral spacing of around 11  $\text{\AA}$ . The 0.15 ML saturation coverage for crotyl alcohol on Pd(111) has a  $7 \times 7$  periodicity, although computational resources prevent the use of such a large supercell. The

consequent small lateral interactions in the simulated energies and spectra are another source of approximation error to be considered when comparing experiment and theory.

The molecules were initially positioned a few Å above the surface in various specific orientations (as shown in **Figure 5.3**), and then relaxed to determine the optimum bonding geometry for each case. The optimisation convergence tolerance for the forces was 0.01 (eV Å<sup>-1</sup>). The adsorption energies were calculated using the formula:

$$E_a = E_{\text{CrOH/Pd}} - E_{\text{CrOH}} - E_{\text{Pd}} \quad \text{Equation 5.1}$$

Where  $E_{\text{CrOH/Pd}}$  is the total energy after optimisation of the adsorbed molecule,  $E_{\text{CrOH}}$  is the relaxed energy of the isolated molecule and  $E_{\text{Pd}}$  is the energy of the relaxed clean surface. DOS spectra for the optimised molecules were calculated using Mulliken population analysis, which determines the contribution from each energy band to a given atomic orbital.

**Figure 5.2** shows the calculated Density of States (DOS) for the isolated molecules of crotyl alcohol and crotonaldehyde along with the MDS spectrum for the alcohol-adsorbed Pd(111) surface. The binding energy scale for the latter was calculated using the high-kinetic-energy cut-off (~12.5 eV) for Auger de-excitation (see **Figure 5.6**). Features D and E are most probably due to emission from both deeper lying molecular orbitals of the adsorbed alcohol and the clean Pd(111) surface. Low-energy secondary electrons account for feature F. Peaks attributed to emission from the hydrocarbon skeleton of the alcohol, the O n non-bonding, and C=C  $\pi$  states are labelled as C, B and A respectively. Interestingly, a previous UPS comparison of allyl alcohol and acrolein<sup>10</sup>, determined that the two lowest energy MOs of these molecules effectively switched positions, as indicated in **Figure 5.2** and discussed further below.

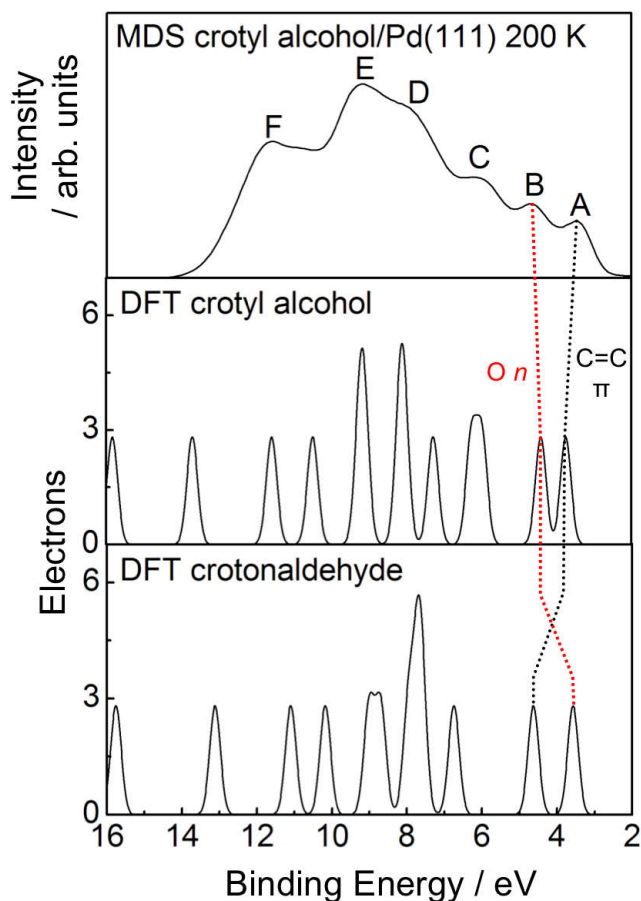


**Figure 5.2** - DFT calculated spectra for isolated crotyl alcohol and crotonaldehyde molecules and, for comparison, the experimentally obtained MDS spectrum of a crotyl alcohol saturated Pd surface at 150 K.

DFT calculations were then performed in order to examine the energetics and calculate spectra of five different molecular orientations of the adsorbed alcohol. Three calculations were performed with the molecule laid flat on the surface (labelled as TOP, BOTTOM, and SIDE) and two additional calculations with the molecule in an end-on configuration (referred to as UP and DOWN). These adsorbate geometries used in calculations are shown in **Figure 5.3**. It should be noted that the lateral position above the surface does not appear to greatly affect the partial DOS, as the energy differences are below the level of noise and therefore not significant. The calculated energies of each molecular orientation are displayed in Table 1. From this data, we can observe that energetically, the most favourable orientation is that of the molecule adsorbed parallel to the surface, on its side (SIDE = -3.27 eV). The energy of the molecule adsorbed flat onto the surface, with

the oxygen and carbon backbone in contact with the Pd, is comparable to that of the ‘SIDE’ configuration (TOP = -3.22 eV). Interestingly, our work also shows that it is also favourable for the molecule to adsorb in an end-on configuration with the oxygen pointing up, away from the surface (UP = -3.05 eV). Such a geometry would not provide the bonding arrangements necessary for the observed high binding energy suggesting that van der Waals interactions may be contributing. A future extension of this work could see these explicitly incorporated in a DFT-D calculation.

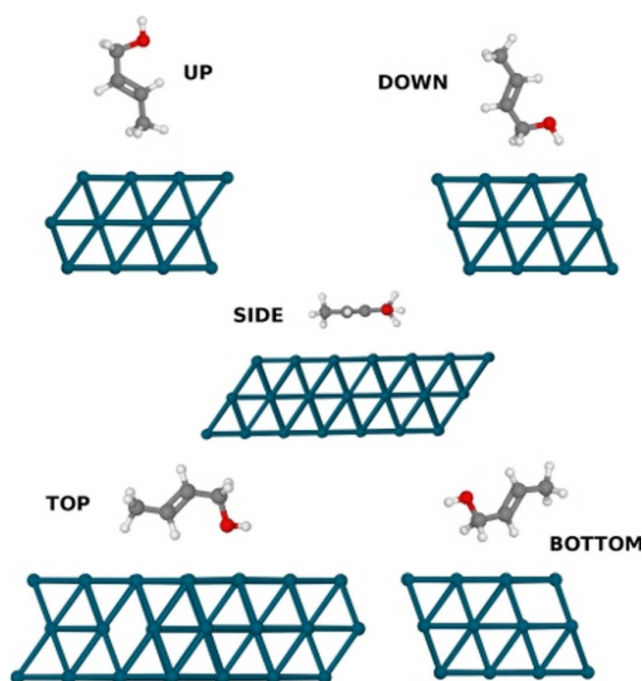


**Figure 5.3** – The five different molecular orientations of crotyl alcohol adsorbed on the Pd(111) surface used in DFT calculations.

Surface Molecular Orientation	Energy / eV
UP	-3.05
DOWN	-0.77
SIDE	-3.27
TOP	-3.22
BOTTOM	-0.87

**Table 5.1** - The energies of the surface molecular orientations shown in **Figure 5.3**.

The DOS for each orientation was then calculated, and the results are shown in **Figure 5.4**. For comparison, also shown in the figure is the MDS spectrum of the alcohol pre-saturated Pd(111) surface at 150 K. Coloured lines are also shown in the figure to aid comparison of the MDS and DFT. As mentioned previously, the peaks C, B and A are due to emission exclusively from the adsorbed molecule, and as such the following analysis will focus on these states. It should be noted that DFT calculations reflect the plane-averaged DOS so that whilst the general trends and positions of electronic states may be compared to MDS spectral features, their relative intensities may differ due to the surface sensitivity of MDS.

With that said, from both sets of data, judging by the shape and intensity of the peaks and also the calculated adsorption energies, it is clear that the ‘SIDE’ and ‘TOP’ molecular orientations yield the best agreement between theory and experiment although distinguishing between these is not possible based on the present data. ‘BOTTOM’ and ‘DOWN’ can be excluded based on their calculated energies whilst the ‘UP’ configuration has the poorest agreement with the experimental spectrum. It may be possible that a tilted geometry or molecular distortion yields an adsorption geometry that is somewhere between ‘SIDE’ and ‘TOP’. It is clear however that both the C=C and O bonds are somewhat coplanar to the substrate allowing access to the metastable He probe and giving rise to the features observed.

These assertions are supported by previous NEXAFS studies of crotyl alcohol on Pd(111)<sup>2</sup> and allyl alcohol on Ag(110)<sup>3</sup> have shown these molecules to adsorb with the allyl moiety coplanar to the Pd substrate, a geometry that permits strong bonding. Additionally, DFT calculations<sup>14</sup> have shown that, over Pd(111), allylic alcohols predominantly chemisorb via di- $\sigma$  coordination of the C=C  $\pi$  bond complemented by a weaker interaction between an O lone pair on the  $-H_2C-OH$  functionality and an atop Pd site.

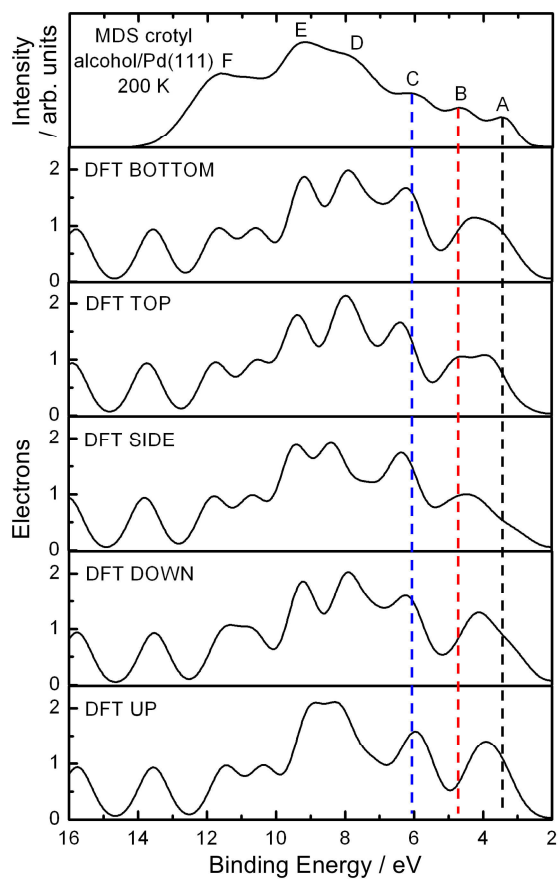


**Figure 5.4** - Density of states spectra of crotyl alcohol calculated by DFT for the molecular adsorption states shown in **Figure 5.3**. The top spectrum is that of the MDS of the alcohol on Pd shown for comparison.

### 5.2.3 Temperature programmed MDS

With the assignment of all states complete, we can now focus on the temperature evolution of the spectra.

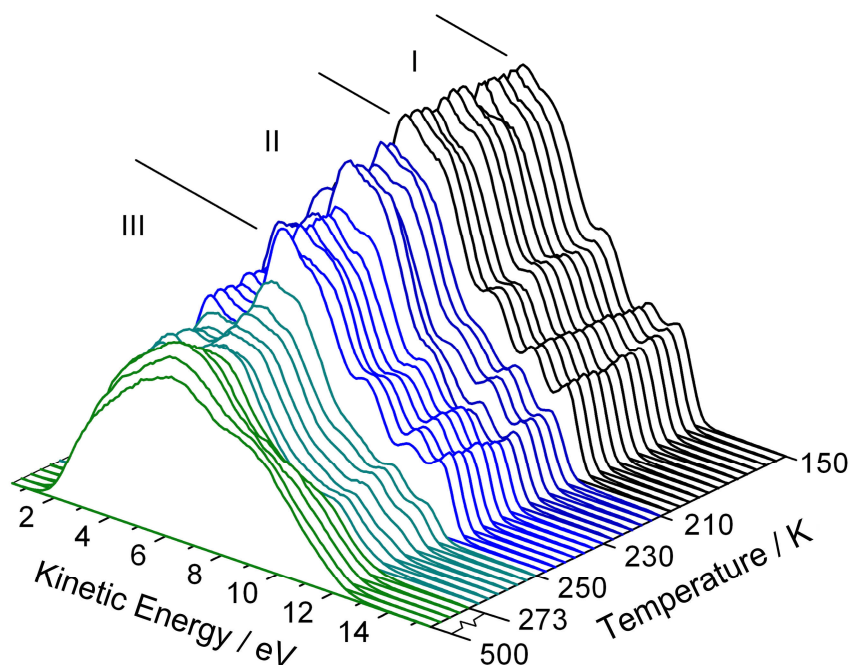


**Figure 5.5** - Temperature evolution of MDS spectra for crotyl alcohol adsorption on clean Pd(111) at 150 K. Temperature regimes where noticeable changes in the spectra occur are highlighted with different colours and grouped together into three distinct adsorption regimes. Note the non-linear temperature scale above room temperature.

**Figure 5.5** shows the evolution of MDS spectra taken after a clean Pd(111) surface was exposed to a 3 L dose of crotyl alcohol at 150 K and then allowed to warm to room temperature before being heated to 500 K. Detailed analysis of the spectra reveal different temperature regimes, highlighted in the figure, with sometimes only subtle variations in the spectral features. To emphasise these differences and aid a discussion of the adsorption kinetics, representative spectra from each temperature regime are shown in **Figure 5.6**. Temperature-programmed C 1s XPS has shown the reaction of crotyl alcohol over Pd(111) to proceed via three distinct steps with the in-tact adsorbed molecule first transforming to crotonaldehyde beginning at 200 K before decarbonylating at room temperature<sup>12</sup>. At higher annealing temperatures, carbonyl and CO surface species are removed from the

surface leaving only graphitic carbon. The MDS spectra presented in **Figures 5.5** and **Figure 5.6** broadly support this interpretation as will now be discussed in more detail.

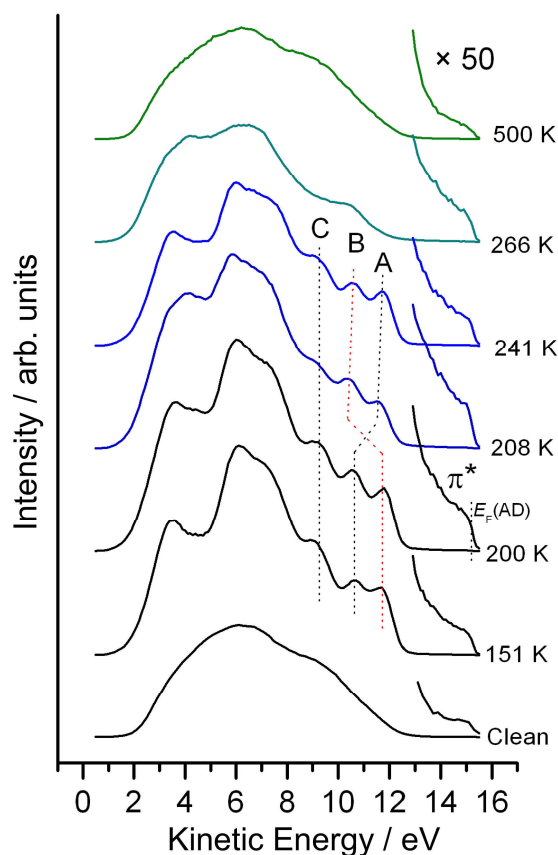


**Figure 5.6** - MDS spectra obtained at critical temperatures from a Pd(111) substrate exposed to 3 L of crotyl alcohol at 150 K, warmed to room temperature and then heated. Key features in the spectra are also labelled A,B and C, the assignment of which is detailed in section 5.2.3.1.

### 5.2.3.1 I. < 200 K: Low-temperature crotyl alcohol adsorption

Low-temperature adsorption of crotyl alcohol at 150 K leads to MDS spectra that display distinct features typical of AD at a molecular adsorbate. Particularly, well-resolved peaks at high kinetic energies are observed (labelled A, B, and C in **Figure 5.6**) which have been assigned to emission from the first few (MOs) of the adsorbed alcohol. However, it is probable that a significant proportion of He  $2^3S$  atoms interacting with the surface de-excite via RI accounting for the steadily rising background of emission on which the AD peaks are superimposed. To focus

on these latter features and gain further insight into evolution of the adsorption kinetics and spectral content with temperature, a peak-fit analysis for each temperature was performed. This involved approximating the RI emission in the energy region of peaks A-C by a straight line and subtracting this from the overall spectrum to yield a qualitative picture of the temperature-dependent AD process. **Figure 5.7** shows representative data from the three identified temperature regimes. As we are now only considering the photoemission-like AD channel, the energy scales for these data may be converted to binding energy using knowledge of the Fermi level which occurs at the high kinetic energy cut-off (indicated in Figure 6).

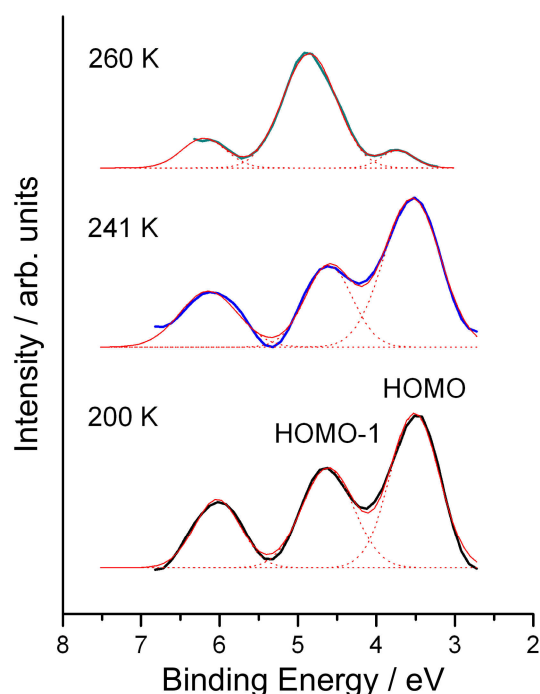


**Figure 5.7** - Molecular orbitals and peak analysis of the MDS data shown in **Figure 5.6** at three distinct temperature regimes. The dotted red lines show the fitted individual components.

As previously mentioned, assignment of the MOs shown in **Figure 5.7** has been accomplished using both DFT calculations and also relatively early valence-band photoemission studies and MO calculations of gas-phase allyl alcohols<sup>18,19</sup>. Emission from both HOMO and HOMO-1 states in the MDS spectra is relatively strong as would be expected for a parallel adsorption mode where incoming He  $2^3S$  atoms are able to access these molecular states. A comparison of UPS spectra from

allyl alcohol, acrolein, and propene<sup>10</sup> also supports this overall assignment. Additionally, in a separate UPS study of crotyl alcohol<sup>9</sup>, the binding energy difference between the first three MOs agree to within 0.1 eV with those shown for the 200 K spectrum in **Figure 5.7**.

As the temperature of the substrate increases within regime I from 150 K toward 200 K, subtle changes in the appearance of the emission peaks occur. At lower temperatures, peaks A and B are closer together and therefore less well-defined with peak C also appearing to shift in energy with increasing temperature. In order to track these temperature-related changes in greater detail, the peak-fitting procedure used to produce **Figure 5.7** was applied to the data shown in **Figure 5.5** to obtain the peak positions of the first three MOs. The resulting graph, displayed in **Figure 5.8**, shows that, in heating from 150 K to around 190 K, all three peaks undergo a small (<0.2 eV) shift in binding energy, before stabilizing up to 200 K. To pre-saturate the Pd(111) surface with crotyl alcohol at low temperature, a previous study showed that a minimum dose of 1.5 L is required<sup>2</sup>, with higher exposures leading to a broadening of XPS features due to the formation of molecular multilayers. For the 3 L exposure used here, multilayers are also expected to form yielding AD spectral features that are closer in form to those of gas-phase crotyl alcohol than the chemisorbed molecule. As the substrate warms, the physisorbed multilayer molecules desorb revealing the chemisorbed saturation coverage and allowing He 2<sup>3</sup>S atoms to access  $\pi^*$  states induced around  $E_F$  as a result of the molecule-substrate interaction. The lack of any major MO energy difference between the multilayer and chemisorbed phases indicates that the molecule is relatively undistorted upon adsorption.

To emphasize the induced  $\pi^*$  states, the data in **Figure 5.6** are also replotted with the kinetic energy scale multiplied by a factor of 50. As the substrate temperature increases and the multilayers desorb, emission at energies close to  $E_F$  intensifies, clearly demonstrating increased de-excitation at the chemisorption states. Electron donation/backdonation exchange between metallic  $d$  states and molecular  $\pi$  and  $\sigma$  states results in rehybridization of the adsorbate-metal system and the filling of empty molecular antibonding  $\pi^*$  states which redistribute above and below  $E_F$  in the LDOS. In the gas phase and when adsorbed in multilayers, crotyl alcohol molecules have a band gap around  $E_F$  and would not give rise to emission in this

region. Similar effects have been observed in MDS studies of many other adsorbate systems, for example benzene adsorption on Fe(110)<sup>15</sup>. However, in the corresponding UPS spectra for crotyl alcohol adsorption (Figure 1 (c)), these states are masked by emission from the Pd substrate.

Emission at high kinetic energies is also observed in the magnified MDS spectrum for the clean Pd(111) surface, which is unexpected as the de-excitation mechanism here is RI + AN. This feature is indicative of slight CO contamination as this molecule is known to strongly chemisorb to Pd(111) yielding bonding states that arise, according to the Blyholder model, due to mixing between CO  $2\pi^*$  orbitals with substrate  $d$  orbitals. That these states are visible, despite the surface being clean to the standards of LEED, AES and UPS, highlights the extreme sensitivity of MDS.

Changes in the relative intensity of the features assigned to emission from C=C and O  $n$  states provide further insight into the adsorption dynamics of crotyl alcohol on Pd(111). As the substrate temperature increases from 150 K, the peak related to the latter states becomes increasingly prominent (see **Figure 5.5**) reflecting the changing coverage of the substrate as molecules desorb upon warming. For the adsorption of crotonaldehyde on Pt(111) at low coverage, the C=C and C=O bonds are known to both align parallel to the surface<sup>2</sup>, although as the coverage increases, the C=O bond undergoes a significant re-orientation by tilting strongly toward the surface. A similar effect may be occurring here with the C-O bond forced closer to the surface at high coverages and tilting further away from it as the coverage reduces to saturation. This would explain the increasing intensity of emission observed for O  $n$  states and also for induced  $\pi^*$  states as the substrate temperature rises to leave a saturation coverage of crotyl alcohol. At low coverages, the C=C bond has a smaller separation from the substrate allowing a greater interaction and thus yielding more intense  $\pi^*$  emission. Whilst this picture of C-O bond behaviour provides a qualitative description of the trends observed, it is not possible to state the degree of tilt, if any exists. However, a significant tilt would yield a more pronounced feature in the MDS spectrum when compared to emission from the C=C bond. The presented data can therefore be taken as evidence for an adsorption mode in which the C-O bond of the alcohol is aligned somewhat parallel to the substrate, in addition to the C=C bond.

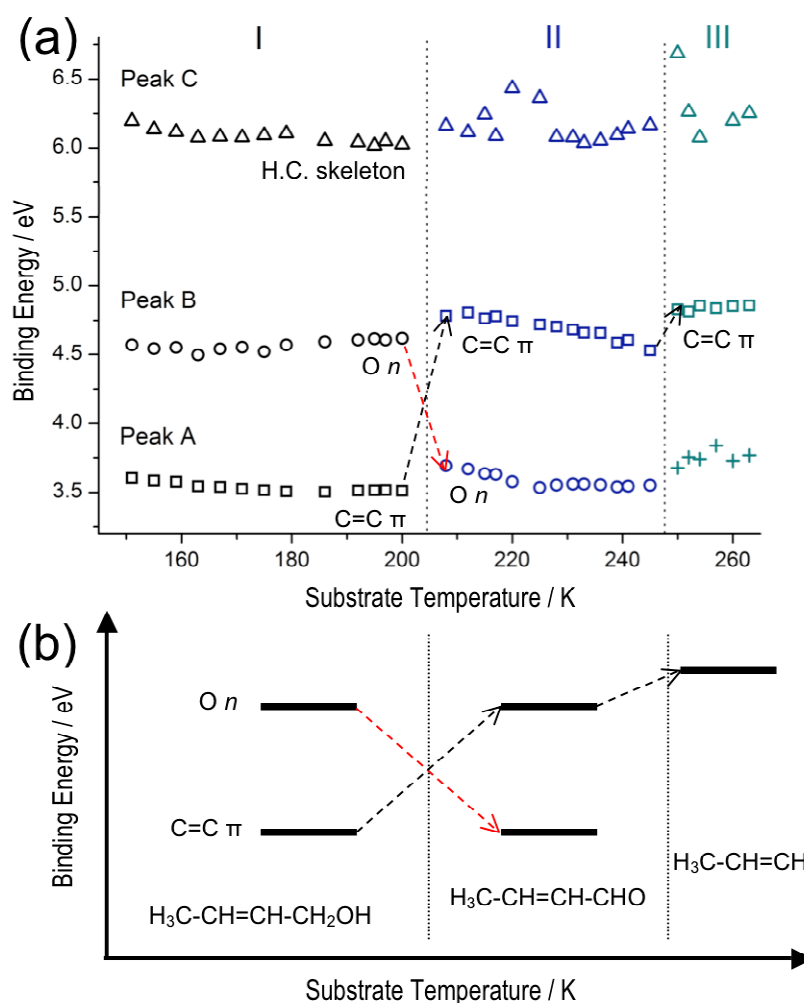


**Figure 5.8 (a)** - Peak positions of the first three molecular orbitals (assigned in **Figure 6**) as a function of temperature. **(b)** – The resulting schematic of the energy level correlation of the O *n* and C=C π MOs

### 5.2.3.2 II. 200-250 K: Selox of crotyl alcohol to crotonaldehyde

Above a substrate temperature of 200 K, distinct changes in the MDS spectra occur marking a transition to a second adsorption regime that ends at around 250 K. The evolution of spectral features across this temperature range is apparent in **Figs. 5.5-5.7** although is perhaps clearest in **Figure 5.8**. Initially, peaks A and B shift to a higher binding energy by  $\sim 0.2$  eV whilst emission from peak C is reduced resulting in its position becoming less well-defined. After 225 K the system is more stable with peaks A and B tending toward slightly lower binding energies and peak C again becoming more prominent. The selective oxidation of crotyl alcohol to surface bound crotonaldehyde over Pd(111) is known to proceed via a reaction

pathway that accounts for ~90 % of the adsorbed molecule with the activation of this process commencing at 200 K. We therefore interpret the changes in the MDS spectra at this intermediate temperature range to originate from the onset and continuation of this reaction channel generating emission from the resultant aldehyde product. A minor channel for crotyl alcohol reaction to 2-butene and water also exists over Pd(111)<sup>2</sup> although a clear signature of this is not apparent in the MDS spectra possibly swamped by emission from the alternative process.

For low coverages of crotonaldehyde on Pt(111), the C=O and C=C bonds both align parallel to the substrate<sup>16</sup> with the  $\pi$  system of the carbonyl functionality not utilized in the adsorption<sup>14</sup>. DFT calculations have shown crotonaldehyde to adopt a similar  $\eta_4$  quasi-planar adsorption mode over Pd(111)<sup>23</sup>. For this in-plane adsorption geometry and a hydrocarbon backbone that is structurally unaltered, MDS features for the aldehyde may be expected to have the same origin as for the alcohol. Whilst this is qualitatively correct, a previous UPS comparison of allyl alcohol and acrolein<sup>10</sup> determined that the two lowest energy MOs of these molecules effectively switched positions with the HOMO of the aldehyde due to C=C  $\pi$  emission and HOMO-1 state due to O  $n$  non-bonding states, in direct anti-correlation to the alcohol. This is in agreement with the DFT results of the isolated molecules presented earlier in this study, which show MO shifts that are similar in magnitude to those observed experimentally (figures 2 and 8). The energy-level realignment for the gas-phase molecules used in that study is schematically illustrated in **Figure 5.8 (b)** and we suggest an equivalent redistribution occurs when adsorbed crotyl alcohol oxidizes to crotonaldehyde over Pd(111). Additionally, considering the known planar geometry of crotonaldehyde on Pd(111), the fact that the relative intensities of peaks A and B are not greatly different for the alcohol and aldehyde lends further evidence to the assertion that the C-O bond of the alcohol is somewhat aligned parallel to the substrate.

Low binding-energy MOs are particularly susceptible to modifications to the conjugation and inductive interactions within a molecule. The additional electronegativity associated with the carbonyl group formed upon crotyl alcohol oxidation leads to further inductive delocalisation of electron density towards the O atom, thus stabilizing the C=C  $\pi$  orbital and allowing the O  $n$  states to acquire more

bonding character. Resonance effects may also contribute to the MO binding energy determination although, due to the large energy separation of the C=C  $\pi$  and O  $n$  states and the in-plane geometry of the aldehyde molecule, these are expected to be small in comparison to inductive interactions<sup>15</sup>. With these intramolecular changes in mind, for peaks A and B to occupy the same approximate energetic positions for both the alcohol and aldehyde would certainly seem unexpected and a reversal in the assignment of the first two MOs, albeit coincident in energy, is altogether more likely.

### 5.2.3.3 III. > 250 K: Decarbonylation

At ~250 K, a further transition in the adsorbate system occurs accompanied by more distinct changes in the MDS spectra. Peaks A and C reduce dramatically in intensity and eventually disappear at around room temperature whilst peak B shifts to a higher binding energy where it remains approximately stable both in position and intensity. C 1s XPS has shown that surface bound crotonaldehyde decarbonylates to propene and CO at room temperature with the former either desorbing or dehydrogenating to graphitic carbon as the temperature increases above ~330 K<sup>2</sup>. With propylidyne being the dominant adsorbate species above 250 K, peak B in this temperature regime is assigned to the C=C  $\pi$  orbital (HOMO) of such molecular fragments. A previous MDS study of CO/Pd(111) by Ertl and co-workers<sup>17</sup> show spectral features at 7.7 and 10.8 eV at 300 K. Unfortunately, these specific features cannot be observed in this study, as this region is swamped by emission from both low-energy secondary electrons and deeper lying molecular orbitals (F, E and D). Unfortunately, further due to the high level of convolution of these states, peak fitting and therefore further interpretation is extremely difficult.

Earlier studies of olefinic adsorption on Pd(111)<sup>14, 18</sup> have shown that significant hybridization of the C=C  $\pi$  bond with metallic  $d$  states results in substituent functionalities (the methyl group in the case of propene) tilting away from the surface. In the gas-phase, the C=C  $\pi$  orbital of propene is de-stabilized with respect to acrolein<sup>19</sup> due to a combination of hyperconjugation and inductive interaction with the methyl group. This leads to the orbital energetically locating between the two outer lying orbitals of acrolein, as illustrated in **Figure 5.8 (b)**. However, when

adopting a di- $\sigma$ -coordination mode in the formation of a chemisorption bond, the C=C  $\pi$  orbital is stabilized and shifts to a higher binding energy explaining its relative position when compared to the MOs of crotonaldehyde (see Figure 5 (a)). A large shift in binding energy of the C=C  $\pi$  orbital upon chemisorption indicates a significant electron donation/backdonation interaction between propene and the Pd substrate, in similarity to ethylene adsorption on Pd(111)<sup>19</sup>. Emission from induced  $\pi^*$  states is also high providing further evidence for a strong chemisorption bond. Heating above room temperature results in the loss of clear, identifiable features in the MDS spectra suggesting that the RI de-excitation channel is now strongly dominant. Propene almost completely desorbs by 500 K and only a small coverage of graphitic carbon remains bound to the surface so that the spectra become increasingly characteristic of clean Pd(111).

### 5.3 Conclusions

A combination of MDS and DFT has been used to study the adsorption of crotyl alcohol on Pd(111). At a substrate temperature of 150 K, three distinct molecular features are observed, typical of such adsorbates, due to predominant Auger de-excitation. Early valence band photoemission studies, MO calculations of gas-phase allyl alcohols, and density functional theory (DFT) calculations have been used to interpret the low temperature spectra. States centred around 6 eV (peak C) can be attributed to the hydrocarbon backbone of the molecule. Further states appearing at around 4.5 eV (peak B, HOMO-1) and 3.5 eV (peak A, HOMO) have been assigned to the C=C  $\pi$  bond and O lone-pair  $2p$   $n$  bonds respectively.

DFT calculations for various adsorption geometries of the alcohol reveal that the lowest energy state results when the molecule adopts an adsorption geometry that is parallel to the surface. This assignment is also supported experimentally, as any significant tilt in the position of the oxygen would lead to a more pronounced feature in the MDS spectrum when compared to emission from the C=C bond. We can therefore conclude from both the experimental and DFT results, that the C-O bond of the alcohol is aligned somewhat parallel to the substrate, in addition to the C=C bond. Judging by the shape and intensity of the peaks, DOS calculations for

such configurations are in excellent agreement with experimentally acquired MDS spectra.

The chemical transformation of the alcohol to the corresponding aldehyde has been investigated by temperature programmed MDS. Heating the pre-saturated substrate causes dramatic changes to be observed in the spectra. In order to track such changes, a peak fitting analysis was performed. Between approximately 200 K and 250 K, the reaction of crotyl alcohol to crotonaldehyde predominates, generating emission from the aldehyde product resulting in a small shift in peaks to higher binding energy. As a result of intramolecular changes, a reversal in the assignment of the first two MOs occurs, albeit almost coincident in energy. This switchover is supported by DFT calculations of the isolated alcohol and aldehyde, which show shifts similar in magnitude to that observed experimentally.

At higher temperatures, peaks A and C dramatically decrease due to decarbonylation of the aldehyde, meaning that propylidyne is the dominant adsorbate species above 250 K. Peak B ( $\sim 4.75$  eV) therefore arises from C=C  $\pi$  orbital (HOMO) of adsorbed propylidyne. Spectral features indicative of CO (7.7 and 10.8 eV)<sup>17</sup> are not observed, due to dominant emission from secondary electrons and lower energy orbitals from 7 - 14 eV. Heating the sample further results in the loss of identifiable features in the spectra, indicative of dominant resonance ionisation de-excitation. Propene completely desorbs by  $\sim 500$  K, with only a small amount of graphitic carbon remaining on the surface, meaning that spectra become increasingly characteristic of Pd(111).

#### 5.4 References

1. A. F. Lee and K. Wilson, *Green Chem.*, 2004, **6**, 37 – 42.
2. A. F. Lee, Z. Chang, P. Ellis, S. F. J. Hackett and K. Wilson, *J. Phys. Chem. C*, 2007, **111**, 18844-18847.
3. J. L. Solomon, R. J. Madix and J. Stohr, *The Journal of Chemical Physics*, 1988, **89**, 5316-5322.
4. Y. Harada, S. Masuda and H. Ozaki, *Chem. Rev.*, 1997, **97**, 1897-1952.

5. A. Pratt, A. Roskoss, H. Menard and M. Jacka, *Review of Scientific Instruments*, 2005, **76**, 053102-053106.
6. J. Naughton, A. Lee, S. Thompson, C. P. Vinod and K. Wilson, *Phys. Chem. Chem. Phys.*, 2010, **12**, 2670-2678.
7. W. Sesselmann, B. Woratschek, J. Küppers, G. Ertl and H. Haberland, *Physical Review B*, 1987, **35**, 1547.
8. S. G. Louie, *Physical Review Letters*, 1979, **42**, 476.
9. L. Klasinc, B. Ruscic, A. Sabljic and N. Trinajstic, *Journal of the American Chemical Society*, 1979, **101**, 7477-7482.
10. A. Katrib and J. W. Rabalais, *The Journal of Physical Chemistry*, 1973, **77**, 2358-2363.
11. S. J. Clark, M. D. Segall, C. J. Pickard, P. J. Hasnip, M. I. J. Probert, K. Refson and M. C. Payne, *Zeitschrift für Kristallographie*, 2005, **220**, 567-570.
12. J. P. Perdew, K. Burke and M. Ernzerhof, *Physical Review Letters*, 1996, **77**, 3865.
13. H. J. Monkhorst and J. D. Pack, *Physical Review B*, 1976, **13**, 5188.
14. F. Delbecq and P. Sautet, *Journal of Catalysis*, 1995, **152**, 217-236.
15. X. Sun, Y. Yamauchi, M. Kurahashi, T. Suzuki, Z. P. Wang and S. Entani, *The Journal of Physical Chemistry C*, 2007, **111**, 15289-15298.
16. A. J. Urquhart, F. J. Williams, O. P. H. Vaughan, R. L. Cropley and R. M. Lambert, *Chem Comm*, 2005, 1977-1979.
17. W. Sesselmann, B. Woratschek, G. Ertl, J. Küppers and H. Haberland, *Surface Science*, 1984, **146**, 17-42.
18. J. E. Demuth, *Chemical Physics Letters*, 1977, **45**, 12-17.
19. L. P. Wang, W. T. Tysoe, R. M. Ormerod, R. M. Lambert, H. Hoffmann and F. Zaera, *The Journal of Physical Chemistry*, 1990, **94**, 4236-4239.

# Chapter 6

## Magnetorefractive Effect in Fe<sub>3</sub>O<sub>4</sub> thin films

### 6.1 Introduction

Jacquet and Valet in 1995 showed theoretically that the change in the optical conductivity of magnetic multilayers in an applied magnetic field is also associated with a significant change in the refractive index of the material<sup>1</sup>. This effect was termed the magnetorefractive effect (MRE) and was also demonstrated experimentally in [Ni<sub>80</sub>Fe<sub>20</sub>/Cu/Co/Cu] magnetic multilayers, which showed reasonable agreement with the theoretical calculations<sup>1</sup>.

The development of techniques to probe useful properties of materials is vital in order to refine and improve such characteristics. The work of Jacquet and Valet therefore represented a new, valuable method to both model and study magneto-transport within metallic magnetic materials and has been applied to both granular and layered materials<sup>2</sup>. Research at York in recent years has also shown that the magnetoresistance (MR) can be directly related to the MRE by an experimental correlation<sup>3</sup>. As a result, this allows the MR of materials of spintronic materials to be determined *via* non-destructive, non-contact measurements<sup>4-8</sup>.

Many different oxide materials also show interesting magnetic properties. The study of magnetism in pure and diluted oxides is a rapidly growing field<sup>9-15</sup>, as such materials have potential for application in spintronic devices<sup>15-17</sup>. Magnetite (Fe<sub>3</sub>O<sub>4</sub>), is one such material, as it has a high Curie temperature (858 K)<sup>18-22</sup>, theoretical calculations predict it to be fully spin polarised at the Fermi level<sup>22-30</sup> and thin-films display MR<sup>20, 31-37</sup>. As outlined in chapter 1 (section 1.4.5), these properties are highly dependent upon the film microstructure<sup>22, 37-39</sup>.

In this chapter, it will be shown that thin-films of Fe<sub>3</sub>O<sub>4</sub> grown on MgO display a thickness dependent MRE. This is due to the large skin depths associated with the material, meaning that the IR light probes both the thin-film and the substrate, a complication not observed for metallic multilayers. A new theoretical model for this

dependence will be outlined, allowing oxide materials to be modelled and probed by MRE. The development of this method not only allows various conductivity mechanisms to be probed for oxides, but also allows the composition and thickness of such thin-films to be measured.

## **6.2 Results and Discussion**

### **6.2.1 Preparation of Fe<sub>3</sub>O<sub>4</sub> thin-films**

The phase diagram of iron oxides is very complex (see chapter 1, section 1.4.5), therefore, exact deposition conditions are vital in order to ensure the exclusive growth of the desired phase. Experiments were first conducted to determine the molecular beam epitaxy (MBE) growth conditions necessary to ensure that Fe<sub>3</sub>O<sub>4</sub> and not other phases of iron oxide could be grown repeatedly. Gao et al<sup>40</sup> determined the phase diagram for MBE growth of Fe<sub>3</sub>O<sub>4</sub> on MgO substrates using O radicals produced by an RF plasma source, by preparing a large number of samples grown at different conditions. The stoichiometry of samples was controlled by independently controlling the growth rate, plasma power and O partial pressure. Depending upon the type of plasma source, size and geometry of the MBE chamber used, there will be slight variations in the growth conditions required for each vacuum system. As a result, Chambers work was used as a starting point in order to prepare Fe<sub>3</sub>O<sub>4</sub> samples.

Two MBE chambers were utilised for the growth of Fe<sub>3</sub>O<sub>4</sub> thin-films on MgO substrates. One chamber was located at Northeastern University in Boston, USA, and the other was housed at the University of York, UK. Further details regarding these MBE chambers can be found in section 2.1.2 of chapter 2. All MgO substrates were first cleaned by sonication in acetone and then isopropyl alcohol, to ensure that the surface was largely free of any organic contaminants. The substrate was then placed into the MBE chamber via a load-lock. For samples grown in the Northeastern MBE, prior to growth the substrates were annealed to 973 K in O<sub>2</sub> for 4 hours. The samples grown in the York MBE were annealed to 973 K in atomic O for 1-2 hours. In both cases the substrate was then cooled to the required growth temperature.

Samples of Fe<sub>3</sub>O<sub>4</sub> were then grown by simultaneously evaporating Fe in the presence of atomic O prepared by an RF plasma source (details in chapter 2, section 2.1.2). The samples grown at Northeastern university were prepared by Dr. Zhuhua Cai. Many

different iron oxide samples of various phases were first grown in order to calibrate growth parameters for the deposition of thin-films of the desired phase ( $\text{Fe}_3\text{O}_4$ ). For both chambers the optimum  $\text{Fe}_3\text{O}_4$  growth conditions are summarised in **Table 6.1**. These growth parameters were determined by creating a calibration matrix, where the oxygen pressure, plasma power and iron growth rate were independently varied. Samples prepared for the calibration matrix were analysed using diffraction, microscopy and spectroscopic techniques in order to determine the phase of iron oxide grown, the result of which will be presented in the following sections of this chapter.

As detailed in chapter 1, section 1.4.5, when  $\text{Fe}_3\text{O}_4$  is grown on MgO, structural defects, known as antiphase boundaries (APBs) form due to the difference in size of the unit cells<sup>33, 35, 41</sup>. There is a strong antiferromagnetic coupling effect across these boundaries, which is thought to be the cause of the MR in these materials. The density of the APBs therefore influences the magnitude of the MR effect. A large amount of work has already been carried out on growth of  $\text{Fe}_3\text{O}_4$  on MgO (100) substrates, yet despite the correlation of MR properties to structure, to the author's knowledge, no work has been carried out on the growth of  $\text{Fe}_3\text{O}_4$  on MgO (110) or MgO (111) substrates. As a result, samples were grown on a variety of different substrates in order to determine the effect of the structure of the substrate upon the MR of  $\text{Fe}_3\text{O}_4$  thin-films.

<b>MBE Chamber</b>	<b>Substrate</b>	<b>Substrate Temp. / K</b>	<b>O pressure / Torr</b>	<b>Plasma power / W</b>	<b>Fe growth rate / <math>\text{\AA s}^{-1}</math></b>
Northeastern	MgO(111)	623 K	$1.0 \times 10^{-6}$	100	0.12
	MgO(111) $\sqrt{3} \times \sqrt{3}$	623 K	$1.0 \times 10^{-6}$	100	0.12
	MgAl <sub>2</sub> O <sub>4</sub> (111)	623 K	$1.0 \times 10^{-6}$	100	0.12
	MgAl <sub>2</sub> O <sub>4</sub> (110)	623 K	$1.0 \times 10^{-6}$	100	0.12
York	MgO(100)	523 - 723 K	$2.0 \times 10^{-5}$	200	0.1

**Table 6.1** – Empirical optimum growth conditions determined for thin-film growth of  $\text{Fe}_3\text{O}_4$  on various substrates for each MBE chamber.

As also described in chapter 1, film thickness is also known to be a factor in terms of the density of the APBs, and as a result, several film thicknesses were prepared.

Substrate	Desired nominal Fe <sub>3</sub> O <sub>4</sub> film thicknesses
	/ nm
MgO(111) 1 × 1	10, 20, 30, 60, 100
MgO(111) $\sqrt{3} \times \sqrt{3}$	10, 20, 30, 60, 100
MgAl <sub>2</sub> O <sub>4</sub> (111)	10, 30, 60, 100
MgAl <sub>2</sub> O <sub>4</sub> (110)	30
MgO(100)	60

**Table 6.2** – A table showing the substrates and desired Fe<sub>3</sub>O<sub>4</sub> film thicknesses used to prepare samples.

### 6.2.2 Reflectance High Energy Electron Diffraction (RHEED)

Reflectance High Energy Electron Diffraction (RHEED) was used to characterise iron oxide thin-films *in-situ*. RHEED patterns were recorded for the Northeastern samples both before and during growth in order to examine the substrate and thin-film surface structure respectively. The RHEED patterns of samples produced at Northeastern were obtained by Dr. Zhuhua Cai. Representative RHEED patterns are presented in **Figures 6.1** to **6.3**. Unfortunately, due to the design of the sample holder in the York MBE, it was not possible to obtain RHEED patterns.

**Figure 6.1 (a)** shows the RHEED pattern recorded for an as received MgO(111) substrate. In this case, the RHEED streaks are broad and relatively weak, indicating that the surface is relatively rough and is not composed of ordered steps or terraces. **Figure 6.1 (b)** shows the RHEED pattern from the same MgO(111) substrate after it has been annealed in a furnace to 973 K for four hours. It is evident that the streaks are sharper and far more intense, showing that the surface is much smoother and indicates possible step formation. **Figure 6.1 (c)** is the same sample which has been subjected to an O plasma for approximately one hour. The streaks appear to be sharper and more intense, indicative of terrace formation. We can conclude from these patterns, that we have obtained a relatively smooth 1 × 1 MgO(111) surface.

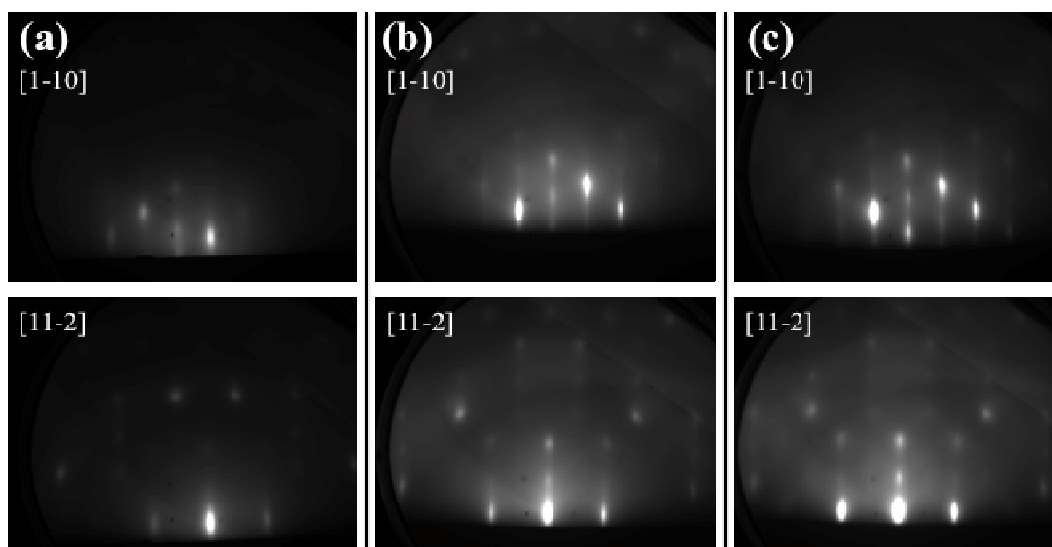


**Figure 6.1** – RHEED patterns recorded for MgO(111) substrates

(a) as received ( $1 \times 1$ ) (b) after annealing at 973 K in a furnace for 4 hours (c) after exposure to a 100 W O plasma for 1 hour. Samples were run by Dr. Zhuhua Cai.

**Figure 6.2 (a)** is the RHEED recorded for an as received MgO(111) sample. It is comparable to that of **Figure 6.1 (a)**, in that it consists of weak, broad streaks, meaning that the surface is relatively rough and will consist of many defects. **Figure 6.2 (b)** are RHEED patterns obtained from the same sample shown in **Figure 6.2 (a)**, which has been annealed in a furnace at 1073 K for six hours. The streaks in this case are much sharper and intense, showing that the surface is far smoother. In the [11-2] direction, it is possible to see additional streaks in between the main lines, which are indicative of a  $\sqrt{3} \times \sqrt{3}$  surface reconstruction. These  $\sqrt{3} \times \sqrt{3}$  streaks are more apparent in the [11-2] direction of the RHEED pattern in **Figure 6.2 (c)**, which was recorded after the substrate was exposed to a 100 W O plasma for one hour.

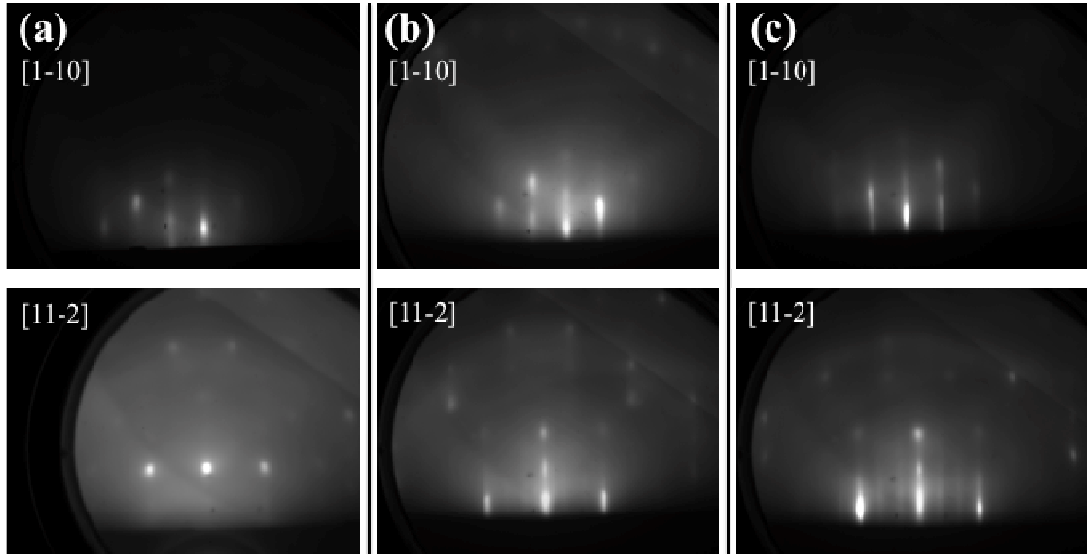


**Figure 6.2** – RHEED patterns recorded for MgO(111) substrates

(a) as received ( $1 \times 1$ ) (b) after annealing at 1073 K in a furnace for 6 hours (c)  $\sqrt{3} \times \sqrt{3}$  surface reconstruction after exposure to a 100 W O plasma for 1 hour. Samples were run by Dr. Zhuhua Cai.

**Figure 6.3** (a) to (d) shows the RHEED patterns recorded during the growth of an  $\text{Fe}_3\text{O}_4$  thin-film on MgO(111). In **Figure 6.3** (a), the additional lines in between the MgO streaks are attributed to  $\text{Fe}_3\text{O}_4$ . This assignment can be made according to the fact that the  $\text{Fe}_3\text{O}_4$  has a unit cell which is twice that of MgO, so due to the nature of reciprocal space, the diffraction pattern corresponding to  $\text{Fe}_3\text{O}_4$  will occur halfway through the MgO. As expected, as the film becomes thicker (**Figure 6.3** (b), (c) and (d)), the MgO streaks become weaker in intensity.

The growth of  $\alpha\text{-Fe}_2\text{O}_3$  can be eliminated as a possibility, as a radically different pattern would be observed. This is because the lattice parameters of  $\alpha\text{-Fe}_2\text{O}_3$  are  $a = 5.038 \text{ \AA}$ <sup>42</sup> and  $c = 13.772 \text{ \AA}$ <sup>42</sup>, meaning that depending upon the orientation of the film, the streaks would either appear to be similar in size to the of MgO or would not occur halfway through MgO.

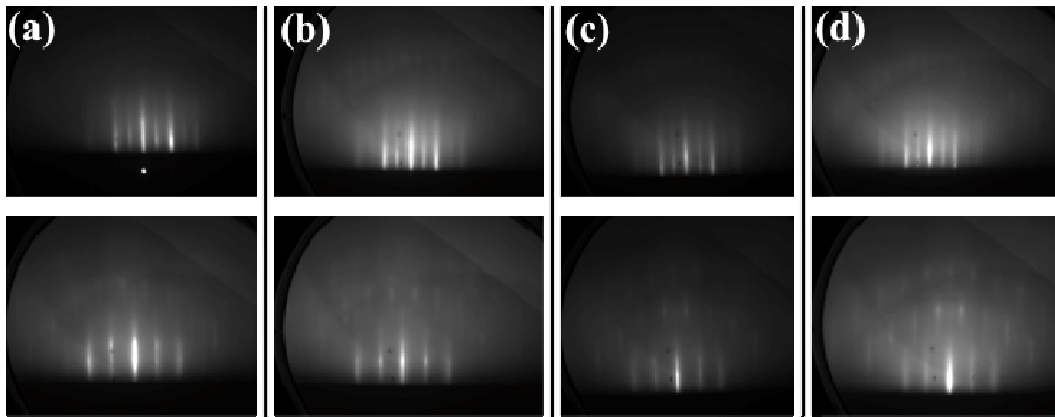


**Figure 6.3** – RHEED patterns recorded for thin-films of  $\text{Fe}_3\text{O}_4$  on reconstructed  $\text{MgO}(111) \sqrt{3} \times \sqrt{3}$  substrates (a)  $\sim 10$  nm  $\text{Fe}_3\text{O}_4$  (b)  $\sim 30$  nm  $\text{Fe}_3\text{O}_4$  (c)  $\sim 60$  nm  $\text{Fe}_3\text{O}_4$  (d)  $\sim 100$  nm  $\text{Fe}_3\text{O}_4$ . Samples were run by Dr. Zhuhua Cai.

The patterns shown in **Figure 6.3**, are assumed to correspond to  $\text{Fe}_3\text{O}_4$ : as RHEED is incapable of differentiating between  $\text{Fe}_3\text{O}_4$  and  $\gamma\text{-Fe}_2\text{O}_3$ , because their unit cell sizes are so similar (8.397 and 8.33 Å respectively)<sup>42</sup>. To this end, other techniques are required to determine the exact phase of iron oxide.

### 6.2.3 X-ray Photoelectron Spectroscopy (XPS)

XP spectra were recorded in order to aid in the determination of the phase of the iron oxide thin-films. In the case of samples prepared in the Northeastern MBE, XP spectra were recorded *in-situ*. For samples grown in the York MBE, XPS was run at the University of Oxford after thin-film growth. Representative spectra of the Fe 2p binding energy region for samples grown in the York MBE system are shown below in **Figure 6.4** (a) to (d).

**Figure 6.4** (a) and (b) show the recorded XP spectra for samples attributed to  $\text{Fe}_3\text{O}_4$  and  $\text{Fe}_2\text{O}_3$  respectively grown in the York MBE. To accentuate the trends and features, background subtracted and peak fitted spectra are shown in **Figure 6.4** (c) ( $\text{Fe}_3\text{O}_4$ ) and (d) ( $\text{Fe}_2\text{O}_3$ ). The background subtraction and peak fitting procedure was performed through the use of the computer programme CasaXPS version 2.3.15.

For both  $\text{Fe}_3\text{O}_4$  and  $\text{Fe}_2\text{O}_3$ , due to spin-orbit coupling, the Fe 2p core levels split into  $2p_{1/2}$  and  $2p_{3/2}$  components, situated at  $\sim 724$  eV and  $\sim 711$  eV, respectively.  $\text{Fe}_3\text{O}_4$

consists of both  $\text{Fe}^{2+}$  and  $\text{Fe}^{3+}$  cations, and as a result, the two Fe 2p states are quite broad, as they consist of both ions. Conversely, for  $\text{Fe}_2\text{O}_3$ , the Fe atoms are fully oxidised to  $\text{Fe}^{3+}$ , resulting in slightly sharper Fe 2p peaks. The ratio of these two fitted component peaks in the case of **Figure 6.4 (c)** is approximately 2:1, as would be expected for an  $\text{Fe}_3\text{O}_4$  thin-film.

In addition,  $\text{Fe}_2\text{O}_3$  also features a shake-up satellite peak (due to charge transfer screening), which exists between the Fe  $2p_{1/2}$  and  $2p_{3/2}$  components<sup>21, 43-47</sup>. This satellite is labeled in **Figure 6.4 (b)** by “ $\text{Fe}^{3+}$  sat”. This feature is accentuated in the background subtracted spectrum in **Figure 6.4 (d)**. This satellite is notably absent from both **Figures 6.4 (a)** and **(b)**, which easily allows  $\text{Fe}_3\text{O}_4$  to be distinguished from  $\text{Fe}_2\text{O}_3$ .

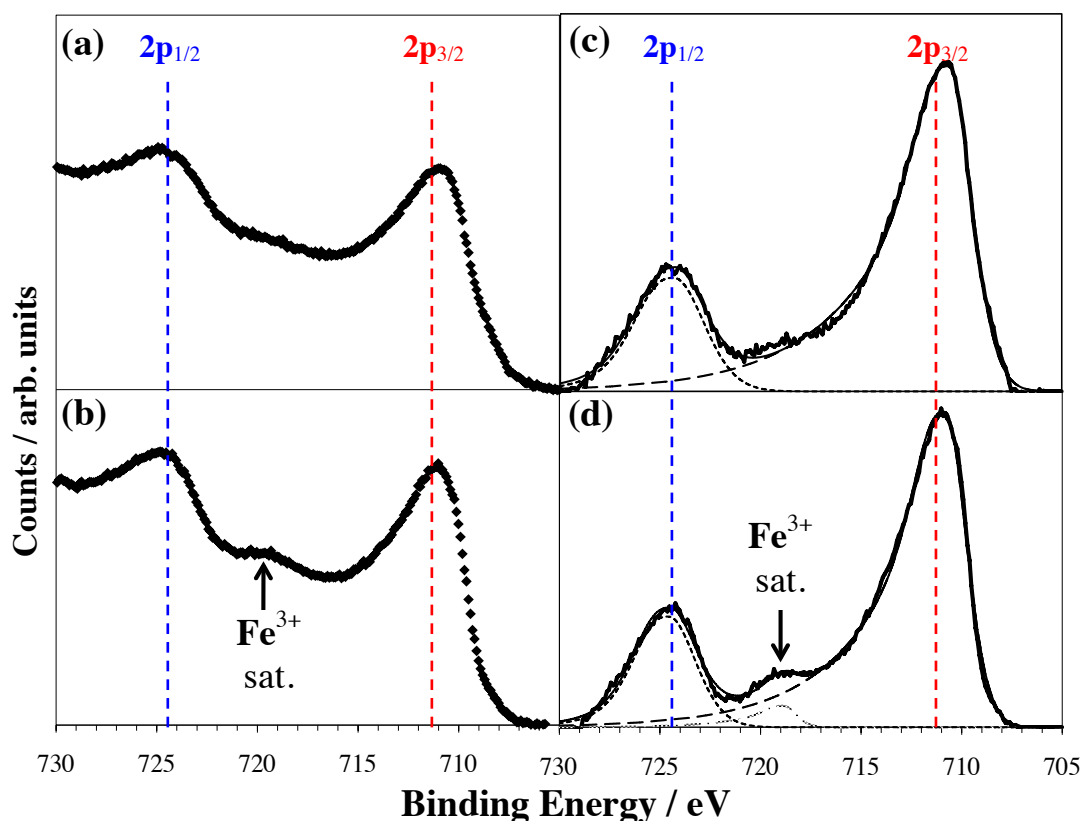


**Figure 6.4** – (a) A representative Fe 2p XP spectrum from a  $\text{Fe}_3\text{O}_4$  thin-film sample grown in the York MBE (b) A Fe 2p XP spectrum recorded from a  $\text{Fe}_2\text{O}_3$  thin-film sample grown in the York MBE, showing the characteristic  $\text{Fe}^{3+}$  satellite (c) Background subtracted and fitted intensities from the York  $\text{Fe}_3\text{O}_4$  sample (d) Background subtracted and fitted intensities from the York  $\text{Fe}_2\text{O}_3$  sample, again showing the characteristic  $\text{Fe}^{3+}$  satellite.

#### 6.2.4 Transmission Electron Microscopy (TEM)

In order to determine both sample film thickness and the atomic structure through the film, cross-sectional transmission electron microscopy (TEM) was employed. Samples were first cut using a diamond saw, polished by lapping pads and then glued together to allow several interfaces to be probed simultaneously. Once glued, samples were thinned further to  $\sim 200 \mu\text{m}$ , before the interface was ion milled by Precision Ion Polishing (PIPS) to a thickness of around 10 nm, so that they would be sufficiently electron transparent in order to be imaged by TEM. The full cross sectional sample preparation procedure can be found in the appendix.

Samples were prepared and imaged by Mr. James Sizeland, a MSc student under the supervision of the author. Two representative cross-sectional TEM images of a 18 nm  $\text{Fe}_3\text{O}_4/\text{MgO}(100)$  sample are shown in **Figure 6.5**. The images show a sharp interface between the two layers, indicating that samples are epitaxial. Also shown in the figure is a diffraction pattern (recorded in the  $[1 -1 0]$  zone) from the sample. The electron beam partially covered both the film and substrate; hence the diffraction pattern is a composite of both layers. The brighter and larger diffraction spots originate from the MgO, whereas the smaller, lower intensity spots can be attributed to  $\text{Fe}_3\text{O}_4$ . The unit cell of  $\text{Fe}_3\text{O}_4$  is approximately twice the size of MgO, hence the  $\text{Fe}_3\text{O}_4$  spots occur at intervals half-way through the MgO spots due to reciprocal space. These results are identical to those obtained by RHEED of the Northeastern samples (see section 7.2.2). These results were consistently observed for all MgO samples, and hence **Figure 6.5** is representative of the entire MgO sample series. The TEM measurements were also used to determine the exact thickness of thin-films.

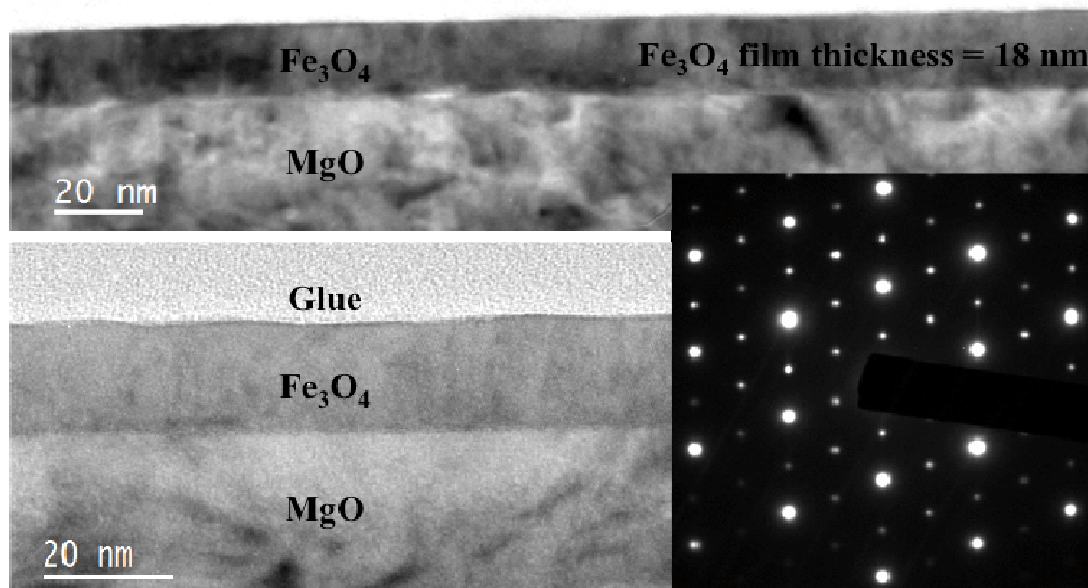


**Figure 6.5** – Cross sectional TEM of  $\text{Fe}_3\text{O}_4/\text{MgO}(100)$   $1 \times 1$  nominal thickness of 15 nm. Inset shows the electron diffraction obtained from the sample.

This sample was prepared and imaged by Mr. James Sizeland.

**Figure 6.6** is a high resolution cross sectional TEM image of a 60 nm  $\text{Fe}_3\text{O}_4/\text{MgO}(100)$  sample showing the atomic structure through the film. This image also shows that the interface between the two layers is relatively sharp. Fast Fourier Transform (FFT) was performed on the individual layers and is also displayed in the figure. These FFT images are akin to individual diffraction patterns from the two layers. From these images, it is clear that the distance between the spots in the iron oxide layer is approximately half that of the  $\text{MgO}$ . This means that in real space, the unit cell of the iron oxide phase grown is roughly twice the size of  $\text{MgO}$ , echoing the results obtained by RHEED and electron diffraction studies. This is further evidence that the correct phase of iron oxide has been grown on the desired substrate. A full analysis of a diffraction pattern in the  $[2\ 2\ 0]$  direction can be found in the appendix.

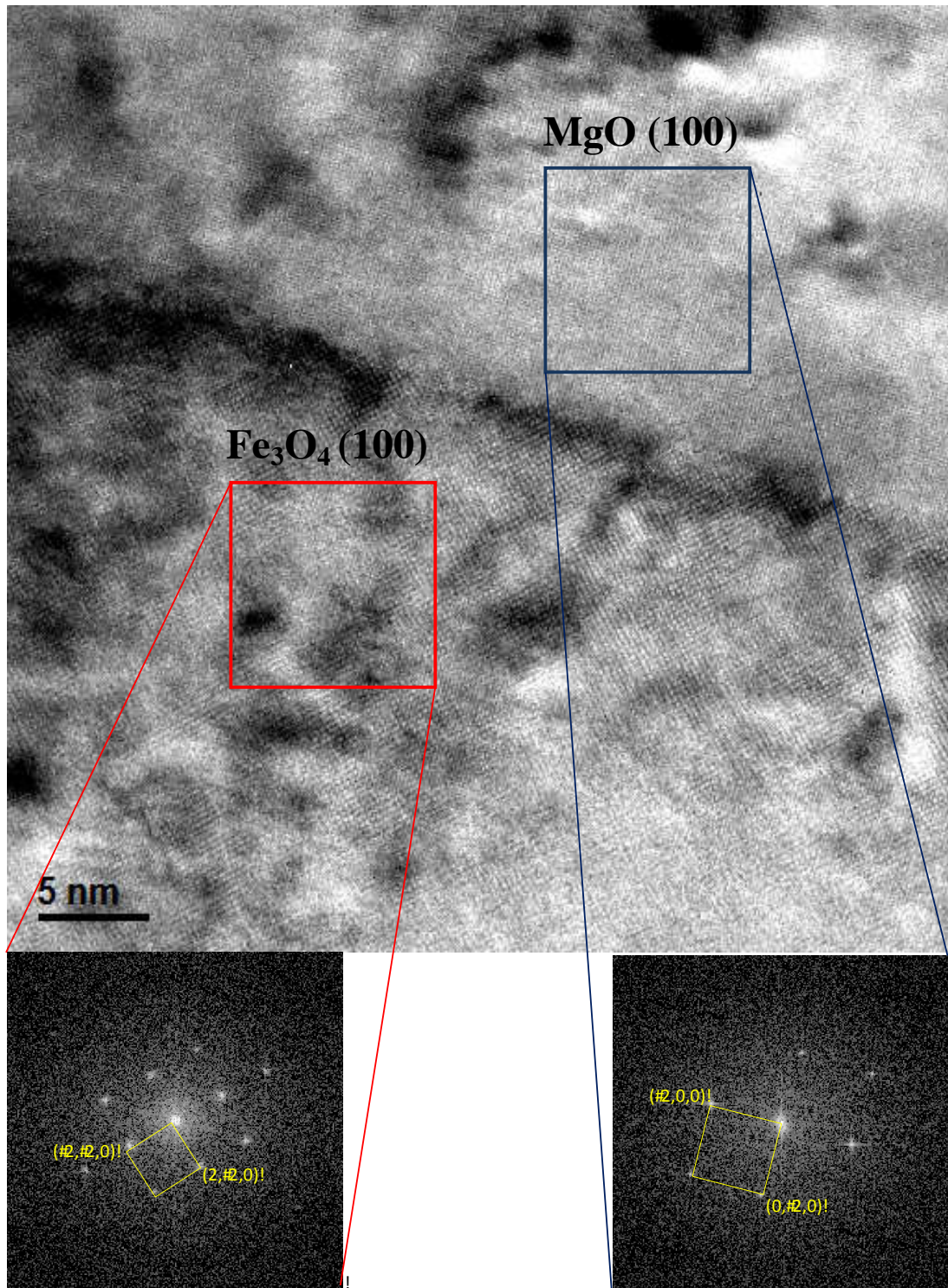


**Figure 6.6** – High resolution cross sectional TEM of an  $\text{Fe}_3\text{O}_4$  thin-film on  $\text{MgO}(100)$ , with corresponding FFT images from both the  $\text{Fe}_3\text{O}_4$  and  $\text{MgO}$  layers.

This sample was prepared and imaged by Mr. James Sizeland.

In order to confirm that samples contain APBs, a thin-film lift off procedure was utilised in order to obtain plan-view dark-field TEM images.  $\text{Fe}_3\text{O}_4$  thin-films were ‘lifted off’ the substrates by immersing samples in concentrated (4 wt%) solution of ammonium sulphate. The process was aided by heating the sample and solution to 70 °C in a water bath for 24 hours<sup>35, 39</sup>. The thin-film came off the substrate in small (~ 1 mm) pieces, which could be lifted off the liquid  $(\text{NH}_4)_2\text{SO}_{4(\text{aq})}$  surface onto a Cu TEM grid. The sample on the grid was then washed with a 50:50 mixture of ethanol and deionised water, before a final wash with deionised water. The grid was then allowed to dry at ambient temperature and then imaged by TEM. **Figure 6.7** is a plan view TEM sample of a thin-film of a 60 nm  $\text{Fe}_3\text{O}_4$  on  $\text{MgO}(100)$ . This image is representative of a wide range of samples prepared and imaged in the same way. The dark, angular lines in the image correspond to the defects that have formed as a result of  $\text{Fe}_3\text{O}_4$  thin-film growth on  $\text{MgO}$ . Similar images attributed to APB formation are widespread in the literature (see chapter 1, section 1.4.5).

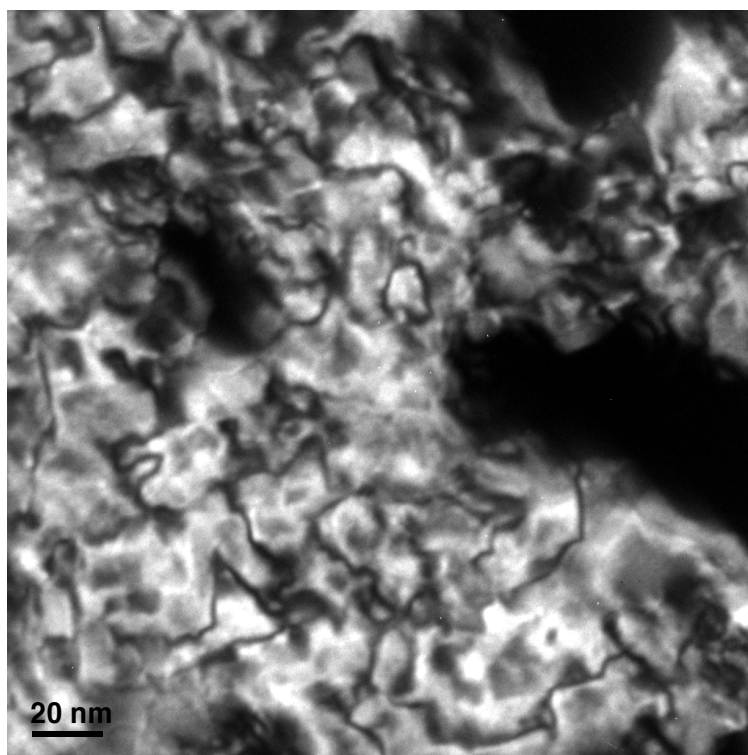


**Figure 6.7** – A representative dark field TEM plan view image of an  $\text{Fe}_3\text{O}_4$  thin film.

The film was lifted off the  $\text{MgO}(100)$  substrate using a concentrated solution of  $(\text{NH}_4)_2\text{SO}_4$ . The jagged lines in the figure correspond to the interfaces between the APBs in the thin-film. This sample was prepared and imaged by Mr. James Sizeland.

### 6.2.5 Vibrating Sample Magnetometry (VSM)

Vibrating Sample Magnetometry (VSM) was used to determine the remanence and coercivity of thin-film  $\text{Fe}_3\text{O}_4$  samples. The VSM data from  $\text{Fe}_3\text{O}_4$  samples on  $\text{MgAl}_2\text{O}_4(111)$  is shown below in Figure 6.8. The trends will first be described, before possible explanations are outlined at the end of the section. The main figure shows the hysteresis loops for a variety of  $\text{Fe}_3\text{O}_4$  film thicknesses on  $\text{MgAl}_2\text{O}_4(111)$  substrates. It should be noted that similar hysteresis curves were obtained for all samples, therefore Figure 6.8 can be said to be representative of all samples. The magnetic field scale (x axis) has been decreased in order to emphasise the shape of the curves, along with the coercivity and remanence. The inset shows the same hysteresis loops at full scale. Examining the curves in this figure, there is also no evidence of multiphase behaviour from data.

It should be noted that the samples have been mathematically corrected for the diamagnetic response of the substrate. This involved dividing the hysteresis loops by a gradient, which is assumed to correspond to the diamagnetic response. For reference, the magnitude and shape of this correction is also displayed in the figure. This correction, coupled with the fact that  $\text{Fe}_3\text{O}_4$  thin-films do not magnetically saturate in high fields<sup>33, 39</sup>, means that it is impossible to determine the magnetic saturation ( $M_s$ ) of samples. With that said, as the magnetisation has been normalised to the approximate volume of each thin-film, it can be observed that all films have approximately the same magnetisation at 15000 Oe and this is in the correct range for  $\text{Fe}_3\text{O}_4$ <sup>48</sup>. It is important to consider the fact that the volume of each sample was calculated from the area (measured by CCD) and nominal thickness of samples. As a result the error associated with this method of correction will be high.

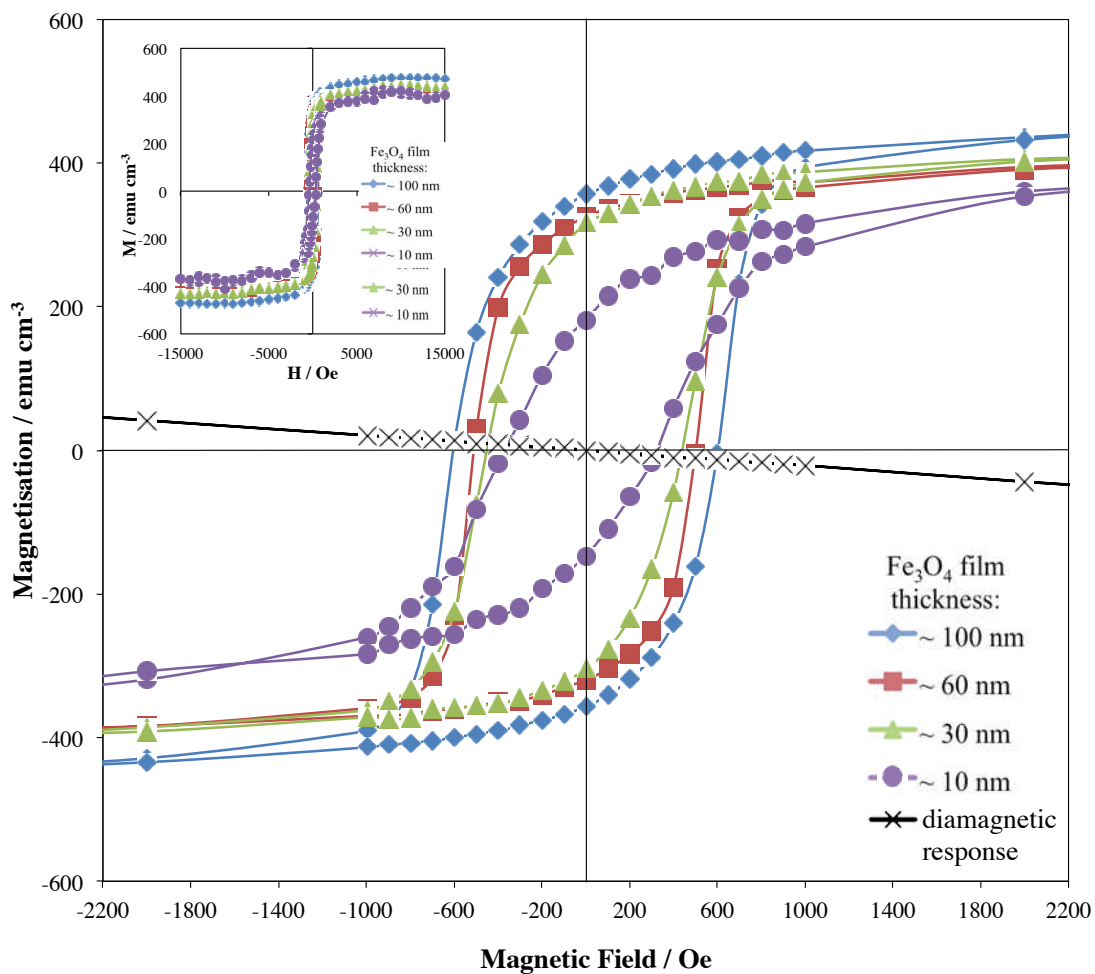


**Figure 6.8** – Representative VSM hysteresis loops for Fe<sub>3</sub>O<sub>4</sub> thin-film samples. The series shown is for various thicknesses of Fe<sub>3</sub>O<sub>4</sub> on MgAl<sub>2</sub>O<sub>4</sub>(111). Also shown in the figure is the diamagnetic response from the substrate, which was used to correct the recorded magnetic response from samples. The inset shows the same hysteresis loops over a larger field range.

From each set of hysteresis loops, values of coercivity were obtained for all samples and are shown in Figure 6.9. The displayed error bars were estimated from the known instrument error and from the noise in the data. It is worth stating that these measurements have a low associated error as they are measured at zero magnetisation, which is not affected by either the film volume correction or diamagnetic response correction. The coercivity ( $H_c$ ) is the magnetic field required to drive the magnetisation of the film to zero. This is essentially a measure of how easily the sample can be demagnetised. Materials are known as ‘hard’ magnets if they have high coercivities (as they are hard to demagnetise). Conversely, ‘soft’ magnets have low

coercive fields. Thus, the coercivity value can also usually be used to identify the material, as different substances have different, often characteristic, coercivity values.

For the MgO(111) 1x1 sample series shown in Figure 6.9, the coercivity of the sample increases with increasing film thickness, before levelling off at around a film thickness of 20 nm. Indeed, this general trend is mirrored by all of the samples. All samples have approximately the same coercivity at each nominal film thickness. Generally, there appears to be a larger variation in the coercivity for the thicker Fe<sub>3</sub>O<sub>4</sub> samples. The Fe<sub>3</sub>O<sub>4</sub> thin-films grown MgAl<sub>2</sub>O<sub>4</sub>, also have a higher coercivity when compared to the thin-films on other substrates, although the reason for this is unclear.

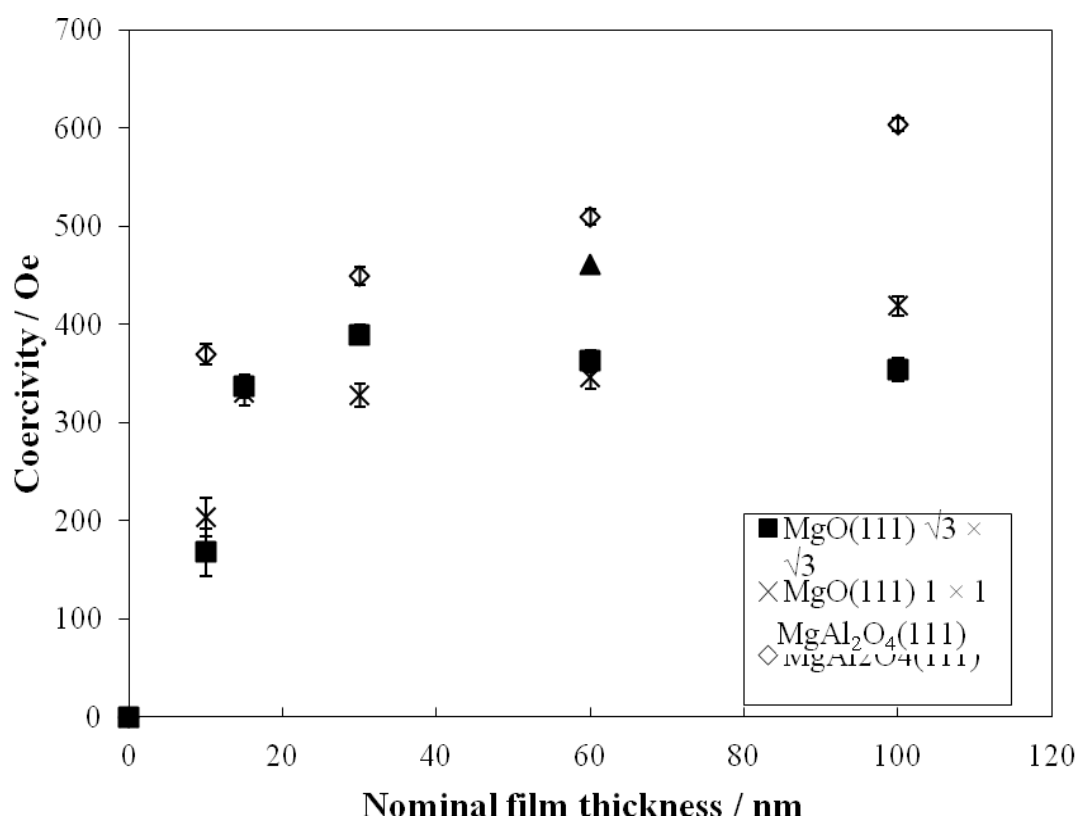


**Figure 6.9** – The coercivity values obtained from VSM data obtained for all thin-film Fe<sub>3</sub>O<sub>4</sub> samples prepared in the Northeastern and York MBEs.

The coercivity values from the literature for a variety of iron oxide thin-films are shown in **Table 6.3**. It was expected that it would be possible to identify the phase of iron oxide from the coercivity obtained by VSM. To a certain extent, this is true, as it is facile to discriminate between FeO (wüstite) and other forms of iron oxide, because wüstite has a coercivity of zero. However, from the **Table 6.3**, it is clear to see that

there is a huge variation in recorded values even for a single phase. This is because the coercivity depends upon a variety of different factors other than the film's chemical composition, including the microstructure of the film, the film thickness and any impurities present within the film. We also cannot compare the results to those obtained for bulk samples as thin-films deviate from bulk behaviour.

In addition to the fact that there are variations for single phases, the values for  $\text{Fe}_3\text{O}_4$ ,  $\alpha\text{-Fe}_2\text{O}_3$  and  $\gamma\text{-Fe}_2\text{O}_3$  are very similar. We can therefore only use the coercivity values shown in **Figure 6.9** to determine that the films do not contain FeO, and the coercivity is in the correct range for  $\text{Fe}_3\text{O}_4$  thin films. As the coercivity of thin-films of Fe are around 5 – 10 Oe, we can also conclude that the samples do not contain much (if any) iron.

<b>Material</b>	<b>Coercivity (<math>H_c</math>) / Oe</b>	<b>References</b>
FeO	0	49
Fe + $\text{Fe}_3\text{O}_4$	318	50
$\text{Fe}_3\text{O}_4$	~ 158, ~ 236, 271, ~280	49-51
$\text{Fe}_2\text{O}_3$	~ 236	49
$\gamma\text{-Fe}_2\text{O}_3$	269, 1150	50
$\alpha\text{-Fe}_2\text{O}_3 + \gamma\text{-Fe}_2\text{O}_3$	273	50
2.5 at% Co, 3.0 at% Cu	460 – 600	52
$\gamma\text{-Fe}_2\text{O}_3$		
3.0 at% Co, 3.0 at% Cu	520 – 540	52
$\gamma\text{-Fe}_2\text{O}_3$		

**Table 6.3** – Coercivity values for various iron oxide thin-films from literature.

From the VSM data, values were obtained for the remanent magnetisation at zero field for all samples, and are shown in **Figure 6.10**. Whilst the error associated with the physical measurement of the remanence values will be low, such measurements are highly reliant on upon the film volume correction. This film volume correction leads to a large overall error, as this correction is subject to estimating both the area and film thickness of a given sample. It is therefore important to be aware that whilst the overall trend will not be affected appreciably, there could be a large error in the

absolute value from this estimation. A similar trend is observed for the remanence as was observed for the coercivity, namely that the remanence increases with increasing thickness, but levels off at roughly 20 nm. The values obtained for the remanence for all samples are what would be expected for  $\text{Fe}_3\text{O}_4$ <sup>25</sup>.

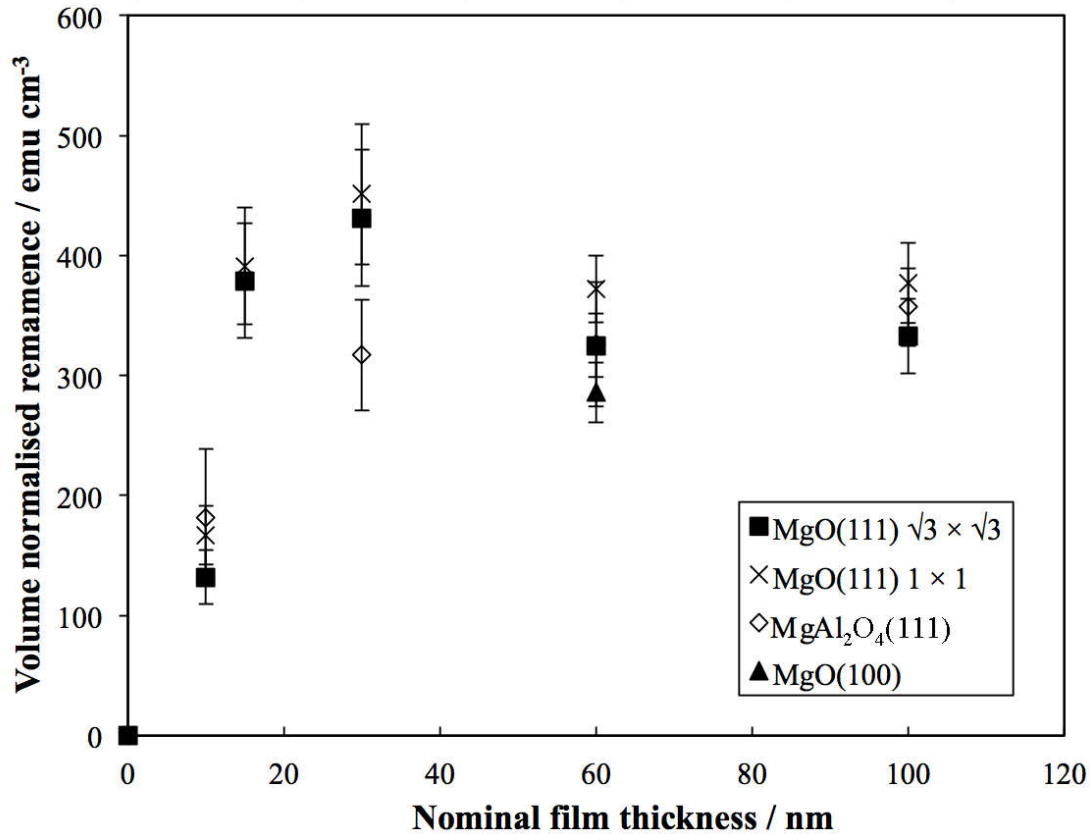


**Figure 6.10** – Remanence values obtained from VSM data obtained for all thin-film  $\text{Fe}_3\text{O}_4$  samples prepared in the Northeastern and York MBEs.

From **figures 6.8, 6.9** and **6.10** we can draw some conclusions from the general trends. It is clear from the VSM curves, an increasingly square hysteresis loop shape results as the film thickness increases. For low film thickness samples, switching is less rapid and it the hysteresis has an appearance akin to that of a magnetically hard axis loop. This hysteresis shape is probably due to stress in samples with low film thicknesses. This stress could be relieved by the formation of APBs, which would give rise to pinning sites and therefore result in a wider loop as the film thickness increases. It is very difficult to draw too many conclusions with such a small section of the M-H loop accessible from such low field measurements. As a result, future work could include using a high-field VSM to investigate these samples further.

## 6.2.6 Magnetoresistance (MR) measurements

The magnetoresistance (MR) of  $\text{Fe}_3\text{O}_4$  thin-films was determined by four-point probe measurements (as detailed in chapter 2, section 2.6.2). Films grown in the York MBE system with a composition corresponding to  $\text{Fe}_2\text{O}_3$  (as determined by XPS, see Figure 6.4 (b) and (d)) did not display any magnetoresistance, meaning that MR could also be used as an indirect method to determine the phase of iron oxide grown in MBE experiments.

A representative MR curve is shown in **Figure 6.11**. From this figure, it can be observed that the MR increases with increasing magnetic field, although no saturation occurs by  $\sim 1$  T. What is also interesting to note from the figure, is the appearance of two ‘humps’ in the MR at low field, which correspond to the coercivity of the sample. **Table 6.4** also displays the magnitude of the MR recorded at  $\sim 1$  T for all samples. All samples display roughly the same MR ( $\sim 1\%$ ) at  $\sim 1$  T. This is surprising, as one would expect there to be a thickness dependence in the MR within the same sample series, as it is known that the density of the APBs varies with film thickness<sup>22,35</sup>. One would also expect there to be a large variation in the MR between different sample sets, as the density of the APBs also depends upon the substrate surface structure. It is thought that the MR values are all approximately 1% as the samples clearly do not saturate in low fields.

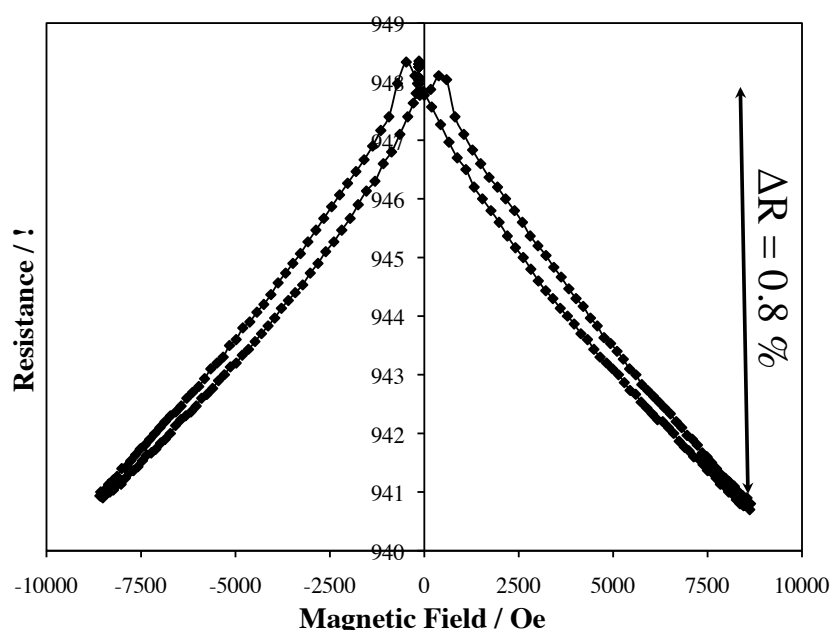


**Figure 6.11** – A representative MR curve from a thin-film of  $\text{Fe}_3\text{O}_4$  on MgO. The MR shown in the figure is from a 100 nm  $\text{Fe}_3\text{O}_4$  thin-film on MgO(111) substrate.

Substrate	Nominal thickness	Magnetoresistance
	/ nm	/ %
MgO(111)	100	0.8
	60	1.0
	30	1.0
	15	0.9
	10	0.9
	100	0.9
MgO(111) $\sqrt{3}\times\sqrt{3}$	60	1.1
	40	0.9
	15	0.9
	10	0.9
	100	1.35
MgAl <sub>2</sub> O <sub>4</sub> (111)	50	1.0
	30	0.8
	10	1.1
MgAl <sub>2</sub> O <sub>4</sub> (100)	10	1.2
MgO(100)	60	1.2

**Table 6.4** – A table to show the nominal thickness and electrical MR of all samples prepared in the York and Northeastern MBE systems.

### 6.2.7 Skin depth measurements

An important optical quantity, the skin depth, can be determined from the conductivity of a material. Skin depth,  $\delta$ , is defined as the depth to which electromagnetic radiation can penetrate a particular conducting surface. In any conductive material, electromagnetic radiation will penetrate the surface and will be attenuate by  $1/e$ , in a given distance,  $\delta$ . This quantity is important, as we shall be examining the infrared and MRE spectra later on in this chapter.

The skin depth for a given material is dependent upon the electrical conductivity of the material and the frequency of incident radiation. The conductivity,  $\sigma$  (in  $\Omega\text{m}^{-1}$ ), of a given film of thickness,  $t$  (in m), is related to resistance,  $R$  (in  $\Omega$ ), of the material

according to **Equation 6.1**. This is an equation specific to the geometry of the four-point-probe method used to measure the magnetoresistance of thin-film samples<sup>53</sup>.

$$\sigma = \frac{\ln 2}{\pi t R} \quad \text{Equation 6.1}$$

From the conductivity, the skin depth can be calculated as follows:

$$\delta = \sqrt{\frac{2}{\sigma \omega \mu_0}} \quad \text{Equation 6.2}$$

where,  $\omega$  is the angular frequency ( $2\pi f$ , in  $s^{-1}$ ) and  $\mu_0$  is the permittivity of free space ( $\Omega s m^{-1}$ ). In this case, the frequency that corresponds to the infrared resonance of  $Fe_3O_4$  was used in order to calculate the skin depth. The skin depth was calculated according to the resistance of thin-film  $Fe_3O_4$  samples recorded at zero field during magnetoresistive measurements (see section 7.2.6).

A representative graph of the skin depth of  $Fe_3O_4$  thin-film samples is shown below in **Figure 6.12**. The general trend is that for very thin-films of  $Fe_3O_4$ , the skin depth drops off rapidly as the film thickness increases and then remains relatively constant at approximately 3000 nm. For all thin-films the calculated skin depths are large, being several thousand nanometres in magnitude. To put this into context, a 100 nm thin-film of Au, with a resistivity,  $\rho$ , of  $2.2 \times 10^{-8} \Omega m$  (and therefore a conductivity ( $\sigma=1/\rho$ ) of  $4.5 \times 10^5 \Omega m^{-1}$ ) at the same infrared frequency would have a skin depth of  $\sim 20$  nm.

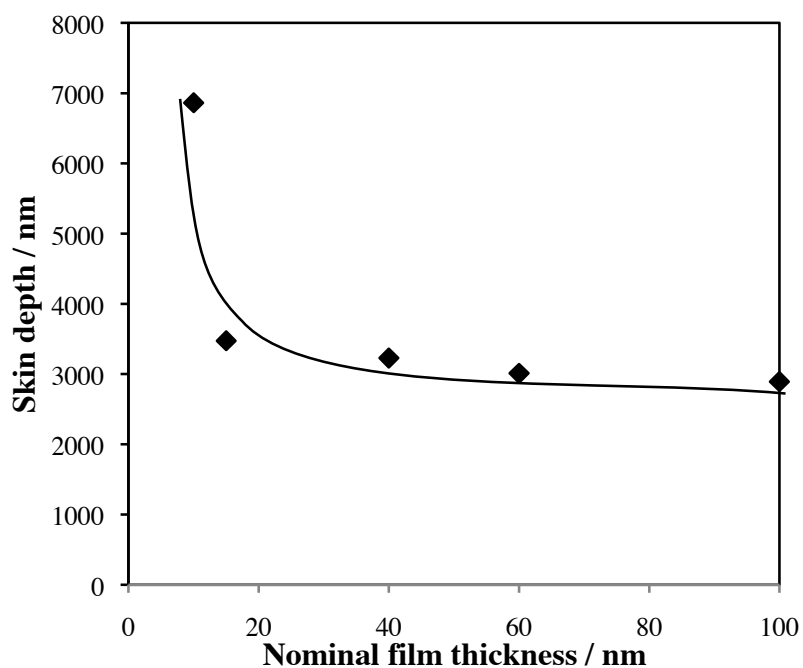


**Figure 6.12** – The skin depth calculated for thin-film Fe<sub>3</sub>O<sub>4</sub> samples on MgO(111).

These results show that for the Fe<sub>3</sub>O<sub>4</sub> samples, in order for no infrared light to probe the substrate, a film thickness of over 3000 nm would be required. As Fe<sub>3</sub>O<sub>4</sub> has such a high resistivity (and therefore a low conductivity) for thin-films the IR light will always probe the substrate.

### 6.2.8 Infrared Spectroscopy

Light in the infrared region of the electromagnetic spectrum is frequently used in spectroscopy, as vibrational modes in many atoms and molecules are resonant at such wavelengths. MgO, MgAl<sub>2</sub>O<sub>4</sub> and Fe<sub>3</sub>O<sub>4</sub> have many spectral features that are sensitive to IR light. Transverse and longitudinal phonon modes are excited which are associated with the stretching and bending modes of the Mg-O, Al-O and Fe-O bonds.

As phonon resonances appear at characteristic frequencies for different compounds, infrared reflectivity spectra can be used to identify composition. To this end, **Table 6.5** below shows phonon resonances for pertinent substrates and thin-films involved in this study. Historically, spectral features were measured using the units of wavenumber ( $k / \text{cm}^{-1}$ ), which is the reciprocal of the wavelength. This practice is continued here, as it is the established convention for spectroscopic results.

<b>Phonon resonances</b>			
<b>Material</b>	<b>Transverse optic modes <math>k_{TO} / \text{cm}^{-1}</math></b>	<b>Longitudinal optic modes <math>k_{LO} / \text{cm}^{-1}</math></b>	<b>Reference(s)</b>
<b>Substrates:</b>			
MgO	401, 640	729	54, 55
MgAl <sub>2</sub> O <sub>4</sub>	485, 670	630, 855	56-58
<b>Thin-films:</b>			
FeO	290	535	59
$\alpha$ -Fe <sub>2</sub> O <sub>3</sub>	299, 437, 526, 524	414, 494, 662	18, 60-62
$\gamma$ -Fe <sub>2</sub> O <sub>3</sub>	440, 550	453, 572	19, 61, 63
Fe <sub>3</sub> O <sub>4</sub>	330, 540	576	19, 61, 63, 64

**Table 6.5** – Literature values for the various resonant phonon modes for both substrates and thin-films.

Infrared spectra of thin-film samples were obtained in reflection using a Nicolet FTIR spectrometer coupled to an MCT detector. The setup is housed in a purpose built CO<sub>2</sub> scrubbed perspex chamber containing hygroscopic crystals. The full setup is described in chapter 2, section 2.6.3. In order to remove any remaining CO<sub>2</sub> and H<sub>2</sub>O peaks from spectra, all IR results were normalised to the spectrum of a sputtered ~ 100 nm Au film, as Au does not contain any resonances in this IR wavelength range.

Spectra for a range of Fe<sub>3</sub>O<sub>4</sub>/MgO(111) samples are below shown in **Figure 6.13**. From data in **Table 6.5**, we can identify the appearance of an Fe<sub>3</sub>O<sub>4</sub> peak at approximately 540 cm<sup>-1</sup>, which increases in size with increasing film thickness. We can confidently assign this as Fe<sub>3</sub>O<sub>4</sub> and not  $\alpha$ -Fe<sub>2</sub>O<sub>3</sub> or  $\gamma$ -Fe<sub>2</sub>O<sub>3</sub> due to the absence of additional TO resonances at 437 cm<sup>-1</sup> ( $\alpha$ ) or 440 cm<sup>-1</sup> ( $\gamma$ ). The magnitudes of the MgO resonances decrease with increasing Fe<sub>3</sub>O<sub>4</sub> film thickness. It is therefore clear that spectra are consistent with an increasing Fe<sub>3</sub>O<sub>4</sub> film thickness on an MgO substrate.

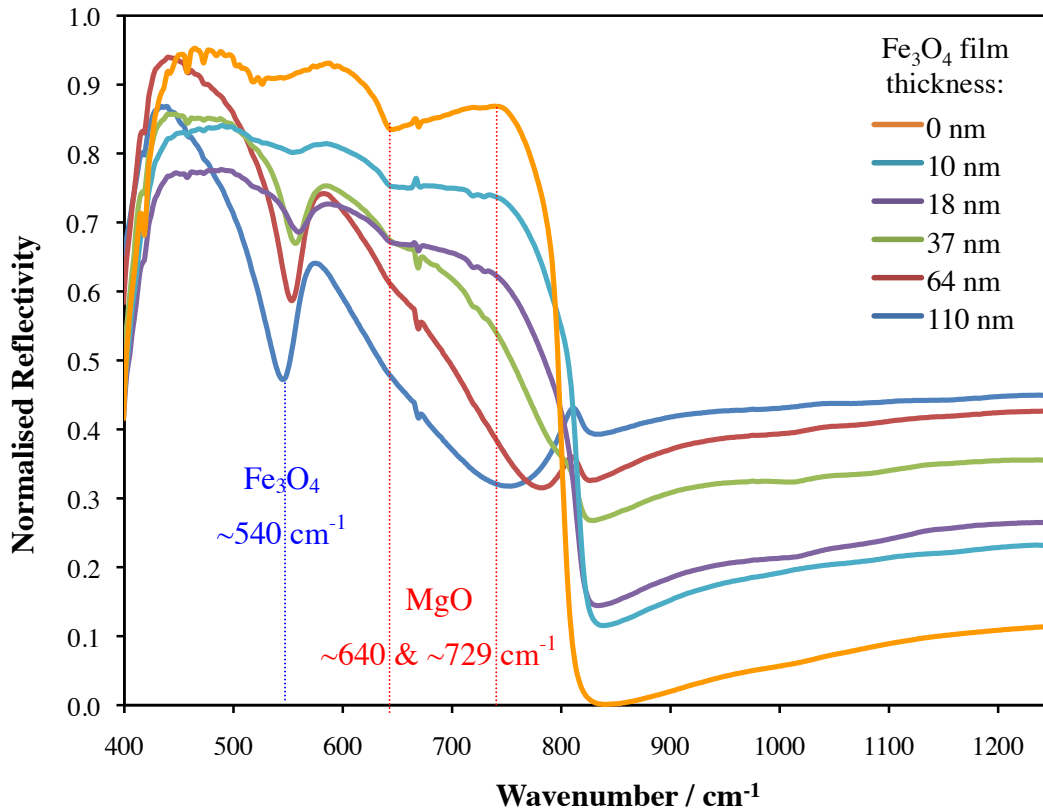


**Figure 6.13** – Infrared spectra recorded for the thin-film Fe<sub>3</sub>O<sub>4</sub>/MgO(111) samples

In sections 7.2.2 to 7.2.7 we have shown by several methods that we have formed various thin-films of the desired phase of iron oxide (Fe<sub>3</sub>O<sub>4</sub>), which all display magnetoresistance. As a result, it was possible to perform magneto-optical measurements in order to examine the magnetotransport within such materials.

### 6.2.9 Magnetorefractive Effect (MRE) measurements

The optical conductivity for magnetoresistive samples changes when a magnetic field is applied. This change is also associated with a significant change in the refractive index of the material<sup>1</sup>, known as the magnetorefractive effect. This effect can be measured by taking the ratio of the change in reflectivity due to an applied magnetic field ( $\Delta R$ ) to the reflectivity recorded solely in a magnetic field ( $R_H$ ). This is represented mathematically in **Equation 6.3**:

$$\text{MRE}(\%) = \frac{\Delta R}{R} \times 100 = \frac{R_0 - R_H}{R_H} \times 100 \quad \text{Equation 6.3}$$

where  $R_0$  is the IR reflectivity in zero field, and  $R_H$  is the IR reflectivity in an applied magnetic field.

MRE spectra were obtained for the same samples shown in the infrared measurements in **Figure 6.13**. As the samples do not display a large magnetoresistance, the magnetorefractive effect will also be small in magnitude. As a result, 500 scans at a resolution of  $4\text{ cm}^{-1}$  were taken and averaged in order to produce MRE spectra. It should also be noted that due to constraints imposed by the apparatus, spectra were recorded with an incident beam angle of approximately  $60^\circ$  to the sample normal, which may not be the optimum.

Representative stacked MRE spectra for a variety of  $\text{Fe}_3\text{O}_4$  film thicknesses are shown below in **Figure 6.14**. All samples display an MRE, and despite the samples not saturating magnetically the magnitude and position varies with film thickness. Also shown in the figure is the average spectrum for the 110 nm  $\text{Fe}_3\text{O}_4$  film obtained from the subtraction of IR spectra recorded at zero field (after sweeping through the hysteresis loop). This shows a flat line at 0 %, meaning that all peaks recorded in the MRE spectra are genuine and not artefacts. Essentially the same result is found if such spectra are acquired in high field (1.2 T) – again highlighting the fact that MRE spectra can only be obtained from the difference of IR spectra acquired in field and at zero field.

The spectra are complicated by the fact that the skin-depth for  $\text{Fe}_3\text{O}_4$  is large (see section 7.2.7) and therefore the IR light probes not only the film, but also the substrate. In order to understand this film thickness dependence and the MRE spectra generally, a theoretical model is required, which will be addressed in the next section of this chapter.

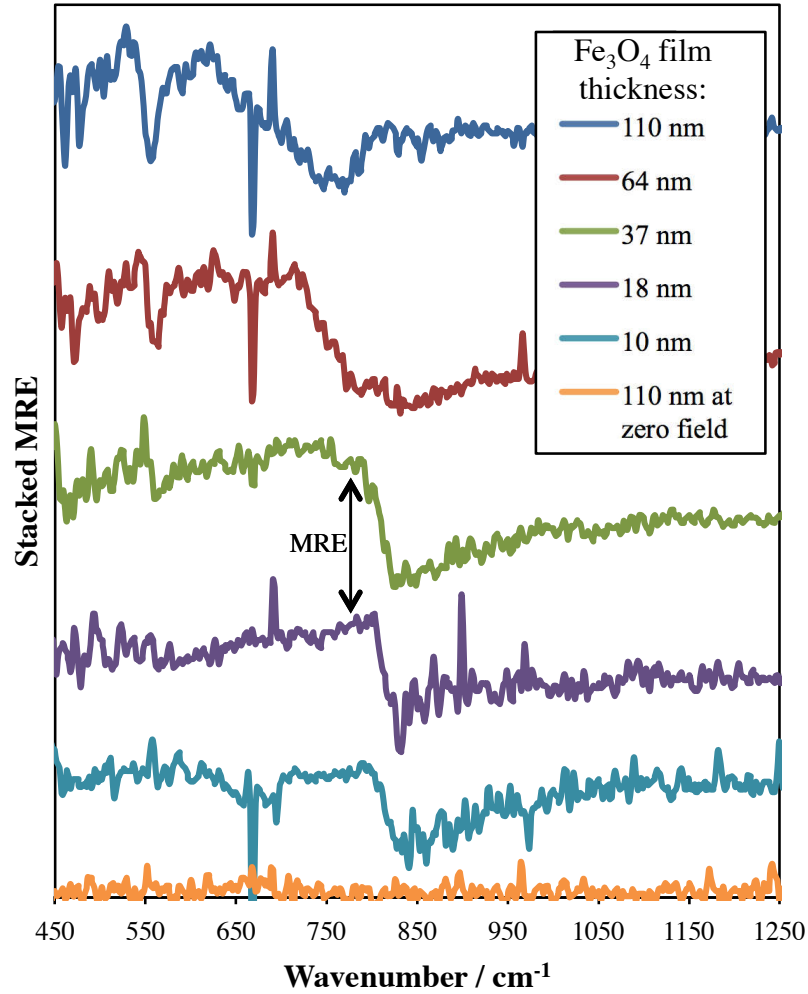


**Figure 6.14** – Stacked MRE spectra recorded for the  $\text{Fe}_3\text{O}_4/\text{MgO}(111)$  samples.

### 6.2.10 MRE modelling

The MRE for simple metallic thin-film multilayers varies linearly with film thickness. However, as we have observed, MRE spectra for oxide thin-films is complicated by the relatively large skin depth in such materials. As a result, MRE spectra greatly vary with increasing film thickness. It is therefore important to model and simulate the MRE in order to understand not only the thickness variation, but also to examine the various conductivity mechanisms present within such materials.

#### 6.2.10.1 The complex dielectric function

The optical properties of any given material are determined by its complex dielectric function,  $\epsilon(\omega)$ . A simple theoretical model of the MRE of a given system can therefore be constructed by determining the form of the complex dielectric function<sup>65</sup>.

### 6.2.10.2 The Drude model

For a metallic system, the complex dielectric function,  $\epsilon(\omega)$  varies linearly with the frequency-dependent conductivity,  $\sigma(\omega)$  according to the Drude (free electron) relation<sup>66</sup>, as shown below.

$$\epsilon_{\text{Drude}}(\omega) = \epsilon(\infty) + \frac{i\sigma(\omega)}{\omega\epsilon_0} \quad \text{Equation 6.4}$$

where  $\omega$  is the frequency of the incident radiation,  $\epsilon_0$  is the permittivity of free space ( $8.85 \times 10^{-12} \text{ F m}^{-1}$ ) and  $\epsilon(\infty)$  is the high frequency response ( $\omega = \infty$ ) of the dielectric function to optical excitation of frequency  $\omega$ .  $\epsilon(\infty)$  is therefore a constant which is material specific.

### 6.2.10.3 Plasma frequency

The natural frequency of oscillation of electrons in a plasma displaced relative to the ion background is known as the plasma frequency,  $\omega_p$ . This frequency determines whether or not waves can propagate in the medium. If  $\omega < \omega_p$  then waves can not propagate and incident waves of lower frequency than the plasma frequency will be reflected.

We can express **Equation 6.4** in terms of this plasma frequency<sup>67,68</sup>:

$$\epsilon(\omega) = \epsilon(\infty) + \frac{i\sigma(\omega)}{\omega\epsilon_0} = \epsilon(\infty) - \frac{\omega_p^2}{\omega^2 + i\gamma\omega} \quad \text{Equation 6.5}$$

where  $\gamma$  is a damping term.

Infrared (IR) light has a frequency lower than the plasma frequency, and is therefore reflected. This forms the basis of an MRE experiment; which uses IR light to probe the changes in the reflectivity of the sample when an external magnetic field is applied.

The plasma frequency is directly related to the number of free carriers (N) and can be described according to the following relationship:

$$\omega_p = \sqrt{\frac{Ne^2}{m_e \epsilon_0}} \quad \text{Equation 6.6}$$

where  $e$  is the charge on the free electron ( $1.60 \times 10^{-19}$  C), and  $m_e$  is the effective mass of the electron ( $\sim 9.11 \times 10^{-31}$  kg for a free electron).

The number of free carriers in a ‘conventional’ metal is of the order of  $10^{28}$  per  $m^3$ . However, for  $Fe_3O_4$ ,  $N$  will obviously be significantly lower than that for a metal, so a relatively low plasma frequency will result.

#### 6.2.10.4 Phonon resonances

IR spectral features reveal resonances in the system, as phonon modes are resonant for specific frequencies of the incident light. Phonon resonances are an integral part of the response of a system to an optical stimulus, and as a result they must be included into the dielectric function for the material. Both the transverse optic and longitudinal optic modes can be incorporated into the complex dielectric by treating the  $j$  resonances of the system as the sum of a series of simple harmonic oscillators. The following resonance term can therefore be added to the overall dielectric function:

$$\sum_{j=1}^n \frac{S_j^2}{k_j^2 - k^2 - i\gamma_j k} \quad \text{Equation 6.7}$$

where  $k_j$  is the wavenumber (of the  $j^{\text{th}}$  resonance),  $k$  is the wavenumber of the incident light,  $\gamma_j$  is a damping term for the resonance and  $S_j$  is the oscillator strength.

This phonon resonance term can be added to the Drude term giving the following form for the complex dielectric function:

$$\epsilon(\omega) = \epsilon(\infty) - \frac{\omega_p^2}{\omega^2 + i\gamma\omega} + \sum_{j=1}^n \frac{S_j^2}{k_j^2 - k^2 - i\gamma_j k} \quad \text{Equation 6.8}$$

#### 6.2.10.5 Fresnel equations

Provided the angle of incidence ( $\varphi$ ) is known, the complex dielectric function can be used to calculate the reflectivity coefficient according to the Fresnel equations. As previously mentioned, due to constraints imposed by the apparatus, spectra were recorded with an incident beam angle of approximately  $60^\circ$  to the sample normal, and hence this value is used in the modelling. This angle may not be the optimum and this should be considered in future modelling. It is important to consider the polarisation

of light at this stage, so we must construct two equations (**Equation 6.9** and **7.10**) for the electric field polarised perpendicular and parallel to the plane of incidence.

$$r^s = \frac{\cos \varphi - \sqrt{\varepsilon(\omega) - \sin^2 \varphi}}{\cos \varphi + \sqrt{\varepsilon(\omega) - \sin^2 \varphi}} \quad \text{Equation 6.9}$$

$$r^p = \frac{\cos \varphi \varepsilon(\omega) - \sqrt{\varepsilon(\omega) - \sin^2 \varphi}}{\cos \varphi \varepsilon(\omega) + \sqrt{\varepsilon(\omega) - \sin^2 \varphi}} \quad \text{Equation 6.10}$$

$r^s$  is the reflectivity coefficient for light where the electric field is polarised perpendicular to the plane of incidence. Conversely,  $r^p$  is the reflectivity coefficient for light where the electric field is polarised parallel to the plane of incidence. This polarisation is illustrated below in **Figure 6.15**.

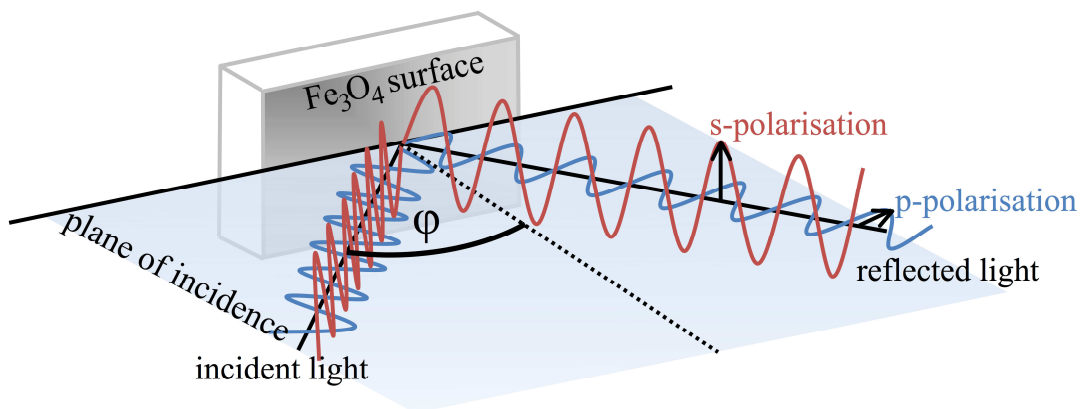


**Figure 6.15** – A diagram showing the electric field polarisation of light at the Fe<sub>3</sub>O<sub>4</sub> surface. The two polarisations result from the electric field being perpendicular (s) and parallel (p) to the plane of incidence.

A reflectivity spectrum can be determined from the mean of the magnitude of the squares of the reflection coefficients for each polarisation.

$$R^{s,p} = \frac{|r^s|^2 + |r^p|^2}{2} \quad \text{Equation 6.11}$$

### 6.2.10.6 Modelling parameters

In order to effectively simulate IR reflectivity spectra for thin-films of Fe<sub>3</sub>O<sub>4</sub>, several parameters needed to be input into the model described above. Values for the high frequency response, number of free carriers and relaxation time were obtained from literature in order to determine the plasma frequency and hence the Drude term in the complex dielectric function. Parameters ( $k_j$ ,  $\gamma_j$  and  $S_j$ ) were also gathered from the literature in order to simulate the phonon resonances, which also contribute to the complex dielectric function. Further parameters were also incorporated which are used to determine the Fe<sub>3</sub>O<sub>4</sub> d-to-s transition, manifested as an additional resonance, as simulated by Degiorgi et al<sup>64</sup>. The full list of parameters determined from previous studies into the Fe<sub>3</sub>O<sub>4</sub> and MgO systems are detailed in **Table 6.6**.

<b>Substrate resonance parameters</b>	<b>j = 1</b>	<b>j = 2</b>
MgO $k_j / \text{cm}^{-1}$	396	643
MgO $\gamma_j / \text{cm}^{-1}$	7.60	90
MgO $S_j$	6.80	0.043
<b>Thin-film resonance parameters</b>	<b>j = 1</b>	<b>j = 2</b>
Fe <sub>3</sub> O <sub>4</sub> $k_j / \text{cm}^{-1}$	330	540
Fe <sub>3</sub> O <sub>4</sub> $\gamma_j / \text{cm}^{-1}$	40	44
Fe <sub>3</sub> O <sub>4</sub> $S_j$	996	821
<b>Thin-film d-s transition</b>		
Fe <sub>3</sub> O <sub>4 d-s</sub> $k_j / \text{cm}^{-1}$	4954	
Fe <sub>3</sub> O <sub>4 d-s</sub> $\gamma_j / \text{cm}^{-1}$	4333	
Fe <sub>3</sub> O <sub>4 d-s</sub> $S_j$	11920	
<b>Other parameters</b>		
MgO $\epsilon_\infty$	3.01	
Fe <sub>3</sub> O <sub>4</sub> $\epsilon_\infty$	4.6	
$\gamma / \text{Hz}$	$1.01 \times 10^{15}$	
$N / \text{m}^{-3}$	$1.86 \times 10^{26}$	

**Table 6.6** – The various modelling parameters necessary in order to calculate infrared reflectivity spectra for Fe<sub>3</sub>O<sub>4</sub> films and MgO substrates

MgO parameters were obtained from Ahn, Choi and Noh<sup>54,55</sup>.

Fe<sub>3</sub>O<sub>4</sub> modelling parameters were converted from Degiorgi, Wachter and Ihle<sup>64</sup>.

The damping term ( $\gamma$ ) and number of free carriers (N) were taken from Šimša **Error!**  
**Hyperlink reference not valid..**

The above modelling parameters were used to calculate infrared reflectivity spectra for the bare MgO substrate and a bulk Fe<sub>3</sub>O<sub>4</sub> sample. **Figure 6.16** shows the modelled reflectivity spectrum for the MgO substrate along with the experimentally determined spectrum. It is clear that the simulated MgO data fits the experimental data well.

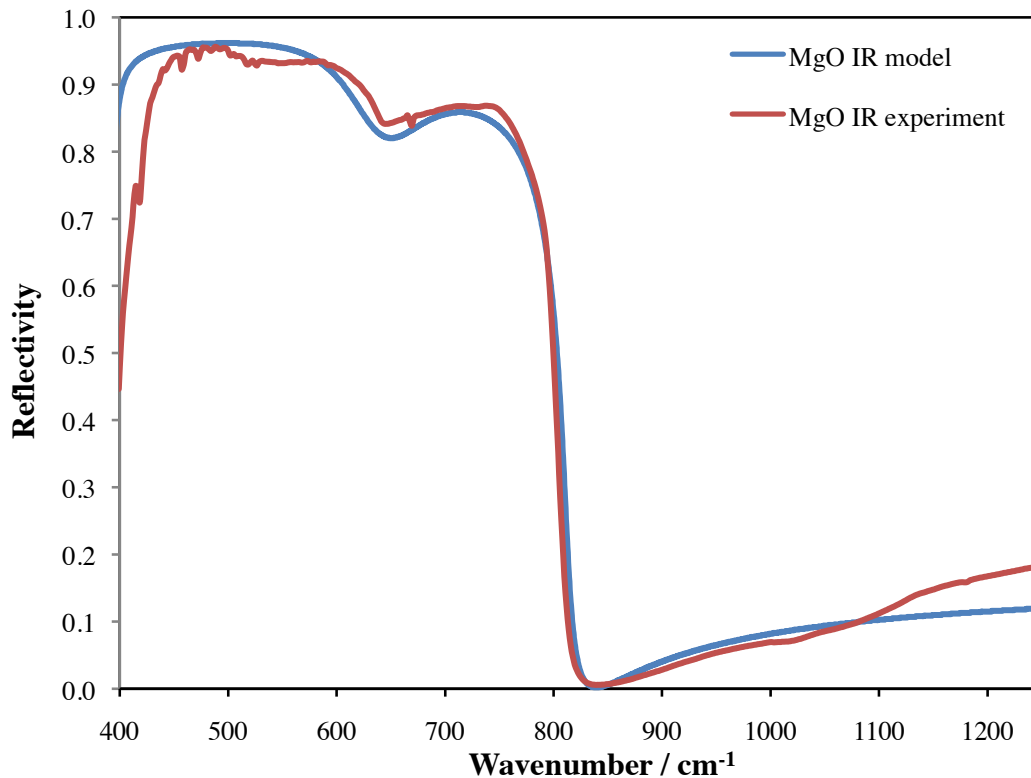


**Figure 6.16** – A modelled infrared reflectivity spectrum for the bare MgO substrate using the parameters from Table 6.6. For comparison, an experimentally determined spectrum is also shown in the figure.

The parameters from **Table 6.6** were also used to model the reflectivity spectrum for a bulk like Fe<sub>3</sub>O<sub>4</sub> crystal and these data are presented in **Figure 6.17**. Also shown in the figure are data from Gasparov et al., who have experimentally determined the reflectivity spectrum for Fe<sub>3</sub>O<sub>4</sub><sup>70</sup>. As with the bare substrate, the model and experiment are in good agreement.

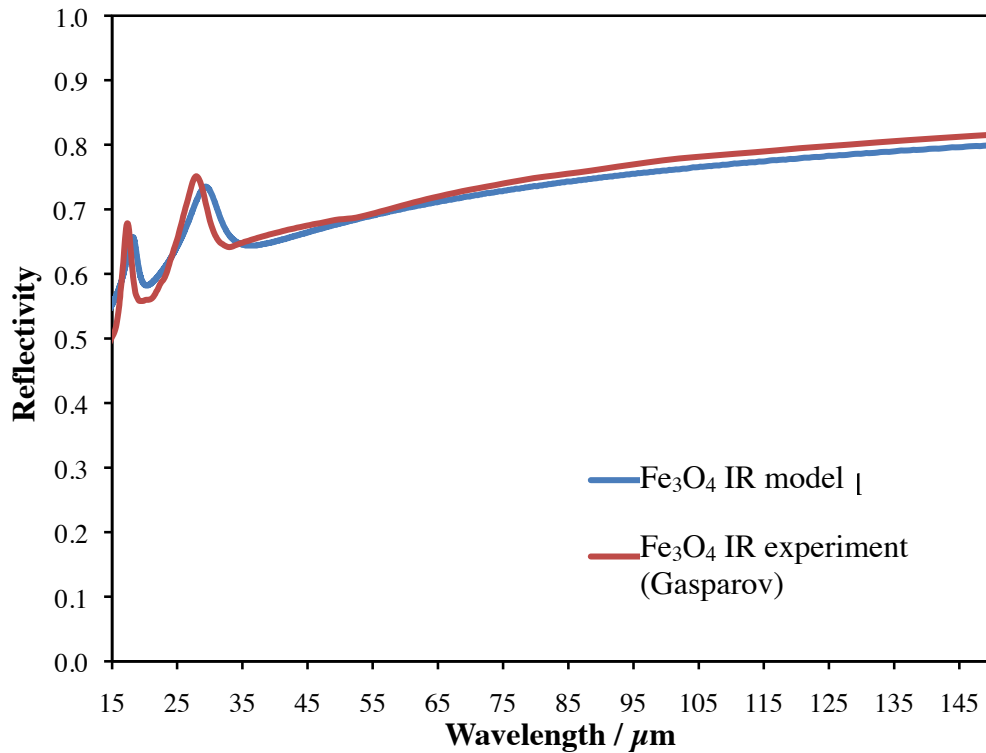


**Figure 6.17** – The modelled reflectivity spectrum for a bulk Fe<sub>3</sub>O<sub>4</sub> sample, along with experimentally determined spectra from Gasparov<sup>70</sup>.

Further modelling was required in order to combine the complex dielectric for the substrate and bulk crystal in order to obtain reflectivity spectra equivalent to thin-film samples.

#### **6.2.10.7 Multiple reflections**

In order to determine the reflectivity spectra for thin-films of Fe<sub>3</sub>O<sub>4</sub> on MgO, a multiple reflection model was adopted<sup>71-74</sup>, where the Fresnel reflectivity coefficients for a three-phase system were determined (as shown in **Figure 6.18**).

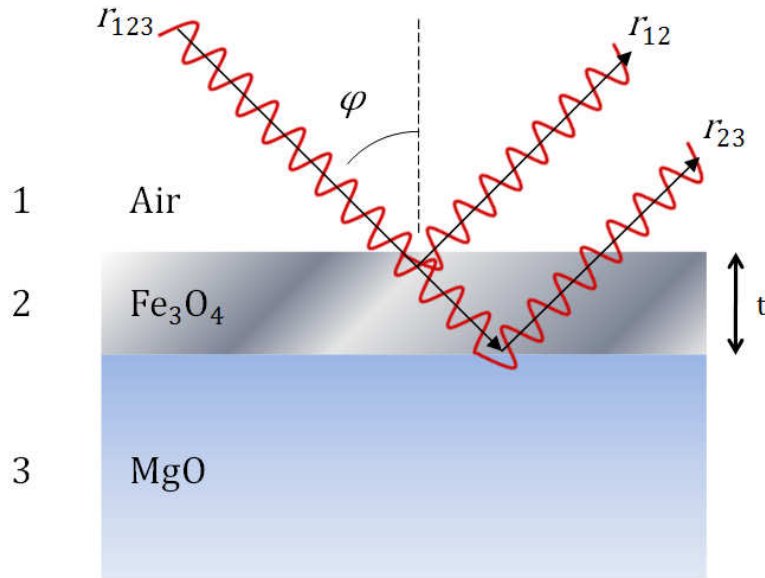


**Figure 6.18** – A diagram representing a multiple reflection model for infrared reflectivity of thin-films of Fe<sub>3</sub>O<sub>4</sub> on MgO.

The Fresnel reflection coefficient for the interface of two phases is defined as the ratio of the complex amplitudes of the electric field vectors of the reflected and incident waves<sup>72</sup>. As we have seen from **Equations 7.9** and **7.10**, this quantity is dependent upon the polarisation of the incident beam and the angle of incidence. Therefore, for any phase *i*, the angular dependent quantity,  $\xi_i$  is defined as:

$$\xi_i = n_i \cos \varphi = \sqrt{n_i^2 - n_1^2 \sin^2 \varphi} = \sqrt{\epsilon_i - \epsilon_1 \sin^2 \varphi} \quad \text{Equation 6.12}$$

where  $n_i$  is the complex index of refraction of phase *i*,  $n_1$  is the complex index of the ambient phase,  $\epsilon_i$  is the complex dielectric of phase *i*,  $\epsilon_1$  is the complex dielectric of the ambient phase and  $\varphi$  is the angle of incidence.

The Fresnel reflection coefficient of the interface between phases 1 and 2 in **Figure 6.19** for s- and p-polarisations are shown in **Equations 6.13** and **6.14**. Ordinarily, **Equation 6.13** would also contain the permeabilities of each layer when examining the reflectivity of thin-films, however, the magnetic permeability can be considered to be unity in the optical range<sup>72</sup>. Hence we can discount these terms, so the only

important parameters for the calculation of reflectivity for s and p polarisations are the permittivities and angular dependent quantities for each of the phases.

$$r_{12}^s = \frac{\xi_1 - \xi_2}{\xi_1 + \xi_2} \quad \text{Equation 6.13}$$

$$r_{12}^p = \frac{\epsilon_2 \xi_1 - \epsilon_1 \xi_2}{\epsilon_2 \xi_1 + \epsilon_1 \xi_2} \quad \text{Equation 6.14}$$

Similarly, the reflection coefficients for the interface between phases 2 and 3 for s- and p- polarisations are shown below in **Equations 6.15** and **6.16**.

$$r_{23}^s = \frac{\xi_2 - \xi_3}{\xi_2 + \xi_3} \quad \text{Equation 6.15}$$

$$r_{23}^p = \frac{\epsilon_3 \xi_2 - \epsilon_2 \xi_3}{\epsilon_3 \xi_2 + \epsilon_2 \xi_3} \quad \text{Equation 6.16}$$

The three-phase system can now be described by independently combining the equations for s- (**Equations 6.13** and **6.15**) and p-polarisations (**Equations 6.14** and **6.16**) in the following manner:

$$r_{123}^{s,p} = \frac{r_{12}^{s,p} + r_{23}^{s,p} e^{-2i\beta}}{1 + r_{12}^{s,p} r_{23}^{s,p} e^{-2i\beta}} \quad \text{Equation 6.17}$$

where  $\beta$  is the change in phase of the beam during one traversal of the thin-film phase (of thickness  $t$ ). This term is given by:

$$\beta = \frac{2 \pi t \xi_2}{\lambda} \quad \text{Equation 6.18}$$

The exponential of the  $\beta$  term in **Equation 6.17**, accounts for the absorption of infrared light by the film.

As with the one phase system (**Equation 6.11**) the overall reflectivity is then calculated by taking the mean of the squares of the magnitude of each reflectivity coefficient, as shown below in **Equation 6.19**.

$$R_{123} = \frac{|r_{123}^s|^2 + |r_{123}^p|^2}{2} \quad \text{Equation 6.19}$$

### 6.2.10.8 Linear approximation for thin-films

As the thickness of the films ( $\sim 1 - 100$  nm) under study are many orders of magnitude smaller than the wavelengths of infrared light ( $\sim 10000$  nm), we can apply a thin-film approximation to the spectral simulations<sup>72-74</sup>.

For this thin-film approximation, we can assume that the phase correction and attenuation vary linearly through the film, rather than exponentially as described above.

$$e^{-2i\beta} \approx 1 - 2i\beta \quad \text{Equation 6.20}$$

As a result, the equations for the Fresnel amplitude coefficients (**Equation 6.17**) can therefore be expanded to terms of first order in  $\beta$  (see appendix), to arrive at the following simplification:

$$r_{123}^{s,p} = \frac{r_{12}^{s,p} + r_{23}^{s,p} (1 - 2i\beta)}{1 + r_{12}^{s,p} r_{23}^{s,p} (1 - 2i\beta)} \quad \text{Equation 6.21}$$

As  $t \ll \lambda$ , the Fresnel reflection coefficients for three phase systems are related to the reflection coefficient for the film free surface ( $r_{13}^{s,p}$ )<sup>74</sup>. The relationship which describes the film free surface in terms of  $r_{12}^{s,p}$  and  $r_{23}^{s,p}$  is as follows:

$$r_{13}^{s,p} = \frac{r_{12}^{s,p} + r_{23}^{s,p}}{1 + r_{12}^{s,p} r_{23}^{s,p}} \quad \text{Equation 6.22}$$

From **Equations 6.21** and **6.22**, it follows that:

$$\frac{r_{123}^{s,p}}{r_{13}^{s,p}} = \frac{1 - 2i\beta \left( \frac{r_{23}^{s,p}}{r_{12}^{s,p} + r_{23}^{s,p}} \right)}{1 - 2i\beta \left( \frac{r_{12}^{s,p} r_{23}^{s,p}}{1 + r_{12}^{s,p} r_{23}^{s,p}} \right)} \quad \text{Equation 6.23}$$

When we perform a Taylor expansion on the denominator of this **Equation 6.23** and neglect terms higher than first order in  $\beta$  (see appendix), we obtain the following equation:

$$\frac{r_{123}^{s,p}}{r_{13}^{s,p}} = 1 + 2i\beta \left( \frac{r_{23}^{s,p} (r_{12}^{s,p} - 1)}{(r_{12}^{s,p} + r_{23}^{s,p})(1 + r_{12}^{s,p} r_{23}^{s,p})} \right) \quad \text{Equation 6.24}$$

As the ambient phase (1) is transparent, the dielectric for this medium ( $\epsilon_1$ ) is real.

Taking this into account and substituting the generalised Fresnel equation (**Equation 6.12**) into **Equation 6.24**, we find that for the s polarisation we obtain:

$$r_{123}^s = r_{13}^s \left( 1 + \frac{4\pi i t \xi_1}{\lambda} \left( \frac{\xi_2^2 - \xi_3^2}{\xi_1^2 - \xi_3^2} \right) \right) \quad \text{Equation 6.25}$$

Similarly, for the p polarisation, we obtain:

$$r_{123}^p = r_{13}^p \left( 1 + \frac{4\pi i t \xi_1}{\lambda} \frac{\epsilon_2}{\epsilon_1} \left( \frac{\eta_2^2 - \eta_3^2}{\eta_1^2 - \eta_3^2} \right) \right) \quad \text{Equation 6.26}$$

where:

$$\eta_i = \frac{\cos \varphi}{n_i} = \frac{\xi_i}{\epsilon_i} \quad \text{Equation 6.27}$$

Using the multiple reflection model and linear approximation, we can obtain reflectivity spectra for different sample thicknesses simply by varying  $t$  in **Equation 6.18**. Simulated infrared spectra analogous to those measured experimentally in **Error! Reference source not found.** are shown below in **Figure 6.19**. As with the

results for the one phase system, the experimental and simulated data correlate well, with similar trends, shapes and spectral features observed. In both cases, the MgO spectral features attenuate and Fe<sub>3</sub>O<sub>4</sub> features increasingly dominate spectra with increasing film thickness.

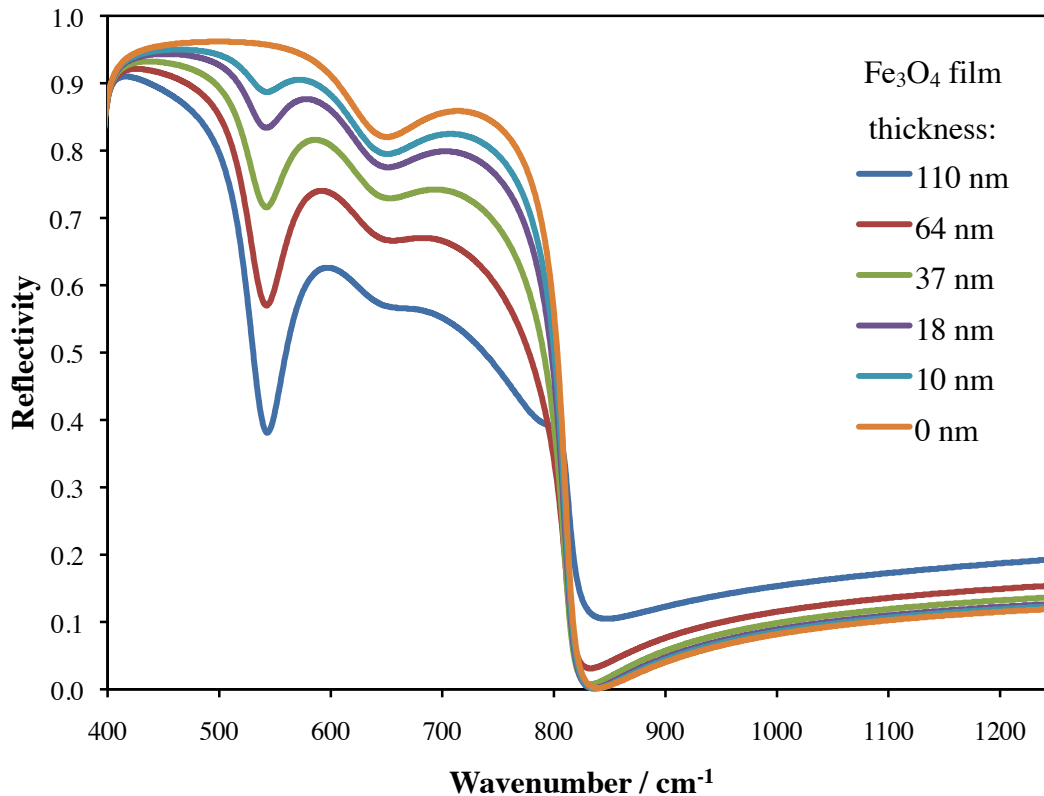


**Figure 6.19** – Modelled infrared reflectivity spectra of various film thicknesses of Fe<sub>3</sub>O<sub>4</sub> for MgO (analogous to **Figure 7.14**).

### 6.2.10.9 Magnetic field dependence

In order to use the infrared spectra to model the MRE, we must introduce a magnetic field dependence to the dielectric function. Adding a term to the Drude part of the dielectric function incorporates this field dependence:

$$\varepsilon(\omega) = \varepsilon(\infty) - \frac{\omega_p^2}{\omega^2 + i\gamma\omega} (1 + \eta m^2) + \sum_{j=1}^n \frac{S_j^2}{k_j^2 - k^2 - i\gamma k} \quad \text{Equation 6.28}$$

where  $m$  is a magnetic field dependent term (with values  $0 < m < 1$ ) which gives a measure of the magnetisation of the sample.  $\eta$  is a scaling parameter, which accounts for the strength of the magnetisation.  $m$  is the fractional magnetisation, and this term

is squared since the MRE is symmetric for both positive and negative applied fields. As a result, the field dependence must be an even function of the applied field.

#### 6.2.10.10 Modelling the MRE

This magnetic dependent complex dielectric can then be input into the multiple reflection model in order to calculate IR reflectivity spectra for thin-films in an ‘applied’ magnetic field. The modelled spectra both in and out of this field can then be used to calculate a model MRE spectrum, according to **Equation 6.3**. The results of these calculations are shown below in Figure 6.20.

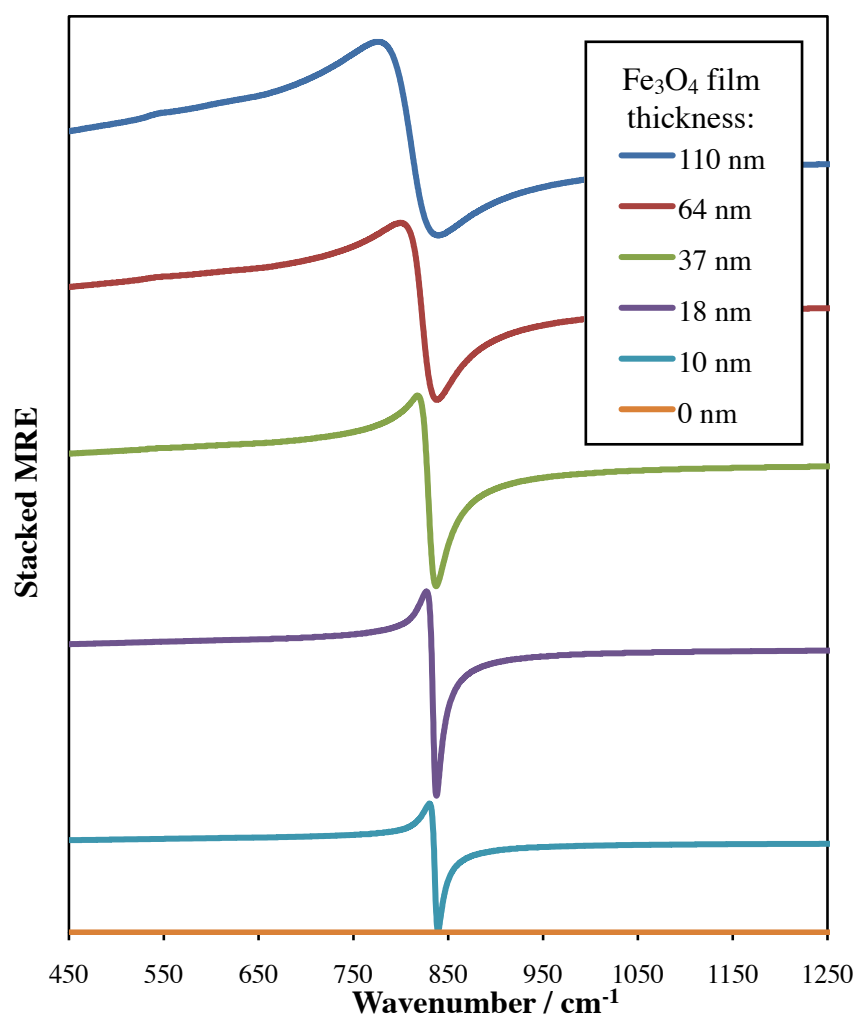


**Figure 6.20** – Stacked modelled MRE spectra of various film thicknesses of Fe<sub>3</sub>O<sub>4</sub> for MgO (analogous to **Figure 7.15**).

The modelled spectra show similar features and trends when compared to the experimentally determined MRE (see **Figure 6.14**). For thin samples, an MRE peak

centred around  $\sim 825 \text{ cm}^{-1}$  is observed for both the experimental and modelled spectra. In the experimentally determined MRE, the peaks are broader and less well defined when compared to the modelled spectra. However, for both the experiment and model, as the film thickness increases, the magnitude of the MRE does not change appreciably, and the position of the MRE shifts to lower wavenumber. This work therefore demonstrates that the thickness dependent MRE of oxide samples can be successfully determined. With further work, it should be possible to use this modelling to determine the various different conductivity mechanisms responsible to the MRE and also extend the model to look at other oxide materials.

### **6.3 Conclusions**

Thin films of iron oxide on various substrates were prepared by MBE. Through careful calibration of the growth variables (Fe deposition rate, O partial pressure and plasma power), it was possible to select the desired phase ( $\text{Fe}_3\text{O}_4$ ). Various different methods were used to determine the phase of iron oxide grown for all of the calibration samples. Diffraction methods showed that certain films had a unit cell approximately twice that of  $\text{MgO}$ <sup>42,75</sup>, confirming the growth of  $\text{Fe}_3\text{O}_4$ .

XPS and other techniques were also employed to provide further evidence of  $\text{Fe}_3\text{O}_4$  formation. For all the XP spectra recorded, the Fe 2p line-shape is complex and broad, with the  $\text{Fe}^{2+}$  and  $\text{Fe}^{3+}$  states hard to resolve as they both have similar binding energies. However, the appearance of a shake-up satellite centred around  $\sim 719 \text{ eV}$  allowed  $\text{Fe}_3\text{O}_4 / \text{Fe}_2\text{O}_3$  to be distinguished. TEM measurements were also used to confirm the nominal thickness of samples and also showed that the  $\text{Fe}_3\text{O}_4$  films grown were epitaxial and contained APBs.

VSM measurements allowed the magnetic properties of the thin-films to be probed. The shapes of the hysteresis curves imply that samples do not contain multiple phases of iron oxide. All samples also showed similar trends in coercivity and remanence. The coercivity values were compared to literature values and showed that no Fe or FeO was present within samples. Samples did not saturate by  $\sim 2 \text{ T}$ , an observation also seen in the literature for thin-films of  $\text{Fe}_3\text{O}_4$ <sup>33</sup>.

MR measurements were performed on all Fe<sub>3</sub>O<sub>4</sub> samples. All samples displayed a similar MR value (~ 1 %) at ~ 1 T, thought to arise from the fact that samples require high fields in order for saturation to occur. For comparison, other calibration samples corresponding to iron oxide phases other than Fe<sub>3</sub>O<sub>4</sub> were measured and displayed no MR. IR spectroscopy and MRE was then employed for non-destructive measurement of both the composition and the MR of the thin-films. IR confirmed the formation of Fe<sub>3</sub>O<sub>4</sub>, due to the presence of a peak at ~ 540 cm<sup>-1</sup>. It was possible to exclude the presence of α-Fe<sub>2</sub>O<sub>3</sub> or γ-Fe<sub>2</sub>O<sub>3</sub> in samples due to the absence of resonances at 437 cm<sup>-1</sup> (α) or 440 cm<sup>-1</sup> (γ). The MRE was discovered to display a thickness dependence, due to the large skin depth of the Fe<sub>3</sub>O<sub>4</sub>.

As a result of the thickness dependent nature of the MRE, simulations based on the Fresnel equations were carried out in order to model the infrared reflectivity and MRE. A multiple reflection model was adopted in order to simulate the reflectivity of a three-phase system. As the thickness of the film was much less than the wavelength of light, a linear approximation was employed in order to simplify the simulation. The resulting infrared spectra showed good agreement with the experimental data. By incorporating a magnetic field dependent term into the complex dielectric function, it was possible to generate a reflectivity in an ‘applied magnetic field’. From this data, MRE spectra were obtained, which show similar features and trends when compared to the experimentally determined spectra. Future work in the group will focus on using this model to examine the different conductivity mechanisms responsible for the MRE in Fe<sub>3</sub>O<sub>4</sub>. It should also be possible to extend the model to look at other oxide materials.

#### 6.4 References

1. J. Jaquet and T. Valet, *Magnetic Ultrathin Films, Multilayers and Surfaces, MRS Symposia Proceedings*, 1995, **348**, 477.
2. R. Mennicke, D. Bozec, V. Kravets, M. Vopsaroiu, J. Matthew and S. Thompson, *Journal of Magnetism and Magnetic Materials*, 2006, **303**, 92-110.
3. V. G. Kravets, D. Bozec, J. A. D. Matthew, S. M. Thompson, H. Menard, A. B. Horn and A. F. Kravets, *Physical Review B*, 2002, **65**, 054415.

4. M. Gester, A. Schlapka, R. A. Pickford, S. M. Thompson, J. P. Camplin, J. K. Eve and E. M. McCash, *Journal of Applied Physics*, 1999, **85**, 5045-5047.
5. J. P. Camplin, S. M. Thompson, D. R. Loraine, D. I. Pugh, J. F. Collingwood, E. M. McCash and A. B. Horn, *Journal of Applied Physics*, 2000, **87**, 4846-4848.
6. M. Vopsaroiu, J. Matthew, K. McNeill and S. Thompson, *IEEE Transactions on Magnetics*, 2003, **39**.
7. R. F. Marques, P. R. Abernethy, J. A. Matthew, C. O. Paiva-Santos, L. Perazolli, M. J. Jr and S. M. Thompson, *Journal of Magnetism and Magnetic Materials*, 2004, **272-276**, 1740-1741.
8. M. Vopsaroiu, D. Bozec, J. Matthew, S. Thompson, C. Marrows and M. Perez, *Physical Review B*, 2004, **70**, 214423.
9. G. F. Dionne, *Magnetic Oxides*, Springer, 2009.
10. A. Ney, M. Opel, T. Kaspar, V. Ney, S. Ye, K. Ollefs, T. Kammermeier, S. Bauer, K.-W. Nielsen, S. T. B. Goennenwein, M. H. Engelhard, S. Zhou, K. Potzger, J. Simon, W. Mader, S. M. Heald, J. C. Cezar, F. Wilhelm, A. Rogalev, R. Gross and S. Chambers, *New Journal of Physics*, 2010, **12**, 013020.
11. M. Calderón and S. D. Sarma, *Annals of Physics*, 2007, **322**, 2618-2634.
12. J. Coey, *Current Opinion in Solid State and Materials Science*, 2006, **10**, 83-92.
13. S. Pearton, W. Heo, M. Ivill, D. P. Norton and T. Steiner, *Semicond. Sci. Technol.*, 2004, **19**, R59-R74.
14. S. Matar, *Progress in solid state chemistry*, 2003, **31**, 239-299.
15. M. Ziese, *Reports on Progress in Physics*, 2002, **65**, 143.
16. H. Yamada, Y. Ogawa, Y. Ishii, H. Sato, M. Kawasaki, H. Akoh and Y. Tokura, *Science*, 2004, **305**, 646-648.
17. A. Gupta and J. Sun, *Journal of magnetism and magnetic materials*, 1999, **200**, 24-43.
18. R. Arras, L. Calmels and B. Warot-Fonrose, *Physical Review B*, 2010, **81**, 104422.
19. D. Venkateshvaran, M. Althammer, A. Nielsen, S. Geprags, M. S. R. Rao, S. T. B. Goennenwein, M. Opel and R. Gross, *Physical Review B*, 2009, **79**, 134405.

20. R. Ramos, S. K. Arora and I. V. Shvets, *Physical Review B*, 2008, **78**, 214402.
21. S. Tiwari, R. Prakash, R. Choudhary and D. M. Phase, *J. Phys. D: Appl. Phys.*, 2007, **40**, 4943-4947.
22. A. Ramos, J.-B. Moussy, M.-J. Guittet, A. Bataille, M. Gautier-Soyer, M. Viret, C. Gautel, P. Bayle-Guillemaud and E. Snoeck, *Journal of Applied Physics*, 2006, **100**, 103902.
23. I. Leonov, A. N. Yaresko, V. N. Antonov and V. I. Anisimov, *Physical Review B*, 2006, **74**, 165117.
24. T. Furubayashi, *Journal of applied physics*, 2003, **93**, 8026-8028.
25. J. Tang, K. Wang and W. Zhou, *Journal of Applied Physics*, 2001, **89**, 7693-7695.
26. T. Taniyama and Y. Yamazaki, *Journal of Applied Physics*, 2001, **89**, 7693.
27. A. Orozco, S. Ogale, Y. Li, P. Fournier, E. Li, H. Asano, V. Smolyaninova, R. L. Greene, R. P. Sharma, R. Ramesh and T. Venkatesan, *Physical Review Letters*, 1999, **83**, 1680.
28. S. K. Park, T. Ishikawa and Y. Tokura, *Physical Review B*, 1998, **58**, 3717.
29. L. Kalev and L. Niesen, *Physical Review B*, 2003, **67**, 224403.
30. S. Jain, A. Adeyeye and C. Boothroyd, *Journal of Applied Physics*, 2005, **97**, 093713.
31. G. Zhang, C. Fan, L. Pan, F. Wang, P. Wu, H. Qiu, Y. Gu and Y. Zhang, *Journal of Magnetism and Magnetic Materials*, 2005, **293**, 737-745.
32. A. Ramos, S. Matzen, J. Moussy, F. Ott and M. Viret, *Physical Review B*, 2009, **79**, 014401.
33. D. Margulies, F. Parker, M. Rudee, F. Spada, J. Chapman and P. Aitchinson, *Physical Review Letters*, 1997, **79**, 5162-5165.
34. M. Ziese and H. Blythe, *Journal of Physics: Condensed Matter*, 2000, **12**, 13.
35. W. Eerenstein, T. Palstra, T. Hibma and S. Celotto, *Physical Review B*, 2002, **66**.
36. J. Coey, A. Berkowitz, L. Balcells, F. F. Putris and F. T. Parker, *Applied Physics Letters*, 1998, **72**, 734-736.
37. W. Eerenstein, T. T. M. Palstra, S. S. Saxena and T. Hibma, *Physical Review Letters*, 2002, **88**, 247204(247204).

38. J. Moussy, S. Gota, A. Bataille, M. Guittet, M. Gautier-Soyer, F. Delille, B. Dieny, F. Ott, T. Doan, P. Warin, P. Bayle-Guillemaud, C. Gatel and E. Snoeck, *Physical Review B*, 2004, **70**, 174448(174449).
39. W. Eerenstein, University of Groningen, 2003.
40. Y. Gao, Y. Kim and S. Chambers, *Journal of Materials Research*, 1998, **13**, 2003-2014.
41. F. Voogt, T. Palstra, L. Niesen, O. Rogojanu, M. James and T. Hibma, *Physical Review B*, 1998, **57**, R8107-R8110.
42. <http://www.mindat.org/>.
43. W. Mi, E. Jiang and H. Bai, *Journal of Physics D-Applied Physics*, 2009, **42**, 7.
44. Y. Lu, J. Claydon, E. Ahmad, Y. B. Xu, S. M. Thompson, K. Wilson and G. van der Laan, *IEEE Transactions on Magnetics*, 2005, **41**, 2808-2810.
45. F. Voogt, P. Smulders, G. Wijnja, L. Niesen, T. Fujii, M. A. James and T. Hibma, *Physical Review B*, 2001, **63**, 125409.
46. Y. Gao and S. Chambers, *Journal of Crystal Growth*, 1997, **174**, 446-454.
47. T. Fujii, F. De Groot, G. Sawatzky, F. Voogt, T. Hibma and K. Okada, *Physical Review B*, 1999, **59**, 25409 (25411).
48. S. Arora, R. Sofin and I. V. Shvets, *Physical Review B*, 2005, **72**, 134404.
49. D. Dimitrov, G. Hadjipanayis, V. Papaefthymiou and A. Simopoulos, *Magnetics*, 1997, **33**, 4363-4366.
50. Z. Zhou and J.-J. Yan, *Journal of magnetism and magnetic materials*, 1992, **115**, 87-98.
51. O. Ishii, A. Terada and S. Ohta, *Magnetics*, 1994, **30**, 1291-1295.
52. S. Ohta and A. Terada, *Thin Solid Films*, 1986, **143**, 73-82.
53. L. Valdes, *Proceedings of the IRE*, 1954, 420-427.
54. J. Ahn, H. Choi and T. Noh, *Physical Review B*, 1996, **53**, 10310.
55. H. S. Choi, J. S. Ahn, W. Jo and T. W. Noh, *Journal of the Korean Physical Society*, 1995, **28**, 636-644.
56. M. Striefler and S. I. Boldish, *Journal of Physics C: Solid State Physics*, 1978, **11**, L237-L224I.
57. M. O'horo, A. Frisillo and W. White, *Journal of Physics and Chemistry of Solids*, 1973, **34**, 23-28.

58. N. Grimes, P. O'Connor and P. Thompson, *Journal of Physics C: Solid State Physics*, 1978, **11**, L505-L507.
59. G. Kugel, C. Carabatos, B. Hennion, B. Prevot, A. Revcolevschi and D. Tocchetti, *Physical Review B*, 1977, **16**.
60. C. Serna, J. Rendon and J. Iglesias, *Spectrochimica Acta Part A*, 1982, **38A**, 797-802.
61. A. Jubb and H. C. Allen, *ACS Applied Materials & Interfaces*, 2010, **2**, 2804-2812.
62. S. Onari, T. Arai and K. Keiei, *Physical Review B*, 1977, **16**.
63. T. D. Glotch and G. Rossman, *Icarus*, 2009, **204**, 663-671.
64. L. Degiorgi, P. Wachter and D. Ihle, *Physical Review B*, 1987, **35**, 9259-9264.
65. P. R. Abernethy, *PhD. thesis, University of York*, 2007, 1-253.
66. V. V. Kaichev, I. P. Prosvirin, V. I. Bukhtiyarov, H. Unterhalt, G. Rupprechter and H.-J. Freund, *Journal of Physical Chemistry B*, 2003, **107**, 3522-3527.
67. H. Conrad, G. Ertl, J. Koch and E. E. Latta, *Surface Science*, 1974, **43**.
68. D. Kim and J. Honig, *Physical Review B*, 1994, **49**, 4438.
69. Z. Šimša, *physica status solidi (b)*, 1979, **96**, 581-587.
70. L. Gasparov, D. Tanner, D. Romero, H. Berger, G. Margaritondo and L. Forro, *Physical Review B*, 2000, **62**, 7939-7944.
71. A. B. Winterbottom, *Trans. Faraday Soc.*, 1946, **42**, 487.
72. J. D. E. McIntyre and D. E. Aspnes, *Surf. Sci.*, 1971, **24**, 417-434.
73. J. D. E. McIntyre, *Optical Reflection Spectroscopy of Chemisorbed Monolayers*, North Holland/Elsevier, 1976.
74. V. P. Tolstoy, I. V. Chernyshova and V. A. Skryshevsky, *Handbook of Infrared Spectroscopy of Ultrathin Films*, Wiley-VCH, 2003.
75. R. Waldron, *Physical Review*, 1955, **99**, 1727-1735.

# Chapter 7

## Conclusions

### 7.1 Conclusions

The main aim of this thesis has been to use and/or develop surface science and thin-film techniques to assist the optimisation of functional materials. Due to their environmental and economical importance, heterogeneous catalysts were identified as one possible group of materials that would greatly benefit from such an approach. To this end, the selox of crotyl alcohol to crotonaldehyde over Au/Pd(111) surface alloys was studied using 'Fast' XPS at the ELETTRA synchrotron. It was found that, unsurprisingly, no chemistry occurs over epitaxial Au overlayers, as the alcohol simply reversibly chemisorbs. Conversely, Au-rich surface Au/Pd alloys show moderate activity crotyl alcohol selox, as crotonaldehyde desorbs intact at room temperature with minimal side-reactions. Pd-rich alloy surfaces convert 100 % of a crotyl alcohol adlayer to crotonaldehyde, although as much as half of this aldehyde subsequently decarbonylates to produce gas phase CO and propene. From these experiments, it was determined that the optimum surface alloy composition, is Au<sub>2</sub>Pd<sub>3</sub>, associated with a bulk alloy composition of AuPd<sub>5</sub>. These results show that even small amounts ( $X_{Au}$  0.2 - 0.3) of Au can promote the selective oxidation of crotyl alcohol whilst suppressing product decomposition.

Further work was then carried out in order to examine the chemistry of both the main product (crotonaldehyde) and by-product (propene) formed during the selox of crotyl alcohol over Au/Pd(111) surface alloys. In doing so, it was hoped that it would be possible elucidate the reaction pathway for allylic alcohol selox by Au/Pd(111) surface alloys. It was found that Au rich surface alloys are able to inhibit decomposition of both the aldehyde (for  $X_{Au} \geq 0.3$ ) and propene (for  $X_{Au} \geq 0.8$ ). Conversely, Pd rich alloy surfaces decompose both reaction intermediates, leading to the formation of CO (solely for the aldehyde) and surface bound C; species responsible for deactivation. In order to mimic 'real' selox conditions, surfaces were then pre-saturated with O. For the aldehyde, O on Au/Pd(111) surfaces hinders the decomposition chemistry further, with a small amount of decomposition also

occurring. However, propene binds more strongly to O pre-covered surfaces, which results in an increase in the amount of propene that reacts relative to the O free surfaces. A larger proportion of the propene therefore undergoes combustion when compared to the aldehyde over the same surface alloys.

Insight into the adsorbate geometry of the alcohol on the Pd(111) surface has been provided by MDS work. When the alcohol is adsorbed onto the Pd(111) substrate at 150 K, three distinct molecular features are observed due to Auger de-excitation. The low temperature spectra were interpreted through the use of early valence band photoemission studies<sup>1</sup>, MO calculations of gas-phase allylic alcohols<sup>2</sup>, and DFT calculations. States within the spectra were identified which correspond to emission from the carbon backbone of the molecule, C=C  $\pi$  bond and O lone-pair  $2p$   $n$  bonds. As the saturated substrate was heated, between  $\sim$  200 K and 250 K, the desired reaction pathway predominates, generating emission from the aldehyde product resulting in a small shift in peaks to higher binding energy. As a result of intramolecular changes, a reversal in the assignment of the first two MOs occurs, albeit almost coincident in energy, an observation that is supported by shifts in similar magnitude for DFT calculations of the isolated alcohol and aldehyde. Heating the sample above 250 K results in a decrease in the emission from both the hydrocarbon skeleton and O  $n$  states due to decarbonylation of the aldehyde, forming propylidyne. Heating above 500 K results in the loss of any identifiable spectral features, consistent with propene desorption and residual C formation. The dominant de-excitation process at this point is due to resonance ionisation, characteristic of Pd(111). DFT calculations have also shown that the lowest energy adsorption state results when the alcohol adsorbs parallel to the Pd surface. Experimental work confirms this, as any large tilt in the position of the O would lead to a more pronounced feature in the MDS spectrum when compared to emission from the C=C bond. By examining the intensity and shapes of the MDS peaks, DOS calculations for such geometries are in good agreement with experimental data.

In order to investigate novel magnetic materials for spintronic applications, Fe<sub>3</sub>O<sub>4</sub> thin-films were prepared on various substrates, with the aim of examining the relationship between the film micro-structure and properties. The composition,

structure and magnetic properties of all such films were characterised. Unfortunately as such films only magnetically saturate in high fields<sup>3</sup>, MR values from all samples were identical. Despite this, the MRE results displayed a thickness dependence, as a result of the large skin-depths of oxide materials, a phenomena not observed for metallic spin-valves. By modelling the complex dielectric function, it was possible to effectively simulate the IR and MRE spectra. Both of which were in good agreement with experimental data. With further work, it should be possible to use the MRE as an accurate means of measuring the thickness of a thin-film. With further theoretical work it also should be possible to probe the different conductivity mechanisms exhibiting characteristic spectral dependences. This method could therefore be adopted to a wide range of oxide materials of interest from a spintronics perspective.

The development and calibration of a combinatorial sputtering rig has allowed libraries of heterogeneous catalysts (AuPd) and magnetic materials (CoAg) to be prepared. EDX and XRF measurements show that a composition gradient exists across both sets of samples, which accesses the bulk of each phase diagram. For CoAg, it has been shown that the GMR also varies across the sample in accordance with the varying composition. Further work is needed to fully optimise the properties of these materials with full spatial resolution, which would include infrared thermography and scanning mass spectrometry. In this basic groundwork, it has demonstrated that combinatorial methods are potentially useful tools for aiding the optimisation of materials.

## 7.2 References

1. A. Katrib and J. Rabalais, *The Journal of Physical Chemistry*, 1973, **77**, 2358-2363.
2. L. Klasinc, B. Ruscic, A. Sabljic and N. Trinajstic, *Journal of the American Chemical Society*, 1979, **101**, 7477-7482.
3. D. Margulies, F. Parker, M. Rudee, F. Spada, J. Chapman and P. Aitchinson, *Physical Review Letters*, 1997, **79**, 5162-5165.

# Appendix 1

## A1.1 List of Publications:

**James Naughton**, Sarah Thompson, Vlado Lazarov, Christopher Kelley, Jim Matthew, Adam F. Lee and Karen Wilson, “Modelling the Magnetorefractive Effect in Thin-Films of Fe<sub>3</sub>O<sub>4</sub> on MgO”, manuscript in preparation

**James Naughton**, Andrew Pratt, Charles W. Woffinden, Christopher Eames, Steve P. Tear, Sarah M. Thompson, Adam F. Lee and Karen Wilson, “A metastable de-excitation spectroscopy and DFT study of the selective oxidation of crotyl alcohol over Pd(111)”, submitted to the Journal of Physical Chemistry C

Adam F. Lee, Christine V. Ellis, **James Naughton**, Mark A. Newton, Christopher M. A. Parlett, and Karen Wilson, “Reaction-Driven Surface Restructuring and Selectivity Control in Allylic Alcohol Catalytic Aerobic Oxidation over Pd”, Journal of the American Chemical Society, 2011, **133**, 5724–5727.

**James Naughton**, Adam F. Lee, Sarah Thompson, C. P. Vinod and Karen Wilson, “Reactivity of crotonaldehyde and propene over Au/Pd(111) surfaces”, Physical Chemistry Chemical Physics, 2010, **12**, 2670–2678.

Adam F. Lee, Simon F.J. Hackett, Graham J. Hutchings, Silvano Lizzit, **James Naughton**, Karen Wilson, “In situ X-ray studies of crotyl alcohol selective oxidation over Au/Pd(111) surface alloys”,

## **A1.2 Conferences/workshops attended:**

Preparation and Patterning of Magnetic Materials Workshop - Institute of Physics (4th November 2008)

17th Interdisciplinary Surface Science Conference (ISSC-17) - University of Reading (30th March - 2nd April 2009)\*

Magnetic Imaging and Spectroscopy Workshop - University of Leeds (10th - 11th June 2009)

Catalysis Summer School Workshop - Liverpool (13th - 17th July 2009)\*

Density Functional Methods for Experimental Spectroscopy Workshop - University of Oxford (23rd - 27th August 2009)\*

Materials Research Society (MRS) Fall Meeting - Boston (30th November - 4th December 2009)

10th Condensed Matter and Materials Physics (CMMP 2010) - University of Warwick (14th - 16th December 2010)\*

Materials Research Society (MRS) Spring Meeting - San Francisco (25th -29th April 2011)##

\*presented a poster

##presented a talk

## **A1.3 Awards received:**

10th Condensed Matter and Materials Physics (CMMP 2010) poster prize: “The Magnetorefractive Effect in Thin-Films of Fe<sub>3</sub>O<sub>4</sub>/MgO (111)”

## Appendix 2

### Development of a combinatorial sputtering rig

#### A2.1 Introduction

In chapters 3 and 4, we increased our understanding of the chemistry of crotyl alcohol over a range of AuPd(111) surface alloys through the use of a variety of surface science techniques. By performing many complex experiments, the optimum surface composition of Au/Pd for this catalytic process was determined. This process involved the preparation and characterisation of many ultrathin-films with similar surface compositions.

Indeed, the optimisation and/or discovery of materials largely proceeds experimentally by the serial synthesis and characterisation of a wide variety of similar samples<sup>1</sup>. This conventional approach is prohibitively long and expensive due to the number of iterative steps required<sup>2</sup>. This arduous approach is necessary due largely to a poor fundamental understanding of systems with several components, meaning our ability to predict materials with specific desirable properties is limited<sup>2,3</sup>.

The case of AuPd alloys for selective oxidation catalysis is but one of many examples of materials optimisation which would greatly benefit from the application of simultaneous preparation techniques<sup>4</sup>. This would involve vast arrays of materials being prepared and rapidly screened for a particular property, not only accelerating the development of many functional materials, but also providing enormous economic benefit from a research and development point of view.

This simultaneous synthetic preparation of large numbers of related compounds is known as ‘Combinatorial Chemistry’<sup>5,6</sup>, a term used predominantly in the area of drug discovery in the pharmaceutical industry. However, this term can be more widely applied to any preparative protocol that permits large numbers of related compounds to be synthesised and rapidly characterised<sup>6,7</sup>. This approach is often also referred to as parallel synthesis or high-throughput synthesis<sup>8,9</sup>. Indeed, many

classes of materials have been investigated using such a combinatorial approach<sup>2</sup>, including catalysts<sup>9-12</sup>, optical<sup>13, 14</sup>, magnetic<sup>8, 15</sup>, and dielectric<sup>15, 16</sup> materials, hydrogen storage materials<sup>17, 18</sup> and structural polymers<sup>2</sup> to give but a few examples.

A procedure for the preparation and characterisation of solid inorganic materials was first outlined by means of RF plasma sputtering by Hanak in 1970<sup>1</sup>. Several other deposition methods have also been utilised for this purpose, including (but not limited to), combinatorial laser molecular beam epitaxy (CLMBE)<sup>3, 4</sup>, pulsed laser deposition (PLD)<sup>15, 18-22</sup>, ion beam sputter deposition<sup>22</sup>, and chemical vapour deposition (CVD)<sup>4, 13</sup>. In this chapter, a specialised high-vacuum chamber (combinatorial sputtering rig) was developed (as outlined in chapter 2, section 2.1.4) which allows the co-deposition of up to four different materials *via* DC magnetron sputter guns, in order to prepare a composition gradient across a substrate (as shown below in **Figure A2.1**).

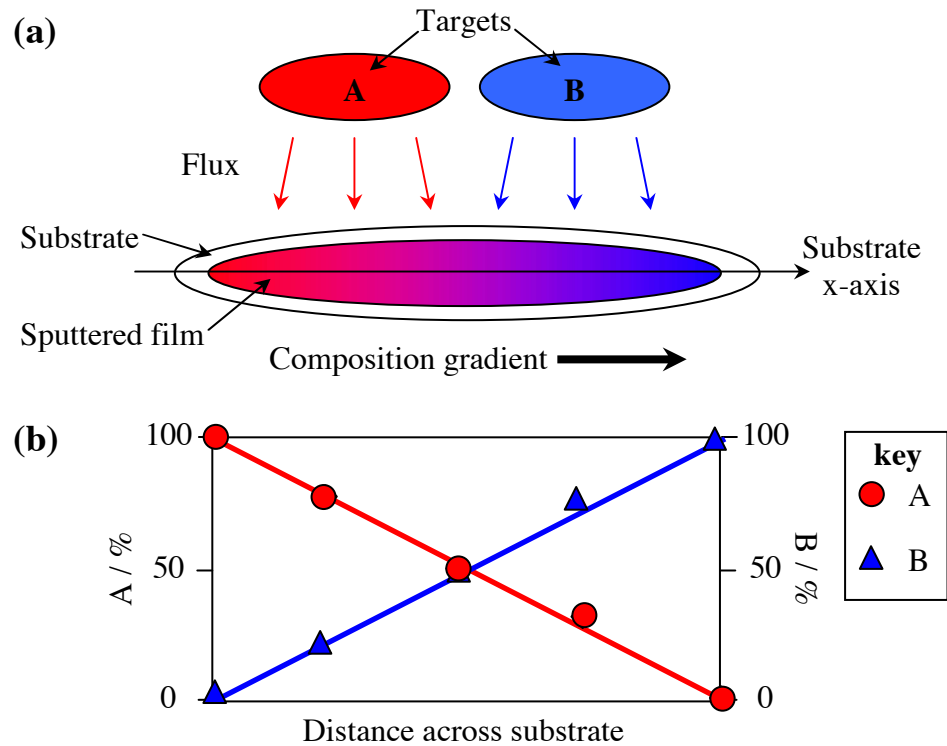


**Figure A2.1** – (a) A simple schematic setup for co-sputtering of a two-component film, modified from Hanak<sup>1</sup> and (b) the resulting XRF composition profile obtained from analysis of such a film.

The complete phase diagram for an  $n$ -component mixture can be deposited on an  $(n-1)$  dimensional surface<sup>1</sup>. Therefore, a two-component phase diagram can be deposited linearly between two sputter sources, and a three-component phase diagram can be prepared on a two-dimensional equilateral triangular surface. Control of the sputtering process and experimental geometry, in theory, should permit deposition of the entire phase diagram for up to three metallic components. Indeed, it should be possible to access any part of such a phase diagram on a flat substrate.

The metal flux generated by plasma sputtering of a metal has a cosine distribution about the centre of a sputtering target<sup>23</sup>. Therefore, metal film sputtered onto a flat substrate directly below the centre of the sputter source results in a film of symmetrical thickness about the centre of the substrate. If the substrate is placed a sufficient distance either side of the centre of the sputter gun, the film thickness will be non-uniform. In this scenario, the substrate is said to be within the non-

uniform deposition zone, with most deposition occurring at a point closest to the centre of the sputter source. If the substrate is located on an axis between the centres of two sources but beyond the uniform deposition range of each, a non-uniform composition profile will result across the film, with each constituent metal most abundant at the edge of the substrate closest to that sputtering target (**Figure A2.1 (b)**).

In this manner, a ‘library’ of materials with varying compositions can be synthesised in a single step. By using this method, arrays of materials relevant for heterogeneous catalysis (AuPd) and magnetic materials (CoAg) can be prepared on Si(100) substrates. It will then be shown that a combination of infrared thermography and/or scanning mass spectrometry could be utilised to rapidly screen all compositions within a library and thus determine the optimum composition for the catalytic activity or giant magnetoresistance in a single experiment.

## **A2.2 Results and Discussion**

### **2.2.1 Calibration matrix**

In order to prepare multi-component libraries with uniform film thickness and a specific composition gradient, it was first necessary to construct a calibration matrix. Films of Cu were deposited onto 2 inch Si(100) substrates using different sputtering parameters. Each of the relevant variables was successively altered (whilst keeping the others constant) and the effect of each parameter upon the Cu film thickness was examined. The factors affecting the sputtering thickness and composition are:

- Sputter gun power (in W)
- Sputtering time (in minutes)
- Ar pressure (in mTorr)
- Sputter gun angle (in degrees, °)

The Cu film thickness was determined using ‘Talystep’ measurements using a Rank Taylor Hobson Talystep 1 instrument. This step-profiling instrument consists

of a needle on a spring, which when passed over a surface; the mechanical deflection of the needle is recorded. In order to obtain step height measurements across the film relative to the Si, an Al mask consisting of 11 grooves (as shown below in Figure A2.2 (a)) was placed over each substrate prior to deposition. During deposition, the Cu film would only be deposited in the grooves, meaning that 11 steps would be created across the surface of the substrate. Each step height was measured across the centre of the substrate. This process was repeated three times in order to determine the standard error in each measurement.

An additional mask, as shown in Figure A2.2 (b), was created for use with a Horiba XGT-7000 microscope and custom built scanning mass spectrometer for performing XRF and TPD/TPR measurements respectively.

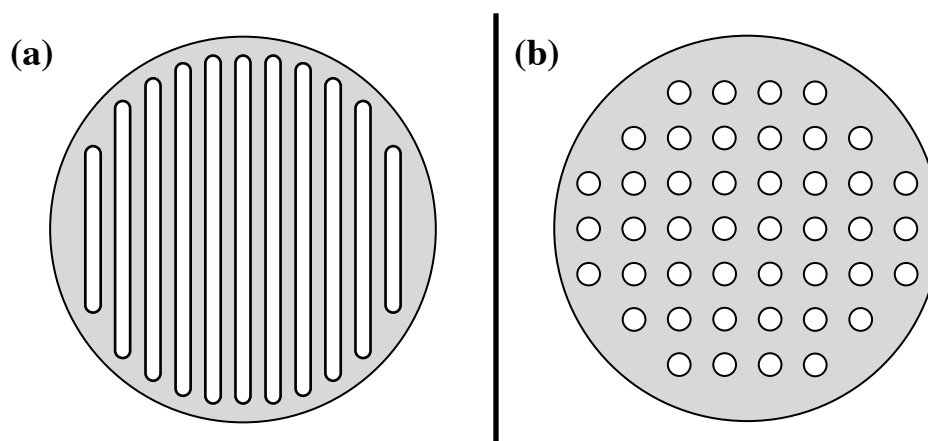


**Figure A2.2** – Al masks constructed (a) for the calibration of the combinatorial sputtering rig by talystep (b) for the calibration of the combinatorial sputtering rig by XRF and for the growth of samples for infrared thermography/thermal desorption spectroscopy measurements. Both diagrams are actual size.

The deposition rates (relative to Cu) for each material within the combinatorial sputter sources were also determined by sputtering the various metals whilst all parameters were fixed (see section A2.2.1.5). The thicknesses of each film were then measured and benchmarked relative to the Cu film thickness. As the sputtering time was known, this enabled a deposition rate to be calculated. In this way, once the calibration matrix was complete, any material within the combinatorial system could be used to grow films of a specific thickness and composition.

### 2.2.1.1 Sputter Gun Power

Figure A2.3 shows the average Cu deposition rate with increasing sputter gun power. The trend suggests that the change in deposition rate is linear with increasing sputter gun power. As the gun power increases, so does the energy of the Ar ions - resulting in an increase in the overall sputtering rate.

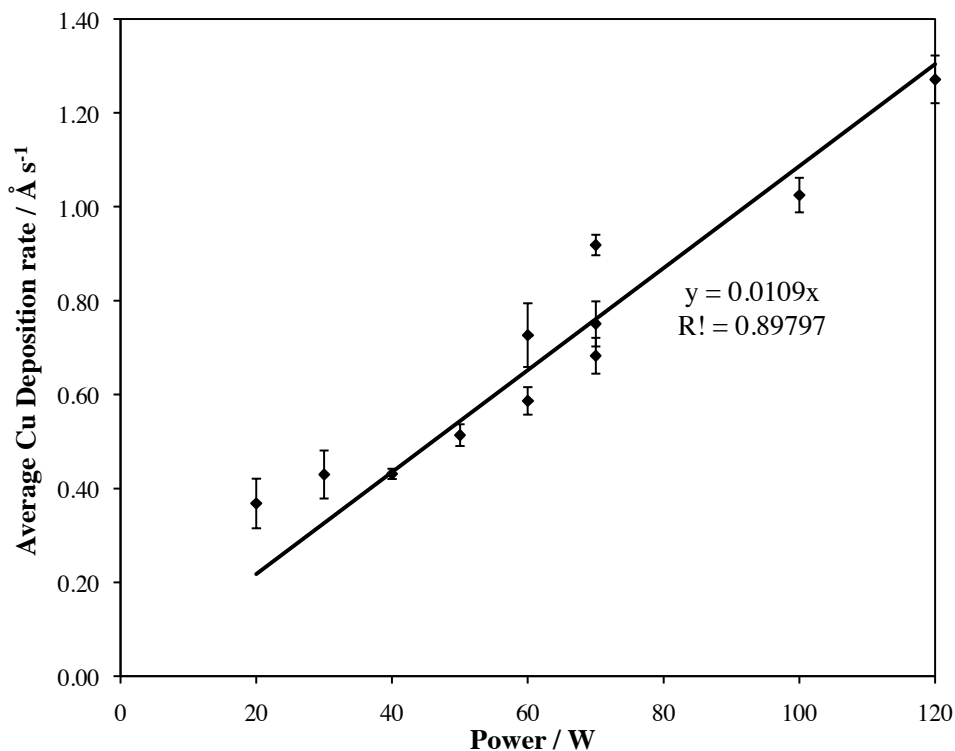


**Figure A2.3** – The change in Cu deposition rate with increasing gun power.

The error bars were calculated based upon the standard deviation and standard error between Talystep measurements.

### 2.2.1.2 Sputtering time

As with the gun power series, a positive linear relationship is also observed (see Figure A2.4). These results are not surprising, as sputtering for a longer time period will obviously result in a thicker film. The sputtering time is therefore a very useful factor in growing samples with a desired thickness.

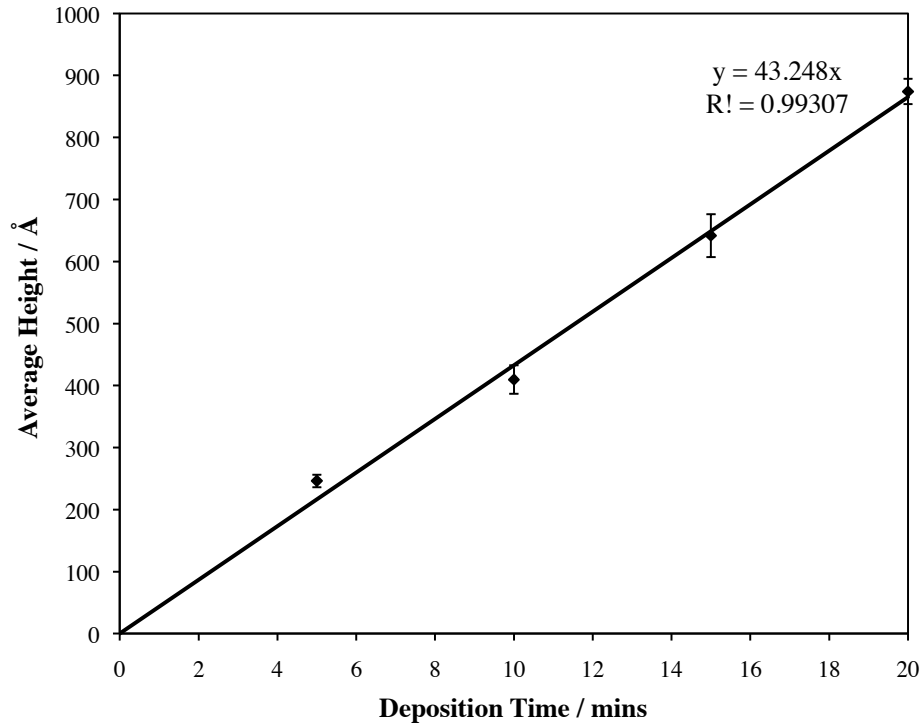


**Figure A2.4** - The change in the average height across the sample, with increasing sputter deposition time. The error bars were calculated based upon the standard deviation and standard error between Talystep measurements.

### 2.2.1.3 Ar pressure

Figure A2.5 shows the effect of argon pressure upon the average deposition rate. The trend indicates that as the pressure increases, the overall deposition rate decreases. This can be rationalised in terms of the Ar gas pressure, as when this is increased, two different effects influence the sputtering rate. In order for sputtering to occur, a suitable plasma density threshold needs to be obtained. Therefore an increase in the sputtering rate may result in an increase in the plasma density.

When increasing the pressure, the number of collisions between the sputtered metal atoms and gas centres will increase (shorter mean free path). This will have the effect of decreasing the sputtering rate, as fewer atoms will be deposited on the substrate. The negative trend observed indicates that over the range of pressures studied, the number of gas collision centres inhibits the sputtering rate. At lower pressures the effect of plasma density is more dominant, thus resulting in an optimum Ar pressure for deposition rate.

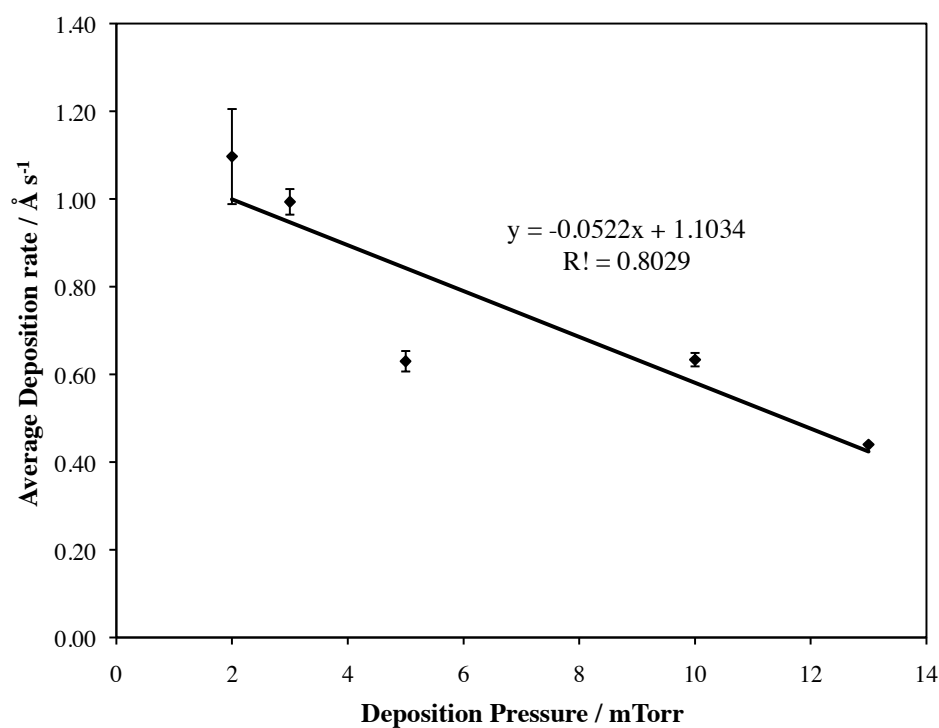


**Figure A2.5** – The average change in deposition rate, with increasing deposition pressure. The error bars were calculated based upon the standard deviation and standard error between Talystep measurements.

#### 2.2.1.4 Gun angle variation

Figure A2.6 shows the change in Cu step height across the substrate for several different gun angles. Trends are rather difficult to determine, probably due to a change in the distance between the gun and substrate with increasing angle (see Figure A2.7).

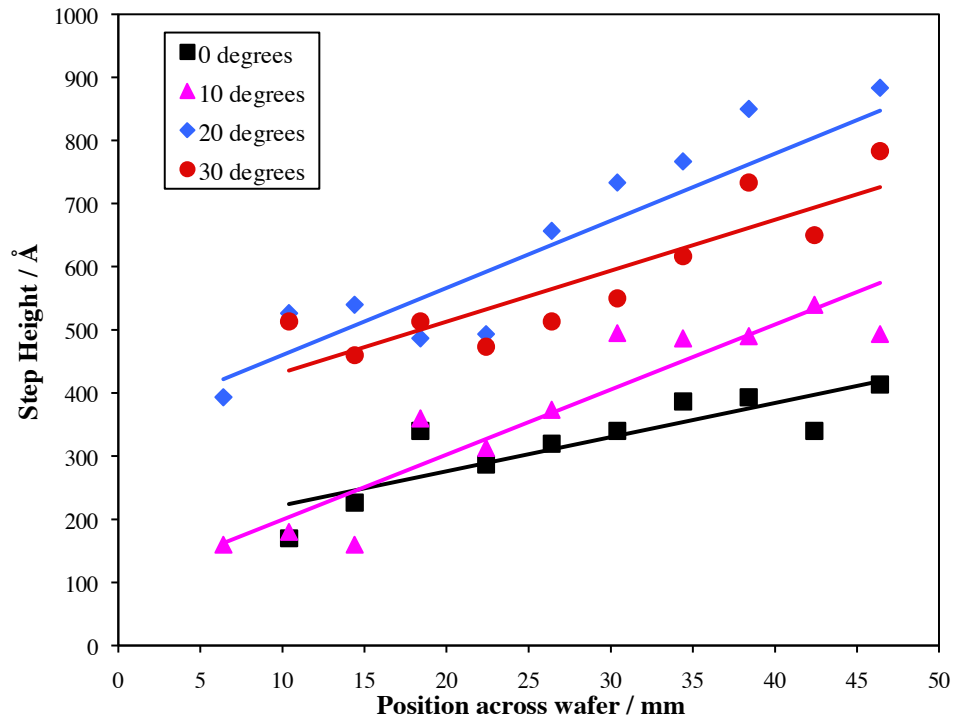


**Figure A2.6** – A graph to show the change in Cu step height across the substrate for different gun angles. Standard error bars are not displayed for clarity. The lines shown on the graph are lines of best fit.

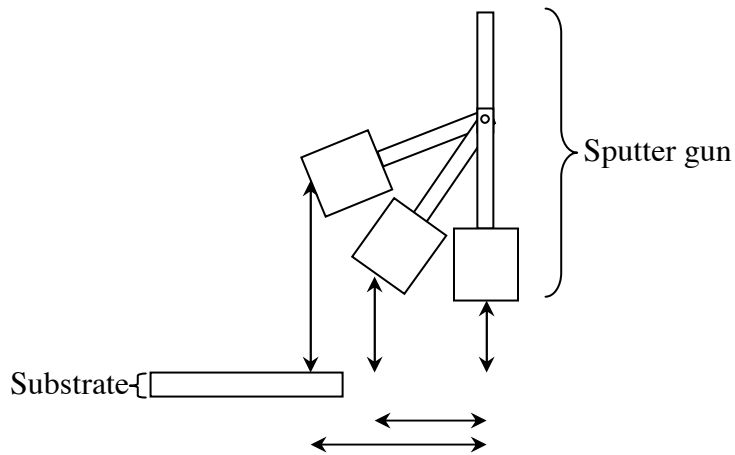


**Figure A2.7** – A diagram to illustrate that the distance from gun to substrate both horizontally and vertically changes with increasing gun angle.

In order to appreciate the general trend, merely the average step height for each gun angle was considered (see Figure A2.8 below).

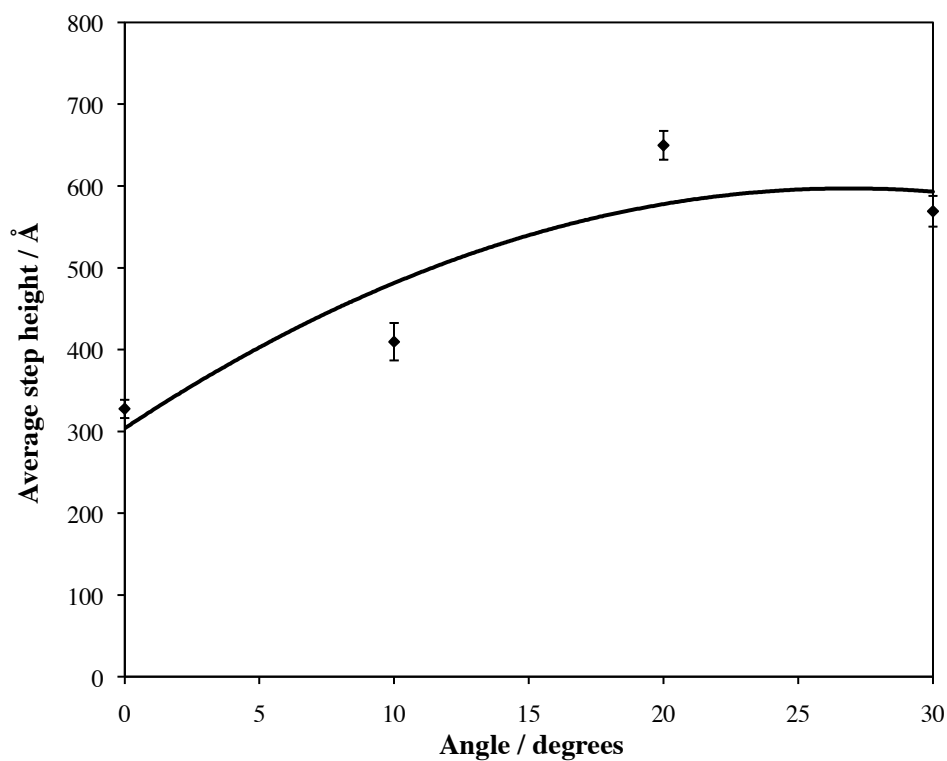


**Figure A2.8** – The average step height across the substrate, against the gun angle employed.

Figure A2.8 therefore shows that the average step height increases with increasing gun angle, up to an optimum. In order to obtain a basic appreciation of the effect of gun angle upon the step height, scale drawings were made for each gun angle. Assuming a 45 ° divergence, flux lines were superimposed on these diagrams (see section A2.5). The amount of flux deposited on both the substrate and the chamber was measured in centimetres from these diagrams. This is represented in Figure A2.9 below.

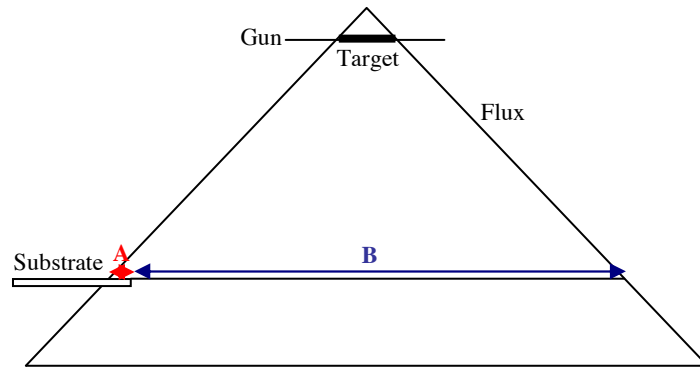


**Figure A2.9** – A diagram illustrating the amount of flux deposited on the substrate (A), compared to the chamber (B), for a 0 ° gun angle (assuming 45 ° flux divergence from target).

From these 2D diagrams, the ratio of the flux on the substrate to that lost to the rest of the chamber was then calculated for each gun angle. This can be thought of as the ‘useful’ flux for each gun angle, based on the 2D diagrams (according to **Equation A2.1**) and is plotted in **Figure A2.10**.

$$\text{Useful flux} = \frac{\text{Flux deposited on substrate (A)}}{\text{Flux deposited on chamber (B)}} \quad \text{Equation A2.1}$$

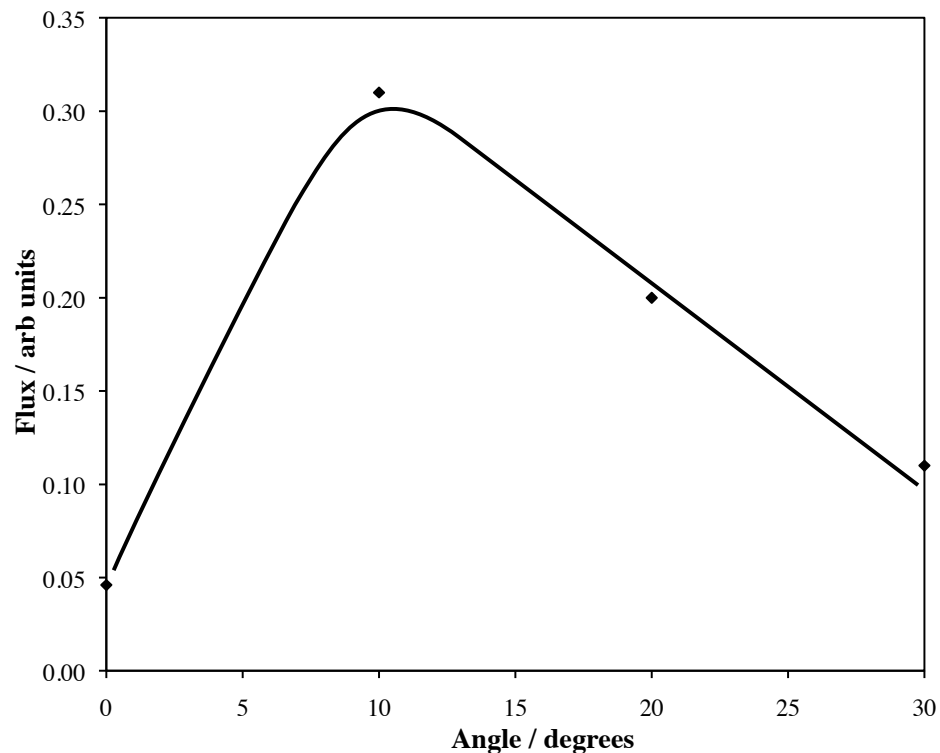


**Figure A2.10** – The calculated ‘useful’ flux against sputter gun angle

A similar (but not identical) trend is observed for that of the average step height versus gun angle (Figure A2.8); the film thickness increases with increasing gun angle up to a certain point. Beyond this, the film thickness either remains much the same (as in the experimental case – Figure A2.8), or decreases (in the case of basic calculation – **Figure A2.10**). The simplistic theoretical approach only takes into account the deposition in one dimension relative to the substrate, hence why it differs from the experimental case. Also, the measurements used to calculate the ‘useful flux’ were crudely made with a 30 cm ruler, as accurate drawings with distances within the chamber were not available. It is therefore important to be mindful of the fact that the associated error with such measurements will be large and hence only the general trend can only be commented on, rather than anything more quantitative.

### 2.2.1.5 Relative deposition rates

When literature deposition rates (relative to Cu) are considered, the results obtained for Cu grown at 60W correlate well to those of Co and Pd grown at 60W (see Table

A2.1). This indicates that data and trends obtained will be applicable to all metal targets within the combi-rig.

<b>Target</b>	<b>Deposition rate relative to Cu</b>	<b>Literature* deposition rate relative to Cu</b>
Ag	No data	2.24
Co	0.58	0.62
Cu	1.00	1.00
Pd	1.38	1.41

**Table A2.1** – Deposition rates for the combinatorial sputter gun sources, relative to Cu. \*Data obtained from Kurt J. Lesker Company.

Despite this encouraging agreement with literature values, it is necessary to use another means of characterisation in order to corroborate the Talystep results. AFM, EDX and XRF were employed for this purpose. Unfortunately, attempts to acquire AFM images with two separate instruments were largely unsuccessful. It was discovered that EDX measurements give similar values to Talystep results; however the technique itself is much more laborious and time consuming. As a result, XRF was identified as the most efficient technique to substantiate the Talystep results.

#### **2.2.1.6 XRF results**

XRF measurements for the calibration matrix were performed on an XGT-7000 microscope manufactured by Horiba. Dr. Simon Fitzgerald of Horiba Jobin Yvon acquired both XRF spot and map measurements of a single Cu sample grown at 70 W, with a 10 ° gun angle, under 5 mTorr of Ar for 10 minutes. An example of XRF mapping is shown in **Figure A2.11** below. The XRF results were plotted alongside the Talystep data for the same 70W Cu sample (see **Figure A2.12**).

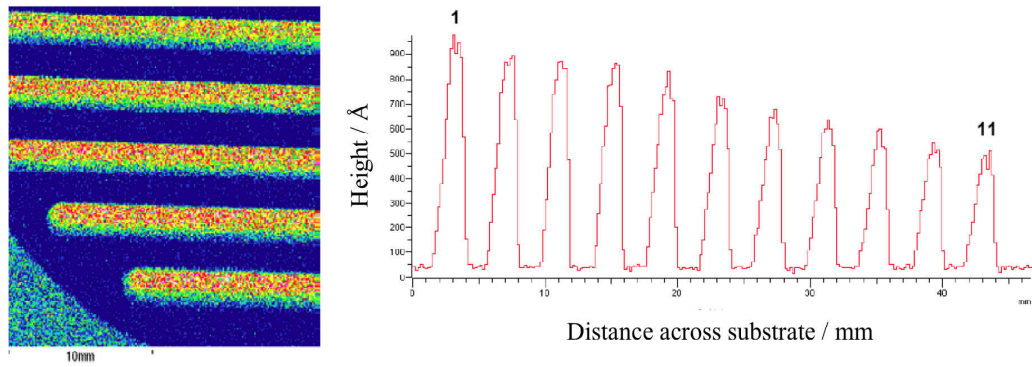


**Figure A2.11** – A section of an XRF map of the sample is shown on the left. The height and was calculated from these maps by means of a line profile. The height against distance across the substrate measured from a central line-scan of the XRF map is displayed by the graph on the right. Dr. Simon Fitzgerald of Horiba Jobin Yvon performed these particular measurements.

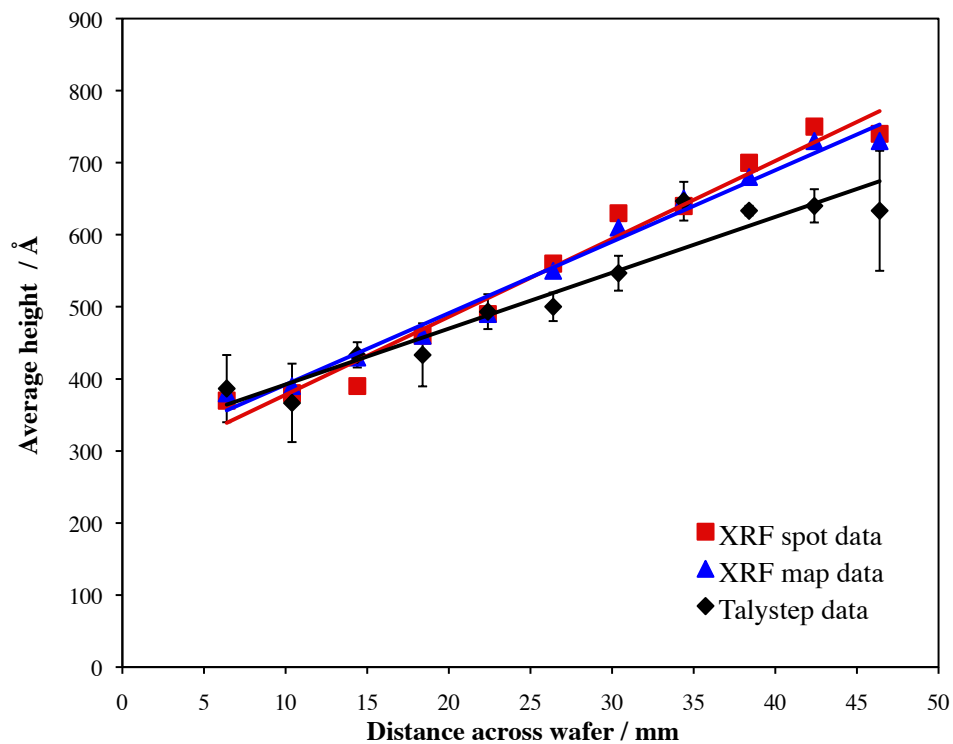


**Figure A2.12** – A comparison of the average height determined by talystep (black diamonds), XRF spot (red squares) and XRF mapping (blue triangles) for a calibration matrix sample grown at 70 W, 5 mTorr for 10 mins.

From **Figure A2.12**, it is clear that there is good agreement between XRF and Talystep measurements. This suggests that the Talystep results are both reliable

and accurate. With the calibration matrix complete, several samples were grown in an attempt to optimise the properties of materials.

### **2.2.2 CoAg combinatorial sample**

Solid precipitates of a magnetic material in a non-magnetic matrix are described as being granular. Granular GMR materials are of technological interest as in principle they are far easier to prepare than an ordered multilayer structure. Magnetic sensors would therefore become much cheaper to produce and would have a wide variety of different applications. In practice, granular GMR is only observed in matrices of immiscible materials<sup>24</sup>. Whilst granular materials do not produced a high GMR when compared to that found for multilayers, the physics of these materials is interesting because the GMR arises from spin-dependent scattering within the grains and at the interfaces between the grains and the non-magnetic matrix<sup>25</sup>.

CoAg is one such granular material, which has been widely studied over the past 10 to 15 years in correlation with structural, magnetic and magneto-optic properties both in layered structures and granular alloys<sup>26</sup>. This is principally because of mutual insolubility of Co and Ag, which offers the possibility of heterogeneity<sup>27</sup>. Due to spin-dependent scattering, the MR properties of these materials are highly dependent upon the granule size and percolation limit. If the granules in samples are large enough, multiple domain formation will occur, resulting in a loss of GMR. Likewise, if multilayers rather than granules are produced in the sputtering process, the sample will not display any GMR. CoAg is therefore a perfect exemplar material for growth within the combinatorial rig, as the properties are well known and are composition dependent.

Using the information obtained from the calibration matrix, it was determined that a uniform combinatorial film would be obtained when co-sputtering Ag (gun power of 35 W and 10 ° gun angle) and Co (gun power of 40 W and 10 ° gun angle) for a deposition time of 5 minutes. The pressure throughout the growth was kept constant at 5 mTorr. Energy Dispersive X-ray spectroscopy (EDX) measurements

were performed by Mr. Jeremy Mitchell using an FEI Siron S-FEG Field Emission Scanning Electron Microscope (SEM).

Measurements of k-ratios were taken of appropriate standards using a 20 keV acceleration voltage. This high voltage was required to obtain both K and L x-ray lines necessary for analysis by EDX. To accommodate the sample in the SEM chamber, the sample was cut into eight equal sized pieces, representing the distance across the substrate. After standards were measured, none of the optics were altered and the sample fragments were measured using the same settings. Due to time constraints, unfortunately it was not possible to obtain thickness measurements from the sample. Measurements of k-ratios were used by an algorithm supplied by the apparatus manufacturer to determine the composition gradient across samples, as shown below in Figure A2.13. These results show that whilst a composition gradient has been established across the sample, the full phase diagram was not accessed when the sample was prepared.

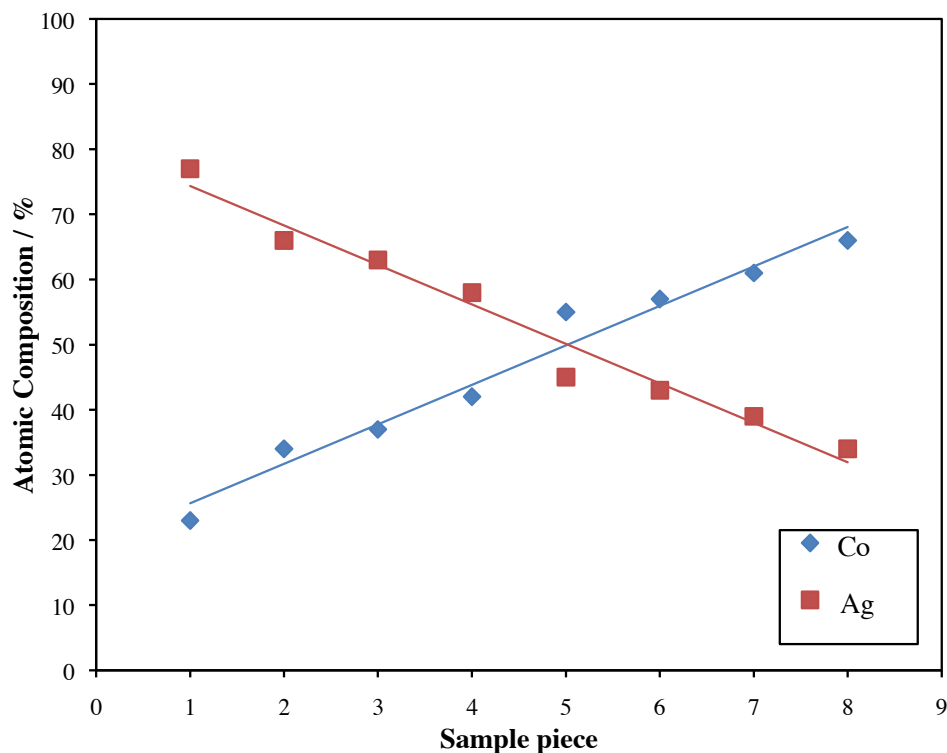


**Figure A2.13** – The variation in Co and Ag composition (in at%) across the substrate, determined by EDX analysis (data were acquired by Mr. Jeremy Mitchell).

MRE measurements were obtained for sample 7 (Co 61 at%, Ag 39 at%) within the 5 to 15 micron ( $66.67$  to  $200\text{ cm}^{-1}$ ) wavelength regime. Mr. Jeremy Mitchell also performed these measurements. The results of this analysis are shown below in Figure A2.14. Also shown in the figure are the MR results, recorded by Mr. Robert Armstrong, for the same sample. A scaling factor of 3.6 was used to correlate the MRE to the electrically determined MR. This scaled MR fits the MRE to within the experimentally determined error within the measurements. As MRE is proportional to the electrical MR, this further confirms that the MR changes across the CoAg library.

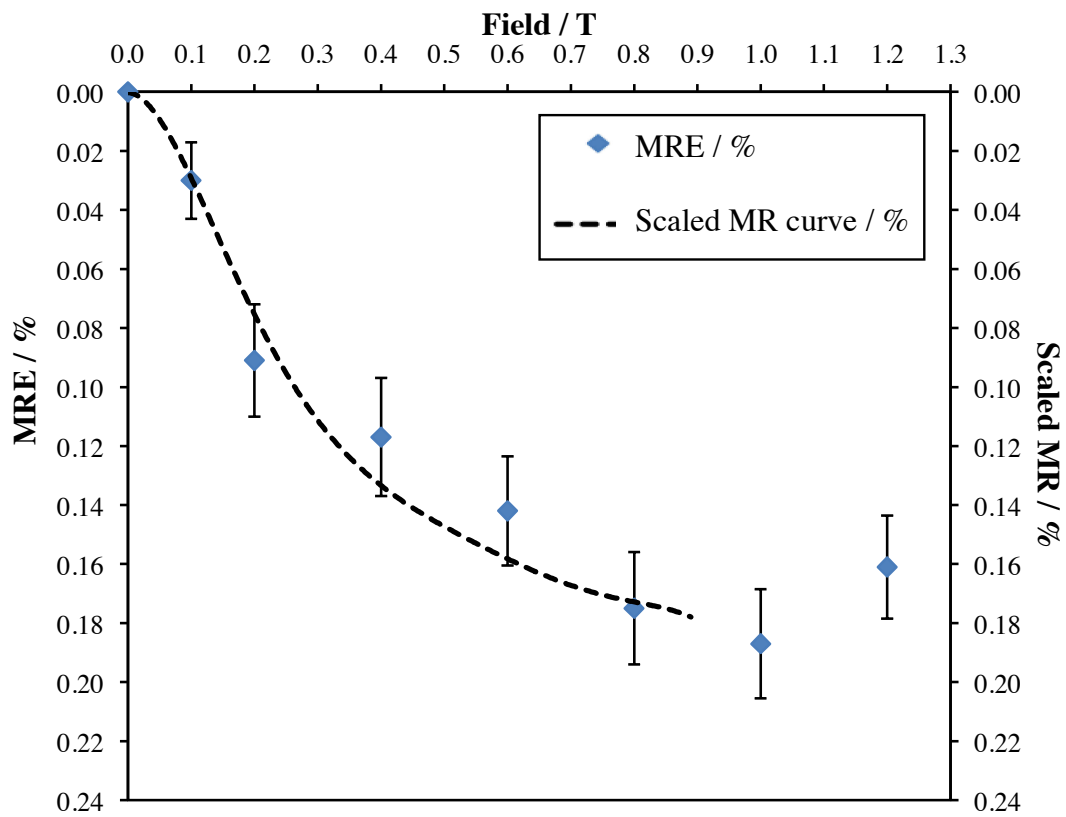


**Figure A2.14** – The MRE and scaled MR for sample piece 7 (Co 61 at.%, Ag 39 at.%) with increasing magnetic field. The MR was scaled by a factor of 3.6 in order to correlate with the MRE.

Mr. Robert Armstrong also measured the MR of all samples fragments using the four-point-probe technique. The results of these measurements for the maximum field ( $\sim 1\text{ T}$ ) are shown below in Figure A2.15. These results show that the MR varies as the composition across the substrate changes. As the Co composition increases, the MR also increases, but eventually plateaus. The maximum MR was

recorded from sample piece six, which corresponds to a composition of Co 57 at%, Ag 43 at%.

This can be rationalised in terms of the Co grain size, separation between grains and the formation of domains. As the concentration of Co increases, so can the granule size. Conversely, as the granule size increases, the separation between the grains decreases. The latter tends to improve the GMR, as the distance by which the spins have to diffuse will be shorter, meaning that the spin orientation is retained, as scattering is less likely. However, as the grain size increases, the magnitude of the GMR tends to decrease. Domain formation also leads to a reduction in the GMR. There are therefore competing factors which influence the magnitude of the GMR, leading to an optimum concentration of Co, where the various different factors balance and lead to a maximum GMR value, which explains the trend observed in Figure A2.15.

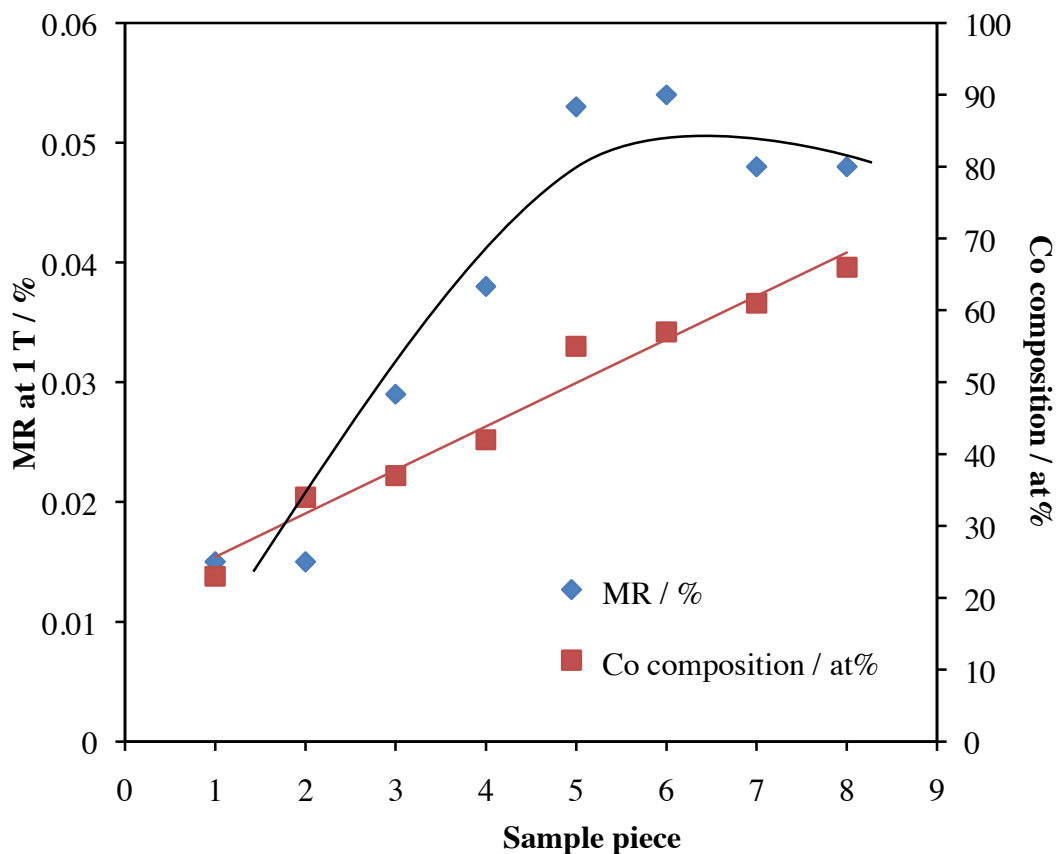


**Figure A2.15** – The variation in MR (at ~ 1 T) across the CoAg substrate (measured by Mr. Robert Armstrong). Also shown in the figure is the Co composition as determined by EDX (measured by Mr. Jeremy Mitchell).

These results show that combinatorial methods can be applied to magnetic materials in order to rapidly determine the composition dependent MR. As the MRE is non-contact, with a single set of measurements one can determine the optimum composition without damaging the sample.

### **2.2.3 AuPd combinatorial sample**

AuPd combinatorial samples were also prepared and analysed by XRF. In order to obtain reliable XRF measurements from consistent areas for a variety of different samples, a mask (Figure A2.2 (b)) was used when preparing the samples. A 50 kV energy and a spot size of 10  $\mu\text{m}$  (with no filters) was used for analysis. The XRF measurements were used to determine both the sample thickness and the composition. The results of these analyses for a representative sample are shown in Figure A2.16, with full data sets available in section A2.6. As with the CoAg sample, these results show that the full phase diagram was not accessed during growth. However, a large range of reactive Pd alloys has been prepared. Aside from two outliers, the thickness is relatively uniform at around 700  $\text{\AA}$ .

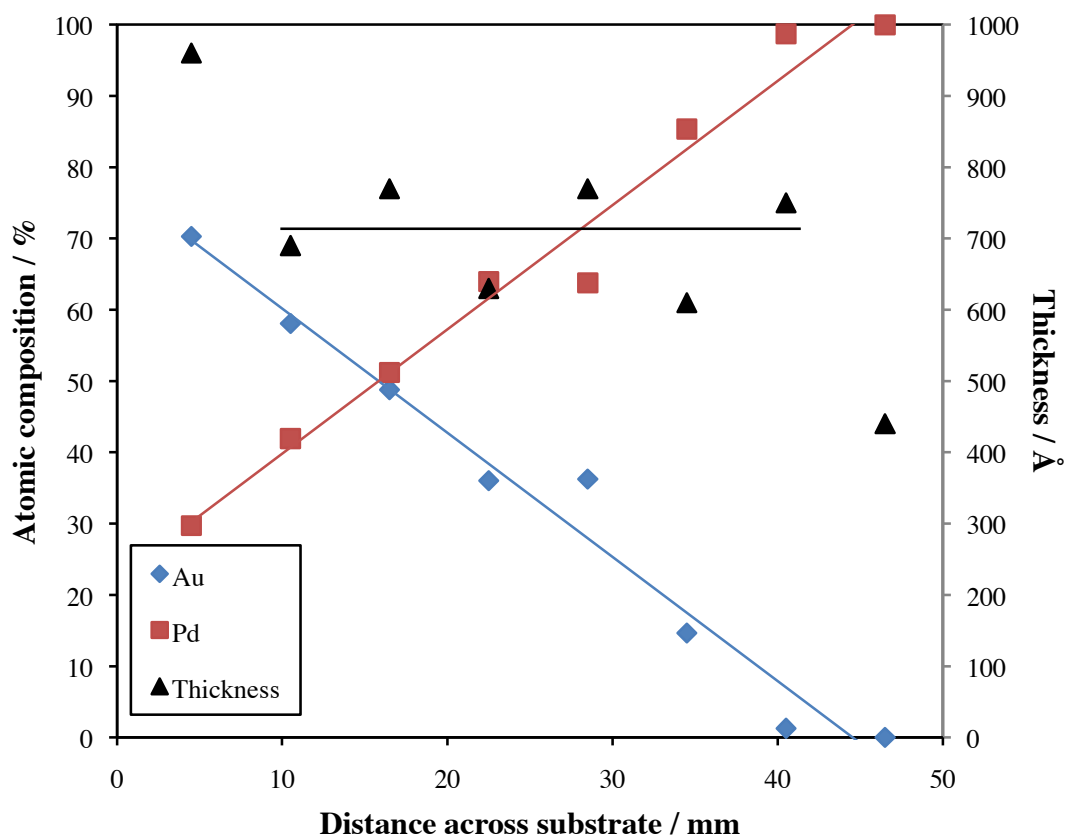


**Figure A2.16** – The variation in composition (in at%) and thickness (in Å) across the middle of the Au/Pd combinatorial film sample determined by XRF.

This shows that it is possible to create a range of alloy compositions with a relatively uniform film thickness. However, further work is required to obtain the full Au/Pd phase diagram within a single substrate, and characterise the reactivity of such catalyst libraries.

### A2.3 Future Work

Infrared thermography was first adopted for rapid screening of catalyst libraries in 1996, when Willson's group utilised the technique to screen arrays for the catalytic oxidation of hydrogen<sup>12</sup>. The combinatorial rig is equipped with a similar thermographic evaluation chamber, as shown in Figure A2.17. The evaluation chamber is fitted with an infrared-transparent ZnSe window designed for service from vacuum to 10 bar. An infrared camera (AIM-AEGIS IR, 256 × 256 PtSi array detector, spatial resolution 100 μm, thermal resolution 0.05 K and temporal

resolution 50 Hz) could be used to record the thermal profile of the catalyst library surface under reaction conditions. This technique requires accurate differentiation between catalyst library spots of similar reactivity. However, thermal analysis is complicated by the varying emissivity from different materials within the library, IR emission from hot gases in the reactor and IR reflection.

Future work would therefore include combining point-by-point emissivity correction and signal averaging available with the AIM IR system, with powerful image processing software (which would be developed using MATHCAD and/or MATLAB software) to facilitate accurate, time-resolved IR thermographic analysis. Au/Pd catalyst libraries could then be introduced into the attached reaction chamber *via* the transfer mechanism and screened using this thermographic technique for catalytic activity. Through the use of the AIM system, the temperature of the sample could be accurately measured during the course of the selective oxidation of crotyl alcohol. Once this was complete, the system could also be used, in principle, to examine different libraries and/or different chemical reactions. For exothermic reactions, the most active catalyst composition could be determined by means of the 'hot spot' on the surface. Conversely for endothermic reactions, this would correspond to a 'cold spot' on the film surface.

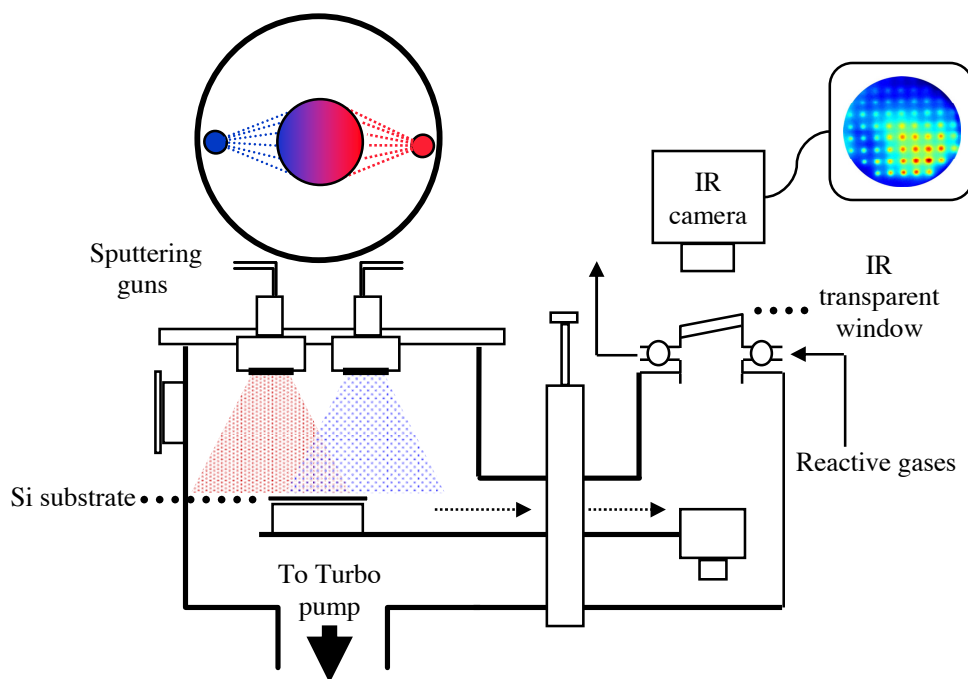


**Figure A2.17** – A simple diagram of the combinatorial sputtering chamber also showing the attached evaluation chamber. The diagram shows that main chamber is bolted (by means of a gate valve) to a thermographic evaluation chamber, whereby catalyst libraries prepared in the main chamber can be transferred for catalytic activity analysis by infrared thermography.

The same principle of infrared thermography could also be used to measure the difference in MR across a compositional gradient for a range of magnetic materials with a high level of spatial resolution. This technique has already been applied to a sample of Co/Cu with a spatial resolution of  $\sim 30 \mu\text{m}$  using a  $\text{CaF}_2$  lens (see Figure A2.18 below).

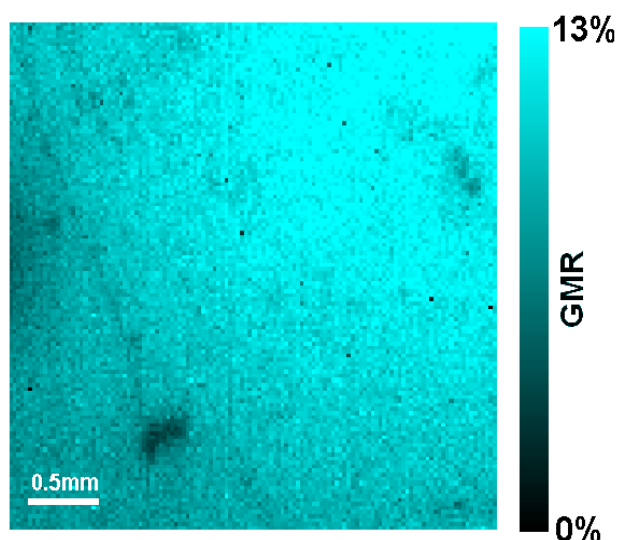


**Figure A2.18** – The spatial GMR calculated from IR emissivity measurements for a Co/Cu multilayer structure (sample provided by Seagate Technology (Ireland)).

The technique involves measuring the emissive,  $\varepsilon$  (rather than reflective) MRE from a heated sample within a magnetic field<sup>28</sup>. Differences in the resistivity ( $\rho$ ) and therefore conductivity result in changes to the emissivity of a material relative to a black body radiator (**Equation A2.2**).

$$\varepsilon \approx 2\sqrt{2\omega\varepsilon_0\rho} \quad \text{Equation A2.2}$$

The MR/GMR can then be related to the change in the emissivity according to an experimentally determined factor,  $\gamma$ , as shown below in **Equation A2.3**. This technique would allow the optimum MR to be determined for a whole library of magnetic materials.

$$\frac{\Delta\varepsilon}{\varepsilon} = \gamma \times \text{GMR} \quad \text{Equation A2.3}$$

In **Figure A2.2 (b)**, it was shown that a custom built mask was developed for the preparation of catalyst library ‘spots’. The selective analysis of product gas mixtures from each catalyst composition ‘spot’ within an alloy library could also be accomplished by means of scanning mass spectrometry. This technique is the critical assay method for determining reaction selectivity for catalyst libraries. For this purpose an evacuated reaction cell was constructed with a heated library stage, sampling probe feed-through and vacuum connections. It also included a gas

manifold and inlet capable of introducing a focused ( $< 1 \text{ mm}^2$ ) reactant beam. Finally, an integrated capillary sampler was developed which could be rastered ( $\sim 2 \text{ s spot}^{-1}$ ) across the library surface. Automation of this scanning process was achieved by interfacing the mass-spectrometer capillary probe with a motorised X-Y table driven by LabVIEW software. A simple diagram of this scanning rig is shown in

**Figure A2.19.**

Using the scanning rig, analysis of the residual gas could be achieved through the use of an MKS 'Mini-Lab' quadrupole mass spectrometer system equipped with triple-filters for high signal:noise/sensitivity and heated capillary inlet. Unfortunately, despite the development of the scanning rig, due to time constraints this instrument but was not used to examine catalyst libraries. Future work would therefore involve the sequential probe of individual catalyst spots in order to gauge the reactivity of Au/Pd libraries (prepared in section A2.2.3) for the selective oxidation of crotyl alcohol. As with the infrared thermography, this apparatus could also be adapted for use with other libraries or in order to examine other reactions of interest.

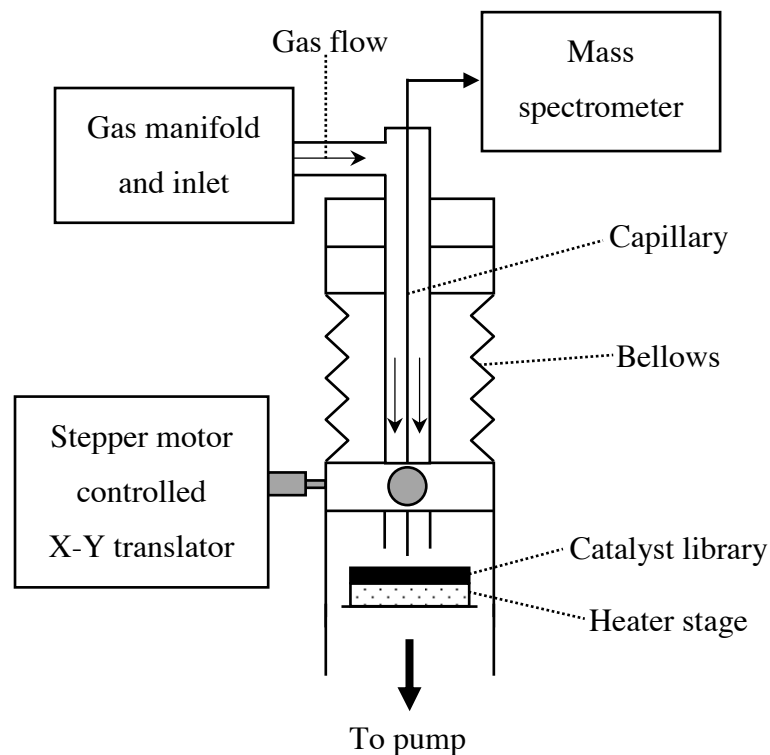


**Figure A2.19** – A simple diagram of the scanning mass spectrometer apparatus developed for screening the selectivity of catalyst alloy libraries.

#### **A2.4 Conclusions**

The calibration of the combinatorial sputtering rig has revealed that there is a linear dependence of the film thickness with increasing sputter-gun power and sputtering time. The situation is more complicated for the Ar pressure where an optimum pressure exists for the sputtering rate. The factor that has the greatest effect upon the composition gradient across the substrate is that of the sputter-gun angle. Despite the calibration matrix, in order to obtain the maximum gradient across the sample, several libraries had to be prepared. The gun angle requires further calibration, and possibly a more rigorous mathematical approach. As the relative sputtering rates are known for the materials within the combi-rig, the calibration matrix can be used to grow any combination of bimetallic materials a uniform film thickness with a composition gradient across the substrate.

Libraries of magnetic materials and catalysts were prepared based upon data recorded for the calibration matrix. EDX and XRF measurements have shown that a composition gradient exists across both sets of samples, although the full phase diagram for each set of materials has not yet been accessed. In the case of CoAg, it has been shown that the GMR and MRE also varies across the sample in accordance with the varying composition. Further work is needed to fully optimise the properties of these materials with full spatial resolution, which would include infrared thermography and scanning mass spectrometry. In this basic groundwork, it has demonstrated that combinatorial methods are potentially useful tools for aiding the optimisation of materials.

#### **A2.5 Flux Calculations/ Scale drawings of gun angles:**

$$\text{Useful flux} = \frac{\text{Flux deposited on substrate (A)}}{\text{Flux deposited on chamber (B)}}$$

0 degrees:

$$\frac{1.00 \text{ cm}}{21.76 \text{ cm}} = 0.046$$

10 degrees:

$$\frac{5.20 \text{ cm}}{(0.87 + 16.09) \text{ cm}} = 0.31$$

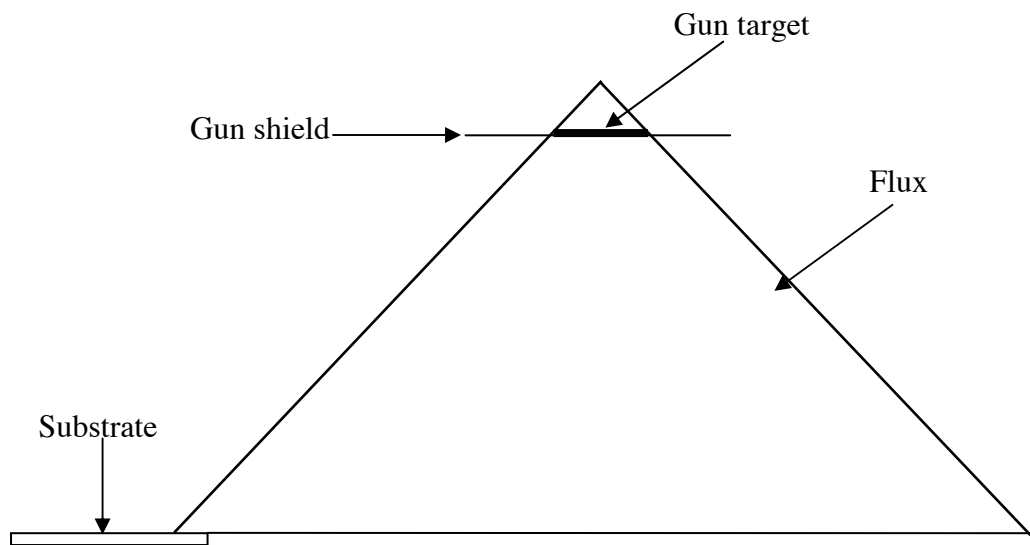
20 degrees:

$$\frac{5.20 \text{ cm}}{(13.27 + 12.81) \text{ cm}} = 0.20$$

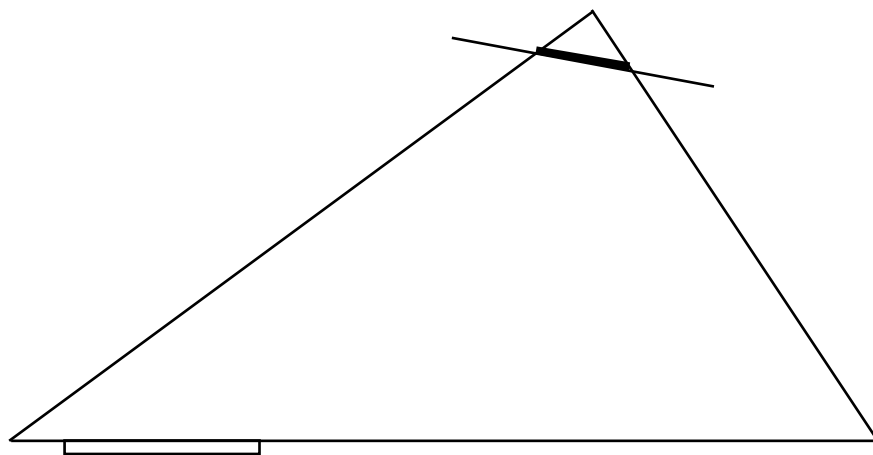
30 degrees:

$$\frac{1 \text{ cm}}{(40.73 + 8.56) \text{ cm}} = 0.11$$

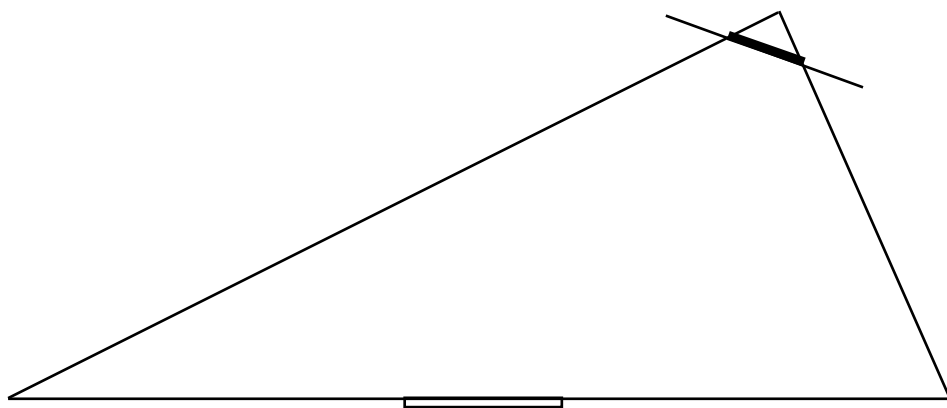
0 degrees (scaled to 50%):



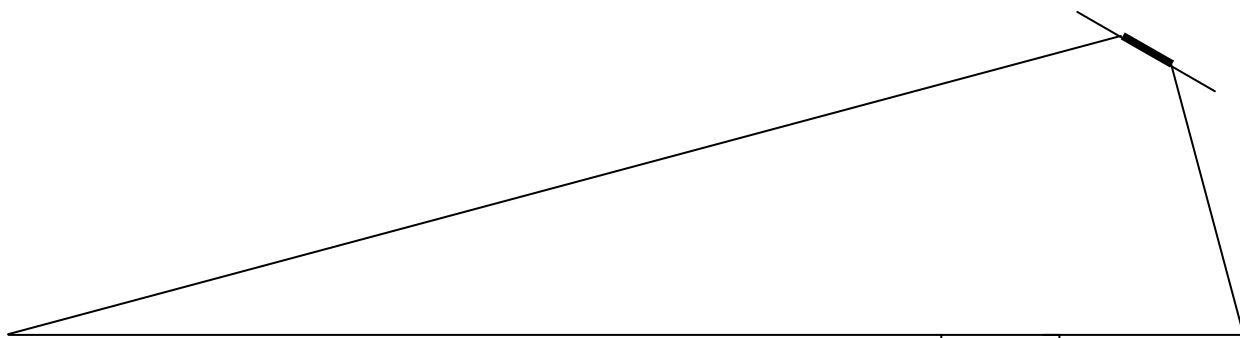
10 degrees (scaled to 50%):



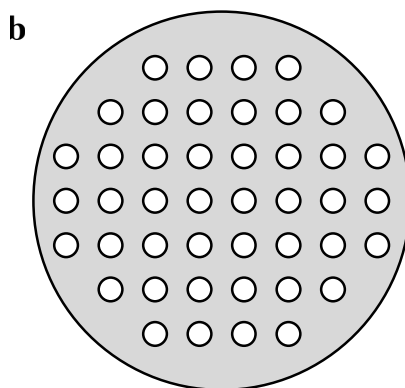
20 degrees (scaled to 40%):



30 degrees (scaled to 30%):



**A2.6 AuPd XRF results:**



Thickness / Å								std dev
		<b>650</b>	<b>750</b>	<b>720</b>	<b>670</b>			45.73
	<b>740</b>	<b>720</b>	<b>780</b>	<b>710</b>	<b>720</b>	<b>660</b>		39.20
<b>960</b>	<b>690</b>	<b>770</b>	<b>630</b>	<b>770</b>	<b>610</b>	<b>750</b>	<b>440</b>	116.76
<b>1010</b>	<b>650</b>	<b>580</b>	<b>700</b>	<b>660</b>	<b>680</b>	<b>730</b>	<b>810</b>	137.94
<b>420</b>	<b>750</b>	<b>620</b>	<b>620</b>	<b>520</b>	<b>790</b>	<b>510</b>	<b>330</b>	133.02
	<b>390</b>	<b>430</b>	<b>320</b>	<b>400</b>	<b>480</b>	<b>490</b>		63.06
		<b>310</b>	<b>330</b>	<b>390</b>	<b>370</b>			36.51
std	327.16	147.58	162.04	190.09	157.78	145.57	121.74	251.46

dev									
								average	614.3182

<b>Au composition / %</b>								std dev
		<b>60.43</b>	<b>36.85</b>	<b>11.83</b>	<b>7.4</b>			24.57
	<b>48.69</b>	<b>54.83</b>	<b>54.84</b>	<b>23.2</b>	<b>10.72</b>	<b>5.96</b>		22.46
<b>70.29</b>	<b>58.08</b>	<b>48.79</b>	<b>36.04</b>	<b>36.24</b>	<b>14.65</b>	<b>1.29</b>	<b>0.02</b>	24.02
<b>66.58</b>	<b>46.88</b>	<b>17.32</b>	<b>33.49</b>	<b>40.43</b>	<b>46.32</b>	<b>7.37</b>	<b>1.8</b>	19.79
<b>0.26</b>	<b>40.49</b>	<b>25.6</b>	<b>22.44</b>	<b>28.29</b>	<b>7.42</b>	<b>0.5</b>	<b>34</b>	15.39
	<b>0.27</b>	<b>0.23</b>	<b>0.32</b>	<b>1.12</b>	<b>0.04</b>	<b>0.08</b>		0.40
		<b>0.33</b>	<b>0.33</b>	<b>0.26</b>	<b>0.3</b>			0.03
39.40	22.48	25.30	20.15	16.19	15.85	3.37	19.12524	

<b>Pd composition / %</b>								std dev
		<b>39.57</b>	<b>63.15</b>	<b>88.17</b>	<b>92.6</b>			24.57
	<b>51.31</b>	<b>45.17</b>	<b>45.16</b>	<b>76.8</b>	<b>89.28</b>	<b>94.04</b>		22.46
<b>29.71</b>	<b>41.92</b>	<b>51.21</b>	<b>63.96</b>	<b>63.76</b>	<b>85.35</b>	<b>98.71</b>	<b>99.98</b>	24.02
<b>33.42</b>	<b>53.12</b>	<b>82.68</b>	<b>66.51</b>	<b>59.57</b>	<b>53.68</b>	<b>92.63</b>	<b>98.2</b>	19.79
<b>99.74</b>	<b>59.51</b>	<b>74.4</b>	<b>77.56</b>	<b>71.71</b>	<b>92.58</b>	<b>99.5</b>	<b>34</b>	15.39
	<b>99.73</b>	<b>99.77</b>	<b>99.68</b>	<b>98.88</b>	<b>99.96</b>	<b>99.92</b>		0.40
		<b>99.67</b>	<b>99.67</b>	<b>99.74</b>	<b>99.7</b>			0.03
39.40	22.48	25.30	20.15	16.19	15.85	3.37	37.59027	

## A2.7 References

1. J. Hanak, *Journal of materials science*, 1970, 5, 964-971.
2. E. McFarland and W. H. Weinberg, *Trends in biotechnology*, 1999, 17, 107-115.
3. H. Koinuma, H. Aiyer and Y. Matsumoto, *Science and Technology of Advanced Materials*, 2000, 1, 1-10.
4. H. Koinuma and I. Takeuchi, *Nature Materials*, 2004, 3, 429-438.
5. M. B. Brennan, *Chemical and Engineering News*, 2000, 78, 63-73.
6. H. Koinuma, *Applied surface science*, 2002, 189, 179-187.
7. J. Cooper, G. Zhang and P. J. McGinn, *Review of Scientific Instruments*, 2005, 76, 062221.
8. W. Maier, K. Stöwe and S. Sieg, *Angewandte Chemie International Edition*, 2007, 46, 6016-6067.
9. D. Farrusseng, *Surface Science Reports*, 2008, 63, 487-513.
10. J. Engstrom and W. Henry Weinberg, *AIChE journal*, 2000, 46, 2-5.
11. R. Hendershot, C. Snively and J. Lauterbach, *Chemistry – A European Journal*, 2005, 11, 806-814.
12. F. Moates, M. Somani, J. Annamalai, J. T. Richardson, D. Luss and R. C. Willson, *Ind. Eng. Chem. Res.*, 1996, 35, 4801-4803.
13. S. Henderson, J. Armstrong, A. Hector and M. T. Weller, *J. Mater. Chem.*, 2005, 15, 1528-1536.
14. J. Perkins, C. Teplin, M. v. Hest, J. Alleman, X. Li, M. Dabney, B. Keyes, L. Gedvilas, D. Ginley, Y. Lin and Y. Lu, *Applied surface science*, 2004, 223, 124-132.
15. X. Xiang, *Materials Science and Engineering B*, 1998, 56, 246-250.
16. R. Van Dover, L. Schneemeyer and R. M. Fleming, *Nature*, 1998, 392, 162-164.
17. C. Olk, *Measurement Science and Technology*, 2005, 16, 14-20.
18. C. Olk, G. Tibbetts, D. Simon and J. J. Moleski, *Journal of applied physics*, 2003, 94, 720-725.
19. K. Chang, M. Aronova and I. Takeuchi, *Applied surface science*, 2004, 223, 224-228.
20. N. Bassim, P. Schenck, M. Otani and H. Oguchi, *Review of Scientific Instruments*, 2007, 78, 072203.

21. H. Christen, C. Rouleau, I. Ohkubo, H. Y. Zhai, H. N. Lee, S. Sathyamurthy and D. H. Lowndes, *Review of Scientific Instruments*, 2003, 79, 4058-4062.
22. P. Ahmet, T. Nagata, D. Kukuruznyak, S. Yagyu, Y. Wakayama, M. Yoshitake and T. Chikyow, *Applied Surface Science*, 2006, 252, 2472-2476.
23. J. Hanak, H. Lehmann and R. K. Wehner, *Journal of Applied Physics*, 1972, 43, 1666-1673.
24. J. Xiao, J. Jiang and C. L. Chien, *Physical review letters*, 1992, 68, 3749-3752.
25. J. Du, W. Liu, Q. Li, H. Sang, S. Zhang, Y. Du and D. Feng, *Journal of Magnetism and Magnetic Materials*, 1999, 191, 17-24.
26. M. Angelakeris, E. Papaioannou, P. Pouloupoulos, O. Valassiades and N. Flevaris, *Sensors and Actuators A*, 2003, 106, 91-95.
27. M. Angelakeris, P. Pouloupoulos, O. Valassiades, N. Flevaris, D. Niarchos and A. Nassiopoulou, *Sensors and Actuators A*, 2001, 180-183.
28. S. Stirk, S. Thompson and J. Matthew, *Applied Physics Letters*, 2005, 86, 102505.

## Appendix 3

### Chapters 3 and 4:

MS fragment m/z	Identification
72	Crotyl alcohol ( $\text{H}_3\text{C}-\text{CH}=\text{CH}_2-\text{CHOH}$ )
70	Crotonaldehyde ( $\text{H}_3\text{C}-\text{CH}=\text{CH}_2-\text{CHO}$ )
56	Butene ( $\text{H}_3\text{C}-\text{CH}=\text{CH}-\text{CH}_3$ )
44	Carbon dioxide ( $\text{CO}_2$ )
41	Propene ( $\text{H}_3\text{C}-\text{CH}=\text{CH}_2$ )
32	Oxygen ( $\text{O}_2$ )
28	Nitrogen ( $\text{N}_2$ ) / Carbon Monoxide ( $\text{CO}$ )
18	Water ( $\text{H}_2\text{O}$ )
2	Hydrogen ( $\text{H}_2$ )

The main mass spectrometer fragments obtained during Thermal Desorption Spectroscopy (TDS) studies, along with their associated identification

### Chapter 6:

#### 6.1 Cross-section TEM sample preparation:

A  $5 \times 5$  mm sample is stuck to a glass slide film-side down by using a crystal bond wax. A diamond saw is used to cut a  $1 \times 5$  mm strip off the end of the sample. Residual wax is dissolved by placing cut the pieces in acetone. The  $1 \times 5$  mm strip is then cut in half using the same procedure. Once complete, the two sample pieces are cleaned using gently but thoroughly using a cotton bud soaked in acetone, in order to ensure that the film is cleaned of any debris. The closer these two pieces can be glued, the better quality the sample will be. Any residual acetone or organic impurity is removed from the surface by cleaning with ethanol and then isopropyl alcohol.

Gatan G1 glue should be mixed to 1 part hardener and 10 parts resin. Once heated this glue cannot be dissolved by acetone. The two  $2.5 \times 1$  mm strips are given a thin but full covering of this resin over the film, before being placed together film to film. The sample is then placed in a firm bulldog clip and placed on a hot plate at  $130\text{ }^{\circ}\text{C}$  for 15 mins to allow the glue to set. Two strips of silicon of  $5 \times 1$ mm are cut, cleaned and glued to the outside of this sandwich to provide structural support and to aid thickness measurements. Once again this is placed in a bulldog clip and heated to  $130\text{ }^{\circ}\text{C}$  for 15 mins.

The sample is then waxed to a glass slide, ensuring that the wax fully surrounds the sample for support. The sample is then polished to a shine by hand on one side, using diamond lapping paper. In doing so, it is important to ensure that polishing is conducted in-line with the interface, so that any scratches introduced are parallel to the interface rather than across it. This process is repeated, whilst successively scaling down from  $15\text{ }\mu\text{m}$  to  $9\text{ }\mu\text{m}$  to  $3\text{ }\mu\text{m}$  to  $1\text{ }\mu\text{m}$  lapping pads until the surface is shiny, flat, scratch free, and the interface is neat.

A  $3.05$  mm diameter copper grid with a  $2 \times 1$  mm slot is glued onto the top of this side, heated to loosen the wax and turned over in order to thin the other side. The sample is then thinned to  $\sim 200\text{ }\mu\text{m}$  thickness (including the thickness of the copper grid, but not the thickness of the glass slide) using the  $15\text{ }\mu\text{m}$  paper, then to  $\sim 120\text{ }\mu\text{m}$  using  $9\text{ }\mu\text{m}$  paper,  $\sim 100\text{ }\mu\text{m}$  using  $3\text{ }\mu\text{m}$  paper, and then using  $1\text{ }\mu\text{m}$  paper. The sample is then thinned to  $\sim 20\text{ }\mu\text{m}$  so that the interface is neat, clean and the silicon is transparent on both sides of the sample. Excess silicon is removed from outside of the copper grid and the sample is then gently washed with ethanol to remove debris. The sample then subjected to PIPS (precision ion polishing system) where the interface is thinned from above and below by Argon bombardment, whilst varying the angle and power of the plasma beams.

Typically for MgO substrates, this process is started  $6^{\circ}$  above and below with a beam of  $3.5\text{keV}$  in  $20 - 30$  min bursts until ‘rainbow fringes’ appear at the

interface, indicating that that area is reaching the ~ 200 – 400 nm thickness range. At this point the power should be decreased to between 2 – 2.5 keV and 15 min bursts applied until a small hole is formed at the interface. The power is then reduced further to 1 keV with 3 minute bursts at 7 ° above and below, followed by 0.5 keV for 3 mins at 7 – 8 ° above and below to clean around the hole. Ideally there will be areas of film on both sides which are around 10 nm thick, which are ideal for TEM imaging.

## 6.2 Crystal lattice spacing calculation based on diffraction pattern:

Calibration of camera length from the microscope (usually 25 cm or 30 cm):

$$d_x = \frac{nl_{hkl}^{MgO}}{nl_x} = \frac{nl_{200}^{MgO} d_{200}^{MgO}}{nl_x}$$

$$d_{200}^{MgO} = 2.105 \text{ \AA} = \text{Actual Distance}$$

$$4(l_{200}^{MgO}) \approx 18.396 \text{ pixels}$$

Example measurement:

$$4(l_{2210}^{MgO}) \approx 25.871 \text{ pixels}$$

$$d_{200}^{MgO} \approx \frac{18.396 \times 2.105}{25.871} = 1.496 \text{ \AA}$$

Actual distance = 1.4885, error of 0.5%, so acceptable

Calibration for 25 cm camera length:

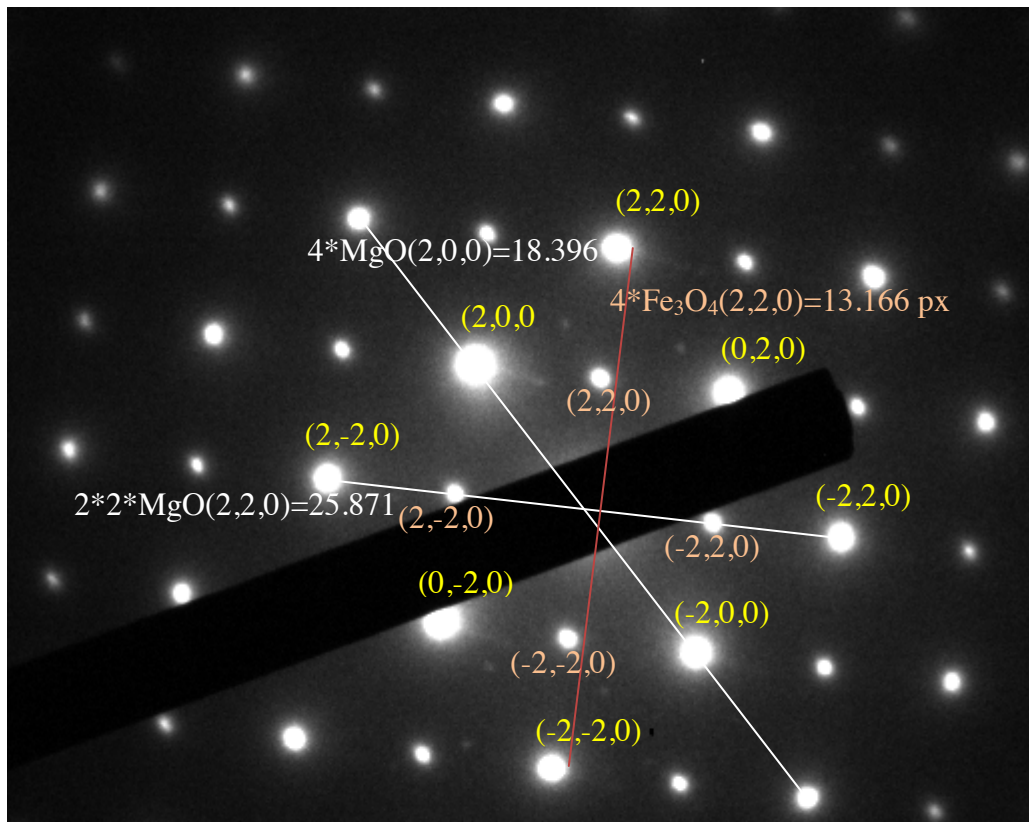
$$d_x \approx \frac{38.72358}{4l_x} \text{ \AA}$$

Confirming the structure of the film done using this calibration:

Suspected  $\text{Fe}_3\text{O}_4$  (2,2,0)  $4(I_{220}^{\text{Fe}_3\text{O}_4}) \approx 13.166$

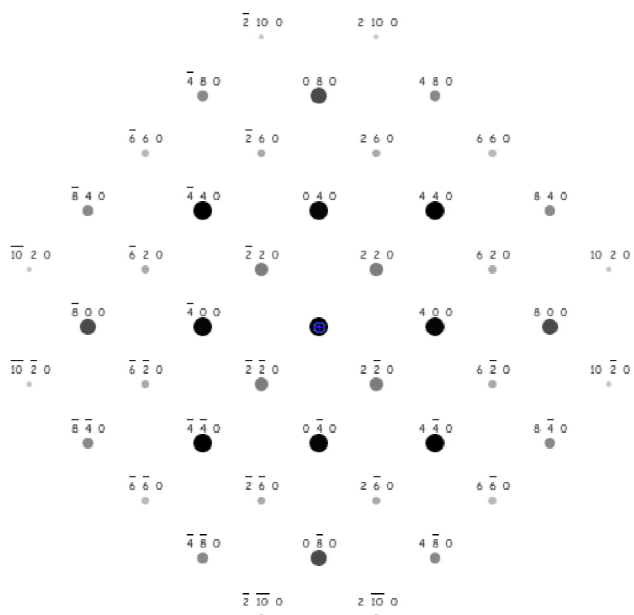
$$d_x \approx \frac{38.72358}{13.166} = 2.9411 \text{ \AA}$$

Real length = 2.9486Å, 0.2% difference, acceptable error.



Diffraction pattern obtained from  $\text{Fe}_3\text{O}_4$  on  $\text{MgO}(100)$

Center of Laue circle : (0.000, 0.000, 0.000)::Zone axis : [0, 0, 1]  
Tilt angle / deg. : 0.00

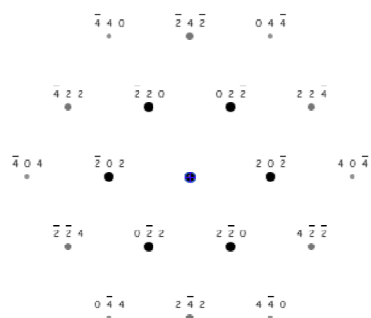


10 nm<sup>-1</sup>

ICSD\_29129 (44 reflections)  
AV/kV:200.00, CL/mm:7204, ZA:[0, 0, 1], FN:[0, 0, 1]

### Fe<sub>3</sub>O<sub>4</sub>(100) diffraction pattern

Center of Laue circle : (0.000, 0.000, 0.000)::Zone axis : [1, 1, 1]  
Tilt angle / deg. : 0.00

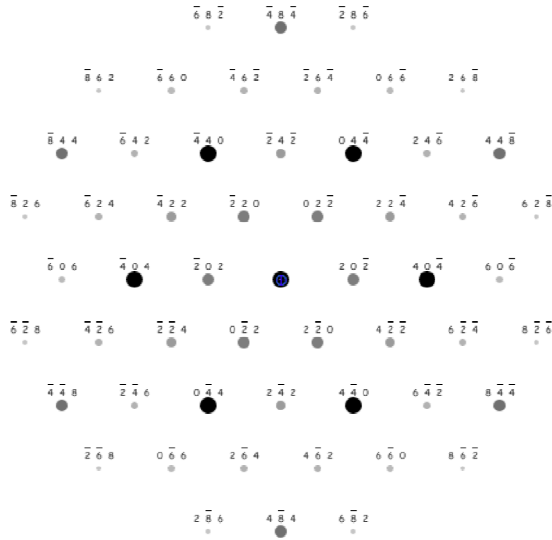


10 nm<sup>-1</sup>

MgO (18 reflections)  
AV/kV:200.00, CL/mm:4000, ZA:[1, 1, 1], FN:[1, 1, 1]

### MgO(111) Diffraction pattern

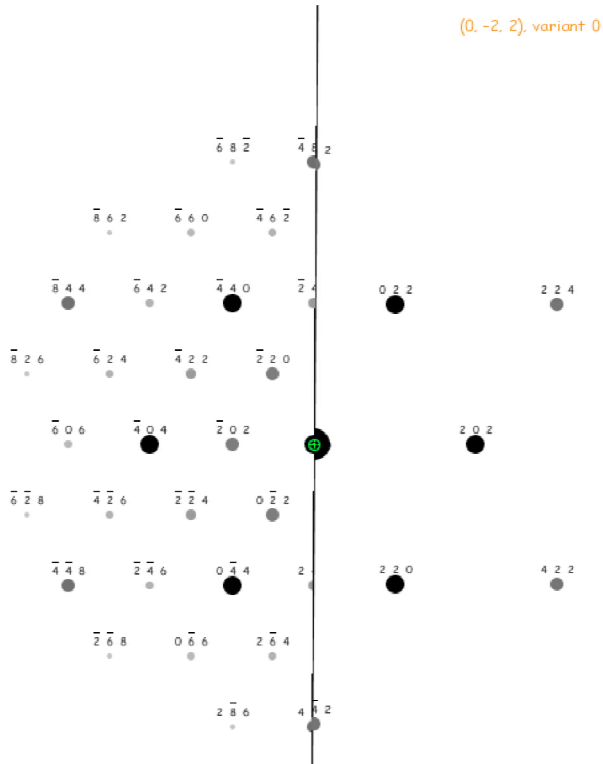
Center of Laue circle : (0.000, 0.000, 0.000); Zone axis : [1, 1, 1]  
Tilt angle / deg. : 0.00



10 nm<sup>-1</sup>

ICSD 29129 (54 reflections)  
AV/kV:200.00, CL/mm:7204, ZA:[1, 1, 1], FN:[1, 1, 1]

### Fe<sub>3</sub>O<sub>4</sub> (111) diffraction pattern



### Fe<sub>3</sub>O<sub>4</sub>(111) MgO(111) composite diffraction image

### 6.3 Derivation of linear approximation (Equations 6.21 to 6.22):

$$r_{123} = \frac{r_{12} + r_{23}(1 - 2i\beta)}{1 + r_{12}r_{23}(1 - 2i\beta)} \quad \text{Equation 6.21}$$

$$r_{13} = \frac{r_{12} + r_{23}}{1 + r_{12}r_{23}} \quad \text{Equation 6.22}$$

Divide  $r_{123}$  by  $r_{13}$ :

$$\frac{r_{123}}{r_{13}} = \frac{[r_{12} + r_{23}(1 - 2i\beta)](1 + r_{12}r_{23})}{[1 + r_{12}r_{23}(1 - 2i\beta)](r_{12} + r_{23})}$$

Expanding this equation:

$$\frac{r_{123}}{r_{13}} = \frac{r_{12} + r_{23}(1 - 2i\beta) + r_{12}^2r_{23} + r_{12}r_{23}^2(1 - 2i\beta)}{r_{12} + r_{12}^2r_{23}(1 - 2i\beta) + r_{23} + 1 + r_{12}r_{23}^2(1 - 2i\beta)}$$

$$\frac{r_{123}}{r_{13}} = \frac{r_{12} + r_{23} - 2i\beta r_{23} + r_{12}^2r_{23} + r_{12}r_{23}^2 - 2i\beta r_{12}r_{23}^2}{r_{12} + r_{12}^2r_{23} - 2i\beta r_{12}^2r_{23} + r_{23} + r_{12}r_{23}^2 - 2i\beta r_{12}r_{23}^2}$$

Factorising the numerator:

$$\begin{aligned} \frac{r_{123}}{r_{13}}(\text{numerator}) &= r_{12} + r_{23} + r_{12}^2r_{23} + r_{12}r_{23}^2 - 2i\beta(r_{23} + r_{12}r_{23}^2) \\ &= (r_{12} + r_{23}) + r_{12}^2r_{23}(r_{12} + r_{23}) - 2i\beta(r_{23} + r_{12}r_{23}^2) \\ &= (1 + r_{12}r_{23})(r_{12} + r_{23}) - 2i\beta(r_{23} + r_{12}r_{23}^2) \\ &= (1 + r_{12}r_{23})(r_{12} + r_{23}) - 2i\beta r_{23}(1 + r_{12}r_{23}) \\ &= (1 + r_{12}r_{23})(r_{12} + r_{23} - 2i\beta r_{23}) \end{aligned}$$

Factorising the denominator:

$$\begin{aligned}
\frac{\mathbf{r}_{123}}{\mathbf{r}_{13}}(\text{denominator}) &= \mathbf{r}_{12} + \mathbf{r}_{12}^2 \mathbf{r}_{23} + \mathbf{r}_{23} + \mathbf{r}_{12} \mathbf{r}_{23}^2 - 2i\beta(\mathbf{r}_{12}^2 \mathbf{r}_{23} + \mathbf{r}_{12} \mathbf{r}_{23}^2) \\
&= (\mathbf{r}_{12} + \mathbf{r}_{23}) + \mathbf{r}_{12} \mathbf{r}_{23} (\mathbf{r}_{12} + \mathbf{r}_{23}) - 2i\beta(\mathbf{r}_{12}^2 \mathbf{r}_{23} + \mathbf{r}_{12} \mathbf{r}_{23}^2) \\
&= (\mathbf{r}_{12} + \mathbf{r}_{23}) + \mathbf{r}_{12} \mathbf{r}_{23} (\mathbf{r}_{12} + \mathbf{r}_{23}) - 2i\beta \mathbf{r}_{12} \mathbf{r}_{23} (\mathbf{r}_{12} + \mathbf{r}_{23}) \\
&= (\mathbf{r}_{12} + \mathbf{r}_{23}) + (1 + \mathbf{r}_{12} \mathbf{r}_{23} - 2i\beta \mathbf{r}_{12} \mathbf{r}_{23})
\end{aligned}$$

Recombining the numerator and the denominator:

$$\frac{\mathbf{r}_{123}}{\mathbf{r}_{13}} = \frac{(1 + \mathbf{r}_{12} \mathbf{r}_{23})(\mathbf{r}_{12} + \mathbf{r}_{23} - 2i\beta \mathbf{r}_{23})}{(\mathbf{r}_{12} + \mathbf{r}_{23}) + (1 + \mathbf{r}_{12} \mathbf{r}_{23} - 2i\beta \mathbf{r}_{12} \mathbf{r}_{23})}$$

Rearranging:

$$\begin{aligned}
\frac{\mathbf{r}_{123}}{\mathbf{r}_{13}} &= \frac{1}{(1 + \mathbf{r}_{12} \mathbf{r}_{23})} \frac{(1 + \mathbf{r}_{12} \mathbf{r}_{23})(\mathbf{r}_{12} + \mathbf{r}_{23} - 2i\beta \mathbf{r}_{23})}{\frac{1}{(\mathbf{r}_{12} \mathbf{r}_{23})} (\mathbf{r}_{12} + \mathbf{r}_{23}) + (1 + \mathbf{r}_{12} \mathbf{r}_{23} - 2i\beta \mathbf{r}_{12} \mathbf{r}_{23})} \\
&= \frac{(\mathbf{r}_{12} + \mathbf{r}_{23} - 2i\beta \mathbf{r}_{23})}{\frac{(\mathbf{r}_{12} + \mathbf{r}_{23}) + (1 + \mathbf{r}_{12} \mathbf{r}_{23} - 2i\beta \mathbf{r}_{12} \mathbf{r}_{23})}{1 + (\mathbf{r}_{12} \mathbf{r}_{23})}} \\
&= \frac{\frac{1}{(\mathbf{r}_{12} + \mathbf{r}_{23})} (\mathbf{r}_{12} + \mathbf{r}_{23} - 2i\beta \mathbf{r}_{23})}{\frac{1}{(\mathbf{r}_{12} + \mathbf{r}_{23})} (\mathbf{r}_{12} + \mathbf{r}_{23}) + (1 + \mathbf{r}_{12} \mathbf{r}_{23} - 2i\beta \mathbf{r}_{12} \mathbf{r}_{23})}
\end{aligned}$$

$$\begin{aligned}
& \frac{(r_{12} + r_{23} - 2i\beta r_{23})}{(r_{12} + r_{23})} \\
= & \frac{(r_{12} + r_{23})}{(1 + r_{12}r_{23} - 2i\beta r_{12}r_{23})} \\
& \frac{1}{1 + (r_{12}r_{23})}
\end{aligned}$$

$$\begin{aligned}
& 1 - \frac{2i\beta r_{23}}{r_{12} + r_{23}} \\
= & \frac{1 - \frac{2i\beta r_{12}r_{23}}{1 + r_{12}r_{23}}}{1 + r_{12}r_{23}}
\end{aligned}$$

$$= \frac{(1 - 2i\beta) \left( \frac{r_{23}}{r_{12} + r_{23}} \right)}{(1 - 2i\beta) \left( \frac{r_{12}r_{23}}{1 + r_{12}r_{23}} \right)}$$

**Equation 6.21**

Now Taylor expand the denominator using  $(1 - x)^{-1} \approx 1 + x$ :

$$\frac{1}{(1 - 2i\beta) \left( \frac{r_{12}r_{23}}{1 + r_{12}r_{23}} \right)} \approx 1 + 2i\beta \left( \frac{r_{12}r_{23}}{1 + r_{12}r_{23}} \right)$$

As a result,  $r_{123}/r_{13}$  becomes:

$$\begin{aligned}
\frac{r_{123}}{r_{13}} & \approx \left[ 1 - 2i\beta \left( \frac{r_{23}}{r_{12} + r_{23}} \right) \right] \left[ 1 - 2i\beta \left( \frac{r_{12}r_{23}}{1 + r_{12}r_{23}} \right) \right] \\
& \approx 1 + 2i\beta \left( \frac{r_{12}r_{23}}{1 + r_{12}r_{23}} \right) - 2i\beta \left( \frac{r_{23}}{r_{12} + r_{23}} \right) \dots \text{higher order terms in } \beta
\end{aligned}$$

$$\begin{aligned}
&\approx 1 + 2i\beta \left( \frac{r_{12}r_{23}}{1+r_{12}r_{23}} - \frac{r_{23}}{r_{12}+r_{23}} \right) \\
&\approx 1 + 2i\beta \left[ \frac{r_{12}r_{23}(r_{12}+r_{23}) - r_{23}(1+r_{12}r_{23})}{(r_{12}+r_{23})(1+r_{12}r_{23})} \right] \\
&\approx 1 + 2i\beta \left[ \frac{r_{12}^2r_{23} - r_{23}}{(r_{12}+r_{23})(1+r_{12}r_{23})} \right] \\
&\approx 1 + 2i\beta \left[ \frac{r_{23}(r_{12}^2 - 1)}{(r_{12}+r_{23})(1+r_{12}r_{23})} \right]
\end{aligned}$$

**Equation 6.22**

$$r_{123} \approx r_{13} \left( 1 + 2i\beta \left[ \frac{r_{23}(r_{12}^2 - 1)}{(r_{12}+r_{23})(1+r_{12}r_{23})} \right] \right)$$

## List of Acronyms

**AES** – Auger Electron Spectroscopy

**amu** – atomic mass unit

**CrCHO** – crotonaldehyde

**CrOH** – crotyl alcohol

**DFT** – Density Functional Theory

**IR** - Infrared

**L** – Langmuir

**LEED** – Low Energy Electron Diffraction

**ML** – monolayer

**MDS** – Metastable De-excitation Spectroscopy

**MRE** – Magnetorefractive Effect

**MR** – Magnetoresistance

**MS** – Mass Spectrometry

**O<sub>(ads)</sub>** – Adsorbed oxygen

**RHEED** – Reflectance High Energy Electron Diffraction

**Selox** – Selective Oxidation

**TDS** – Thermal Desorption Spectroscopy

**TPD** – Temperature Programmed Desorption

**TPRS** – Temperature Programmed Reaction Spectroscopy

**UHV** – Ultra-high Vacuum

**UPS** – Ultra-violet Photoelectron Spectroscopy

**XPS** – X-ray Photoelectron Spectroscopy